Title
Modeling the Observational Signatures and Feeding of Super-massive Black Holes using Monte Carlo Radiative Transfer

Author
Roth, Nathaniel Jacob

Publication Date
2016

Peer reviewed|Thesis/dissertation

Modeling the Observational Signatures and Feeding of Super-massive Black Holes using Monte Carlo Radiative Transfer

By

Nathaniel Jacob Roth

A dissertation submitted in partial satisfaction of the

requirements for the degree of

Doctor of Philosophy

in

Physics

in the

Graduate Division

of the

University of California, Berkeley

Committee in charge:

Associate Professor Daniel Kasen, Chair
Professor Eliot Quataert
Professor in Residence Phillip Colella

Spring 2016

Modeling the Observational Signatures and Feeding of Super-massive Black Holes using Monte Carlo Radiative Transfer

Abstract

Modeling the Observational Signatures and Feeding of Super-massive Black Holes using Monte Carlo Radiative Transfer

by

Nathaniel Jacob Roth

Doctor of Philosophy in Physics

University of California, Berkeley

Associate Professor Daniel Kasen, Chair

This thesis presents numerical calculations designed to understand aspects of the feeding of, and feedback from, super-massive black holes at the centers of galaxies. The first portion of the thesis describes the development of radiative transfer tools used to address these problems. I present a description of how the Monte Carlo technique can be used to solve the radiative transfer equation, and I demonstrate a coupling of the transfer solution with the equations of hydrodynamics and statistical equilibrium. I next present two major applications of these ideas. The first is to quantify the effects of radiative feedback in active galactic nuclei in the form of radiation pressure on dust at the center of a gas-rich galaxy. The second is a calculation of the spectral energy distributions and optical spectral line strengths emitted during the tidal disruption of a star by a massive black hole. In so doing, I help to answer a number of puzzling questions relating to such disruptions, such as whether the lack of hydrogen emission in their spectra can be the result of radiative transfer effects rather than a lack of hydrogen in the disrupted star.

I dedicate this dissertation to my parents

Contents

Acknowledgments

Getting through graduate school is a collaborative project. Anything I've achieved has been the product of a great many people helping me along the way.

I can't overstate the gratitude I feel to my advisor, Dan. He has been supportive and attentive, always providing me with the time and resources to succeed. Most importantly, he has been kind, understanding, and patient friend. I consider myself incredibly fortunate to have worked with him. I've also learned a great deal from my academic siblings, Jennifer Barnes and Janos Botyanszki. Our "core 4" meetings were a great chance to reflect on our progress and the research challenges we were facing.

I've also been fortunate to work with co-authors and mentors who share the remarkable traits of providing unparalleled scientific insight while also being extraordinarily kind and supportive mentors. Eliot Quataert has provided me with helpful guidance throughout my time and Berkeley. I've benefitted greatly from regularly attending his group meetings, and he has graciously helped me prepare for my qualifying exam, apply for postdoctoral positions, and complete this thesis. Enrico Ramirez-Ruiz has been a superbly helpful collaborator and advocate for me. I thank him for his role in sparking my interest in tidal disruption events (TDEs), and for all of his help in my job search. James Guillochon also helped to inspire my interest in TDEs, and his impeccable attention to detail helped to ensure that our work together was of the highest quality. Philip Hopkins is largely responsible for my interest in super-massive black holes in general, and I thank him for his help as I sank my teeth into my first serious project in graduate school. Phillip Colella worked closely with me in developing the hydrodynamics solver used in Chapter 2 as part of an excellent course he taught on computational fluid mechanics; his willingness to spend time helping the students he instructs is exceptional.

My ability to choose my own path through graduate school was greatly enhanced through the Department of Energy Office of Science Graduate Fellowship Program (DOE SCGF), made possible in part by the American Recovery and Reinvestment Act of 2009. The fellowship not only helped me cover my basic needs but also provided travel funding that was invaluable in terms of allowing me to make professional connections early in my career.

The administrators of both the physics and astronomy departments at Berkeley have been a joy to work with. In physics, I want to especially thank Anne Takizawa, Donna Sakima, and Claudia Trujillo and Kathy Lee for all their hard work supporting me and all the other physics students. Thanks to Dexter Stewart, Nina Ruymaker, Rayna Helgens,

Bill Boyd, and the rest of the staff for "adopting" me into the astronomy department and supporting me every step of the way.

The life of a graduate student can be demoralizing at times, but my path was brightened by the many friends I made throughout my time in Berkeley. My friends from first year were crucial for helping me to get through quantum mechanics problem sets and the early grad school blues. I also found a home in the Berkeley Compass Project, which not only opened my eyes to the opportunities and challenges within undergraduate science education, but also allowed me to grow with and learn from the most thoughtful and dedicated students, researchers and educators I have ever met. And many of my happiest moments in grad school have come from spending time with my board game friends, who have helped to keep me sane and grounded, especially as I've made the final push to graduate.

I would not have been able to accomplish anything without the steadfast care of my parents. They have helped me every step of the way. I thank them for their willingness to listen patiently to my all of my worries and stresses, and then to calmly help me see how to move forward. They worked hard to help me graduate, not to mention everything else they've done for me my entire life.

Finally, I thank Kristi. It's been a long journey, and it has definitely been challenging, especially with an entire continent between us. I'm extremely fortunate to have her love and support over all these years. I wouldn't have made it to this point without her.

This dissertation was typeset using the ucastrothesis LaTeX template.

Chapter 1

Introduction

Before presenting the calculations relating to the observational signatures and feedback from super-massive black holes, it will be helpful to review the history of the discovery of these objects and the realization of their physical significance.

1.1 The discovery of super-massive black holes (SMBHs)

The story of SMBHs goes back to discovery of unusual point-like sources of radio emission given the name quasi-stellar radio sources, or quasars. A remarkable aspect of these objects was the unusually high redshift of the emission lines found in their spectra, such as the measurement of $z = 0.158$ for the quasar 3C 273 (Schmidt 1963). For this redshift to be cosmological in origin, it places the source at a luminosity distance of hundreds of Mpc, requiring a luminosity of at least $10^{12}\ L_{\odot}$ to match the observed radiative flux, a brightness that exceeds the combined stellar output of most nearby galaxies.

The following year, Salpeter and Zeldovich independently suggested accretion onto very dense objects as a way to achieve these luminosities (Salpeter 1964; Zel'dovich, Y. B. and Novikov, I. D. 1964). This was motivated by the fact that accretion onto a compact object is a highly efficient way of liberating energy. A test particle that loses angular momentum and spirals down to the innermost stable circular orbit of a Schwarzchild black hole will give up about 6% of its rest mass energy in the process. This fraction can grow as large to 40% for particular flows around Kerr black holes with maximal spin, but 10% is a typical value for radiatively efficient accretion (e.g. Frank et al. 2002).

It was later suggested (Lynden-Bell 1969, 1978; Rees 1978) that accretion onto SMBHs could explain the diverse emission from nearby galaxies harboring Active Galactic Nuclei (AGN), with quasars being the most luminous case. This argument was bolstered by Soltan (1982) who connected the present-day spatial density of quasar remnants to the integrated quasar luminosity over cosmological volumes and found it to be consistent with the presence of roughly one quasar remnant per present-day galaxy cluster. Thus, many nearby AGN could be the remnants of more luminous quasars, and nearby inactive galaxies (of sufficiently large total mass) likely harbor SMBHs that once grew through quasar-level accretion.

Additional arguments emerged in favor of the SMBH accretion model for powering AGN. For example, spatially resolved radio emission from quasars such as the aforementioned 3C 273 traced apparent super-luminal motion in the plane of the sky (Gubbay et al. 1969). This posed no conflict with special relativity provided that the material giving rise to the emission had a line-of-sight velocity component that was highly relativistic – the resulting Doppler beaming allows the light emitted at various locations along the source to chase each other and arrive in rapid succession from the observer's perspective, a situation anticipated by Rees (1966). These observations of collimated and highly relativistic outflows, known as jets, were most naturally explained by via physical processes that take place in the vicinity of a black hole with high spin (Blandford & Znajek 1977; Blandford & Payne 1982), although a complete understanding of their mechanics remains a topic of investigation to this day (e.g. Tchekhovskoy et al. 2011).

Another line of evidence came from the observation that the x-ray emission from some AGN exhibited variability on timescales as short as several minutes (Mushotzky et al. 1993). The appearance of an object generally cannot vary more rapidly than the light-crossing time across its diameter (Terrell 1967), with some exceptions including the case of highly relativistic jets as discussed above. Thus, the rapid variability points to emission from a region, presumably the inner portion of an accretion disk, localized within a radius of several times 10^{13} cm. This is approaching the Schwarzschild radius for a $10^8 M_\odot$ black hole.

Given these converging lines of evidence for the ubiquitous presence of SMBHs, the hunt was on to detect their presence more directly via their dynamical effect in galactic centers. Measurements of the velocity dispersion of the stars in the innermost portion of galactic bulges provided an approximate measurement of the amount of mass enclosed within that volume. A steep rise in the mass-to-light ratio toward at the center of a galaxy pointed to the presence of a SMBH there. Early success was reported by Kormendy & Richstone (1995), who summarized the dynamical evidence in favor of SMBHs residing at the center of the Milky Way and seven nearby galaxies. The case was made even stronger with the use of water maser emission to trace out a Keplerian rotation curve for the gas within the central tenths of parsecs of a galaxy, suggesting a mass density that could only be explained by a SMBH (Miyoshi et al. 1995). In the Milky Way, the orbits of individual stars at the galactic center could be measured, allowing for an inference of the central mass (several times $10^6 M_\odot$) with unprecedented precision (e.g. Genzel et al. 2000).

1.2 Galaxy correlations and the role of feedback

By this time, observations had suggested that SMBHs exist at the centers of most galaxies. The astrophysical significance of these objects grew as correlations were established between the inferred black hole masses and properties of their host galaxies. The early dynamical measurements had indicated a relationship between the SMBH mass and the estimated mass of the stellar bulge in which they reside (Richstone et al. 1998; Magorrian et al. 1998). Soon, an even tighter correlation was found between the SMBH mass and the

velocity dispersion of the bulge, a proxy for bulge mass, which has become known as the $M_{\rm BH} - \sigma$ relation (Ferrarese & Merritt 2000; Gebhardt et al. 2000; Tremaine et al. 2002). These correlations were highly mysterious, given that the gravitational sphere of influence of the SMBH is typically at least two orders of magnitude smaller than the diameter of the bulge, requiring additional physical processes to explain the connection. Nevertheless, it was clear that somehow a tight connection existed between the growth of SMBHs and the growth of their host galaxies, compelling researchers to study their relationship more intently.

As already discussed, black hole accretion is an incredibly efficient mechanism for extracting rest-mass energy and converting it to radiation or kinetic energy in outflows. Researchers began to investigate what might happen if a small fraction of that energy was reabsorbed by the host galaxy, a process that is now broadly termed feedback (Silk & Rees 1998). In one early study along these lines, Di Matteo et al. (2005) used hydrodynamic simulations to follow the aftermath of mergers of two comparably sized galaxies, a process that funnels a large amount of gas to the center of the merged galaxy and initiates a period of rapid SMBH growth and quasar-level accretion. These allowed 5% of the energy released during accretion to reheat the gas in merged galactic nuclei. As the black holes in these simulations grew, energy from the accretion was eventually deposited at rapid enough rates to unbind most of the remaining galactic gas that would have eventually formed stars had it been left undisturbed. This process therefore established a potential link between the mass of SMBHs and the mass of the stars in their host galaxies, in a manner consistent with the $M_{\rm BH} - \sigma$ relationship. As a bonus, this process suggested a mechanism for explaining an observed dichotomy in galaxies between those full of gas that are forming stars, and those that have lost their gas and have had their star formation quenched (Springel et al. 2005).

While promising, results of this type only scratched the surface of the SMBH-galaxy connection. An obvious limitation of such simulations was that they did not explain in detail what processes could allow for the recapture the required energy released during accretion to allow for effective feedback. Due to limitations in computational resources, this energy was put in "by hand" in the simulations – it was impossible to resolve all the relevant length and time scales to demonstrate how this process would work from first principles and go on to affect the entire galaxy.

An additional set of complications relates to the fact that black holes are not the only source of feedback in star-forming galaxies. Stars themselves play a role in limiting their own growth. Stellar feedback can take a variety of forms: massive stars can ionize and photo-evaporate their natal clouds; supernova explosions can disrupt the interestllar medium; and stellar radiation can be especially well-absorbed by dust particles, allowing for the transfer of large amounts of momentum via radiation pressure. Murray et al. (2005) derived analytic expressions demonstrating how the momentum transfer from these last two channels (supernovae and radiation pressure) may regulate the process of star formation and establish observed correlations between galactic luminosity and stellar velocity dispersion in galaxies that have ceased most of their star formation (Faber & Jackson 1976). These authors were also able to demonstrate how the $M_{\rm BH} - \sigma$ relation can arise via a similar mechanism in which radiation released during accretion exerts pressure on dusty gas and launches galactic

outflows that sweep away gas (see also King 2003).

Despite the vast body of work that has since arisen to explaining the $M_{\rm BH} - \sigma$ in terms of SMBH feedback, no consensus has been reached for the causal mechanism underlying it. The relative effectiveness of black hole vs stellar feedback in various circumstances remains under debate. This puzzle is connected to the aforementioned question of whether the energy released by black hole accretion can be successfully captured by galactic gas, or whether gas cooling is so efficient that the feedback must primarily rely on momentum-conserving processes like radiation pressure on dust. This is a topic to which we will return in Chapter 3.

1.3 The unexpectedly rapid growth of SMBHs

Observations of quasar emission over cosmic volumes indicate that a large portion of SMBH growth occurs during short periods of rapid accretion (recall Soltan 1982). However, recent discoveries of just how rapid this growth can be have highlighted our incomplete understanding of the manner by which accretion can proceed. For example, surveys of quasars by the Sloan Digital Sky Survey have uncovered dozens of quasars that formed at redshifts of $z > 6$, very shortly after the reionization of the universe (Fan 2006). In an infrared survey, a particularly striking discovery was that of a quasar at $z = 7.085$ with an estimated mass of at least $10^9 M_\odot$ (Mortlock et al. 2011). What makes these observations so surprising is that, in the case that the seeds of SMBHs are primordial stars of masses on the order of $10^2 M_\odot$ that form as early as $z \gtrsim 20$, then to achieve such large masses by $z = 7$ they must steadily accrete at a rate close to or above the Eddington rate (defined as the mass feeding rate at which the luminosity produced with some fiducial radiative efficiency would produces spherically averaged radiation pressure on free electrons that exceeds the gravitational attraction of the black hole) (Madau et al. 2014).

Accretion in these extreme (super-Eddington) conditions has remained a poorly understood process, at least until very recently. The most well-studied instances of disk accretion, those along the lines of the radiatively efficient thin disks originally described by Shakura & Sunyaev (1973), do not apply at mass feeding rates approaching the Eddington rate (separate but related departures from the thin-disk model also occur at much lower mass feeding rates). At higher feeding rates, the disk cannot cool as effectively, causing the disk to thicken (e.g. Paczyński & Wiita 1980; Abramowicz et al. 1988) and likely launching outflows(Shakura & Sunyaev 1973). Photons may become trapped and advected along with the accretion flow (Narayan & Yi 1994). The dynamical effects of radiation pressure become important in this regime, so that a fully self-consistent study of the flow requires a solution of the radiative transfer equation along with the equations of hydrodynamics. Outstanding questions include: what is the radiative efficiency for flows such as these, and to what extent can the radiated luminosity exceed the Eddington luminosity? What fraction of the incoming mass is accreted, and what fraction is launched in an outflowing wind? What is the kinetic luminosity of such a wind? Encouraging progress toward answering these questions has been made

in the last few years (McKinney et al. 2014; Jiang et al. 2014; Sądowski & Narayan 2016, e.g), although discrepancies and disagreements remain. In addition to further improvements in numerical techniques, more observational data relating to super-Eddington accretion onto SMBHs is likely required before a consensus can be reached.

1.4 Tidal disruption events (TDEs) as probes of feeding and feedback

Within the last few years, a new window onto SMBH accretion has opened. One of the most violent ways a SMBH can interact with its surroundings is by tidally tearing apart stars that pass too close to it. The resulting stellar debris streams can collide, shock, and accrete onto the black hole, giving rise to a luminous flare that peaks on timescales of weeks to months. TDEs were first predicted and explored theoretically decades ago (Hills 1975; Lacy et al. 1982; Carter & Luminet 1982; Rees 1988). There were some tantalizing early x-ray detections (e.g. Komossa & Bade 1999; Komossa et al. 2004), but it is only recently that TDEs have been observed systematically at a variety of wavelengths (e.g Bloom et al. 2011; Gezari et al. 2012; Arcavi et al. 2014; Miller et al. 2015; Cenko et al. 2016). A more comprehensive discussion of TDE observations will be presented in Chapter 4.

TDEs provide signals from SMBHs in galactic nuclei that would otherwise be unobservable. Ideally, TDEs can be used to measure the associated black hole masses. Given the well-stablished correlations between SMBHs and their host galaxies discussed above, this is crucial information for understanding galactic evolution at distances beyond which we can measure these black hole masses dynamically. In particular, TDE rates should be higher in galaxies hosting lower mass black holes (Phinney 1989). Recent observations suggest that the well-known correlations begin to break down in lower mass systems (Greene et al. 2010), making TDEs an especially valuable probe in such galaxies.

TDEs also provide data about the physics of SMBH accretion. The simplest theoretical models of TDEs predict that the rate at which mass falls back onto the black hole at late time should follow a characteristic $t^{-5/3}$ decline (Phinney 1989), and indeed this decline is often seen in the observed light-curves. This feeding rate provides a well-defined boundary condition for theoretical models of accretion, leading to the observation by Antonucci (2015) that TDEs may be conceptualized as the "Green's functions" for AGN accretion (an oversimplification, but still an evocative notion). Moreover, for a large range of black hole masses, the initial fallback rate is super-Eddington, followed by a transition to a sub-Eddington feeding rate (Rees 1988; Evans & Kochanek 1989). This provides an excellent opportunity to test the recent theoretical advances in radiation-pressure dominated accretion disks described earlier.

The recent breakthroughs in TDE observations, however, have exposed our incomplete theoretical understanding of how they operate. It is not clear how the stellar debris falls back, circularizes, and accretes onto the SMBH, producing observable emission at wavelengths spanning the x-ray to the optical. One explanation is that radiation from an accretion

disk is intercepted by an envelope of material at large radii and is reprocessed to longer wavelengths (Loeb & Ulmer 1997). However, the origin and structure of the reprocessing envelope is unknown. The envelope may be quasi-static and supported by radiation pressure (e.g. Coughlin & Begelman 2014). Other possibilities include outflows, or emission from rotationally supported disks involved in the circularization of the bound debris. Radiative transfer calculations can relate each of these models to observable light-curves and SEDs, allowing us to constrain which of them is responsible for the observed emission.

1.5 Outline of this thesis

In Chapter 2, I provide an overview of the equations of radiative transfer, including some description of how these equations are solved using Monte Carlo techniques. Additionally, I show how the terms in the radiative transfer equation relating to integrated energy and momentum exchange between the radiation field and the gas enter as source terms in the equations of hydrodynamics. I discuss a numerical method to solve the coupled radiation and hydrodynamics equations, along with a suite of test problems to validate the technique. Finally, I include a discussion of how the ionization state and bound electron level populations of a fluid are determined via the assumption of statistical equilibrium, without assuming local theromdynamic equilibrium (NLTE). I then demonstrate a successful coupling of the statistical equilibrium equations to the radiative transfer solver via a comparison to an analytic solution in the optically thin regime.

In Chapter 3, I discuss an application of these ideas to quantifying the effects of radiative feedback in AGN. In particular, I consider the effects of radiation pressure on dust at the center of a gas-rich galaxy, in a region commonly referred to as the dusty torus. I construct an ensemble of time-independent, three-dimensional snapshots of the radiation pressure on the gas while varying parameters such as the torus opening angle, the accretion luminosity, and the total amount of material in the torus. I then use these snapshots to estimate the time-evolved properties of the feedback such as the mass, momentum, and energy fluxes in the resulting outflows. The results of this chapter demonstrate that SMBH accretion may launch molecular outflows that play a role in quenching star formation, but they are not quite capable of generating the highest momentum-fluxes in the outflows that are seen in observations.

Finally, in Chapter 4 I present calculations of the x-ray through optical spectra near peak light for TDEs in a model in which the accretion luminosity is reprocessed through, a thick and extended static envelope. I demonstrate that the reprocessed optical radiation is a blend of emission at various temperatures, which argues against the practice of fitting a single blackbody to optical photometry data. I also find that varying the amount of material in the reprocessing envelope causes the overall optical flux to vary in a manner that keeeps the inferred color of the optical continuum unchanged, in agreement with one of the most mysterious aspects of optical TDE observations.

However, the most important result in this chapter relates to a debate about the emission

lines in TDE optical spectra. The ratio of the equivalent width of the He II line at 4686 to that of Hα varies substantially between events; in some cases the two lines are of comparable strength, while in other cases, the helium line appears at least twice as bright relative to the continuum compared to the hydrogen line. In at least two especially notable events, there did not appear to be any hydrogen emission at all (for a compilation of spectra, see Arcavi et al. 2014). These variations in the spectra have been interpreted to correspond to variations in the composition of the disrupted star (Gezari et al. 2012; Strubbe & Murray 2015). Under that interpretation, pure-helium stars are being observed at rates orders of magnitude above what one would expect based on the expected population of such stars. This claim is difficult to substantiate (see especially the arguments from MacLeod et al. 2012), and it has motivated theorists to seek alternative explanations for the variations in the line ratios.

Prior to this work, all such explanations were tested with photoionisation codes best suited for the irradiation of optically thin clouds. However, given the high densities of the stellar debris in a tidal disruption event, the problem called for a full radiative transfer calculation suited for optically thick environments. When the optically thick line transfer is properly treated, the helium-to-hydrogen line ratios can vary simply by adjusting properties of the reprocessing envelope such as its radial extent, even when exclusively considering stars with a solar helium-to-hydrogen composition. This can explain the diversity of line ratios across the observed TDEs, and it removes the need to postulate exotic processes that would lead to an exceptionally high tidal disruption rate for very rare stars.

Chapter 2

Methods

The content of this chapter, excluding Section 2.12, is drawn from Roth & Kasen (2015), with permission from the AAS and the co-author.

We explore the application of Monte Carlo transport methods to solving coupled radiation-hydrodynamics problems. We use a time-dependent, frequency-dependent, 3-dimensional radiation transport code that is special relativistic and includes some detailed microphysical interactions such as resonant line scattering. We couple the transport code to two different 1-dimensional (non-relativistic) hydrodynamics solvers: a spherical Lagrangian scheme and a Eulerian Godunov solver. The gas-radiation energy coupling is treated implicitly, allowing us to take hydrodynamical time-steps that are much longer than the radiative cooling time. We validate the code and assess its performance using a suite of radiation hydrodynamical test problems, including ones in the radiation energy dominated regime. We also develop techniques that reduce the noise of the Monte Carlo estimated radiation force by using the spatial divergence of the radiation pressure tensor. The results suggest that Monte Carlo techniques hold promise for simulating the multi-dimensional radiation hydrodynamics of astrophysical systems.

2.1 Introduction

The dynamical effects of radiation can be important in astrophysical contexts, so numerical simulations must often address the radiation transport problem. The radiation field, when treated fully, is a function of not only three spatial coordinates, but also of time, frequency and two direction angles. The high dimensionality of the problem makes it computationally very challenging, and approximate methods that ignore certain dependencies (e.g., on frequency and/or angle) are often employed. Recent efforts aim to relax these approximations and improve the accuracy of the transport scheme. Given the difficulty of the radiation-hydrodynamics (RHD) problem, and the critical importance of it in astrophysical simulation, a number of different numerical techniques should be explored. Ultimately, no single approach may prove ideal in every conceivable application, and the relevant tradeoffs in performance will need to be considered on a case by case basis.

In this paper we explore the coupling of Monte Carlo radiative transfer (MCRT) to hydrodynamics. The Monte Carlo approach offer several advantages as compared to a deterministic solution of the radiative transfer equation. MCRT generalizes readily to arbitrary 3-dimensional geometries, and can naturally incorporate multi-frequency, multi-angle, and time-dependent transport effects. It is also straightforward to include complex physical interactions, such as anisotropic and inelastic scattering processes, polarization, and resonant line scattering. MCRT methods generally parallelize well (although not necessarily trivially for memory intensive problems (Kasen et al. 2008)) and so can be run profitably on massively-parallel machines. This last consideration may ultimately prove to be the most significant, as the available computing power increases over time.

The main disadvantage of MCRT methods is the presence of stochastic error, such that the computation of a large number of packet trajectories may be required. A number of variance reduction techniques exist to help limit the unwanted effects of noise, and certain acceleration techniques can alleviate the well known computational inefficiency of MCRT in regimes of high optical depth. The ultimate expense of MCRT relative to other transport methods is difficult to estimate, but generally as the dimensionality of the problem increases, the advantages of Monte Carlo methods become more apparent. This suggests that MCRT will be competitive in addressing the full 3-D multi-angle multi-frequency RHD problem.

Here we present calculations using a MCRT code designed to handle the full-dimensionality of the Boltzmann transport problem – i.e., the dependence on 3 spatial dimensions, time, frequency and angle. The code is special relativistic and includes some more complex physical interactions, such as resonant line scattering. It makes use of implicit techniques (Fleck & Cummings 1971) in order to permit time-steps larger than the gas-radiation energy coupling time. For the sake of demonstrating the essential principles and assessing the viability of the approach, we restrict ourselves to coupling to a one-dimensional hydrodynamics solver; upcoming work will generalize to multi-dimensional RHD.

In section 2.2, we review some of the existing literature on RHD in astrophysics, including previous efforts in MCRT. In section 2.3 we outline the equations solved and the simplifying assumptions employed. Section 2.4 describes the Monte Carlo implementation, while section 2.5 describes our numerical hydrodynamics scheme. Section 2.6 describes the implicit Monte Carlo technique and its use in our code. Section 2.7 describes some radiation-only tests of our frequency-dependent transfer code. Section 2.8, the centerpiece of this paper, presents a suite of RHD test problems. Section 2.9 shows how Monte Carlo noise can be reduced by computing the radiation force via spatial derivatives of the Eddington tensor, rather than through a direct Monte Carlo force estimator. Section 2.10 provides some brief considerations of the numerical performance of our code and the possibilities for improving it in the future. Finally, Section 2.11 presents our conclusions.

2.2 Existing astrophysical radiation-hydrodynamics techniques

Radiation-hydrodynamics is a vast topic that spans many scientific disciplines. In this brief (and necessarily incomplete) review, we will emphasize multi-purpose astrophysical fluid codes.

One of the oldest and most commonly used techniques is flux-limited diffusion (FLD) (Levermore & Pomraning 1981; Swesty & Myra 2009). As its name suggests, in this approach radiation is transported via a diffusion equation , which amounts to dropping all terms in the radiative transfer (RT) equation with a higher-order than linear angular dependence. An interpolation procedure connects the optically thick to optically thin regimes and ensures that the transfer rate of radiative energy never exceeds the speed of light. Grid-based hydrodynamic and magneto-hydrodynamic (MHD) codes in use today making use of FLD include those described in Turner & Stone (2001); Hayes et al. (2006), Krumholz et al. (2007a), Gittings et al. (2008), Swesty & Myra (2009), Commerçon et al. (2011), van der Holst et al. (2011), Orban et al. (2013), Tomida et al. (2013), Zhang et al. (2013), Bryan et al. (2014), Kolb et al. (2013), and D'Angelo & Bodenheimer (2013). Additionally, Whitehouse & Bate (2004) describe a smoothed-particle hydrodynamics code that makes use of FLD.

While fast and relatively easy to implement, FLD suffers from some well-characterized shortcomings. It restricts the radiative flux to be in the direction of the radiative energy gradient, which can lead to misdirected radiation forces. As a result, the radiation in an FLD simulation will wrap around opaque barriers rather than cast sharp shadows.

An alternative method which alleviates this problem is the M_1 closure for the Eddington tensor (Dubroca & Feugeas 1999). Here, the two lowest-order angular moments of the RT equation are used. The radiation energy and pressure are related via an entropy minimization procedure, which results in the correct behavior in the free-streaming and diffusion limits. The M_1 closure has been implemented in astrophysical RHD codes including those described in González et al. (2007), Aubert & Teyssier (2008), Vaytet et al. (2011), Skinner & Ostriker (2013), Rosdahl et al. (2013), Sądowski et al. (2014), and McKinney et al. (2014).

Another option is to solve the full RT equation for discretized solid angle bins. This can be accomplished by solving the equation along rays that extend through multiple cells in the domain, a technique referred to as ray-tracing or a long-characteristics method. An early example of an astrophysical RHD code to use this approach is the stellar atmoshpere code described in Nordlund (1982), Nordlund & Stein (1990), and Stein & Nordlund (1998), using a variation of a method first proposed by Feautrier (1964). The long characteristics approach is especially effective in situations where a single or small number of luminous point sources are present, and a common application is tracking the ionizing radiation emitted from massive stars. Abel & Wandelt (2002) describes an an adaptively branching ray tracing procedure, and it has been applied to HD and MHD calculations coupled to ionizing radiation as described in Sokasian et al. (2003), Krumholz et al. (2007b) and Wise & Abel (2011). Other uses of ray tracing to track ionizing radiation include those described in

Whalen & Norman (2006), Alvarez et al. (2006), Henney et al. (2009), and smoothed-particle hydrodynamics implementations are described in Gritschneder et al. (2009) and Greif et al. (2009). Kuiper et al. (2010) introduced a hybrid approach in which ray tracing is used to follow the direct radiation from a point source, while FLD is used simultaneously to follow diffuse radiation.

A related method is the short-characteristics technique, which is a subset of S_N methods. Here, the RT equation is solved for a fixed set of angles within every grid cell. Early descriptions of such a technique were given by Mihalas et al. (1978) and Kunasz & Auer (1988). For problems in which the radiation enters the diffusion regime, so that the radiative emissivity is distributed over many grid cells, the short-characteristics approach allows the the computational expense of the problem to scale more slowly with the size of the grid than in the long characteristic case (Davis et al. 2012). An early example of an astrophysical RHD code to make use of the short-characteristics technique for two-dimensional problems is described in Stone et al. (1992). Liebendörfer et al. (2004), Livne et al. (2004), Buras et al. (2006), and Ott et al. (2008) describe codes that use short characteristics for neutrino transport, which is coupled to hydrodynamics in simulations of core-collapse supernovae. Vögler et al. (2005) describe an RHD code that uses short-characteristics in the context of stellar atmospheres. Rijkhorst et al. (2006) developed a hybrid method that combined techniques from both short- and long-characeterstics radiative transfer codes in the context of adaptive mesh refinement in three dimensions. Three-dimensional MHD simulations with radiation tracked using short characteristics include those described in Heinemann et al. (2007), Hayek et al. (2010), and Jiang et al. (2012). Overall, the short characteristics approach has proven to be accurate and reasonably fast. One potential drawback is the appearance of ray artifacts at large distances from luminous sources.

Petkova & Springel (2011) introduced an advection technique to solve the monochromatic radiative transfer equation on both structured and unstructured meshes. In the most general implementation of this scheme, the flux of radiative energy between zones is discretized into solid angle cones, which bears some resemblance to the short-characteristics method.

MCRT, while used for decades to simulate spectra and light curves of astrophysical objects (e.g. Mazzali & Lucy 1993; Kasen et al. 2006; Kerzendorf & Sim 2014), has only recently been employed in the context of astrophysical RHD. Lucy (2005) developed time-dependent (non-stationary) MCRT techniques for outflows in which radiation was not dynamically important. Ercolano & Gritschneder (2011) used MCRT to process snapshots of HD simulations to demonstrate that the diffuse radiation field in stellar ionization problems can differ significantly from an on-the-spot approximation for remitted ionizing photons. Haworth & Harries (2012) moved beyond snapshots and coupled MCRT of ionizing radiation, including the diffuse radiation field, to a hydrodynamics solver. Abdikamalov et al. (2012) applied MCRT to neutrino transport in core-collapse supernova simulations, and introduced extensions to the implicit Monte Carlo technique to the case of velocity-dependent transfer case (see section 2.6). Ghosh et al. (2011) and Garain et al. (2012) used MCRT to simulate the effects of Compton cooling in black hole accretion, and coupled this to a hydrodynamics solver. Noebauer et al. (2012) presented a general-purpose code that couples MCRT with

a Godunov solver for hydrodynamics, and validated its performance in a suite of common RHD test problems. Wollaeger et al. (2013) combined implicit Monte Carlo with discrete diffusion techniques in high velocity outflows on a Lagrangian grid.

In this work, we proceed in a manner similar to Noebauer et al. (2012), and repeat some of the test problems contained therein. We keep our radiation equations exact to all orders in v/c (see sections 2.3 and 2.4), although our hydrodynamics equations remain non-relativistic. Unlike previous studies of RHD using Monte Carlo, we include test problems in which the radiation energy is dominant over thermal energy, and where the radiation pressure is dynamically important. We compare two techniques that may be used to calculate the force from radiation pressure. Our approach also makes use of the implicit Monte Carlo technique.

2.3 Equations solved and simplifying assumptions

We review here a basic formulation of radiation-hydrodynamics. For this, we rely heavily on the expositions in Mihalas & Mihalas (1984) and Mihalas & Auer (2001), quoting directly many of the equations therein for ease of reference throughout the rest of this paper.

The equations governing the fluid flow are the mass conservation equation, the gas momentum conservation equation and the gas total (kinetic plus thermal) energy conservation equation, with source terms relating to radiative transfer. To order v/c, where v is the fluid velocity and c the speed of light, the equations are (Mihalas & Auer 2001)

$$\frac{\partial \rho}{dt} + \frac{\partial (\rho v^i)}{\partial x^i} = 0 \ , \tag{2.1}$$

$$\frac{\partial (\rho v^i)}{dt} + \frac{\partial}{\partial x^j}\left(\rho v^i v^j + p_0 \delta^{ij}\right) = \rho f^i + G^i - \frac{v^i}{c} G^0 \ , \tag{2.2}$$

$$\begin{aligned} \frac{\partial}{dt}\left[\rho\left(\frac{1}{2}v^2 + e_0\right)\right] \ &+ \ \frac{\partial}{\partial x^i}\left\{\left[\rho\left(\frac{1}{2}v^2 + e_0\right) + p_0\right] v^i\right\} \\ &= \ \rho v^i f^i + c G^0 \ . \end{aligned} \tag{2.3}$$

We have used the Einstein summation convention for indices, and the generic superscript index i may refer to the x, y, or z component of a vector in a Cartesian coordinate system. The subscript 0 denotes that quantities that are evaluated in the local comoving frame of the fluid. Otherwise, the quantity is evaluated in the frame of the fixed coordinate system, which we refer to as the lab frame. Thus, ρ is the lab frame fluid density, p_0 is the comoving gas pressure, e_0 is the comoving gas specific internal energy (units energy per mass), and f^i is a body force such as gravity as measured in the lab frame. The quantities G^0 and G^i are the lab frame components of the force four-vector, $\mathbf{G}$. This four-vector specifies the energy and momentum coupling between the fluid and the radiation, and will be defined explicitly below.

An ideal gas equation of state relates the comoving pressure and specific internal energy of the gas

$$p_0 = (\gamma_{\rm ad} - 1)\rho e_0 \ . \tag{2.4}$$

We do not consider here the fully special relativistic fluid equations. However, in our treatment of the radiation transport we will be careful to include all special relativistic terms. We also have not included terms for viscous transport, thermal heat conduction, or an internal energy source terms such as would arise in a fluid undergoing nuclear reactions, although these can in principle be included as well (Mihalas & Auer 2001).

To find the the radiation force four-vector $\mathbf{G}$, we begin with the lab frame radiative transfer equation

$$\frac{1}{c}\frac{\partial I_\nu(\mathbf{n})}{\partial t} + n^i \frac{\partial I_\nu(\mathbf{n})}{\partial x^i} = -\chi_\nu(\mathbf{n}) I_\nu(\mathbf{n}) + \eta_\nu(\mathbf{n}) \ . \tag{2.5}$$

Here I_ν is the specific intensity of the radiation, ν is the frequency, χ_ν (units cm^{-1}) is the total extinction coefficient, η is the total radiative emissivity, and $\mathbf{n}$ is a unit vector representing a direction. We may also make reference to the radiative source function $S_\nu \equiv \eta_\nu/\chi_\nu$. For notational brevity we will henceforth suppress writing the dependence of I_ν, χ_ν and η_ν on direction $\mathbf{n}$, and keep in mind that I_ν, χ_ν and η_ν are also be functions of position and time. Both χ_ν and η_ν have contributions from scattering as well as thermal absorption and re-emission, as we will discuss below.

It is useful to define moments of the radiation intensity which correspond to radiative energy density, flux, and pressure

$$E_\nu = \frac{1}{c}\oint I_\nu \, d\Omega, \qquad E = \int_0^\infty E_\nu d\nu \ , \tag{2.6}$$

$$F^i_\nu = \oint I_\nu n^i \, d\Omega, \qquad F^i = \int_0^\infty F^i_\nu d\nu \ , \tag{2.7}$$

$$P^{ij}_\nu = \frac{1}{c}\oint I n^i n^j \, d\Omega, \qquad P^{ij} = \int_0^\infty P^{ij}_\nu d\nu \ . \tag{2.8}$$

Equation 2.5 may be integrated over frequency and solid angle to obtain the radiation energy equation

$$\frac{\partial E}{dt} + \frac{\partial F^i}{\partial x^i} = \int_0^\infty d\nu \oint d\Omega \, (-\chi_\nu I_\nu + \eta_\nu) \equiv -cG^0 \ . \tag{2.9}$$

This is a conservation equation for the radiation energy density. The integral represents an energy loss term for the radiation field, and hence an energy source term for the fluid, and can therefore be identified with $-cG^0$.

Integrating equation 2.5 over frequency and then integrating with respect to $n^i d\Omega$ results in the radiation momentum equation

$$\frac{1}{c^2}\frac{\partial F^i}{dt} + \frac{\partial P^{ij}}{\partial x^j} = \frac{1}{c}\int_0^\infty d\nu \oint d\Omega \left[(-\chi_\nu I_\nu + \eta_\nu)\, n^i\right] \equiv -G^i \ . \tag{2.10}$$

This is a conservation equation for the radiation momentum density, and the integral can be identified with the term $-cG^i$. The problem has now been fully posed up to the specification of initial conditions and boundary conditions for the radiation and the fluid.

At this point, we will introduce some simplifying assumptions that will allow us to derive relatively simple expressions for the radiation four-force. These remain in effect for the entirety of this paper, although some or all of them could be relaxed in future work: (1) All absorption and emission, including scattering processes, are isotropic in the comoving frame. (2) Scattering in the comoving frame is elastic (energetically coherent). (3) The quantities η and χ can be decomposed into separate thermal and scattering contributions

$$\begin{aligned} \chi_{0\nu} &= \chi^t_{0\nu} + \chi^s_{0\nu} \ , \\ \eta_{0\nu} &= \eta^t_{0\nu} + \eta^s_{0\nu} \ . \end{aligned} \tag{2.11}$$

We will sometimes refer to $\chi^t_{0\nu}$ as the absorption coefficient. We will also find it useful to define an opacity[1] (units cm^2 g^{-1}) as $\kappa_{0\nu} = \chi_{0\nu}/\rho_0$, and $\kappa^t_{0\nu} = \chi^t_{0\nu}/\rho_0$, $\kappa^s_{0\nu} = \chi^s_{0\nu}/\rho$. We define an opacity ratio

$$\epsilon_\nu \equiv \frac{\kappa^t_{0\nu}}{\kappa_{0\nu}} = \frac{\chi^t_{0\nu}}{\chi_{0\nu}} \ . \tag{2.12}$$

The case $\epsilon_\nu = 0$ corresponds to complete scattering of photons, without any thermal absorption or re-emission. The case $\epsilon_\nu = 1$ corresponds to a situation with no scattering, in which every photon interaction corresponds to a photon being absorbed and its energy transferred to the gas.

For the thermal emission, we assume local thermodynamic equilibrium (LTE). In this case Kirchoff's law implies that the thermal component of the emissivity, $\eta^t_{0\nu}$, is equal to $\chi^t_{0\nu}B_{0\nu}$, where $B_{0\nu}$ is the Planck function calculated using the gas temperature measured in the comoving frame. Then we may write the total (thermal plus scattering) emissivity in the comoving frame as

$$\eta_{0\nu} = \chi_{0\nu}\left[\epsilon_\nu B_{0\nu} + (1-\epsilon_\nu)\frac{cE_{0\nu}}{4\pi}\right] \ . \tag{2.13}$$

When this expression for $\eta_{0\nu}$ is plugged into the comoving frame analogue of Equation 2.9, the scattering out of the beam ($\chi^s_{0\nu}I_{0\nu}$) cancels the scattering into the beam ($\eta^s_{0\nu}$) , and the energy component of $\mathbf{G_0}$ becomes

$$cG^0_0 = \int_0^\infty \epsilon_\nu \chi_{0\nu}\left(cE_{0\nu} - 4\pi B_{0\nu}\right) d\nu \ . \tag{2.14}$$

Meanwhile, the assumed isotropy of emitted radiation, both thermal and scattering, allows us to simplify the spatial components of the force four-vector,

$$G^i_0 = \frac{1}{c}\int_0^\infty \chi_{0\nu}F^i_{0\nu}d\nu \ . \tag{2.15}$$

[1]Our notation here differs slightly from Mihalas & Auer (2001), in which the symbol κ_0 is used for the extinction coefficient (units cm^{-1}) rather than for an opacity (units cm^{-2} g^{-1}).

Finally, we introduce three mean extinction coefficients (energy-weighted mean, Planck mean, and flux-weighted mean, respectively),

$$\chi_{0E} = \frac{\int_0^\infty \epsilon_\nu \chi_{0\nu} E_{0\nu} d\nu}{\int_0^\infty E_{0\nu} d\nu} , \tag{2.16}$$

$$\chi_{0P} = \frac{\int_0^\infty \epsilon_\nu \chi_{0\nu} B_{0\nu} d\nu}{\int_0^\infty B_{0\nu} d\nu} , \tag{2.17}$$

$$\chi_{0F} = \frac{\int_0^\infty \chi_{0\nu} F_{0\nu} d\nu}{\int_0^\infty F_{0\nu} d\nu} . \tag{2.18}$$

The expressions for the components of $\mathbf{G_0}$ then reduce to

$$cG_0^0 = c\left(\chi_{0E} E_0 - \chi_{0P} a_r T_{0,g}^4\right) , \tag{2.19}$$

$$G_0^i = \chi_{0F} F_0^i / c , \tag{2.20}$$

where $a_r = 7.5657 \times 10^{-15}$ erg cm^{-3} Kelvin^{-4} is the radiation constant, which arises from the integration of the Planck function over frequency.

We may then use a Lorentz transformation to determine the components of $\mathbf{G}$ in the lab frame

$$G^0 = \gamma \left[G_0^0 + \left(\frac{v^i}{c}\right) G_0^i \right] , \tag{2.21}$$

$$G^i = G_0^i + \gamma \frac{v^i}{c} \left[G_0^0 + \frac{\gamma}{\gamma + 1} \left(\frac{v^j}{c}\right) G_0^j \right] , \tag{2.22}$$

where $\gamma \equiv (1 - v^i v^i / c^2)^{-1/2}$. Equations 2.21 and 2.22 are accurate to all orders of (v/c) (Mihalas & Auer 2001). These two equations, along with the fluid equations (2.1 through 2.3), provide the high-level schematic for what our code solves. It is important to recognize that these are mixed-frame equations in the sense that the left-hand side refers to a lab frame quantity, while the right-hand side is written in terms of comoving quantities.

We still must specify the expressions we will use to compute the comoving quantities E_0 and F_0^i. One approach would be to first construct the radiation energy density, flux and pressure entirely in the lab frame, and then relate the lab and comoving values of these quantities using the fact that they are components of a second rank Lorentz covariant tensor, the radiation stress-energy tensor. This approach is described in Mihalas & Auer (2001), and it is also the way to derive the equations used in Lowrie et al. (1999) and Jiang et al. (2012), which have been truncated at order $(v/c)^2$. However, as will become clear below and in section 2.4, we are able to easily construct estimators of the flux in the comoving frame, and so we have a means of accurately calculating $\mathbf{G}$ without needing to compute and store the components of the pressure tensor.

We note that the radiation field, I_ν, is ultimately composed of photons with four-momenta given by $\mathbf{M} = (h\nu/c)(1, n^i)$. The lab frame and comoving frame components of the four-momentum are related via a Lorentz transformation

$$\frac{\nu_0}{\nu} = \gamma(1 - n^i v^i / c) , \tag{2.23}$$

and

$$n_0^i = \left(\frac{\nu_0}{\nu}\right)^{-1} \left[n^i - \frac{\gamma v^i}{c}\left(1 - \frac{\gamma n^j v^j/c}{\gamma+1}\right)\right] \ . \tag{2.24}$$

These equations incorporate the relevant Doppler shift and aberration effects. Two final transformations we will need are (Thomas 1930)

$$I_{0\nu} = \left(\frac{\nu_0}{\nu}\right)^3 I_\nu \ , \tag{2.25}$$

$$d\nu_0 d\Omega_0 = \left(\frac{\nu_0}{\nu}\right)^{-1} d\nu d\Omega \ . \tag{2.26}$$

Then we may write the comoving radiation energy density and flux as

$$E_0 = \frac{1}{c}\int_0^\infty d\nu_0 \oint I_0 d\Omega_0 = \frac{1}{c}\int_0^\infty d\nu \oint I_\nu \left(\frac{\nu_0}{\nu}\right)^2 d\Omega \ , \tag{2.27}$$

$$F_0^i = \int_0^\infty d\nu_0 \oint I_0 n_0^i d\Omega_0 = \int_0^\infty d\nu \oint I_\nu \left(\frac{\nu_0}{\nu}\right)^2 n_0^i d\Omega \ . \tag{2.28}$$

Equations 2.27 and 2.28 provide us with a means of computing E_0 and F_0, accurate to all orders in v/c, in terms of integrals of lab frame quantities (with the help of equations 2.23 and 2.24). It is straightforward to show that these equations are equivalent to those that follow from the Lorentz covariance of the stress-energy tensor (Mihalas & Mihalas 1984).

Finally, we consider an approximate alternative to equation 2.22 that is valid in the raditaive diffusion regime. Consider once again the convservation of radiation momentum as expressed in equation 2.10. As noted in Mihalas & Auer (2001), when the radiation is diffusing, the time-derivative on the left-hand side of that equation is at most on the order λ_p/l compared to the radiation force term on the right-hand side of the equation, where λ_p is the photon mean free path and l is the fluid flow length scale. Since $\lambda_p/l \ll 1$ by definition in the radiative diffusion regime, this term can be safely dropped, leaving us with

$$\begin{aligned} G^i &= -\frac{\partial P^{ij}}{\partial x^j} \ , \qquad \text{or} \\ G^i &= -\frac{\partial \left(f^{ij} E\right)}{\partial x^j} \ , \end{aligned} \tag{2.29}$$

where in the second line we have introduced the Eddington tensor f^{ij} which satisfies

$$P^{ij} = f^{ij} E \ . \tag{2.30}$$

In some situations, using equation 2.29 for G^i may reduce the Monte Carlo sampling noise (see section 2.9).

2.4 Monte Carlo Transport

To make use of equations 2.27 and either 2.28 or 2.29, we still must solve the radiation transfer equation. In the MCRT approach, one forgoes a direct numerical solution in favor of a stochastic simulation of photon transport. The radiation field is represented by discrete packets which are tracked through randomized scatterings and absorptions. Each packet is described by a lab frame energy E_p and a lab frame photon momentum four-vector $M_p = (h\nu/c)(1, n^i)$ where ν is the photon frequency and $\mathbf{n}$ the normalized propagation direction vector measured in the lab frame. The number of photons represented per packet is then $N = E_p/h\nu$.

In many cases, we initialize the radiation field based on the assumption of local thermodynamic equilibrium (LTE). This assumption is justified in most test problems we consider here, as the gas is optically thick to radiation across each zone. At the start of the calculation, a set number of packets, $N_{\rm init}$, are initiated in each zone. The radiation energy $a_r T_{0,g}^4 V_0$ is distributed equally among the packets in each zone. The packet comoving frequencies are sampled from a blackbody distribution at the local temperature and their directions are sampled isotropically in the comoving frame.

If necessary, it is possible to initialize photon packets without assuming LTE, as we will discuss for two test problems (section 2.8.1 and section 2.8.4).

Photon packets are tracked in the lab frame, but the gas extinction coefficients and emissivities are calculated in the comoving frame. The extinction coefficient in the comoving frame $\chi_{0\nu}$ is then transformed into the lab frame using (Thomas 1930)

$$\chi_\nu = \frac{\nu_0}{\nu}\chi_{0\nu} \ . \tag{2.31}$$

While we have assumed that the comoving extinction is isotropic, in moving flows the lab frame extinction χ_ν is direction dependent (because of equations 2.31 and 2.23). The mean free path is longer for photons propagating along the flow and smaller for photons propagating against it, a property that is essential to include to get the correct advection of radiation (see section 2.8.2).

The distance l_k a photon travels in the lab frame before an interaction can be randomly sampled using

$$l_k = \chi_\nu^{-1}[-\ln(R)] \ , \tag{2.32}$$

where R is a uniform random number between 0 and 1, not including 0. This distance can be compared to the distance to the nearest cell boundary and the distance to the end of the time-step ($\Delta t/c$) to determine the next event. In an interaction event, a packet may be either scattered or absorbed, with the probability of absorption at a given frequency denoted by ϵ_ν. More details about how photon interactions are implemented are given in section 2.4.1

At each time-step, new packets may be generated to represent freshly radiated thermal energy. The emission of this energy provides the cooling contribution in equation 2.19. The

number of photon packets emitted in a zone over a lab frame time-step Δt is

$$N_{\rm emit} = \frac{V\,\Delta t\,\epsilon\,\chi_{0P}\,c\,a_r\,T_{0,g}^4}{E_{0,p}}\ . \tag{2.33}$$

This expression will be modified slightly when implicit MCRT techniques are employed (section 2.6). Here V is the zone volume measured in the lab frame. We have made use of the fact that $V dt = V_0 dt_0$ (Mihalas & Mihalas 1984), so to lowest order we may write $V\Delta t = V_0\Delta t_0$. $E_{0,p}$ is the energy (not energy density) of each packet in the comoving frame. The value of $E_{0,p}$ can be chosen arbitrarily and ultimately sets the total number of packets included in a calculation. Typically, we choose the packet energy to be a small fraction of the zone energy, $E_{0,p} = 10^{-4}E_0V_0$, however we limit the number of packets emitted per zone per time-step to a manageable maximum value (see Table 2.1). The emitted packet's direction is sampled uniformly from an isotropic distribution in the comoving frame. The frequency of the packet is sampled from a distribution weighted by the comoving thermal emissivity, $\chi_{0\nu}\epsilon_\nu B_{0\nu}$. The packet energy, frequency and direction are then transformed into the lab frame using equations 2.23 and 2.24.

Radiative heating could, in principle, be evaluated by tallying the number of photon packets absorbed in each zone over a time interval. In any given time-step, however, the number of packets actually absorbed may be very small, especially if the medium is scattering dominated ($\epsilon_\nu \ll 1$). Instead, we can construct estimators in each cell of the comoving radiation energy density and radiation flux (equations 2.27 and 2.28) by summing over all path lengths of packets moving through the zone (Lucy 1999)

$$E_0 = \tfrac{1}{cV\Delta t}\textstyle\sum_p E_p \left(\frac{\nu}{\nu_0}\right)^2 l_p \tag{2.34}$$

$$F_0^i = \tfrac{1}{cV\Delta t}\textstyle\sum_i E_p \left(\frac{\nu}{\nu_0}\right)^2 l_p n_0^i\ , \tag{2.35}$$

where E_p is the lab frame energy of packet p, l_p is the length of the path the packet travels through the zone (which may be composed of multiple redirections), and we are again substituting $V\Delta t$ for $V_0\Delta t_0$.

The flux estimator relies on the cancellation of packets moving in opposite directions, so it may be poorly sampled in practical calculations. As noted in Section 2.3, when the radiation is diffusing we may use the divergence of the lab-frame radiation pressure tensor to compute G^i (equation 2.29). In this case, P^{ij} is computed with the estimator

$$P^{ij} = \frac{1}{cV\Delta t}\sum_p E_p l_p n^i n^j\ . \tag{2.36}$$

2.4.1 Interaction Physics

One advantage of MC transport methods is that it is relatively straightforward to simulate complicated physical interactions, such as anisotropic scattering, line transport, or polarization. In this section, we describe the treatment of select matter/radiation interactions.

Absorption and Coherent Scattering

In the simplest of interaction events, a packet may be either coherently scattered or absorbed, with the probability of absorption at a given frequency, ϵ_ν, determined by the nature of the absorption interaction. In an explicit MC calculation, absorbed packets are simply removed from the calculation. In implicit MC calculations, some absorbed packets are not removed but instead undergo "effective scattering", as will be described in Section 2.6.

To simulate an isotropic, coherent scattering event, a packet is first Lorentz transformed to the comoving frame of the scatterer using 2.23 and 2.24. A new direction is then sampled isotropically in the comoving frame, and the inverse transformation is applied to return the lab frame. In this process, the lab frame energy of the photon becomes

$$E_{\rm out} = E_{\rm inc} \frac{1 - n^i_{\rm inc} v^i/c}{1 - n^i_{\rm out} v^i/c} \ , \tag{2.37}$$

where $n^i_{\rm inc}$ and $n^i_{\rm out}$ are the incoming and outgoing packet direction vectors in the lab frame. The packet frequency changes in a corresponding way. When averaged over many scattering events, Eq. 2.37 accounts for the adiabatic losses of the radiation field. Advection is captured via the anisotropy of the lab frame extinction coefficient χ and the outgoing direction vector $n^i_{\rm out}$.

If desired, one can also take into account the random motions of scatterers, which may introduce additional Doppler shifts. In this case, the velocity vector of the individual scatterer must be randomly sampled at each interaction event. For example, the speed of a scatter could be randomly sampled from a Maxwell Boltzmann distribution with velocity dispersion $v_{\rm d} = (2KT/m_s)^{1/2}$, where m_s is the mass of the scatterer. The direction of the scatterer velocity vector is sampled from an isotropic distribution. The photon packet is then Lorentz transformed into the rest frame of the scatterer, a new propagation direction is chosen, and then the packet transformed back into the lab frame.

Line Interactions

The frequency-dependent cross-section of a line with rest frequency ν_0 and oscillator strength $f_{\rm osc}$ is

$$\sigma(x) = \frac{\sqrt{\pi} e^2}{m_e c} \frac{f_{\rm osc}}{\Delta\nu_{\rm d}} H(a,x) \ , \tag{2.38}$$

where x is the frequency relative to line center in units of Doppler widths $x = (\nu - \nu_0)/\nu_{\rm d}$, where $\Delta\nu_{\rm d} = \nu_0(v_{\rm d}/c)$ and we take the velocity dispersion $v_{\rm d}$ to be due to thermal line broadening. The line profile is described by the Voigt function

$$H(a,x) = \frac{a}{\pi} \int_{-\infty}^{\infty} \frac{e^{-y^2}}{(x-y)^2 + a^2} dy \ . \tag{2.39}$$

The parameter a describes the importance of the wings relative to the core of the line profile, and is a function of temperature

$$a = 4.7 \times 10^{-3} \ (T/10^4 \ {\rm K})^{-1/2} \ . \tag{2.40}$$

We use the analytic fits for the Voigt profile provided by Tasitsiomi (2006).

The line absorption coefficient, $\alpha = n_l\sigma(x)$, depends on the the number density, n_l, of ions occupying the lower level of the transition, and hence requires knowledge of the ionization and excitation state of the gas. In the case of LTE, the state of the gas is readily determined by solving the Saha/Boltzmann equations. When LTE does not hold, the level populations must be determined by solving a set of coupled rate equations, with the radiative transition rates estimated from the Monte Carlo transport. We postpone a discussion of the non-LTE problem, and assume here that the level population n_l is known.

To account for the thermal motions of ions, we randomly sample the ion velocities in a manner similar to that described in Section 2.4.1. However, since the line cross-section depends sensitively on frequency, the line-of-sight velocity $v_\parallel$ must be sampled from the modified distribution (Zheng & Miralda-Escudé 2002)

$$f(u_\parallel) = \frac{a}{\pi}\frac{e^{-u_\parallel^2}}{(x-u_\parallel)^2+a^2}H^{-1}(a,x) \ , \tag{2.41}$$

where $u_\parallel = v_\parallel/v_d$. The transverse velocity components are sampled from the ordinary Maxwell-Boltzmann distribution

$$\begin{aligned} v_{\perp,1} &= v_\mathrm{d}\sqrt{-\ln(R_1)}\cos(2\pi R_2) \ , \\ v_{\perp,2} &= v_\mathrm{d}\sqrt{-\ln(R_1)}\sin(2\pi R_2) \ , \end{aligned} \tag{2.42}$$

where R_1 and R_2 are independently generated uninform random variables between 0 and 1, not including 0. R_1 sets the magnitude of the transverse velocity of the ion, and R_2 sets its direction in the transverse velocity plane. Packets can either be absorbed or scattered in a line, in the way described in Section 2.4.1. If desired, a treatment of fluorescence can also be included by randomly sampling the branching probability of de-excitation into all possible line transitions (Lucy 2002). We will not discuss such a treatment here.

2.5 Hydrodynamics

Our primary method for solving the hydrodynamics equations is a second-order Godunov scheme based on the PPM solver of Colella & Woodward (1984). While this paper only presents results based on the one-dimensional version of this solver, we intend to extend it to higher spatial dimensions in a spatially unsplit manner following the description in Colella (1990).

For 1-D spherically symmetric problems, we use a Lagrangian hydrodynamics solver because it allows for adaptive grid resolution. This solver is based on the von Neumann-Richtmyer staggered mesh scheme as described in Castor (2004).

As is well known, the inclusion of artificial viscosity is useful to damp numerical oscillations behind strong shocks, but has the negative effect of smearing out the shock front over

a number of zones determined by a constant C_q, an adjustable parameter (see Table 2.1). For the Lagrangian solver we can include a standard artificial viscosity of the form

$$q = C_q \rho \max(v_{\rm down} - v_{\rm up}, 0)^2 \ , \tag{2.43}$$

where $v_{\rm down}$ and $v_{\rm up}$ are the lower and upper zone velocities of the Lagrangian mass element. For the Godunov solver, the artificial viscosity is quite similar, although it involves modifying the numerical fluxes in the manner described in Lapidus (1967). We find that including artificial viscosity is helpful both in our Lagrangian solver and our Godunov solver, although for problems with strong shocks we can typically obtain similar results with a smaller value of C_q in the Godunov case than in the Lagrangian case.

We use an operator-splitting procedure for coupling the radiation source terms to the hydrodynamics equations in a way similar to that of Noebauer et al. (2012). Every time-step, we first perform the packet propagation through the fluid to construct the comoving frame estimators defined in equations 2.34 and 2.35. For the Eulerian version of the code, we use these estimators to construct the components of $\mathbf{G}$ in the lab frame, as given by equations 2.21 and 2.22. We next use our Godunov solver to calculate the updates to the hydrodynamical state variables that would have occurred in the absence of radiation. Finally, we use our computed components of $\mathbf{G}$ to evaluate the right-hand sides of equations 2.2 and 2.3. These source terms indicate the *rate* at which momentum and energy are transferred per time per zone, so we multiply these rates by Vdt to compute the radiation contribution to energy and momentum for that time-step. In other words, our treatment of the radiative source terms is first order in time.

In the Lagrangian version of the code, we use a similar first-order approach to include the radiative source terms, but in this case we use the comoving quantity cG_0 for the rate of radiative heating or cooling. We multiply this rate by Vdt and add the result to the internal energy of the gas in each zone. For the radiative momentum contribution we use use the radial component of the radiative force. We multiply this force by Vdt and add this contribution to the total force that accelerates each zone boundary[2].

Future work might include the developments described in Miniati & Colella (2007), Sekora & Stone (2010), and Jiang et al. (2012) for including stiff radiative source terms more consistently within the Godunov solver. Indeed, once we have used MCRT to construct the radiation energy density, flux, and Eddington tensor, then the manner in which this information is incorporated into the Godunov solver could proceed in a manner identical that described in Jiang et al. (2012).

[2]This may introduce an error for moderately relativistic flows, because the velocities of the zone boundaries are measured in the lab frame, yet we are using a radiative force computed in the comoving frame to modify their acceleration

2.6 Implicit Monte Carlo

On the fluid flow time scale, the Monte Carlo simulation always provides a stable and accurate representation of the radiation field regardless of the time-stepping. However, an explicit treatment of the matter-radiation coupling will be unstable unless the time-steps are smaller than the time scale for radiative heating/cooling to significantly change the gas energy, given by

$$t_{\rm rad} \approx \frac{1}{c\chi_{0P}} \frac{(\rho/\mu)kT_{0,g}/(\gamma_{\rm ad}-1)}{a_r T_{0,g}^4} \ . \tag{2.44}$$

Under certain conditions, in particular cases where the radiation energy exceeds that of matter, $t_{\rm rad}$ may be much smaller than the Courant time-step. To avoid excessively small time-steps while maintaining stability, we implement the implicit Monte Carlo (IMC) methods first developed by Fleck & Cummings (1971) (see also Abdikamalov et al. (2012)). In this case one defines the Fleck factor

$$f \equiv \frac{1}{1+4\alpha_f \left(\frac{E_0}{e_0}\right)(c\,\Delta t\,\chi_{0P})} \ , \tag{2.45}$$

where α_f is a nondimensional parameter that can be given a value between 0.5 and 1 in order to ensure stability. The second term in the denominator can be thought of intuitively as the ratio of Δt to $t_{\rm rad}$ (up to order unity factors).

The Fleck factor has several important roles. First, it is used to define an "effective scattering" rate. The true absorption fraction ϵ_ν is multiplied by f to determine a new probability that a photon interaction is treated by the code as an absorption event, rather than a scattering event. When $f \ll 1$ (i.e. the hydro time-step is much larger than $t_{\rm rad}$), then nearly all photon interactions are ffective scatttering interactions. Conversely, if $f \approx 1$ then the Fleck factor factor has little effect on the course of the simulation, and the probability of an absorption event remains approximately equal to ϵ_ν.

Second, the amount of thermal energy radiated each time step is also multiplied by f. This affects the second term in our calculation of G_0^0 in equation 2.19, and the number of packets emitted each time step as given by equation 2.33.

Finally, the Fleck factor is used to modify the process of adiabatic heating and cooling of the gas. Following Fleck & Cummings (1971), we will define an adiabatic heating term S^γ:

$$S^\gamma = -(p+C_q)\frac{D}{Dt}\left(\frac{1}{\rho}\right) = (p+C_q)\frac{1}{\rho^2}\left(\frac{\partial\rho}{\partial t} + v\frac{\partial\rho}{\partial x}\right) \ . \tag{2.46}$$

This expresses the rate at which gas kinetic energy is converted into internal energy (or vice versa), and accounts for artificial viscosity. If desired, other heating source terms, such as energy released from nuclear reactions, could be added here. This rate S^γ will also be multiplied by f, which amounts to subtracting $(1-f)S^\gamma$ from the gas heating rate. In order to conserve energy, this same amount of energy per time step must then be added to the radiation field (which could amount to a negative contribution if S^γ is negative).

In detail, for the Eulerian version of the code, we use the results of our Godunov scheme to construct the quantities $\partial\rho/\partial t$ and $\partial\rho/\partial x$, which are in turn used to consruct S^γ. We subtract $(1-f)S^\gamma\rho\Delta t$ from the total energy density update of the hydro state vector[3]. During the subsequent radiative transfer step, we add this contribution to the emission terms in equations 2.19 and 2.33.

In the Lagrangian version of the code, when it is time to update the internal energy density of the fluid, we use fS^γ for the amount of adiabatic heating or cooling, rather than the full S^γ that we would use in the absence of implict Monte Carlo. The emission in the next radiative transfer step is modified in the same manner as in the Eulerian case.

2.7 Radiation Test Problems

We have carried out a number of tests calculations to verify our code in a variety of physical situations.

2.7.1 Frequency-dependent absorption with scattering

First, we compare our MCRT implementation against analytic treatments of plane-parallel, semi-infinite, stratified, static atmospheres with frequency-dependent photon opacities. We follow the traditional convention of setting $\tau = 0$ at the observer's location at infinity, so that τ increases deeper into the atmosphere, along the z-axis of our coordinate system. Since the gas has zero bulk velocity in this test, we make no distinction between lab frame and comoving frame quantities for the rest of this subsection.

If, in addition to the assumptions listed in the previous paragraph, the source function is istropic, scattering is absent, and the temperature profile of the atmosphere is known, then the first three moments of the radiation intensity can be found exactly in terms of exponential integrals (e.g. Chandrasekhar 1950; Kourganoff 1952). Here we follow Rutten (2003) in writing the expressions for these moments as

$$E_\nu(\tau_\nu) = 2\pi \int_0^\infty S_\nu(t_\nu) E_1\left(|t_\nu - \tau_\nu|\right) dt_\nu \tag{2.47}$$

$$\begin{aligned} F_\nu^z(\tau_\nu) &= 2\pi \int_{\tau_\nu}^\infty S_\nu(t_\nu) E_2\left(t_\nu - \tau_\nu\right) dt_\nu \\ &- 2\pi \int_0^{\tau_\nu} S_\nu(t_\nu) E_2\left(\tau_\nu - t_\nu\right) dt_\nu \end{aligned} \tag{2.48}$$

$$P_\nu^{zz}(\tau_\nu) = 2\pi \int_0^\infty S_\nu(t_\nu) E_3\left(|t_\nu - \tau_\nu|\right) dt_\nu \ , \tag{2.49}$$

[3]To be even more accurate we should transform the adiabatic heating/cooling rate, which is defined in the comoving frame, into a lab frame rate when performing this subtraction. Such a transformaion was not performed in this version of the code

where

$$E_n(x) \equiv \int_0^1 e^{-x/\mu} \mu^{n-1} \frac{d\mu}{\mu} \ . \tag{2.50}$$

We next consider including a frequency-independent scattering extinction χ^s, meant to represent electron scattering, in addition to the frequency-dependent absorption coefficient χ^t_ν. When scattering is included, an exact solution for the moments of the radiation intensity is rarely possible, although excellent approximate solutions can be derived, as we will now show.

It is conventional to introduce $J_\nu \equiv (c/4\pi)E_\nu$, $H_\nu \equiv (1/4\pi)F_\nu$ and $K_\nu \equiv (c/4\pi)P^{zz}_\nu$. If all radiative cross sections are assumed to be isotropic, then the lowest two moment equations of the steady-state, plane-parallel transfer equation can be written

$$\frac{dH_\nu}{d\tau_\nu} = \epsilon_\nu \left(J_\nu - B_\nu\right) \tag{2.51}$$

$$\frac{dK_\nu}{d\tau_\nu} = H_\nu \ . \tag{2.52}$$

If we employ the Eddington approximation, $K_\nu = J_\nu/3$, then the last two equations may be combined to yield (e.g. Rybicki & Lightman 1986)

$$\frac{d^2 J_\nu}{d\tau_\nu^2} = 3\epsilon_\nu \left(J_\nu - B_\nu\right) \ . \tag{2.53}$$

This is a linear, inhomogeneous ordinary differential equation for J_ν. As such, it may be solved via the method of variation of parameters. Illarionov & Sunyaev (1972) present such a solution for the case when χ^t_ν corresponds to *bremsstrahlung*, so that it depends on both the density and temperature of the atmosphere at each depth. Here, we consider a slightly simpler situation in which ϵ_ν is independent of depth. To specify the boundary conditions, we assume that B_ν approaches some finite value $B_{\nu,\infty}$ as $\tau_\nu \to \infty$, and that

$$J_\nu = a_{\rm out} H_\nu \qquad \text{at } \tau_\nu = 0 \ , \tag{2.54}$$

where $a_{\rm out}$ is some constant value used to normalize the outgoing flux. If the two-stream approximation were to hold exactly as $\tau_\nu \to 0$, then $a_{\rm out}$ would equal $\sqrt{3}$ (Rybicki & Lightman 1986).

In that case, the solution for J_ν becomes[4]

$$\begin{aligned} J_\nu(\tau_\nu) = e^{\tau_\nu\sqrt{3\epsilon_\nu}} \int_{\tau_\nu}^{\infty} \frac{\sqrt{3\epsilon_\nu}}{2} B_\nu(t_\nu) e^{-t_\nu\sqrt{3\epsilon_\nu}} dt_\nu \\ + e^{-\tau_\nu\sqrt{3\epsilon_\nu}} \Bigg[\int_0^{\tau_\nu} \frac{\sqrt{3\epsilon_\nu}}{2} B_\nu(t_\nu) e^{t_\nu\sqrt{3\epsilon_\nu}} dt_\nu \\ - \frac{1 - a_{\rm out}\sqrt{\frac{\epsilon_\nu}{3}}}{1 + a_{\rm out}\sqrt{\frac{\epsilon_\nu}{3}}} \int_0^{\infty} \frac{\sqrt{3\epsilon_\nu}}{2} B_\nu(t_\nu) e^{-t_\nu\sqrt{3\epsilon_\nu}} dt_\nu \Bigg] \ . \end{aligned} \tag{2.55}$$

[4]Unlike Illarionov & Sunyaev (1972), we allow the radiation to escape to $\tau_\nu = 0$, rather than cutting off the solution at $\tau_\nu = 1$. Additionally, we have not made the approximation $\chi^s_{0\nu} \gg \chi^t_{0\nu}$.

The emergent flux can then be computed as

$$\begin{aligned} F_\nu(0) &= 4\pi H_\nu(0) = \frac{4\pi}{3}\frac{dJ_\nu}{d\tau_\nu}(0) \\ &= 4\pi\frac{\epsilon_\nu}{1+a_{\rm out}\sqrt{\frac{\epsilon_\nu}{3}}}\int_0^\infty B_\nu(t_\nu)e^{-t_\nu\sqrt{3\epsilon_\nu}}dt_\nu \ . \end{aligned} \tag{2.56}$$

Since the Eddington approximation was used to derive equation 2.56, taking its limit as $\epsilon_\nu \to 1$ (i.e., in the limit of no scattering) does not recover equation 2.48 evaluated at $\tau_\nu = 0$. However, if we consider equation 2.48 under the the two-stream approximation so that μ is fixed at $1/\sqrt{3}$ in equation 2.50, and $a_{\rm out} = \sqrt{3}$, then we do indeed recover the $\epsilon_\nu \to 1$ limit of equation 2.56.

To gain insight into equation 2.56, we consider the thermalization depth

$$\Lambda_\nu \equiv 1/\sqrt{\epsilon_\nu} \ . \tag{2.57}$$

This is the average depth that a freshly emitted photon with frequency ν will travel via scattering before being reabsorbed. The heuristic derivation (following Rutten (2003)) for equation 2.57 is as follows. During each scattering event, the probability that the photon is absorbed is ϵ_ν, by definition. Thus, an emitted photon will scatter an average of $1/\epsilon_\nu$ times before being reabsorbed. Meanwhile, for any random-walk process, the mean displacement of a packet that has undergone N re-directions, each of mean free path l, is approximately $l\sqrt{N}$. Consequently, the average distance between emission and absorption events is $l/\sqrt{\epsilon}$. Converting this distance to an optical depth gives us our result. A factor of $\sqrt{3}$ in front of ϵ_ν can account for the average angle with respect to the z-axis along which the photons travel in the Eddington approximation.

We do not expect escaping photons to have been emitted at temperatures corresponding to optical depth much greater than the thermalization depth. In other words, frequencies with large thermalization depths allow us to see such photons that were emitted from deeper, hotter portions of the atmosphere.

We ran three test calculations, each with a different degree of scattering, to test the code against these solutions. In all three cases, we used a domain of total height $h = 10^{14}$ cm. For the first two tests we divided the domain into 128 zones of equal height, and for the final test we used 256 zones. The domain was filled with gas following a power-law density profile

$$\rho(z) = \rho_{\rm max}\left[1+\left(\frac{h-z}{z_s}\right)^p\right]^{-1} \ , \tag{2.58}$$

where we have chosen $\rho_{\rm max} = 2.09 \times 10^{-11}$ g cm^{-3} (yielding an optical depth to electron scattering of 100, where the electron scattering opacity is 0.4 cm^2 g^{-1} for fully ionized hydrogen), $z_s = 10^{13}$ cm, and $p = 3$. Photons were emitted from the $z = h$ plane and propagate toward the $z = 0$ plane, where they are tallied to generate an outgoing spectral energy distribution (SED). Any photons that scattered back past the $z = h$ plane were treated as absorbed by the luminous source and were no longer tracked. We adjusted the

photon flux from the inner emitting surface (at $z = h$) so that the bolometric, steady-state radiative flux escaping to infinity would equal a constant value of 1.64×10^{20} erg s^{-1} cm^{-2} in all three calculations.

We chose a normalization for χ^t_ν so that it would match the electron scattering extinction at 100 Angstroms. We also let χ^t_ν scale as ν^{-1}. Our wavelength resolution was set by dividing the interval between 1 and 10^4 Angstroms into 100 bins equally spaced logarithmically.

Anticipating that the densities and temperatures in these calculations would correspond to cooling times that were orders of magnitude shorter than the radiative diffusion time through the computational domain, we used a fully implicit treatment of the radiative heating and cooling. Absorption events were always treated as effectively scattered, and we periodically re-computed the temperature of the gas in each zone by enforcing radiative equilibrium until a steady state was reached.

Figure 2.1 shows the outgoing SED for three test cases. In the first case, shown in the top panel, we used only the absorption coefficient χ^t_ν, and neglected scattering entirely. This allowed us to solve for the outgoing flux by invoking equation 2.48 at $\tau_\nu = 0$ for all ν. The match between the analytic formula and the Monte Carlo results is excellent.

In the second case, shown in the middle panel of Figure 2.1, we add Thomson scattering but we keep all other details of the simulation the same as before. Given our functional form for χ^t_ν described above, ϵ_ν ranges from 10^{-2} at 1 Angstrom to 0.9 at 1000 Angstroms. As shown in Figure 2.2, the inclusion of scattering along with absorption, while forcing the escaping flux to be the same, leads to higher temperatures in all regions of the atmosphere. Remarkably, this temperature adjustment occurs in such a way as to keep the shape of the outgoing SED nearly identical to the case without scattering (compare the first and second panels of Figure 2.1). The Eddington approximation prediction for the shape of the SED (equation 2.56) still matches the computed SED quite well.

Finally, the bottom panel of Figure 2.1 shows the results of another test that includes both absorption and scattering, but this time the absorption opacity is reduced to a value of 0.01 times the value we had used previously. Now ϵ_ν ranges from 10^{-4} at 1 Angstrom to 0.09 at 1000 Angstroms. In this case there is a slight drop in temperature compared to the previous case at all depths in the atmosphere, as seen in Figure 2.2. However, this time the SED shifts markedly in the blueward direction, which is evident in the bottom panel of figure 2.1. This can be understood in terms of the thermalization length described earlier. As the atmosphere becomes increasingly scattering dominated, the photons that escape to the observer tend to have been emitted at higher Thomson optical depth, where the temperature is higher. Again, agreement with the analytic formula is very good, verifying the MCRT calculation of multi-frequency transport in a scattering dominated regime.

2.7.2 Line Transport

We next test the transport of line radiation in both moving and static media. We use the spherical Lagrangian version of the code and inject photons into a uniform density sphere of radius $r_{\rm max} = 10^{15}$ cm. The thermal motions of ions are taken into account, with a

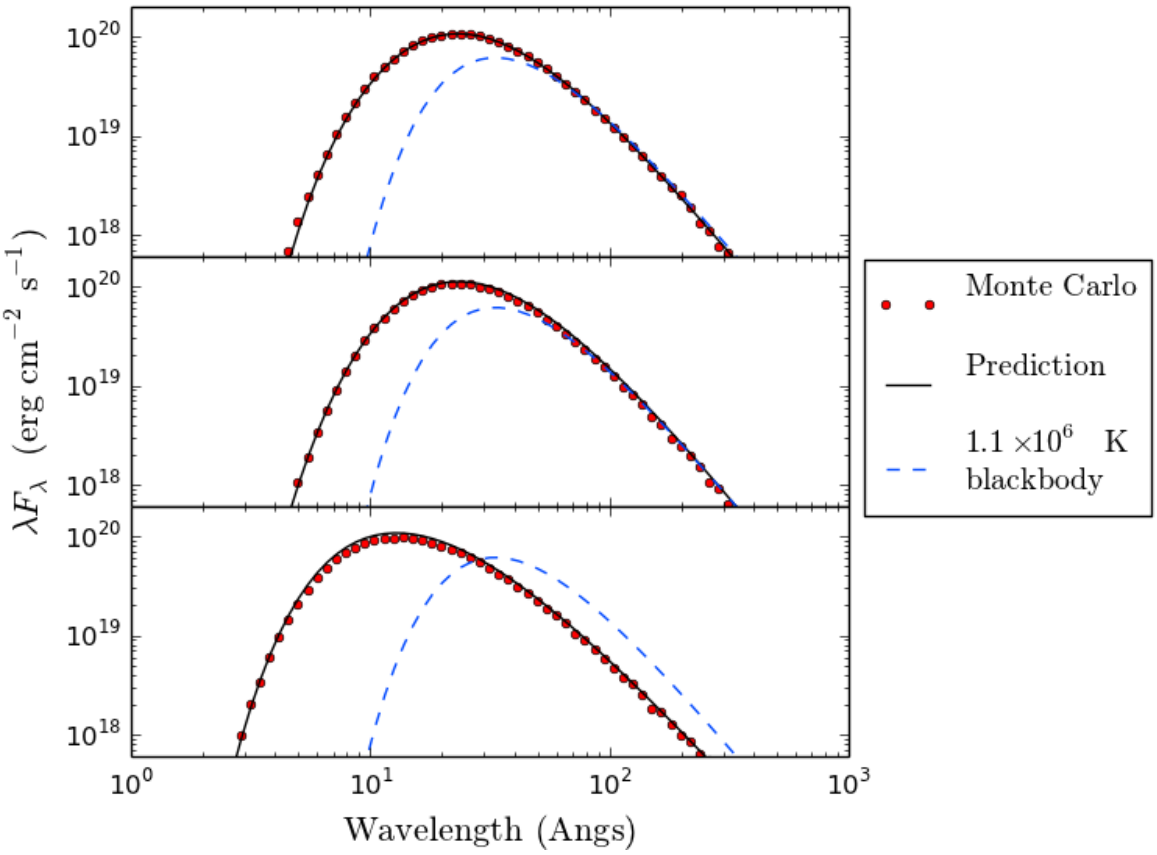

Figure 2.1: Tests of outgoing SEDs for static, stratified, plane-parallel atmospheres with frequency-dependent opacities. Top panel: No scattering. The absorption coefficient χ^t_ν is chosen so that it matches the Thomson extinction at 100 Angstroms, and declines as ν^{-1}. The exact analytic solution used for comparison is given in equation 2.48. The blackbody spectrum is included to guide the eye and to illustrate how the emergent flux in this calculation includes emission from gas layers at a range of temeperatures. Middle panel: Thomson scattering has been added as a contribution to the opacity, but all other details of the calculation remain the same as the top panel. The analytic prediction now uses the Eddington approximation and is given by equation 2.56. Bottom panel: The thermal opacity is now multiplied by a factor of 0.01, but all other details remain the same as in the middle panel. For sufficiently small ϵ_ν, as in this panel, the SED shifts toward smaller wavelengths even while the peak value of λF_λ remains nearly the same as in higher ϵ_ν runs. The slight over-prediction of flux in this case seems to improve as spatial resolution is increased. Higher spatial resolution is needed in this case because the photons that escape were initially emitted from deeper, hotter portions of the atmosphere with higher temperature gradients than in the previous two cases.

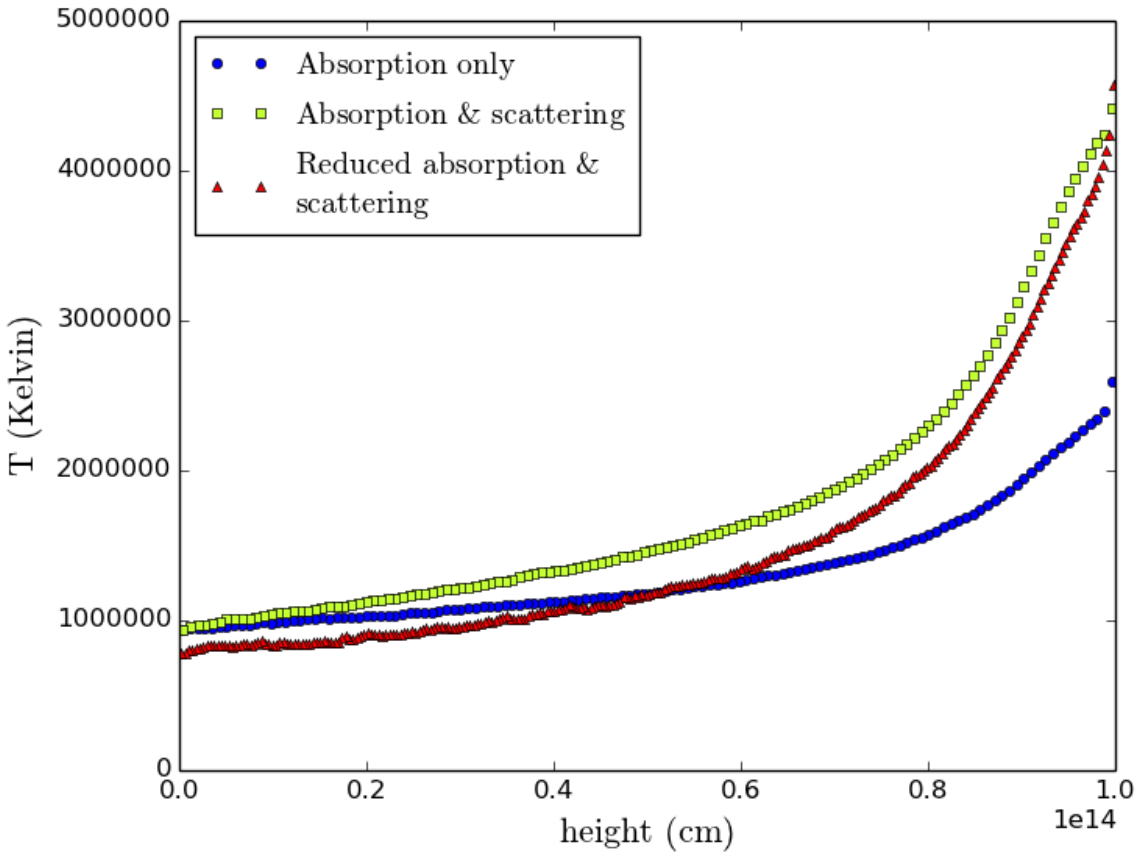

Figure 2.2: The gas temperature as a function of height for the static atmosphere tests. The three curves correspond to the three panels in Figure 2.1. Although the temperatures are noticeably different between all three runs, the outgoing flux has been adjusted to be the same in all three cases.

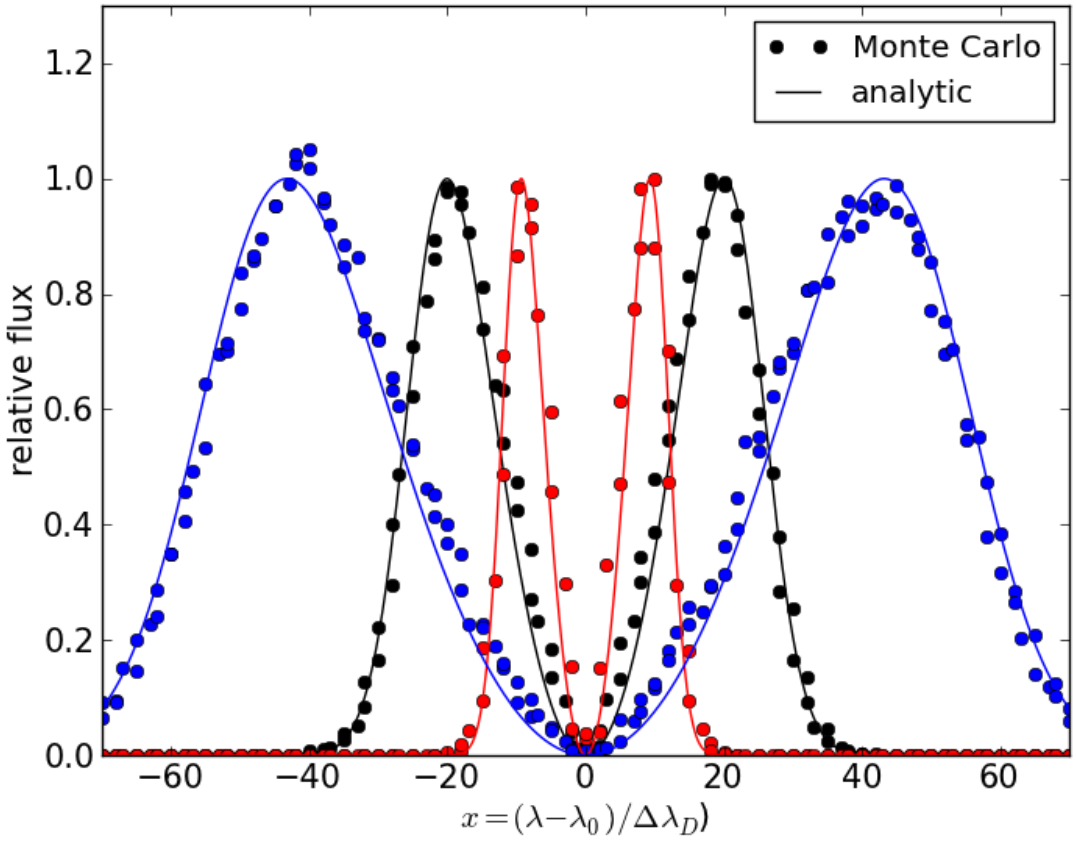

Figure 2.3: Test of line transport in a static medium, comparing Monte Carlo results (circles) to an analytic solution based on the diffusion approximation (Equation 2.59, solid lines). In this problem, a point source radiates line photons into a uniform spherical medium with a pure-scattering optical depth at line center of $\tau_c = 10^4$ (red), $\tau_c = 10^5$ (black) and $\tau_c = 10^6$ (blue).

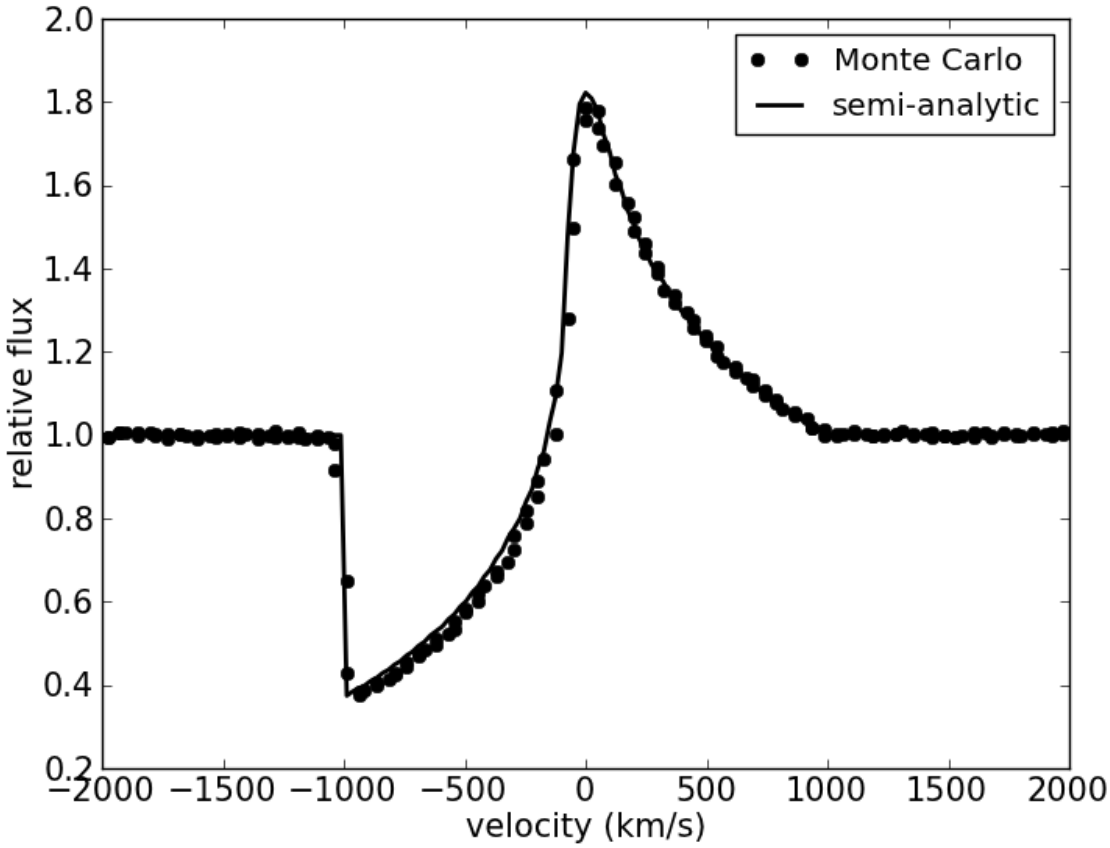

Figure 2.4: Test of line transport in a moving homologously expanding medium. A spherical source radiates continuum photons into a uniform pure-scattering medium with Sobolev line optical depth of $\tau_s = 1$. Results from the Monte Carlo (circles) are compared to the semi-analytic solution based on the Sobolev approximation (Equation 2.60).

velocity dispersion of $v_{\rm d} = 25$ km s^{-1}. The line opacity is taken to be pure-scattering, and for computational expediency we adopt a large Voigt parameter of $a = 0.1$ (see equation 2.40).

In the first test, we consider a static atmosphere with a total radial optical depth at line center of τ_c. Photons are injected at the center of the sphere and at the line center rest frame frequency ν_c. An analytic solution to the line scattering problem in the plane parallel case was derived by Neufeld (1990) under the Eddington approximation, and generalized to a spherical atmosphere by Dijkstra et al. (2006), who find a total flux density at the surface of the sphere

$$J(x) = \frac{\sqrt{\pi}}{24\sqrt{\pi a \tau_c}}\left[\frac{x^2}{1+\cosh[\sqrt{2\pi^3/27}(|x^3|/a\tau_c)]}\right] \tag{2.59}$$

In Figure 2.3 we show results of the MC transport for spheres of optical depth $\tau_c = 10^4$ and 10^6. The resulting line features show a characteristic double peaked profile. This is because photons are Doppler shifted by the thermal motions of the scatterers, and preferentially escape in the less opaque line wings. Our MC results show favorable agreement with the analytic solution Equation 2.59, comparable to those seen in other MCRT line transport codes (Dijkstra et al. 2006).

To test line transport in a moving atmosphere, we consider the case where the sphere of gas is expanding homologously (i.e., velocity proportional to radius). We emit photon packets from the surface of a spherical inner boundary of uniform specific intensity I_p in the lab frame at a radius $r_p = 10^{14}$ cm. The velocity structure is given by $v(r) = v_{\rm max}(r/r_{\rm max})$, with $v_{\rm max} = 10^8$cm s^{-1}. Because the velocity scale height of this problem is much greater than the ion thermal velocities, the Sobolev approximation applies. The emergent line profile in the lab frame is then given by an integral over the impact parameter p, (e.g., Jeffery & Branch 1990)

$$F(\nu) = 2\pi \int_0^\infty \left[I_p e^{-\tau_{\rm s}} + S(r)(1-e^{-\tau_{\rm s}})\right] p dp \tag{2.60}$$

where the Sobolev optical depth is

$$\tau_s(r) = \frac{\pi e^2}{m_e c}\frac{c}{\nu_c}\frac{f_{\rm osc} n_l}{dv/dr}. \tag{2.61}$$

In the present example the velocity gradient is $dv/dr = v_{\rm max}/r_{\rm max}$. The source function for a pure-scattering line is equal to the mean intensity of the radiation field, $S(r) = J(r) = W(r)I_p$ where the dilution factor is

$$W(r) = \frac{1}{2}\left[1 - \sqrt{1-(r_p/r)^2}\right]. \tag{2.62}$$

As discussed in Jeffery & Branch (1990), to properly treat the boundary condition of the photosphere, $\tau_s(r)$ and $S(r)$ are zero for the spatial region inside and behind the photosphere, while $I_p(p)$ is zero for $p > r_p$.

Figure 2.4 shows results for a constant density atmosphere with $\tau_s = 1$. The spectrum of the MCRT code, which resolves the line profile, is in good agreement with the Sobolev semi-analytic solution.

2.8 Radiation-hydrodynamics Test Problems

We next discuss test problems in which the energy and momentum coupling of the gas and radiation is considered. In what follows, we define the radiation temperature as $T_{0,r} = (E_0/a_r)^{1/4}$, where E_0 is the comoving radiation energy density. We use an ideal gas equation of state with $\gamma_{\rm ad} = 5/3$.

Table 2.1 lists the numerical parameters used in each radiation-hydrodynamics test problem.

2.8.1 Evolution to radiative equilibrium

We begin with a standard test of the heating and cooling of the gas by radiation, which also provides clear a demonstration of the application of implicit MC techniques. We chose here a setup identical to that of Turner & Stone (2001), although modified versions of the test have appeared elsewhere, including Noebauer et al. (2012).

In this test we use the Eulerian version of the hydro solver. We again consider gas with zero bulk velocity, so that the lab frame and the comoving frame are identical, although we retain the comoving frame notation. The computational domain is filled with static gas at a uniform density of $\rho_0 = 10^{-7}$ g cm^{-3}, a mean atomic mass of $\mu = 0.6$, and a gray opacity $\kappa_0 = 0.4$ cm^2 g^{-1}. Additionally, a uniform and isotropic radiation field is initialized with energy density 10^{12} erg cm^{-3}, so that $T_{0,r} = 3.4 \times 10^6$ K. Here $\epsilon = 1$, so that the gas and radiation are fully thermally coupled. Although the radiation pressure overwhelms the gas pressure in this test, the radiation field is isotropic, so the radiation pressure does not accelerate the gas. Reflecting boundary conditions were used for the radiation.

In this context, the gas energy equation (Equation 2.3) simplifies to

$$\begin{aligned} \frac{de_0}{dt} &= \chi c a_r T_{0,r}^4 - 4\chi B(T_{0,g}) \\ &= \chi c a_r (T_{0,r}^4 - T_{0,g}^4) \end{aligned} \tag{2.63}$$

where B is the frequency-integrated Planck function Turner & Stone (2001). We consider two versions of the test, one in which the gas is heated by radiation, and another in which the gas cools. For the heating case, the gas is given an initial thermal energy density of 10^2 erg cm^{-3}, corresponding to $T_{0,g} = 11$ K. For the cooling case, the initial thermal energy density is 10^{10} erg cm^{-3}, corresponding to $T_{0,g} = 1.1 \times 10^9$ Kelvin. In both cases, the radiation energy greatly exceeds the gas energy density, and so remains nearly constant during the energy exchange. This means that the gas will ultimately heat or cool to reach the radiation temperature, corresponding to an equilibrium gas energy density of 7.8×10^7 erg cm^{-3}.

Table 2.1:

Test	# of zones	Zone width (cm)	dt	$t_{\rm stop}$ (s)	α_f	C_q	Initial packets per zone, per step	Max packets emitted per zone, per step
Rad. equilib. (no IMC)	2	5.0×10^9	1.0×10^{-11} s	1.0×10^{-7}	0.	0.	1	0
Rad. equilib. (IMC)	2	5.0×10^9	1.0×10^{-14} s	1.0×10^{-7}	0.5 or 1.0	0.	1	0
Advected pulse	201	0.00995	1.0×10^{-13} s	1.0×10^{-10}	N/A	0.	10^5 (center zone)	0
Homologous expansion	64	Variable	CFL 0.2	1.0×10^5	N/A	0.	10	0
Bondi accretion	2048	Variable	CFL 0.2	3.0×10^6	1.0	0.	10	40 (from source)
$\mathcal{M} = 2$ steady shock	512	5.86×10^{-5}	CFL 0.5	1.0×10^{-9}	1.0	0.1	10	400
$\mathcal{M} = 5$ steady shock	2048	1.95×10^{-5}	CFL 0.5	1.9×10^{-9}	1.0	0.1	10	100
$\mathcal{M} = 70$ steady shock	896	1.29×10^{-3}	CFL 0.1	1.0×10^{-9}	1.0	0.1	7680	7680
Sub-critical moving shock	512	1.37×10^8	CFL 0.5	4.0×10^4	0.	0.5	1000	4000
Super-critical moving shock	512	1.37×10^8	CFL 0.2	1.3×10^4	1.0	0.5	1000	1000

Note. — Numerical parameters. When zone width is listed as "variable", the Lagrangian version of the code is being used. When α_f is listed "N/A", the radiation energy and gas are thermally decoupled (i.e. $\epsilon = 0$ so that radiation always scatters and is never absorbed).

This test only follows the evolution of the gas up to an elapsed time of 10^{-5} s, whereas the photon interaction time $1/(\rho\kappa c)$ is approximately 10^{-3} s. In the absence of explicit photon interactions, the energy exchange between gas and radiation is deterministic, and so the number of photon packets employed has no effect on the solution.

Figure 2.5 displays the gas heating and cooling curves compared to the analytic solution of Equation 2.63. Consider the cooling curve first. According to equation 2.44, the cooling time at the beginning of the simulation is 1.7×10^{-15} s. If we take a time-step smaller than this, such as 10^{-15} seconds, then no implicit methods are needed, and the gas temperature follows the analytic cooling curve to an accuracy of better than 1.3% at all times. If we wish to take much larger time-steps, then we must turn on the implicit Monte Carlo by setting $\alpha_f \geq 0.5$, otherwise the code generates negative temperatures and crashes after the first step of the calculation. Figure 2.5 shows the results of taking $\alpha_f = 0.5$ and $\alpha_f = 1.0$ for $dt = 10^{-11}$ s. In both cases, the cooling curves approach the analytic solution after many time-steps, but the cooling is artificially slow at early times. The $\alpha_f = 0.5$ case converges to the correct solution more quickly than the $\alpha_f = 1.0$ case, demonstrating that one should strive for the smallest value of α_f that still maintains stability.

The heating curves follow the analytic solution to within one part in 10^{-4} at all times, regardless of the value of α_f chosen or the size of the time-step up to 10^{-11} that we tested, although larger time-steps could be used for the heating case.

2.8.2 Advected radiation pulse

In a moving, optically thick medium, radiation should be swept along with the matter. This represents an important and non-trivial test of the MCRT routine, as advection is not explicitly included in the code. Instead, advection is a statistical consequence of the lab frame anisotropy of the lab frame extinction coefficient and scattering function. When averaged over many scatters, these effects preferentially guide packets upstream.

Our test is similar to the radiation diffusion tests presented in Harries (2011) and Noebauer et al. (2012), but with the added effect of advection. We use the Eulerian version of the code, and consider a homogeneous gas distribution from $x = -1$ cm to $x = 1$ cm. The gas is pure-scattering ($\epsilon = 0$) with $\mu = 0.5$, and is given a uniform lab frame velocity of 2×10^9 cm s^{-1}. The scattering opacity is taken to be $\kappa_0 = 10^9$ cm^2 g^{-1}, which gives an optical depth across each zone equal to 1 in the comoving frame. The radiation is initialized isotropically in the comoving frame of the central zone only, with a comoving energy density of 10^{10} erg cm^{-3}.

Since the gas and radiation are thermally decoupled in this test, and we are primarily interested in the advection and diffusion of the radiation energy, the value chosen for the gas temperature is arbitrary. However, a lower temperature results in a higher mach number. In the test corresponding to Figure 2.6 (discussed below), we chose to set the gas temperature to 10^4, corresponding to an isothermal mach number of roughly 1560. In this case, we found it necessary to include a floor for the gas energy to prevent it from dropping below zero. Radiation is allowed to escape through either side of the domain, and periodic boundary

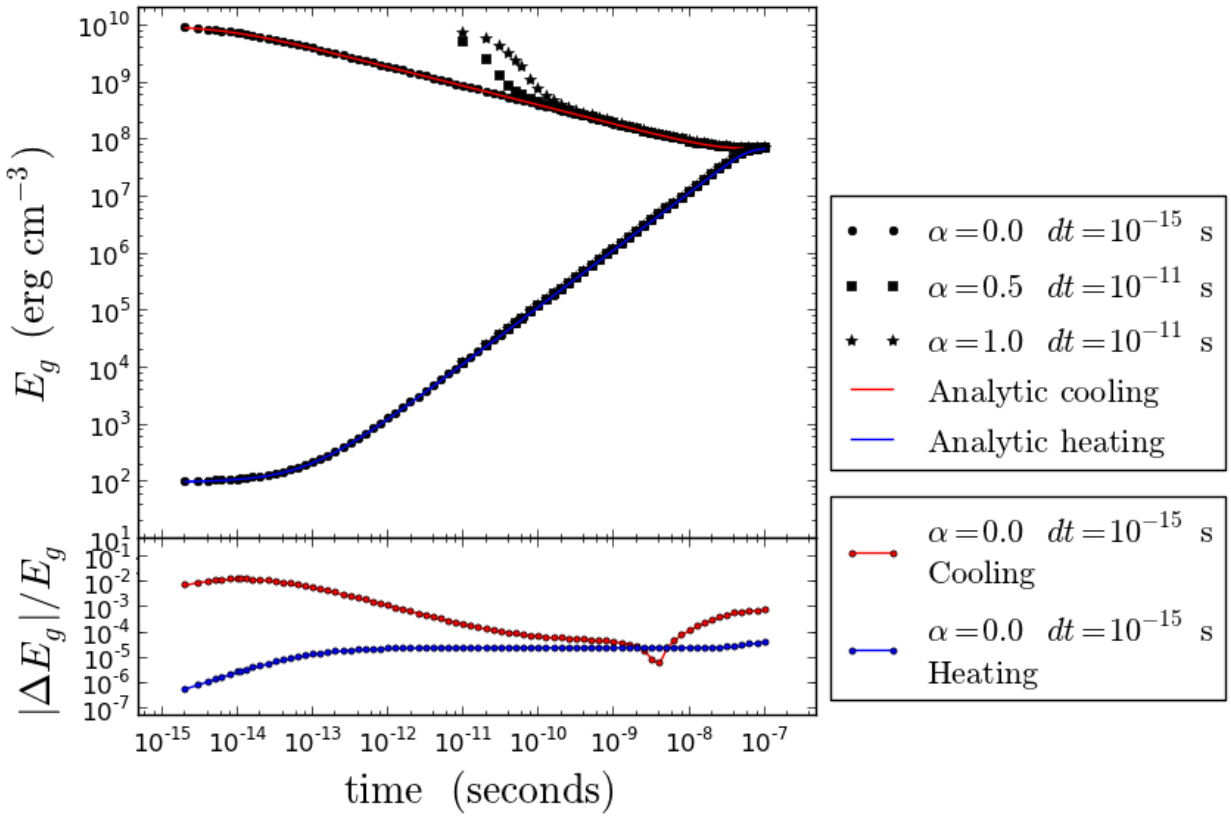

Figure 2.5: Tests of the approach to radiative equilibrium in a radiation-energy dominated gas, with gray radiative opacity. The red and blue curves represent the analytic gas heating and cooling curves as computed from equation 2.63. The points represent values computed from the Monte Carlo simulation for three sets of numerical parameters as described in the legend. All other numerical parameters are held at the values specified in Table 2.1. Two different implicit treatments of the heating and cooling are used for large time-steps, in addition to an explicit numerical treatment at time-step much shorter than the cooling time. The bottom panel shows the fractional error compared to the analytic solution for the case of explicit heating and cooling.

conditions are employed for the hydrodynamics solver.

As discussed in Harries (2011) and Noebauer et al. (2012), the evolution of the radiation energy can be solved for analytically in the diffusion approximation. Figure 2.6 compares our computed radiation temperature to this solution at various times. One sees that the radiation pulse moves along with the gas at the expected velocity. We confirmed that *both* the transformation of the extinction coefficient (Equation 2.31) and the effect of aberration (Equation 2.24) must be included to reproduce the proper advection velocity. Thus, even in problems with velocities $v \ll c$, a special relativistic MC treatment is desirable to recover the proper advection behavior.

2.8.3 Opaque Expanding sphere

We next consider a problem designed to test whether the code properly handles radiation energy losses due to expansion. This is also a non-trivial test of the MCRT routine, as no explicit term for radiation pdV work is included in the code. Instead, the change in the radiation energy density is a statistical result of the multiple Doppler shifts photon packets incur as they scatter anisotropically off of moving gas.

We consider a spherical gas cloud undergoing homologous expansion (i.e., velocity proportional to radius) and opaque enough that photons do not diffuse significantly, but are rather advected along with the flow. Such an adiabatically expanding flow cools as $T \propto V^{1-\gamma_{\rm ad}}$, with $V \propto r_{\rm out}^3$. We assume the medium is pure-scattering ($\epsilon = 0$), so that the radiation and gas are thermally decoupled. Hence the gas ($\gamma_{\rm ad} = 5/3$) should evolve as $T_{0,g} \propto r_{\rm out}^{-2}$ while the radiation ($\gamma_{\rm ad} = 4/3$) should evolve separately as $T_{0,r} \propto r_{\rm out}^{-1}$.

For this test, we use the Lagrangian version of the hydro solver. The outer edge of the computational domain expands homologously as $r_{\rm out} = r_{\rm out,i} + v_{\rm out}t$, where t is the time elapsed. We take $r_{\rm out,i} = 10^{13}$ cm and $v_{\rm out} = 10^9$ cm s^{-1}. The gas is initially uniform with a temperature of 10^4 K, a density of $\rho = 4.75 \times 10^{-7}$ g cm^{-3}, $\mu = 0.5$, and $\kappa_0 = 0.4$ cm^2 g^{-1}. Reflecting boundary conditions at $r_{\rm out}$ are used for the radiation. To compute the fluid pressure gradient at the outer boundary we linearly extrpolate the pressure from the outermost two zones to evaluate the pressure beyond the outermost radial zone, although the gas pressure does not play an important role in this test.

Figure 2.7 displays the spatially-averaged gas and radiation temperatures as a function of $r_{\rm out}$ (each zone was given equal weight in the average). The code recovers the expected adiabatic loses of the gas and radiation field. We ran two versions of this test, one in which the gas velocity was taken to be piece-wise constant in each zone, and the other in which the gas velocity was linearly interpolated within each zone.

As is evident in the figure, the evolution of the radiation temperature is more accurately computed for the case in which velocity interpolation was used, indicating that an adequate resolution of the gas velocity field is necessary properly calculate the radiation pdV work.

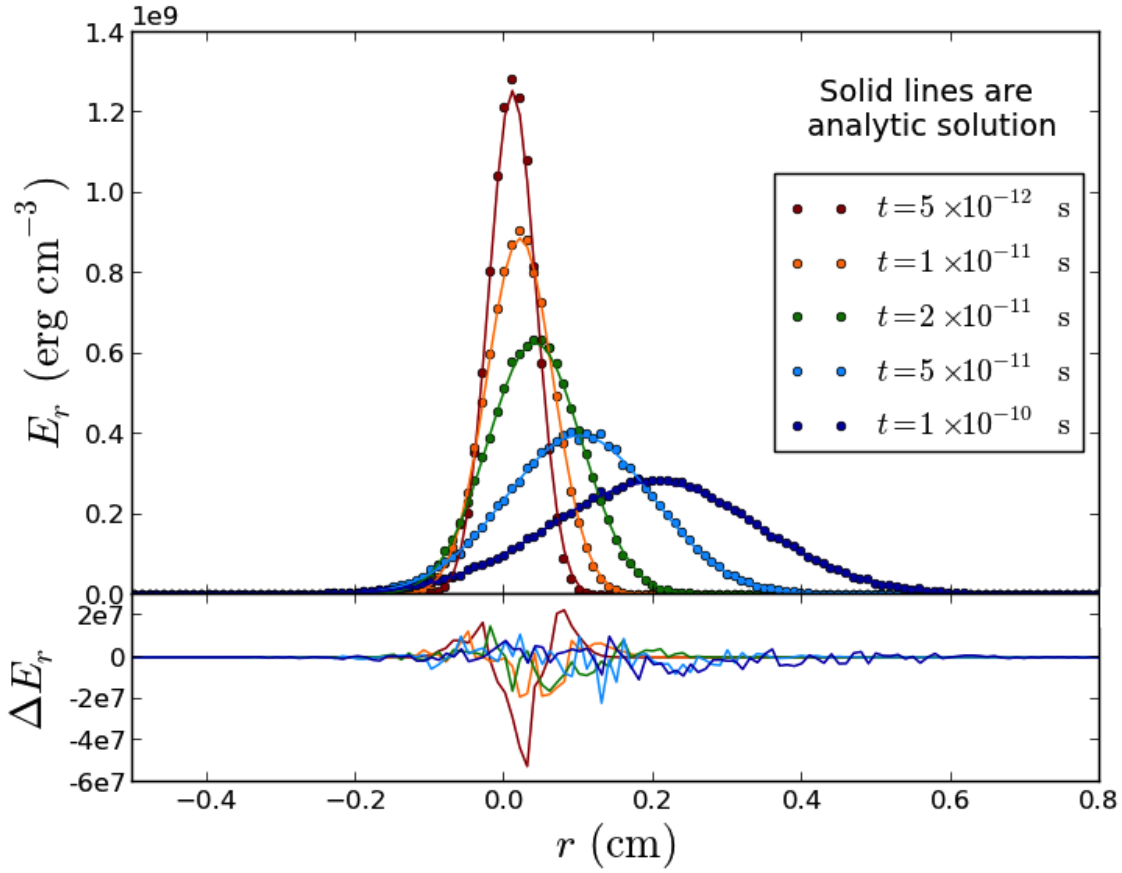

Figure 2.6: Test of advection and diffusion of radiative energy in a moving fluid with gray scattering opacity. The mean free path of the photons is approximately 0.01 cm, so the fluid is highly optically thick to the radiation and sweeps the radiative energy along with it. The analytic solution is given by the advection-diffusion equation, and the bottom panel shows the absolute error in the computed radiative energy density as compared to the analytic solution. The numerical parameters used in this test are specified in Table 2.1.

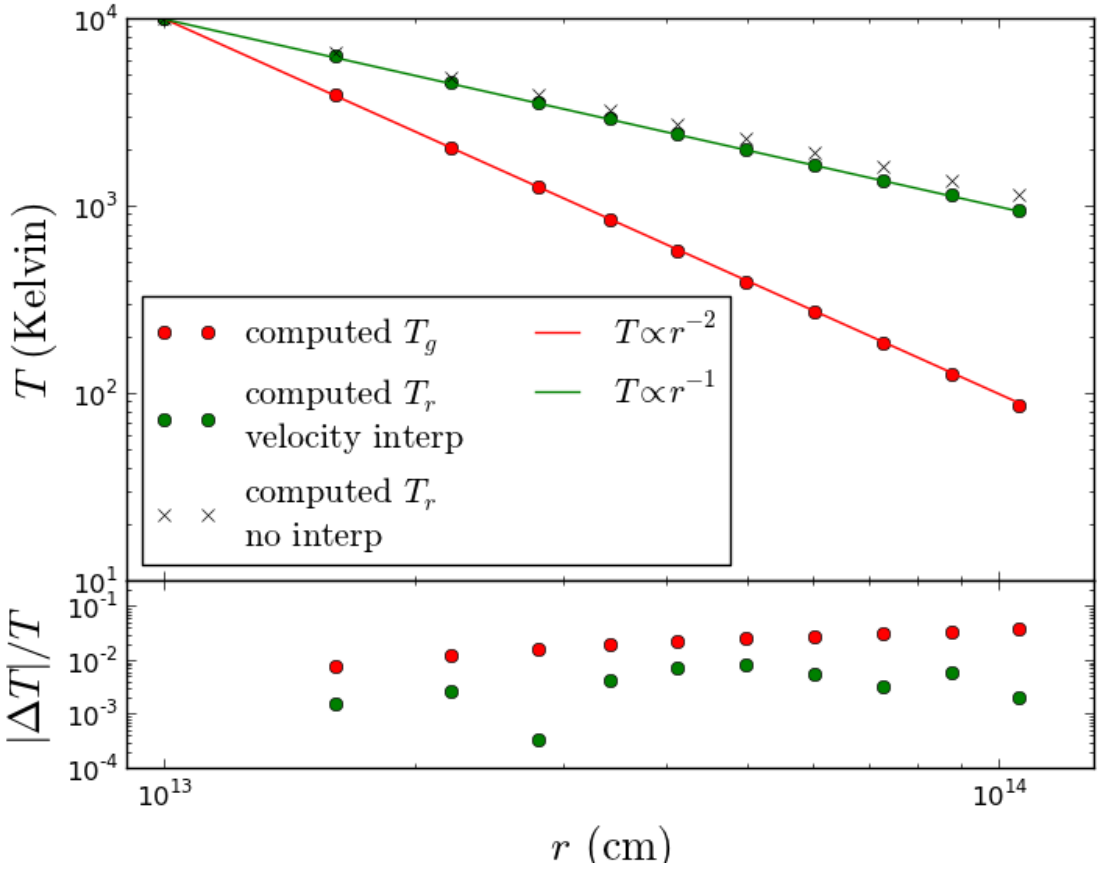

Figure 2.7: Test of the temperature evolution of a homologously expanding sphere of fluid that is optically thick to scattering radiation. Since the gas and radiation have different adiabatic indices, their temperatures as a function of radius/time follow different relationships. We find that in order to achieve a percent-level match to the expected temperature profiles, we must interpolate the velocity of the fluid between neighboring Lagrangian mass cells. The fractional error in the computed versus expected temperatures is shown in the bottom panel. The numerical parameters used in this test are listed in Table 2.1.

2.8.4 Bondi accretion with optically thin radiation pressure

The classic Bondi problem of steady-state, spherically symmetric gravitational accretion (Bondi 1952) provides an opportunity for us to test the effect of radiation force in the optically thin limit. Our treatment of the problem closely follows that of Krumholz et al. (2007a). For an accreting object with mass M and isotropic radiative luminosity L we may define the Eddington factor

$$f_{\rm Edd} = \frac{\kappa_0 L}{4\pi G M c}, \tag{2.64}$$

where κ_0 is the gas opacity, taken here to be gray. We consider the isothermal case. For a sound speed c_s, we may then define the radiatively-inhibited Bondi radius as

$$r_{\rm B} = (1 - f_{\rm Edd})\frac{GM}{c_s^2}. \tag{2.65}$$

The expected steady-state mass accretion rate is then

$$\dot{M}_{\rm B} = 4\pi \left(\frac{e^{3/2}}{4}\right) c_s \rho_\infty r_{\rm B}^2, \tag{2.66}$$

where ρ_∞ is the gas density at the outer boundary of the domain.

We set $M = 10\ M_\odot$, $L = 1.63 \times 10^5\ L_\odot$, $c_s = 1.29 \times 10^7$ cm s^{-1}, $\rho_\infty = 10^{-18}$ g cm^{-3}, $\mu = 1$, and $\kappa_0 = 0.4$ cm^2 g^{-1}, so that $f_{\rm Edd} = 0.5$ and $r_{\rm B} = 4 \times 10^{12}$ cm. The spherical domain has inner radius $0.2\ r_{\rm B}$ and outer radius $6 r_{\rm B}$. We initialize the gas density and velocity according to the analytic solution as described in Krumholz et al. (2007a), in a manner such that each of our Lagrangian zones contains roughly equal mass.

We enforce inflow boundary conditions by removing the innermost Lagrangian zone from the calculation when its outer radius drops below $0.25 r_B$. We then simultaneously add a zone at the outer edge of the computational domain with density equal to ρ_∞ and with outer velocity equal to the velocity of the formerly outermost zone. As in the previous test, to compute the fluid pressure gradient at the outer boundary we linearly extrpolate the pressure from the outermost two zones. Radiation escapes through the outer boundary.

Figure 2.8 displays the gas density and velocity as a function of position at time $t = 9.7\ r_B/c_s$. The fractional deviation between the computed and expected solutions is at most 7% in the innermost zone. The average accretion rate over this time was 1.06 times the expected mass accretion rate computed from equation 2.66.

2.8.5 Steady sub-critical and super-critical radiating shocks

A more complicated set of tests involve steady radiating shocks[5]. The structure of these shocks differs from the pure hydrodynamic case because radiation emitted by the shocked

[5]We use the term "shock" here in a broad sense that also includes the case of very high upstream Mach number (e.g. our $\mathcal{M} = 70$ case) in which there is no embedded *viscous* shock, although there is still a radiation-mediated shock.

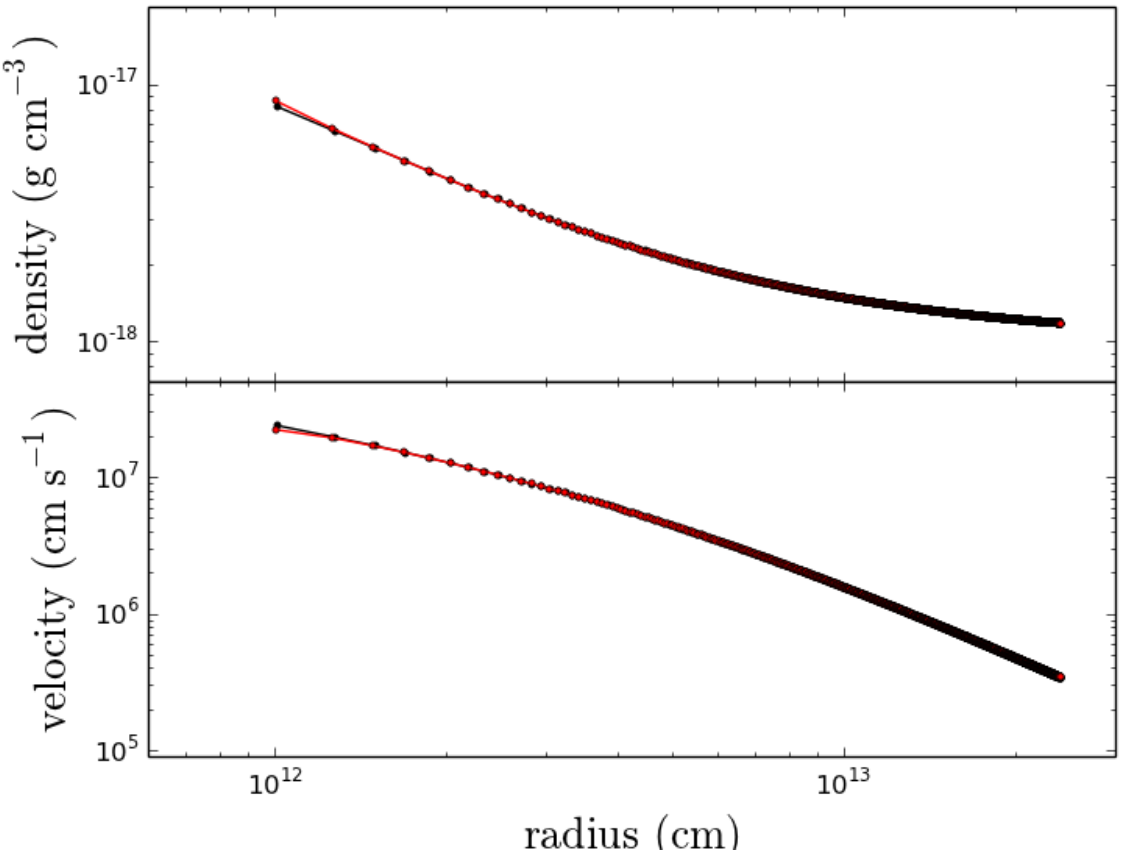

Figure 2.8: The velocity and density profiles of a radiatively-inhibited Bondi accretion test, set up to replicate the corresponding test in Krumholz et al. (2007a) at time $t = 9.7\ r_B/c_s$. The red curve is our computed solution and the black is the analytic solution. The maximum disagreement between these two solutions is 7% for the velocity in the innermost zone. The numerical parameters used in this test are listed in Table 2.1.

gas leaks out ahead and behind the shock, heating the gas and forming a radiative precursor region (upstream) and a radiative relaxation region (downstream). Additionally, the shock obeys a modified set of jump conditions in which the total energy and momentum carried by both gas and radiation is conserved (Zel'dovich & Raizer 1969).

In the gray nonequilibrium diffusion approximation, there exists a semi-analytic solution for the shock structure (Lowrie & Edwards 2008). For the case where scattering is neglected, and for an adiabatic equation of state with fixed index $\gamma_{\rm ad}$ and mean particle mass μm_p, this solution is completely characterized by four dimensionless parameters: the Mach number, $\mathcal{M}$, of the upstream gas in the rest frame of the shock, the ratio of the speed of light to the upstream sound speed $\mathbb{C}$, the ratio of the upstream radiation pressure (times 3) to upstream gas pressure $\mathbb{P}$, and the optical depth to the radiation, τ, for a chosen comoving radiative extinction χ_0 (units of cm^{-1}) and lab frame length scale L

$$\mathcal{M} = v_u/a_u = v_u\sqrt{\frac{\mu m_p}{\gamma_{\rm ad}k_B T_{u,g}}} \tag{2.67}$$

$$\mathbb{P} = \frac{a_r T_{u,g}^4}{\rho_u a_u^2} = \frac{aT_{u,g}^3\mu m_p}{\rho_u\gamma_{\rm ad}k_B} \tag{2.68}$$

$$\mathbb{C} = c/a_u = c\sqrt{\frac{\mu m_p}{\gamma_{\rm ad}k_B T_{u,g}}} \tag{2.69}$$

$$\tau = \chi_0 L\ . \tag{2.70}$$

Here, quantities with subscript u refer to upstream values[6]. For consistency with equations 2.1 through 2.3 we take ρ_u and v_u to be measured in the lab frame and T_u, a_u, and χ_0 to be measured in the comoving frame, although this distinction is not made in Lowrie & Edwards (2008). Also note that when setting these parameters, the upstream gas is considered to be in radiative equilibrium so that $T_{u,g} = T_{u,r}$.

Following Lowrie & Edwards (2008) and Jiang et al. (2012), we choose $\mathbb{P} = 10^{-4}$, $\mathbb{C} = 1.732 \times 10^3$, and $\tau = 577$. We take $L = 1$ cm, so that[7] $\chi_0 = 577$ cm^{-1}. We have also set $\mu = 0.5$. The upstream density, temperature, and velocity of the fluid can be determined from these values, and the downstream values can be calculated using the jump conditions and the procedure for solving them outlined in Bouquet et al. (2000).

We used the Eulerian version of the code. For $\mathcal{M} = 2$ and $\mathcal{M} = 5$, we initialized the computational domain with a step function obeying the jump conditions, not the full semi-analytic solution, and let the shock structure develop on its own. Then, once a structure emerged that was stable over multiple shock crossing times, we spatially translated this solution to compare the numerical shock structure to the semi-analytic solution. We used Dirichlet boundary conditions for the hydrodynamics solver. On the upstream side of the

[6] Lowrie & Edwards (2008) use a slightly different set of nondimensional parameters, but they are directly mappable to the ones listed here.

[7] In terms of the parameters used in Lowrie & Edwards (2008), we are using $\sigma_a = 10^6$ and $\kappa = 1$.

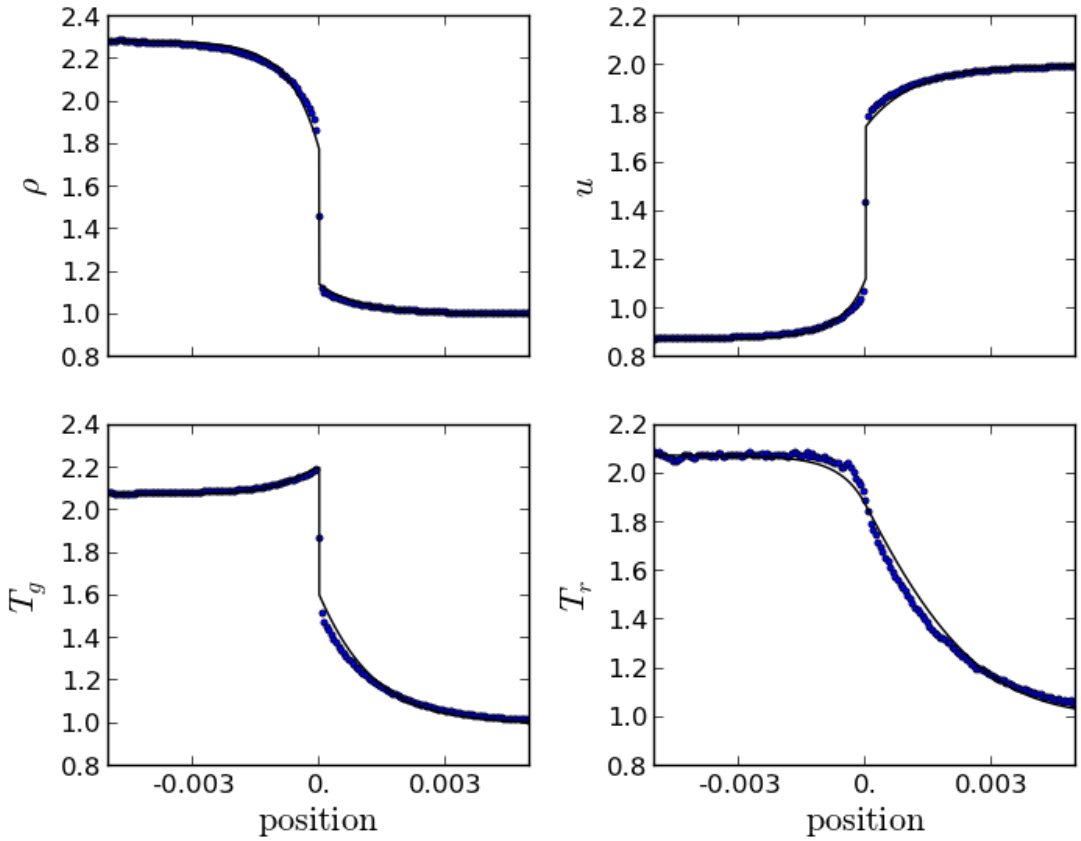

Figure 2.9: Steady radiating shock test as in Lowrie & Edwards (2008), with $\mathcal{M} = 2$. The points are output from our Monte Carlo rad-hydro calculation, and the solid line is the semi-analytic solution. All hydrodynamic variables have been nondimensionalized (see text for details). The numerical parameters used for this test are listed in Table 2.1.

domain, we used reflecting boundary conditions for the radiation. On the downstream side, we let the radiation escape freely.

Figure 2.9 shows the results for the $\mathcal{M} = 2$ case at $t = 1.0 \times 10^{-9}$ s, and Figure 2.10 shows the results for the $\mathcal{M} = 5$ case at $t = 1.9 \times 10^{-9}$ s. In general, there is excellent agreement with the semi-analytic solution. One slight issue relates to resolving the narrow Zeldovich temperature spike. For the $\mathcal{M} = 5$ case, we increased our resolution all the way to 2048 zones, and even then the spike is slightly underestimated.

For the $\mathcal{M} = 2$ case, we also display our computed value of the Eddington tensor element f^{zz} as a function of position in Figure 2.11. FLD assumes that the diagonal elements of f^{ij} never drop below 1/3. We find, as in Sincell et al. (1999) and Jiang et al. (2012), that f^{zz} does indeed drop below 1/3 near the shock.

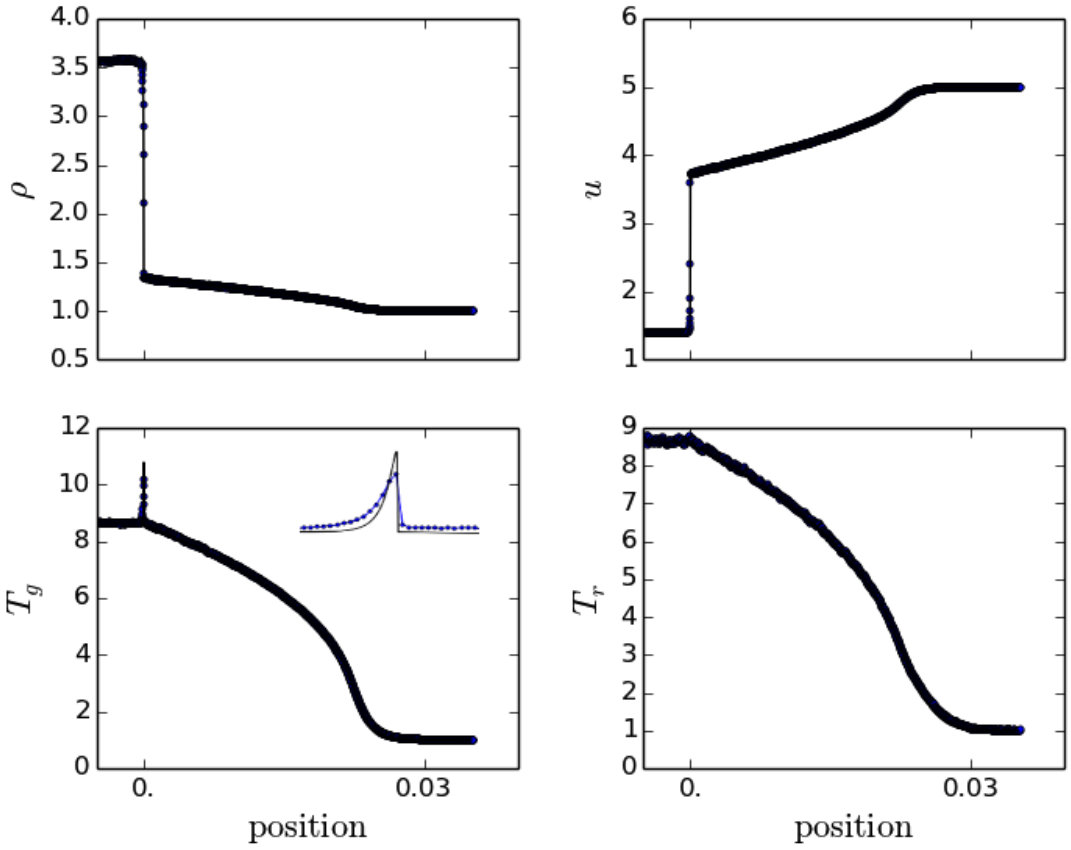

Figure 2.10: Similar to Figure 2.9, but for $\mathcal{M} = 5$. The inset in the gas temperature plot is a zoomed-in plot in the region of the Zeldovich spike, and is not to scale with the rest of the figure.

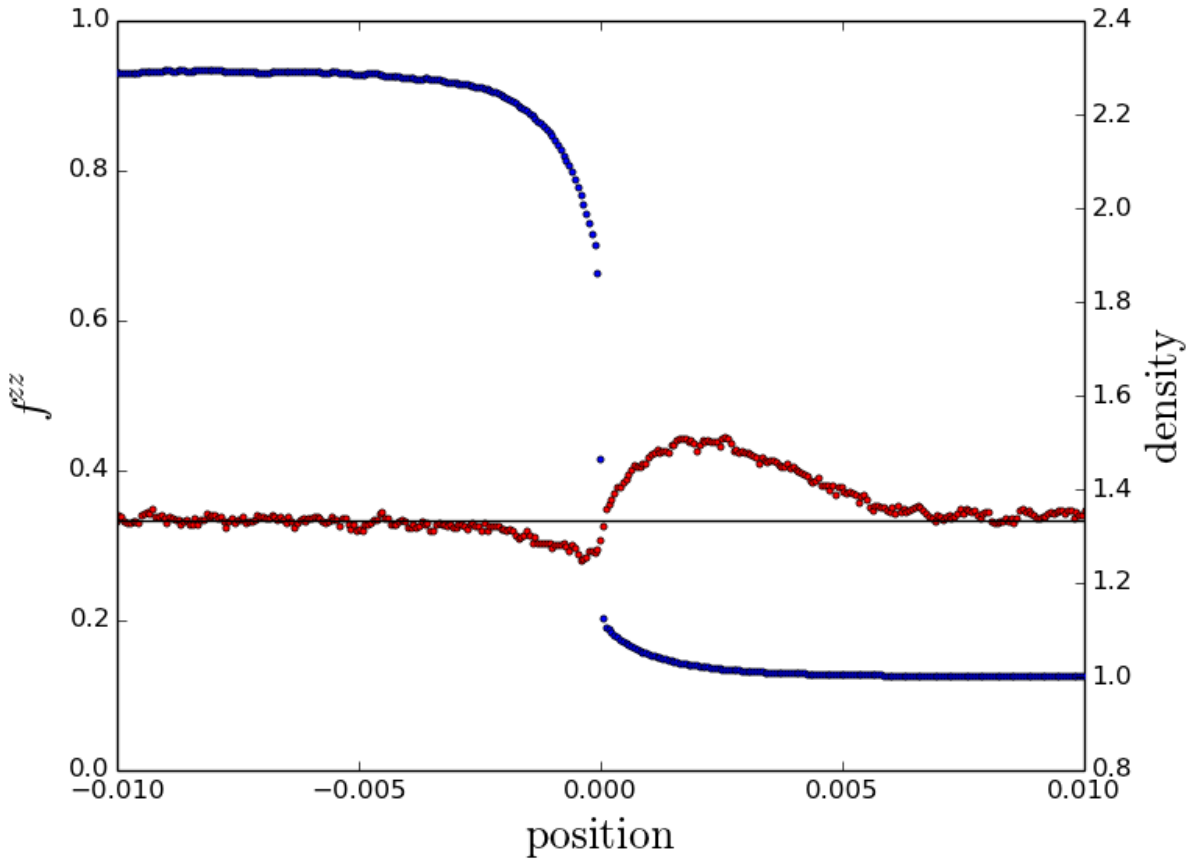

Figure 2.11: Eddington tensor element f^{zz} (red) for the $\mathcal{M} = 2$ steady radiating shock test, with the nondimensional density (blue) over-plotted. The solid black line represents a constant value of 1/3, which holds in the diffusion approximation. We that f^{zz} does indeed drop below 1/3 near the shock, as previous authors have observed (see text for details).

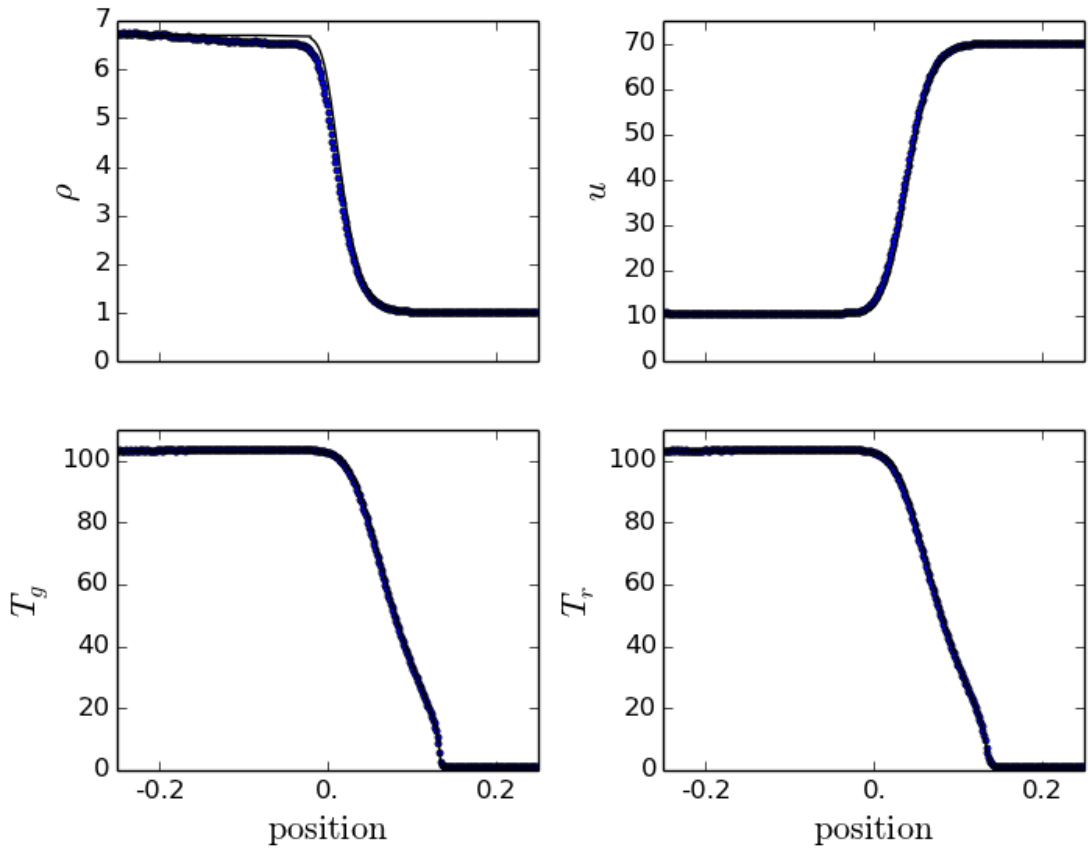

Figure 2.12: Similar to Figures 2.9 and 2.10, but for $\mathcal{M} = 70$.

We also considered a stronger shock, with $\mathcal{M} = 70$. In this case, we initialized the problem with the steady-state solution and tested to make sure it maintained that solution over several shock crossing times. Also for the $\mathcal{M} = 70$ case, rather than implementing a constant radiative flux boundary condition on the downstream side, we used a reflecting boundary condition for the downstream radiation, and extended the downstream domain so that any spurious effects from this boundary condition did not have time to reach the region of interest near the shock.

Figure 2.12 shows the results for the $\mathcal{M} = 70$ case at $t = 10^{-9}$ s. This case is particularly interesting because downstream of the shock, the radiation energy density is larger than the gas thermal energy by a factor of about 9. Here radiation pressure becomes dynamically important, and we are testing the behavior of the radiation pressure force in our code in the optically thick regime. We find good agreement between our computed results and the semi-analytic solutions for the gas and radiation temperatures. However, we find that the gas density on the downstream side is about 5% lower than expected based on the jump

conditions. The cause of this discrepancy is unclear, but it might be related to our method for coupling the radiation momentum source terms to the Godunov solver. Our hydro time-steps are large enough that we are in the highly implicit regime for the Monte Carlo, although our solution does not appear to change signficantly if we reduce our CFL number by a factor of 2.

2.8.6 Non-steady radiating shocks

This test involves a super-critical radiative shock driven by the supersonic motion of a piston into initially uniform and static gas, as defined by Ensman (1994). The test has been revisited many times, including in Hayes et al. (2006), in which the ZEUS-MP2 code was used to solve the problem while making use of the flux-limited diffusion approximation for the radiation. More recently, Noebauer et al. (2012) compared the results of their Monte Carlo radiation-hydrodynamics code to the ZEUS results for this problem.

The numerical parameters for these tests are reported in Table 2.1. Additionally, we used reflecting boundary conditions for both the radiation and the hydrodynamics at the piston boundary. On the other side of the domain, we let radiation escape freely, and we used Dirichlet boundary conditions for the hydrodynamics.

In Figures 2.13 and 2.14 we display our results for the sub-critical and super-critical versions of the test, respectively. The agreement between the two codes is encouraging. As Noebauer et al. (2012) found, we see deeper penetration of the radiation into the radiative precursor than in the FLD result. We also find that the radiative precursor in our results takes slightly more time to develop than in Zeus, and this might be due to our implicit treatment of the radiative cooling.

2.9 Radiation Force Calculation Using the Divergence of the Eddington Tensor

One of the main concerns with applying MCRT methods to RHD problems is that the estimators of the radiation field possess stochastic errors that may propagate into the dynamics. In general, the radiation force is more poorly sampled than the radiation energy deposition, due to the fact that packets traveling in opposite directions cancel out in the estimator of the flux. The problem becomes more acute in regions of high optical depth, where the radiation becomes nearly isotropic and the flux constitutes only a small fraction of the total radiation mean intensity.

In this case, a better approach (mentioned in section 2.3) may be to use the divergence of the Eddington tensor (equation 2.29) to derive the radiation force. As noted before, this approach is only guaranteed to be accurate when the radiation is diffusing, but that is precisely the situation in which such an approach becomes most attractive. The P^{zz} element of the radiation pressure tensor does not suffer from the same packet cancellation as does the flux, and so is typically better estimated. To calculate the radiation force, we used a

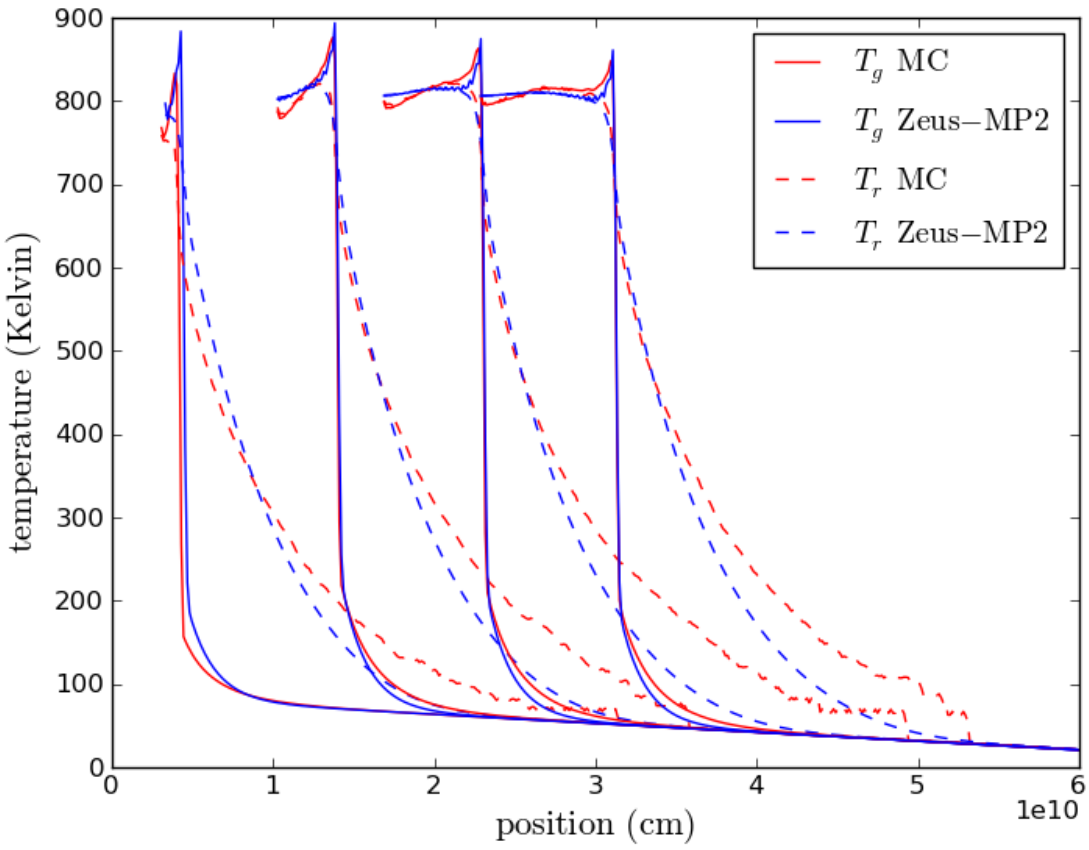

Figure 2.13: Gas and radiation temperatures for the sub-critical moving shock test as described in Ensman (1994). We compare our solutions for the radiation and gas temperatures to those computed by the ZEUS-MP2 code. While the two calculations agree very well in the vicinity of the shock, the radiative precursor in the Monte Carlo calculation extends farther into the upstream gas, as was also observed in Noebauer et al. (2012). The numerical parameters used in this test are listed in Table 2.1.

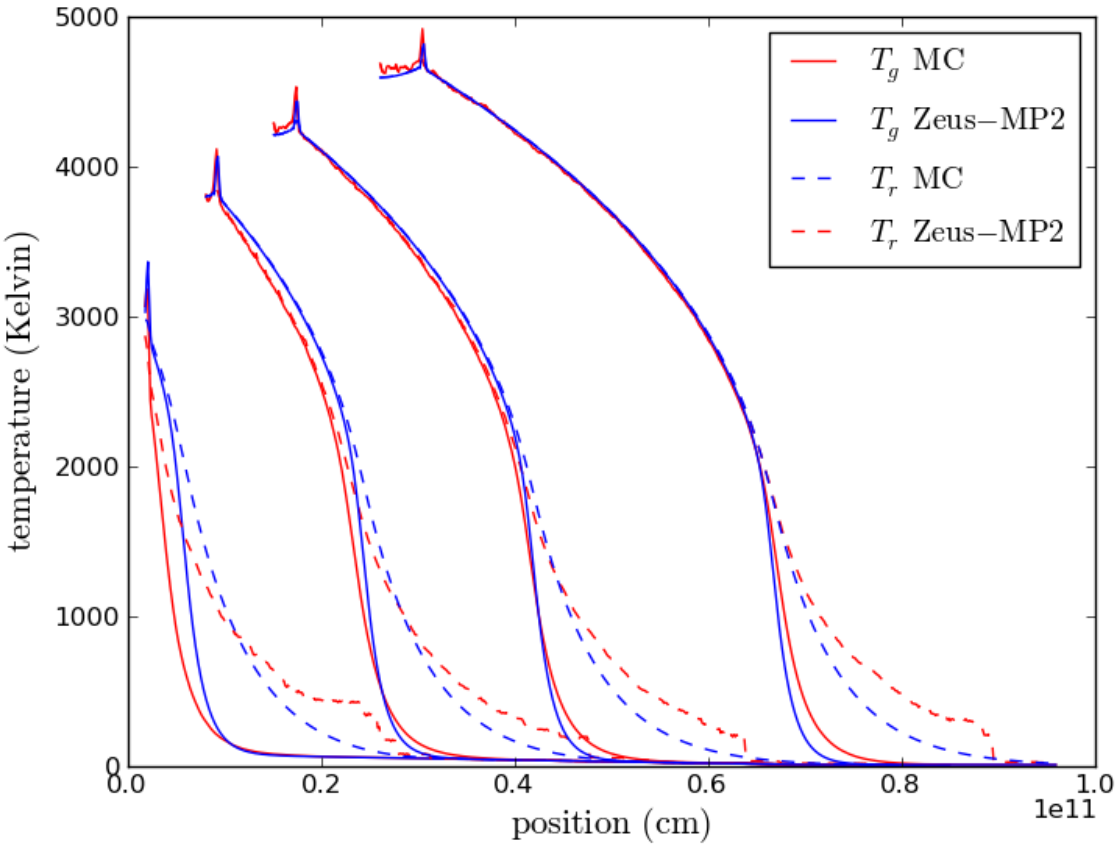

Figure 2.14: Similar to Figure 2.13, but for a super-critical radiating shock.

simple centered difference to take a second-order spatial derivative of the pressure tensor. We note that there are more sophisticated methods for taking numerical derivatives of noisy data, and that these may lead to superior results.

Figure 2.15 compares the noise in the calculation of the radiation force in the $\mathcal{M} = 70$ steady radiating shock test using our two different methods (in all other tests, only the direct Monte Carlo estimator of the force was used, not the divergence of the pressure tensor). The figure demonstrates that although the two methods converge to a similar result at high spatial resolution and for a large number of packets, the pressure tensor divergence method converges must faster - it provides much less noise than the direct Monte Carlo summation method for coarser spatial resolutions and lower packet number.

These results suggest the possibility of using MCRT in a hybrid approach with other radiation transport schemes. In particular, solution of the radiation moment equations require a closure relation, which is often taken to be an approximate analytic prescription. Solution of the MCRT, however, provides estimator of the true Eddington tensor, which could then be used as a closure to the moment equations. In this case, the MCRT may not need to be run every time-step, allowing for a reduced computational load.

2.10 Performance

The relative performance of the MCRT compared to traditional radiation-hydrodynamics schemes depends sensitively on the particular problem at hand — the spatial resolution, optical depth, degree of radiation domination, and level of tolerable noise. For the test problems discussed in the last section, we find that MCRT execution times are in some cases comparable to grey FLD techniques, and in others considerably more expensive.

Table 2.2 summarizes the execution times for the Ensman super-critical shock test for a varying number of Monte Carlo packets employed, and two separate spatial resolutions. These tests were performed on a 2012 MacBook Pro laptop (2.6 Ghz Intel Core i7 processor) and compiled with g++. For comparison, we have included tests run with the flux-limited diffusion code Zeus-MP, run on the same machine and compiled with gfortran.

When a smaller number of packets is used, the radiation field in the MCRT calculation naturally possesses increased noise, as illustrated in Figure 2.16. The error is most apparent in the high-temperature shocked gas, and in the stair step behavior at the leading edge of the radiative precursor. The latter effect arises because only a small number of high energy packets manage to diffuse ahead of the shock in any given time-step. This behavior is in part due to our unoptimized choice to emit equal numbers of packets in every zone, despite the fact that the emissivity behind the shock is at least 10^6 times greater than that of the coldest gas ahead of it. Applications of so-called importance sampling techniques may substantially reduce the error without increasing the execution time. In particular, one could increase the number of high-energy packets emitted near the shock interface, while at the same time reducing the number of low-energy packets emitted in the pre-shock region.

It is comforting to see that, despite the noisy radiation field of Figure 2.16, the gas density

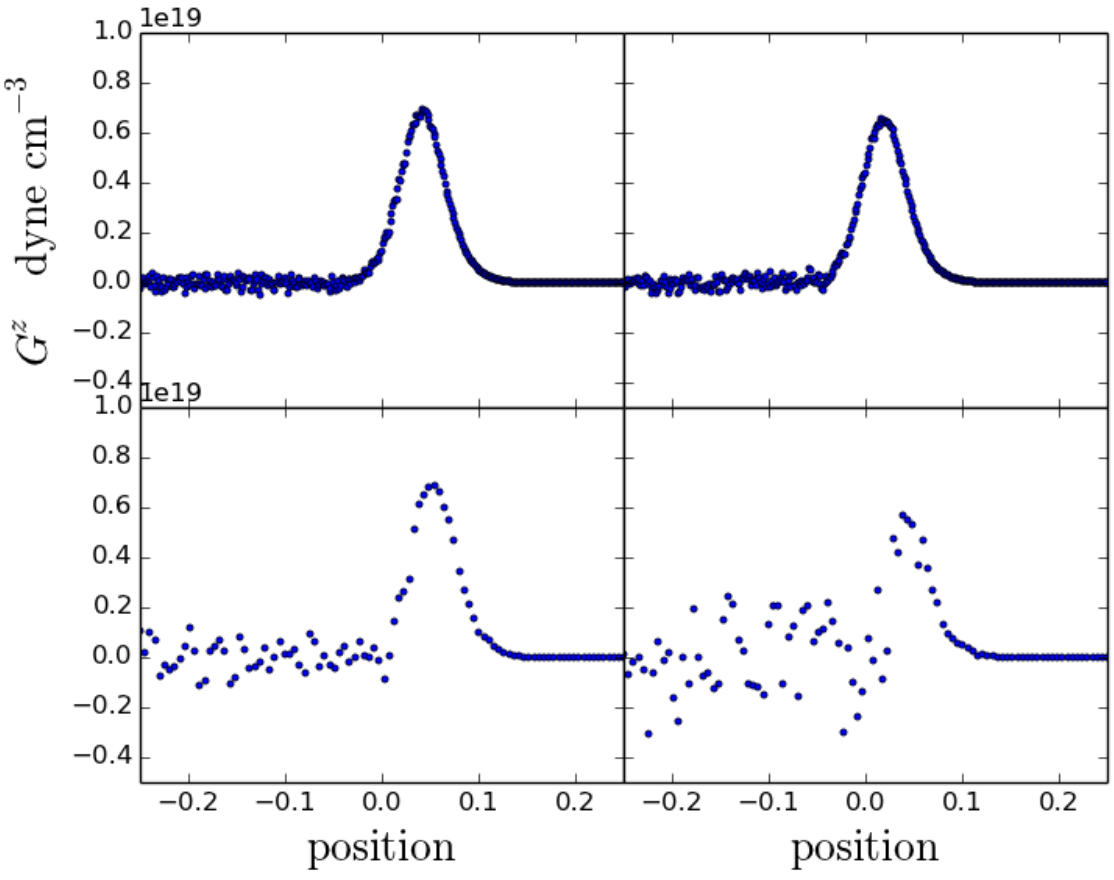

Figure 2.15: Comparison of calculations of the radiation force in the $\mathcal{M} = 70$ steady radiating shock problem. The left panels use the divergence of the pressure tensor to calculate the radiation force, whereas the right panels use the direct Monte Carlo summation method. The top two panels use numerical parameters as listed in Table 2.1. The bottom two panels use a spatial resolution that is four times as coarse, and a maximum of 4000 packets per zone instead of 7680.

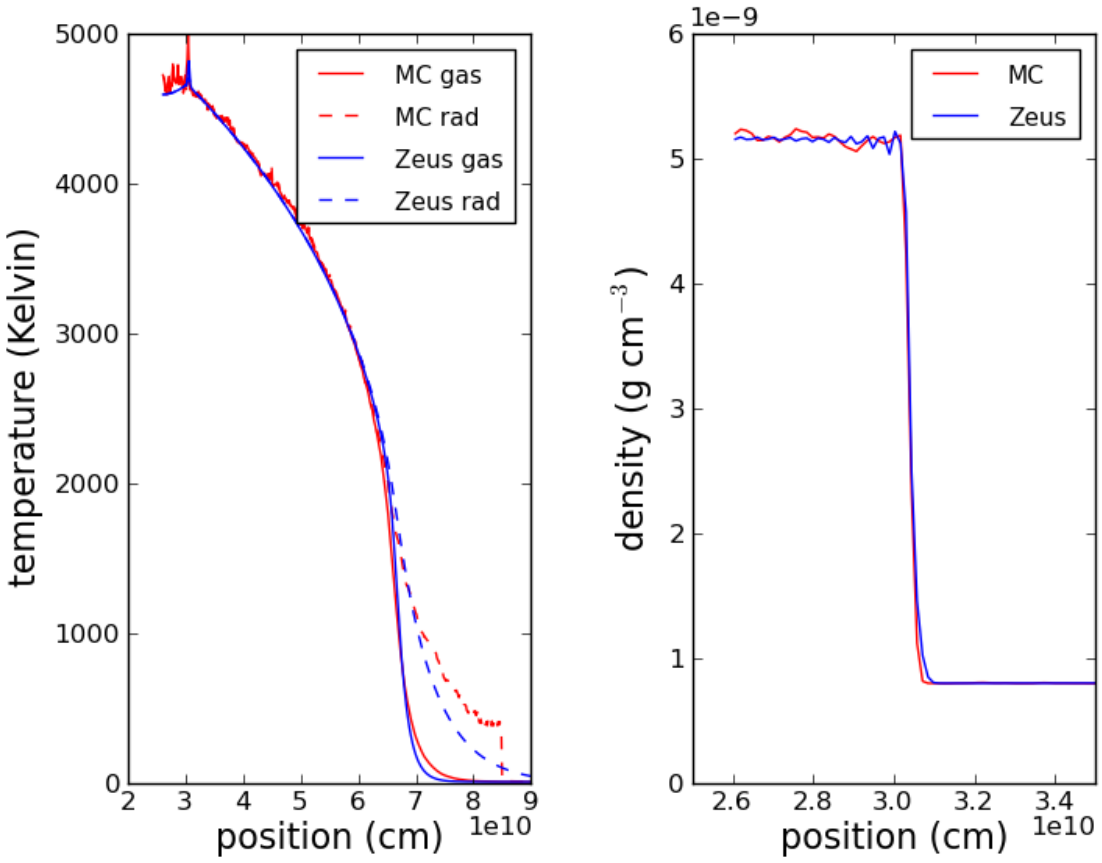

Figure 2.16: The left panel corresponds to the fourth time output in Figure 2.14, but with a maximum of only 100 packets emitted per zone per time-step, instead of 1000. The right panel shows the corresponding gas densities.

suffers less from noise. This is because the gas properties are determined by the radiative heating and acceleration integrated over many time-steps. These time-averaged quantities are more accurately sampled than the instantaneous radiation field snapshot plotted in the figure. In general, we find that for problems where gas energy dominates, the dynamics of the problem are rather robust against instantaneous radiation noise. For problems where radiation energy and pressure dominate, the radiation noise is more problematic and can propagate into the gas properties. The deleterious effect of noise may also be more significant in multi-dimensional simulations where instabilities might develop.

Figure 2.17 shows the gas temperatures computed for each of the calculations in Table 2.2, zoomed in to the region surrounding the Zeldovich spike. In addition to the noise present at the scale of a few zone widths, the value of the temperature averaged over larger scales also varies between the individual Monte Carlo calculations at the level of a few percent, as is evident in Figure 2.17 and listed in Table 2.2. In order to quantify the small-scale noise, we focus on the region upstream (left) of the spike, where the effect of the noise is most severe. We apply an offset to the Monte Carlo temperatures so that their mean value in this region matches that of the Zeus calculation. Then, we measure the root mean square difference between these offset gas temperatures and the temperatures computed by Zeus, excluding the 3 zones directly adjacent to the left boundary. The effect of increasing the number of packets on the RMS error for the four calculations with 1200 zones agrees especially well with the rule of thumb that the random error should scale as $1/\sqrt{N}$ where N is the number of packets employed. We see that to decrease the RMS error associated with small-scale noise to within 1%, the CPU time requirement is approximately four times that of Zeus in the runs employing 512 zones, and twice that of Zeus in the runs employing 1200 zones.

The potential performance advantages of the MCRT method would become more apparent if, instead of comparing to Zeus-MP, we were to compare to a non-grey radiation code. For most deterministic transport methods, the execution time scales with the number of angle bins and frequency groups employed, and therefore become significantly more expensive than grey FLD. Our MCRT calculations, on the other hand, already include the angular information and can be run in multi-frequency mode with minimal additional computational expense. Photon packets are distributed across the relevant frequency range and, because the radiation force four-vector is given by integrals over frequency, no additional packets are needed to construct source term estimators of comparable noise, at least in the case that the opacity has a reasonably smooth frequency dependence. In cases where the opacity has sharp dependencies (e.g., lines), importance sampling technique can be used to increase packet statistics at the most important frequencies. Convergence tests varying the number of packets would be required to determine whether the frequency sampling had been sufficient.

As already mentioned, the execution time of the MCRT code is highly problem-dependent, in particular because of the well-known inefficiency of Monte Carlo methods in regions of high optical depth, where many photon interactions must be tracked per time-step. For high optical depth cases, a substantial speed-up can be obtained through the inclusion of the discrete diffusion technique, which has been described for the gray radiation case in Gentile (2001); Densmore et al. (2007) and the non-gray case in Abdikamalov et al. (2012).

Table 2.2: Performance comparison for the Ensman super-critical shock test

Description	Mean gas temperature (K)	RMS noise (K), percent error	CPU Time (minutes)
Zeus 512 zones	4617.5		1.8
MC 512 zones, 100 packets	4686.9	44.7 (0.95 %)	6.4
MC 512 zones, 300 packets	4618.0	29.3 (0.63 %)	18.3
MC 512 zones, 1000 packets	4639.0	24.7 (0.53 %)	56.4
Zeus 1200 zones	4613.8		17.8
MC 1200 zones, 50 packets	4535.5	50.1 (1.1 %)	35.4
MC 1200 zones, 100 packets	4574.1	35.5 (0.75 %)	68.3
MC 1200 zones, 200 packets	4622.2	25.2 (0.55 %)	133.6
MC 1200 zones, 500 packets	4680.6	14.3 (0.31 %)	298.3

Note. — The number of packets in the description refers to the maximum number of packets emitted per zone per time step. All other numerical parameters are as listed in Table 2.1. The mean gas temperature is computed in the upstream region left of the Zeldovich spike, excluding the three zones nearest to the left boundary. For the details of how the RMS noise is computed, please see the text.

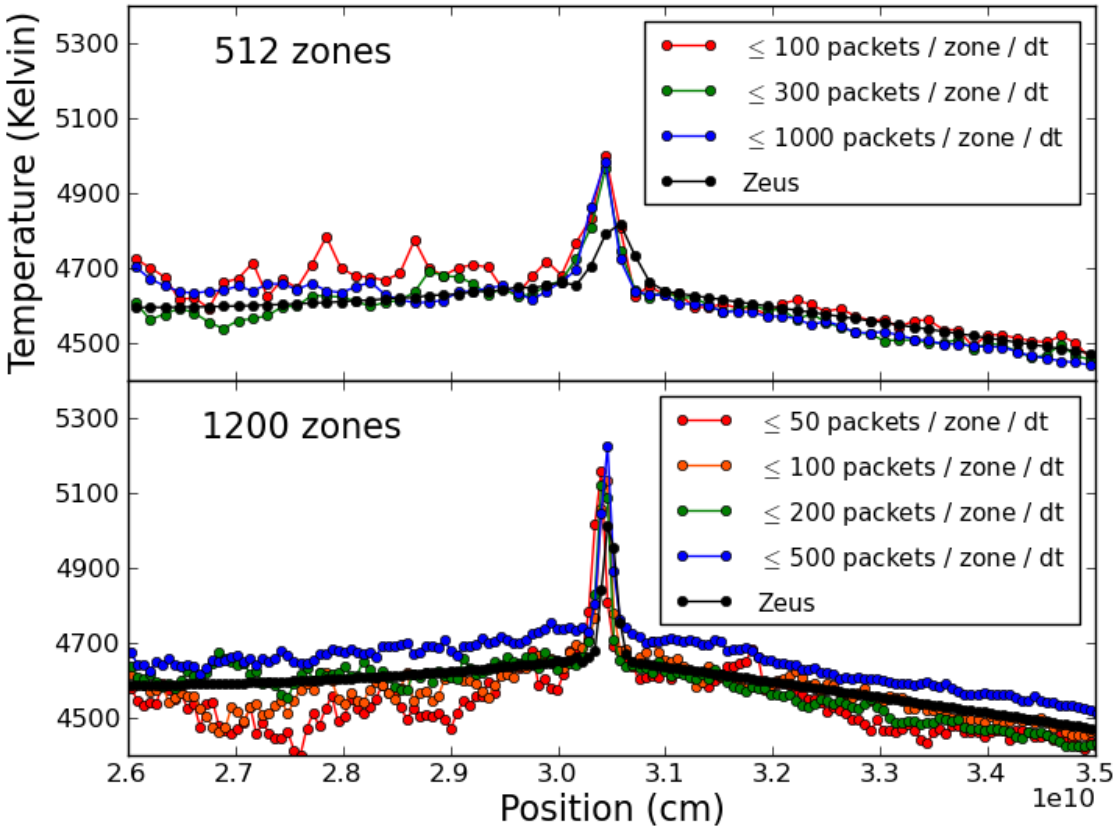

Figure 2.17: Gas temperatures calculated for the Ensman super-critical shock test, zoomed in to the region surrounding the Zeldovich spike, for various packet counts and two separate spatial resolutions.

For problems with one spatial dimension, or problems of higher dimension and sufficiently coarse spatial resolution, the entire computational domain can be stored in the memory of a single computational node. With the added fact that Monte Carlo packets propagate independently of one another over a single time-step, this permits an "embarrassingly parallelizable" treatment for the radiation portion of the problem. The transport step may be replicated over as many computational nodes as are available, and then the results of the packet propagation during each time-step for each node can be summed together with an Message Passing Interface (MPI) reduction.

We have run MPI-parallelized versions of the Ensman sub-critical shock test in which the total number of photon packets per time-step is held constant, but is divided over varying numbers of CPUs. Although we have only parallelized the radiation portion of the code, the CPU time required to execute the hydro update is negligible compared to the radiation. We see perfect strong parallel scaling in the time for this test, which is to say that the amount of wall time needed to complete the test is cut in half each we double the number of cores we use, as shown in Figure 2.18.

2.11 Conclusions regarding the radiation-hydrodynamics coupling

We have demonstrated that MCRT coupled to both Lagrangian and Eulerian hydrodynamics solvers can result in accurate, robust treatments of RHD problems, including those in which the radiation energy dominates. Although we have focused here on 1-dimensional test problems, our Eulerian code is multi-dimensional, and subsequent studies will address astrophysical problems in higher spatial dimensions.

Our approach makes use of the implicit MCRT method to allow us to take hydrodynamical time-steps much larger than the gas cooling time. We also showed how to use Monte Carlo estimators to construct expressions for the radiation force four-vector G^i that are accurate to all orders of v/c, although the hydrodynamics equations are only solved to order v/c. We compared simulations using our exact expression for G^i to those using a more approximate expression based on the divergence of the radiation pressure tensor, which is valid when the radiation is in the diffusion regime. We found that the latter method can lead to a significant reduction in Monte Carlo noise in cases of coarse spatial resolution. In most of the problems studied here, the presence of stochastic noise did not introduce substantial error in the dynamics, however the effects of noise become a larger concern in problems where radiation energy is strongly dominated.

Several additional refinements will be explored in the future. We will consider the use of a more sophisticated treatment of the radiative source terms in the Godunov scheme. Improvements in performance may be realized by incorporating the discrete diffusion technique. It is straightforward to incorporate the effects of more complicated radiation-matter interactions, including photoionization and anisotropic scattering processes such as Compton scattering with Klein-Nishina corrections. Possible applications of this technique include radiatively-

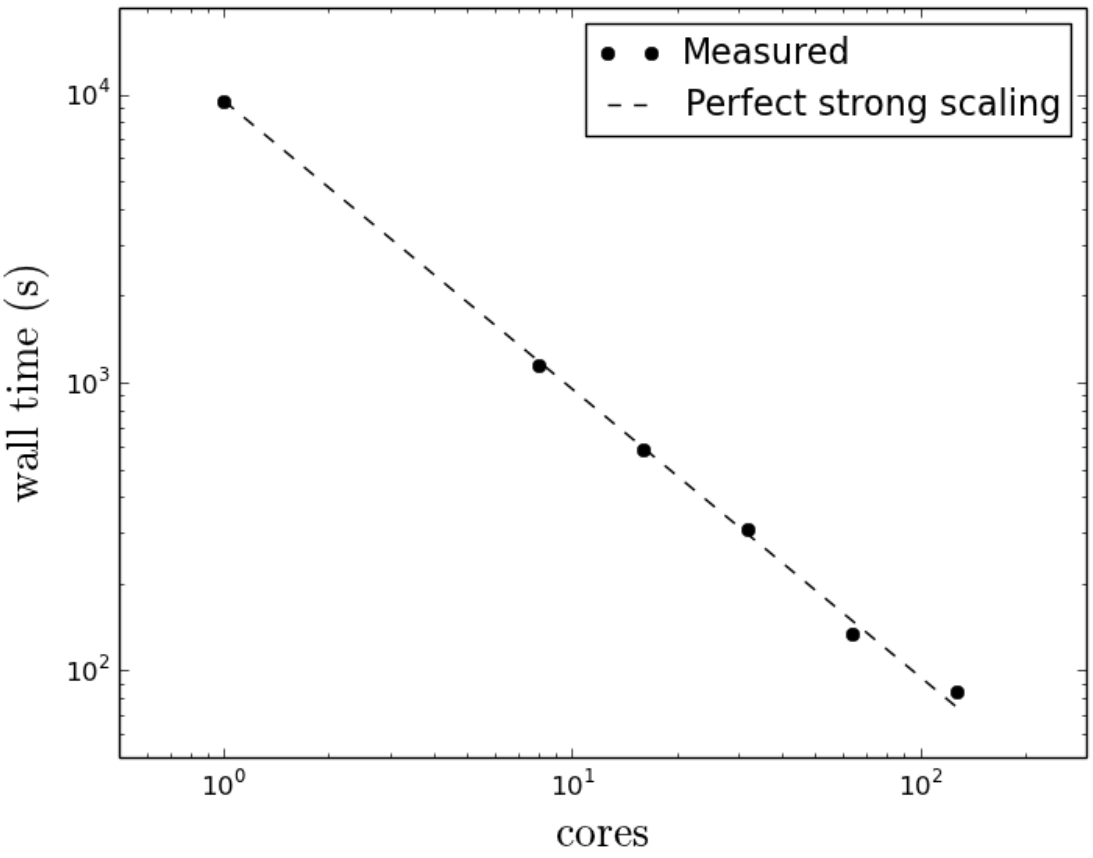

Figure 2.18: Parallel scaling for the Ensman sub-critical shock test.

launched winds from galaxies, tidal disruptions of stars, shock breakouts and ejecta-ISM interactions in supernovae.

2.12 Non-LTE solution of ionization states and bound electron level populations

The goal here is to understand, given statistical equilibrium, the behavior of the level populations as a function of radius for *spherically symmetric*, *pure hydrogen* gas illuminated by a *source radiating as a blackbody* at some fixed (position-independent) temperature T_s. The gas itself might have a radial temperature dependence which can affect its electron recombination rates. We assume that collisional transition rates are negligible. This simple case is the starting point for the more detailed non-LTE calculations presented in Chapter 4.

Note that Johnson & Klinglesmith (1965), with help from White (1961), wrote down the formal solution for the case with three bound levels plus continuum, and for a more arbitrary source spectrum. Here, with our restriction of the source to a blackbody, and by factoring out the optically thin solution, we obtain formuale more suitable for gaining physical intuition.

2.12.1 Two bound levels

Let the levels have energies E_1 and E_2, $E_2 > E_1$, with statistical weights g_1 and g_2. Also let $\nu_{12} = (E_2 - E_1)/h$. Statistical equilibrium at each position gives

$$n_2 A_{21} = n_1 \bar{J}_\nu B_{12} - n_2 \bar{J}_\nu B_{21} \tag{2.71}$$

where, as usual, $\bar{J}_\nu$ is equal to J_ν integrated over the line profile.

We rearrange to get

$$\frac{n_1}{n_2} = \frac{A_{21} + \bar{J}_\nu B_{12}}{\bar{J}_\nu B_{21}} \tag{2.72}$$

This equation, along with the total conservation equation $n_1 + n_2 = n_H$ and a manner of obtaining J_ν, specify the level populations completely. In general it is not easy to solve because $\bar{J}_\nu$ can depend on the level populations - in the formal soluiton for J in terms of the source function S, S depends on the level populations.

We will factor J as follows

$$J_\nu(r) = W(r) s_\nu B_\nu(T_s) \tag{2.73}$$

where W is the geometrical dilution factor

$$W(r) = \frac{1}{2}\left[1 - \sqrt{1 - \left(\frac{r_p}{r}\right)^2}\right] \tag{2.74}$$

and s_ν is any further enhancement/dehancement of the radiation field with respect to a diluted blackbody at each frequency. When the gas is optically thin, $s_\nu \to 1$ for all ν.

We will also consider the line to be sufficiently narrow such that $\bar{J}_\nu = J_{\nu_{12}}$ to a high degree of accuracy. Then we have

$$\frac{n_1}{n_2}(r) = \frac{A_{21} + s_{\nu_{12}} W(r) B_{\nu_{12}}(T_s) B_{12}}{s_{\nu_{12}} W(r) B_{\nu_{12}}(T_s) B_{21}} \tag{2.75}$$

One must be careful here not to confuse the Einstein coefficients with the Planck function evaulated at ν_{12} in the above expression.

After writing out the Planck function, using the relations between the Einstein coefficients, and going through some algebra, we get

$$\frac{n_1}{n_2}(r) = \left[\frac{g_1}{g_2} e^{\zeta_{12}}\right] \left[\frac{1 + e^{-\zeta_{12}} \left(s_{\nu_{12}} W(r) - 1\right)}{s_{\nu_{12}} W(r)}\right] \tag{2.76}$$

where

$$\zeta_{12} \equiv \frac{h\nu_{12}}{kT_s} \tag{2.77}$$

We see that if $sW \gg \exp(h\nu_{12}/kT_s)$ (which automatically implies $sW \gg 1$), then the ratio of the level populations approaches the ratio of the g's. That is, all states at all energy levels are occupied with nearly equal probability, because the radiation field is so energetic. As sW goes down, the ratio n_1/n_2 increases montonically.

2.12.2 Two bound levels plus continuum

The photoionization rate from level i, with photoionization cross-section $\sigma_i(\nu)$, is given by

$$\int_{\nu_{ci}}^{\infty} \frac{\sigma_i(\nu) J_\nu}{h\nu} d\nu \equiv \mathcal{I}_i \tag{2.78}$$

where ν_{ci} is the minimum frequency for photo-ionizing from level i to the continuum.

Then statistical equilibrium for the $n = 2$ level gives

$$n_2 A_{21} + n_2 \mathcal{I}_2 = n_1 \bar{J}_\nu B_{12} - n_2 \bar{J}_\nu B_{21} + n_e n_p \alpha_2 \tag{2.79}$$

Statistical equilibrium for the continuum gives

$$n_1 \mathcal{I}_1 + n_2 \mathcal{I}_2 = n_e n_p \left(\alpha_1 + \alpha_2\right) \tag{2.80}$$

Considering the equilibrium for $n = 1$ gives no new information. Of course, we still have the total conservation condition $n_1 + n_2 + n_p = n_H$. We're considering pure hydrogen for the moment, so $n_p = n_e$. We can use the continuum equation to write the product $n_e n_p$ in terms of other quantities, use the Einstein relations and go through the algebra to finally obtain

$$\frac{n_1}{n_2} = \frac{g_1}{g_2} e^{\zeta_{12}} \left[\frac{1 + e^{-\zeta_{12}}(s_{\nu_{12}} W - 1) + \frac{\mathcal{I}_2}{A_{21}} \left(1 - e^{-\zeta_{12}}\right) \frac{\alpha_1}{\alpha_1 + \alpha_2}}{s_{\nu_{12}} W + \frac{\mathcal{I}_1}{A_{21}} \frac{g_1}{g_2} \left(e^{\zeta_{12}} - 1\right) \frac{\alpha_2}{\alpha_1 + \alpha_2}}\right] \tag{2.81}$$

As a consistency check, we see that this reduces to the two-level solution without continuum when both $\mathcal{I}_1$ and $\mathcal{I}_2$ are zero. Now, as T_s varies, there exists a maximum value for n_2, instead of the monotonic behavior we saw without the continuum.

2.12.3 Three bound levels plus continuum

Statistical equilibrium for the $n = 2$ level gives

$$n_2 A_{21} + n_2 \bar{J}_\nu B_{21} + n_2 \bar{J}_\nu B_{23} + n_2 \mathcal{I}_2 = n_3 A_{32} + n_1 \bar{J}_\nu B_{12} + n_3 \bar{J}_\nu B_{32} + n_e n_p \alpha_2 \tag{2.82}$$

For the $n = 3$ level:

$$n_3 A_{32} + n_3 A_{31} + n_3 \bar{J}_\nu B_{31} + n_3 \bar{J}_\nu B_{32} + n_3 \mathcal{I}_3 = n_1 \bar{J}_\nu B_{13} + n_2 \bar{J}_\nu B_{23} + n_e n_p \alpha_3 \tag{2.83}$$

For the continuum:

$$n_1 \mathcal{I}_1 + n_2 \mathcal{I}_2 + n_3 \mathcal{I}_3 = n_e n_p \left(\alpha_1 + \alpha_2 + \alpha_3\right) \tag{2.84}$$

The $n = 1$ level euilibrium equation gives no new information. The condition $n_1 + n_2 + n_3 + n_p = n_H$, and hydrogen charge conservation $n_e = n_p$, close the system.

Our factoring of J_ν and the relations between the Einstein coefficients eventually let us write

$$\frac{n_1}{n_3} = \frac{1 + \frac{s_{\nu 31} W}{e^{\zeta_{31}} - 1} + \frac{\mathcal{I}_3}{A_{31}} \left(1 - \frac{\alpha_3}{\alpha_1 + \alpha_2 + \alpha_3}\right) + \frac{A_{32}}{A_{31}} \left(1 + \frac{s_{\nu 32} W}{e^{\zeta_{32}} - 1}\right)}{\frac{g_3}{g_1} \frac{s_{\nu 31} W}{e^{\zeta_{31}} - 1} + \frac{\mathcal{I}_1}{A_{31}} \left(\frac{\alpha_3}{\alpha_1 + \alpha_2 + \alpha_3}\right) + \frac{n_2}{n_1} \left[\frac{g_3}{g_2} \frac{A_{32}}{A_{31}} \frac{s_{\nu 32} W}{e^{\zeta_{32}} - 1} + \frac{\mathcal{I}_2}{A_{31}} \left(\frac{\alpha_3}{\alpha_1 + \alpha_2 + \alpha_3}\right)\right]} \tag{2.85}$$

and

$$\frac{n_1}{n_2} = \frac{1 + \frac{s_{\nu 21} W}{e^{\zeta_{21}} - 1} + \frac{\mathcal{I}_2}{A_{21}} \left(1 - \frac{\alpha_2}{\alpha_1 + \alpha_2 + \alpha_3}\right) + \frac{g_3}{g_2} \frac{A_{32}}{A_{21}} \frac{s_{\nu 32} W}{e^{\zeta_{32}} - 1}}{\frac{g_2}{g_1} \frac{s_{\nu 21} W}{e^{\zeta_{21}} - 1} + \frac{\mathcal{I}_1}{A_{21}} \left(\frac{\alpha_2}{\alpha_1 + \alpha_2 + \alpha_3}\right) + \frac{n_3}{n_1} \left[\frac{A_{32}}{A_{21}} \left(1 + \frac{s_{\nu 32} W}{e^{\zeta_{32}} - 1}\right) + \frac{\mathcal{I}_3}{A_{21}} \left(\frac{\alpha_2}{\alpha_1 + \alpha_2 + \alpha_3}\right)\right]} \tag{2.86}$$

So schematically, if

$$\frac{n_1}{n_3} = \frac{A}{B + C \frac{n_2}{n_1}} \qquad \frac{n_1}{n_2} = \frac{D}{E + F \frac{n_3}{n_1}} \tag{2.87}$$

then

$$\frac{n_1}{n_3} = \frac{AD - CF}{BD + CE} \qquad \frac{n_1}{n_2} = \frac{AD - CF}{AE + BF} \tag{2.88}$$

A note of caution: The presence of the terms such as $e^{\zeta_{32}} - 1$ in denominators will result in division by zero when two of the three levels are degenerate.

2.12.4 Concluding remarks about the analytics

The main challenge we face when making use of these expressions for the level populations is their dependence on the exact structure of J_ν. This determines the values of the photoionization rates $\mathcal{I}_i$ and the line radiation enhancements $s_{\nu_{ij}}$.

In the optically thin limit all the $s_{\nu_{ij}} \to 1$ and the photoionization rates can be straightforwardly integrated numerically given expressions for the photoionization cross-sections.

When there is non-negligible optical depth to photoionization and the line transitions, the only way to proceed exactly is to simultaneously solve the transfer equation for J_ν along with the expressions for the level populations in terms of J_ν at each radius working outward, or using full Monte Carlo. The presence of electron scattering and/or bremsstrahlung complicates the soluiton even more.

Given certain guesses about the level populations, it might be possible to simplify the expressions for the population ratios by dropping terms and then check for self-consistency.

There might also be a way to make further progress on paper by assuming homologous expansion and working with line escape probabilities.

2.12.5 Test problem

To put the preceding ideas into action, we set up a test problem with the following parameters: $T_s = 5 \times 10^4$ K, inner radius 3×10^{13} cm, outer radius 1×10^{14} cm, uniform gas density of 1 cm^{-3} (although this value does not matter, as long as the gas remains optically thin), and uniform gas temperature of 5×10^4 K.

The simplified hydrogen atomic strucutre consists of three bound levels, with principal quantum numbers n of 1, 2, and 3. An additional level representing unbound (continuum) electrons is also included in the model atom. The excitation energies for the bound levels are 0 eV, 10.20 eV, and 12.09 eV for the n = 1, 2, and 3 levels, respectively. The statistical weights for the levels are 2, 8, and 18, respectively. The einstein A coefficients for those three levels are 4.696e8 Hz, 5.572e7 Hz, and 4.408e7 Hz, respectively. The photoionization cross sections are taken to follow a ν^{-3} law, as in Rybicki & Lightman (1986) Equation 10.56, and the Gaunt factors are set to 1. The recombination rate coefficients α_n can then be computed using the Milne relation, as in Rybicki & Lightman (1986) Equation 10.62, and assuming that free electrons follow a Maxwellian velocity distribution at the specified temperature. For the parameters listed above, the recombination coefficients are found to be 5.83e-14, 2.02e-14, and 9.67e-15 cm^3 s^{-1}, respectively.

Figure 2.19 shows the results of the test problem. The solid lines correspond to the ratios $\frac{n_1}{n_2}$ and $\frac{n_1}{n_3}$ as analytically derived from equations (2.85) and (2.86), as a function of radius. The points are the output of the NLTE solver implemented in Sedona. We find that the Sedona values match the analytic function to within 1% error over most of the computational domain, although the error rises to above 5% at the innermost radial zones.

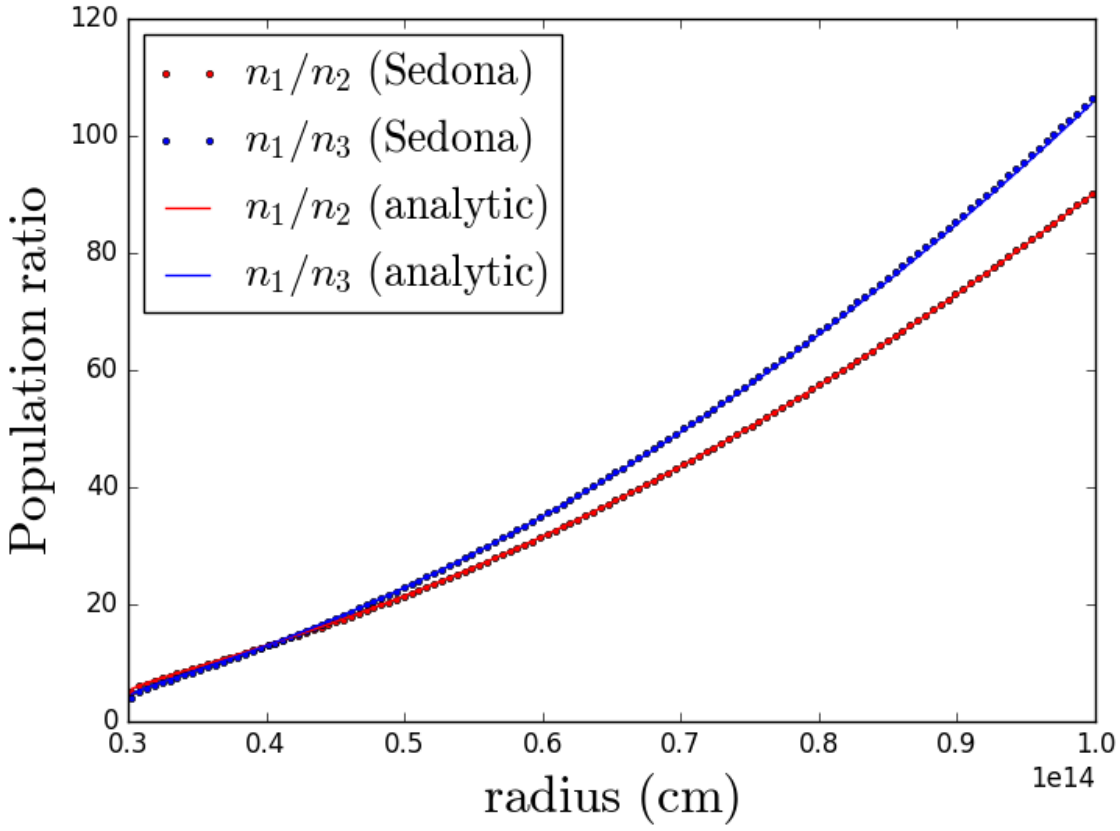

Figure 2.19: Level population ratios as a function of radius for the NLTE test problem

2.13 Acknowledgments

We thank Phil Colella for guidance while developing the Godunov solver. We thank Weiqun Zhang for providing the script to compute the semi-analytic radiating shock solutions, and we thank Ulrich Noebauer for helpful correspondence regarding the comparison to Zeus-MP2.

Throughout the work, Nathaniel Roth was supported by the Department of Energy Office of Science Graduate Fellowship Program (DOE SCGF), made possible in part by the American Recovery and Reinvestment Act of 2009, administered by ORISE-ORAU under contract no. DE-AC05- 06OR23100. Daniel Kasen was supported by a Department of Energy Office of Nuclear Physics Early Career Award (DE-SC0008067). This research used resources of the National Energy Research Scientific Computing Center, which is supported by the Office of Science of the U.S. Department of Energy under Contract No. DE-AC02-05CH11231. This research used resources of the Oak Ridge Leadership Computing Facility at the Oak Ridge National Laboratory, which is supported by the Office of Science of the U.S. Department of Energy under Contract No. DE-AC05-00OR22725.

Chapter 3

AGN Radiation Pressure Feedback on Dusty Gas and the Launching of Massive Molecular Outflows

The content of this chapter is drawn from Roth et al. (2012), with permission from the AAS and the co-authors.

Observational and theoretical arguments suggest that the momentum carried in mass outflows from AGN can reach several times L/c, corresponding to outflow rates of hundreds of solar masses per year. Radiation pressure on lines alone may not be sufficient to provide this momentum deposition, and the transfer of reprocessed IR radiation in dusty nuclear gas has been postulated to provide the extra enhancement. The efficacy of this mechanism, however, will be sensitive to multi-dimensional effects such as the tendency for the reprocessed radiation to preferentially escape along sightlines of lower column density. We use Monte Carlo radiative transfer calculations to determine the radiation force on dusty gas residing within approximately 10 parsecs from an accreting super-massive black hole. We calculate the net rate of momentum deposition in the surrounding gas and estimate the mass-loss rate in the resulting outflow as a function of solid angle for different black hole luminosities, sightline-averaged column densities, clumping parameters, and opening angles of the dusty gas. We find that these dust-driven winds carry momentum fluxes of 1-5 times L/c and correspond to mass-loss rates of 10-100 $M_\odot$ per year for a 10^8 $M_\odot$ black hole radiating at or near its Eddington limit. These results help to explain the origin of high velocity molecular and atomic outflows in local ULIRGs, and can inform numerical simulations of galaxy evolution including AGN feedback.

3.1 Introduction

3.1.1 Motivations from observations and theory

The nature of the interaction between an accreting super-massive black hole (SMBH) and its host galaxy remains a challenging problem in the study of galaxy evolution. Numerical simulations reveal that gas can be drawn inward toward the nucleus by gravitational torques arising from a series of gravitational instabilities (Hopkins & Quataert 2010). This gas typically forms a dusty structure at small radii with a characteristic length scale of ∼1-10 parsecs which in some cases has been imaged directly (Jaffe et al. 2004; Raban et al. 2009). Phenomenologically, this structure can be modelled as a torus (Lawrence 1991; Antonucci 1993), but it remains an outstanding theoretical challenge to provide a convincing explanation of its configuration and what supports it. If a sufficiently strong poloidal magnetic field is present at the parsec scale, one possible explanation is that the dusty gas is launched as a hydromagnetic wind (Konigl & Kartje 1994; Keating et al. 2012). Heating of the ISM from stellar feedback might support the dusty gas in a puffy disk (Hopkins & Quataert 2011a). The disk might be simultaneously supported by infrared radiation pressure (Pier & Krolik 1992; Krolik 2007), or the infrared radiation pressure may generate a failed wind (Dorodnitsyn et al. 2011; Dorodnitsyn & Kallman 2012).

Regardless of what supports the torus, gas continues to be drawn in to the black hole accretion disk at small radii ($< 10^{17}$ cm), where it powers an active galactic nucleus (AGN). The radiation emitted from SMBH accretion disks influences the dynamics of the torus itself, along with the dynamics of the host galaxy. This feedback may act through a number of channels that include radiative heating (e.g. Di Matteo et al. 2005), jets (Silk 2005; Croton et al. 2006; McNamara & Nulsen 2007), and winds driven by radiation pressure on lines (Murray et al. 1995; Proga et al. 2000) and dust (Konigl & Kartje 1994; Murray et al. 2005; Keating et al. 2012). Our challenge is to understand the combined effect of all these modes of interaction. Improving our understanding of this connection will be crucial for answering questions about the growth of SMBHs, observations of AGN, and the star formation histories in galaxies.

Recent observations have begun to reveal the violent impact that AGN may have on their host galaxies. Observations of obscured quasars such as SDSS J1356+1026 have revealed outflows extending out to tens of kiloparsecs from the galactic nucleus (Greene et al. 2012). The estimated mechanical luminosity of these outflows (10^{44-45} ergs s^{-1}) is too large to be explained by the inferred star formation activity. Other obscured quasars possess more massive outflows, with mass-loss rates of hundreds of solar masses per year (Moe et al. 2009; Dunn et al. 2010). Meanwhile, observations of local ultra-luminous infrared galaxies (ULIRGs) have led to the discovery of outflows with velocities that are correlated with the AGN bolometric luminosity (Sturm et al. 2011). These outflows also have mass-loss rates equal to several times the star formation rate and in some cases exceeding 1000 solar masses per year, depleting the gas on timescales as short as 10^6 years. Adding to our picture are studies of post-starburst galaxies, exhibiting outflows with median velocity of approximately

1000 km s^{-1}, suggesting that past AGN activity played a role in launching the gas (Tremonti et al. 2007).

These observations are complemented by numerical simulations of AGN feedback (Ciotti et al. 2010; DeBuhr et al. 2011; Debuhr et al. 2011) that account for deposition of both energy and momentum from the accretion radiation, including a combination of heating by X-rays and photoionizations, radiation pressure at the kiloparsec scale, and winds driven from within a radius of less than 100 parsecs. Taken together, these effects can help to explain both the $M_{\rm BH}$ - σ relation (Ferrarese & Merritt 2000) and the existence of galactic outflows observed at speeds of thousands of km s^{-1}. The results, particularly those of Debuhr et al. (2011), also suggest that line-driven winds may be insufficient to drive observed outflows, and that a large amount of momentum ($\gtrsim 3\,L/c$) may need to be deposited via absorption by dust grains during the period when the SMBH is optically thick to both ultraviolet and far-infrared radiation, the time when most black hole growth is believed to occur (Hopkins et al. 2005; Hopkins & Quataert 2011a).

A large uncertainty in the numerical calculations referenced above is the amount of radiative momentum deposited within the central unresolved radius. The velocity and mass-loss rate of the resulting wind depend sensitively on this coupling. Moreover, in those studies the momentum was deposited in a spherically symmetric manner. In reality, multidimensional effects, such as the tendency for radiation to escape out the rarefied, polar regions of the gas distribution, will be crucial. A multidimensional study that linked the parsec and kiloparsec radial scales was undertaken by Novak et al. (2011), and a treatment of the radiative transfer through dusty gas as a boundary value problem was performed in Novak et al. (2012). Our study extends this work by performing three dimensional Monte Carlo radiative transfer calculations for dusty gas that is optically thick to the infrared.

The momentum flux in radiation from a SMBH accretion disk with luminosity L is L/c. Generally L will not exceed $L_{\rm Edd}$, the Eddington luminosity set by the electron scattering (Thomson) opacity. Dust will contribute to the opacity seen by the radiation at large radii, but only at distances greater than the radius $r_{\rm sub}$ at which its temperature drops below the sublimation temperature $T_{\rm sub} \approx 1400$ K. Although the sublimation temperature varies for each grain depending on its composition and its size, we choose to adopt the simplification of assigning a uniform sublimation temperature to all the dust in our calculations. The sublimation radius may be estimated as

$$r_{\rm sub} \approx \sqrt{\frac{L}{4\pi\sigma_{\rm SB}T_{\rm sub}^4}} = 0.62\ {\rm pc}\left(\frac{L}{10^{46}\ {\rm ergs}^{-1}}\right)^{1/2}\left(\frac{T_{\rm sub}}{1400\ {\rm K}}\right)^{-2}. \quad (3.1)$$

When the gas distribution surrounding the SMBH is not isotropic, $r_{\rm sub}$ may vary with angle. Within this radius, electron scattering dominates the opacity, and the usual Eddington limit applies.

Once the intrinsic photons from the accretion disk encounter dust in the surrounding gas,

they are absorbed and the energy is re-emitted at infrared wavelengths. If the gas is also optically thick to the infrared, then the re-emitted radiation will continue to be absorbed and re-emitted in a random-walk pattern until it exits the optically thick region. Along the way, momentum will be imparted by the photons to the gas multiple times. In this scenario it is possible for the radiation to transfer momentum to the gas at a rate that exceeds $L_{\rm Edd}/c$. For a spherically symmetric problem, this "boost" factor to the infrared radiation force is exactly the infrared optical depth of the gas, which can be shown as follows: In steady-state, when radiative equilibrium holds and the luminosity as a function of radius is constant, we may compute the radiation force per volume $f_{\rm rad}$ as

$$f_{\rm rad} = \frac{L}{4\pi\, r^2\, c}\, \rho(r)\, \kappa(r)\ . \tag{3.2}$$

The total outward force exerted by the radiation is

$$\int_V f_{\rm rad}\, dV = 4\pi \left(\frac{L}{4\pi\, c}\right) \int_0^\infty \rho(r)\, \kappa(r)\, dr = \tau \frac{L}{c}\ , \tag{3.3}$$

where τ is the radial optical depth for the infrared photons.

In a gas rich galactic nucleus with a column density of 10^{25} cm^{-2}, a mean mass per particle of 1.5 times the proton mass, and an infrared dust opacity of 10 cm^2 per gram of gas, an initial guess for the optical depth would be approximately 250. There are two primary effects that will reduce the actual radiation force from such a high value. The first is the lack of spherical symmetry: a torus obscures only a fraction of the solid angle surrounding the accretion disk, and the presence of clumps and voids in the torus can increase the photon mean free path for certain sightlines. The second effect is dust sublimation: dust will be absent from the innermost regions of the nucleus that contribute a substantial fraction to the gas column density, and the force integral can be well-approximated by setting its lower limit to $r_{\rm sub}$.

To get a sense of the sort of momentum deposition rates that have been observed, consider the case of Mrk 231. This system features an outflow of neutral gas with velocities in the range 360-900 km s^{-1} and a mass-loss rate estimated at 420 solar masses per year (Rupke & Veilleux 2011). The momentum flux in the outflow, estimated by multiplying the mass loss rate by the velocity, and find that it is likely between 2.6 to 6.5 times L/c where L is measured to be 1.1×10^{46} ergs s^{-1}. The kinetic luminosity of the outflow, on the other hand, is estimated at 7.3×10^{43} ergs s^{-1}, less than 1% of the bolometric AGN luminosity.

Modeling the force from radiation pressure and predicting by what factor it exceeds L/c, becomes a difficult problem to tackle analytically in the absence of spherical symmetry, the presence of clumps, and with an accounting for dust sublimation. For these reasons, we turn here to three-dimensional radiative transfer calculations using the wavelength-dependent Monte Carlo radiative transfer code SEDONA (Kasen et al. 2006). Given that the radiative diffusion time in these systems is shorter than the dynamical times, we restrict ourselves to steady-state configurations that do not include an explicit coupling to hydrodynamics.

In section 3.2, we describe how we parametrize the gas configurations surrounding the black hole and how we treat the key physical processes in the radiative transfer. In section 3.3, we present our results for a series of calculations in which we vary the opening angle of the torus, the amount of gas present, the radial variation in the gas density, and the accretion disk luminosity. We also examine how our dynamical conclusions are affected by accounting for a clumpy rather than smooth distribution of dust and gas. Finally, in section 3.4 we present our conclusions.

3.2 Methodology

3.2.1 Initial gas configuration - parameterized, smooth model

Although the specific region we are studying is difficult to observe directly, gravito-hydrodynamic simulations (Hopkins & Quataert 2011a) provide information about its configuration before the effects of radiative feedback are felt. The gas and stars form a thick disk roughly in vertical hydrostatic equilibrium (our usage of the word "disk" throughout the remainder of this study refers to what is usually labelled as the torus and should not be confused with a reference to the black hole accretion disk, which is unresolved at our scales of interest). The puffiness of the disk in the Hopkins & Quataert (2011a) simulations is to some extent determined by the sub-grid turbulent velocity dispersion when strong stellar feedback in the ISM is included, but also by bending modes (firehose instabilities) driven by resolved velocities when less stellar feedback is included. While further accretion of the gas at this scale will rely on non-axisymmetric torques, we first adopt a simple axisymmetric, hydrostatic disk model analogous to one used in Hopkins & Quataert (2011a). This parametrization captures the key features of the gas configuration seen in the hydrodynamics simulations, but allows us greater control over free parameters and removes unnecessary complications in our attempt to isolate the effects of the radiation. Such a parametrization also allows us to systematically introduce clumpiness into the gas for certain calculations (which, among other effects, breaks axisymmetry), as will be described in section 3.2.2

The vertical structure of the smooth disk model may be calculated by solving the equation of hydrostatic equilibrium in the normal (z) direction, assuming an isothermal equation of state with effective sound speed c_s set by both the resolved and sub-grid velocity dispersion, along with any contribution from the thermal pressure of the gas,

$$\frac{{c_s}^2}{\rho}\frac{d\rho}{dz} = -\frac{d\Phi}{dz}\ , \tag{3.4}$$

with solution

$$\rho(R,z) = \rho(R,0)\exp\left\{c_s^{-2}\Big[\Phi(R,0) - \Phi(R,z)\Big]\right\}\ . \tag{3.5}$$

Here Φ denotes the gravitational potential, ρ denotes the density of the gas, and R is the cylindrical radius. If we assume that the gravitational potential is dominated by the mass

of the central black hole $M_{\rm BH}$ at these scales, then the density distribution is

$$\rho(R,z) = \rho(R,0)\exp\left\{\frac{GM_{\rm BH}}{R\,c_s^2}\left[\frac{1}{\sqrt{1+z^2/R^2}} - 1\right]\right\} \tag{3.6}$$

In the limit of small z/R, this yields a Gaussian vertical structure. In this limit, the ratio of the squared sound speed to the squared Keplerian velocity V_c functions as the ratio of the disk scale height to the cylindrical radius, and for convenience we choose to define a parameter that makes this identification universal:

$$\frac{h_s}{R} \equiv \frac{c_s}{V_c} = c_s\left(\frac{G\,M_{\rm BH}}{R}\right)^{-1/2} . \tag{3.7}$$

Typical values of h_s/R found in Hopkins & Quataert (2011a) range from 0.1 to 0.5. Moderately large values of $h/R \gtrsim 0.2-0.3$ are suggested by the fraction of obscured versus unobscured quasars, although generally this fraction correlates strongly with luminosity (Maiolino et al. 2007).

From the simulations in Hopkins & Quataert (2011a), we note that the mid-plane density may be well-fit with a power-law $R^{-\gamma}$ where γ falls between 1.5 and 2.0. This is also in agreement with the arguments for a column density distribution $\Sigma \propto R^{-\eta}$ with η falling between 0.5 and 1, as argued for in Hopkins & Quataert (2011b). We fix γ to 1.5 for the numerical calculations in this study. The total mass in the disk will not converge for this value of γ, and in reality the power law cuts off on a scale of roughly 1 kpc. Additionally, observations indicate that γ may vary with the accretion luminosity (Kishimoto et al. 2011). Indeed, such a relationship might arise self-consistently in a coupled radiation hydrodynamic simulation.

Converting to spherical polar coordinates r and θ, where θ is taken to be zero along the z-axis, we obtain

$$\rho(r,\theta) = \rho_0\left(\frac{r\sin\theta}{r_0}\right)^{-\gamma}\exp\left[(h_s/R)^{-2}(\sin\theta - 1)\right] . \tag{3.8}$$

Here r_0 represents some inner cut-off radius where the density is ρ_0, and to prevent the radial column density from diverging we take $\rho(r < r_0) = \rho_0$.

One undesirable aspect of this model is that it leads to an accumulation of mass in the polar region of the disk, where $\sin\theta$ is small. To correct for this, we allow the density profile to drop as a power law in the spherical radius r rather than in the cylindrical radius R. This amounts to dropping the factor of $(\sin\theta)^{-\gamma}$, which is only significant far from the disk mid-plane. This leaves

$$\rho(r,\theta) = \rho_0\left(\frac{r}{r_0}\right)^{-\gamma}\exp\left[(h_s/R)^{-2}(\sin\theta - 1)\right] . \tag{3.9}$$

The results from Hopkins & Quataert (2011a) indicate that h_s/R does not change by more than a factor of order unity for all R. For simplicity, we take h_s/R to be a constant for all R

Table 3.1: Fiducial parameters for the calculation of massive molecular outflows launched by AGN radiation pressure.

h_s/R	$\overline{N}_{\rm H}$ (cm^{-2})	radial density power-law γ	$L/L_{\rm Edd}$	$M_{\rm BH}$ ($M_\odot$)
0.3	3.4×10^{24}	1.5	1	10^8

Note. — The first three parameters set the gas density distribution, while the last two set the relative strengths of the radiation pressure and gravity. The mean mass per particle is always set to 1.5 times the proton mass. Note that the column density presented in this table corresponds to integrating the gas density from large radii to a distance of 0.1 pc from the BH. The column density computed by integrating to the edge of the dust sublimation radius is 9.5×10^{23} cm^{-2} if the other fiducial parameters are fixed.

and allow it to vary as a free parameter for different disk models. For all calculations in this study we assume a black hole mass $M_{\rm BH}$ of 10^8 $M_\odot$, and we parametrize the luminosity as a fraction of the electron-scattering Eddington luminosity for that mass. Another free parameter is ρ_0, which sets the sightline-averaged column density $\overline{N}_{\rm H}$. Unless stated otherwise, $\overline{N}_{\rm H}$ corresponds to the column density integrated to a distance of 0.1 parsecs from the central black hole. Also, unless $\overline{N}_{\rm H}$ is being varied explicitly, ρ_0 is set so that the sightline-averaged column density is 3.4×10^{24} cm^{-2}, with a mid-plane column density of 1.0×10^{24} cm^{-2}. These values are consistent with the calculations from Hopkins & Quataert (2010) of surface densities of 10^{11} – 10^{12} $M_\odot$ kpc^{-2} for the central 10 parsecs surrounding the black hole. The fiducial parameters are summarized in Table 3.1.

For this smooth density model we use a two-dimensional grid with spherical polar (r, θ) coordinates, with logarithmic spacing in the radial coordinate and linear spacing in the angular coordinate. Our resolution is 192 radial zones and 64 θ zones for θ ranging from 0 to $\pi/2$, with an assumed symmetry for $\theta \rightarrow \pi - \theta$. Slices of the gas density for the model developed in this section, along with a simulation from Hopkins & Quataert (2011a), are shown in Figure 3.1.

3.2.2 Initial gas configuration - clumpy models

It has long been predicted on theoretical grounds that the dusty gas surrounding an accreting SMBH will not be smoothly distributed, but will instead form clumps (Krolik & Begelman 1988). This prediction has been supported by observations such as the variability of x-ray absorbing column densities in type 2 Seyferts (Risaliti et al. 2002) as well as IR spectroscopy (Mason et al. 2006; Hönig et al. 2010; Deo et al. 2011). A vast literature exists concerning radiative transfer through clumpy torus models, with many prescriptions for generating clumpy density distributions from an underlying smooth density model (Nenkova

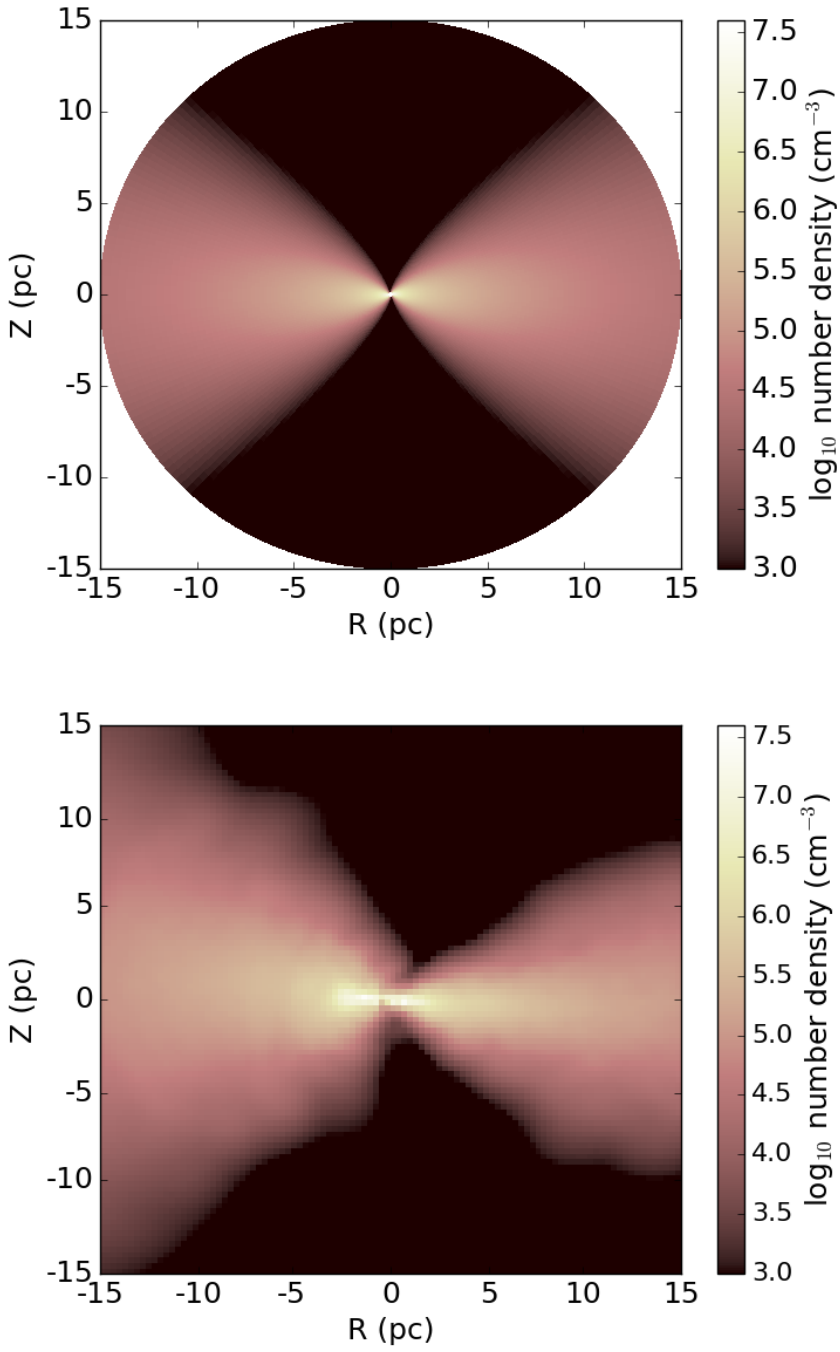

Figure 3.1: Top: An example of a slice through the smooth model density distribution with the fiducial parameters listed in Table 3.1, except $\overline{N}_{\rm H} = 1.0 \times 10^{25}$ cm^{-2}. Bottom: A density slice taken from a hydrodynamical simulation of gas accretion onto a central black hole (see Hopkins & Quataert (2011a)).

et al. 2002; Hönig et al. 2006; Schartmann et al. 2008; Stalevski et al. 2012; Siebenmorgen & Heymann 2012).

Our method for generating the clumpy gas distribution most closely resembles those of Hönig et al. (2006) and Schartmann et al. (2008). We use a three dimensional grid and spherical-polar (r, θ, ϕ) coordinates, with logarithmic spacing in the radial coordinate and linear spacing in the angular coordinates. Our resolution is 128 radial zones, 96 θ zones for all θ ranging between 0 and π, and 192 ϕ zones for all ϕ ranging from 0 to 2π. The density of each clump in a given simulation is the same, and a preset number of clumps are placed on the grid. The clump positions are sampled from a probability distribution derived from a smooth density distribution as described in section 3.2.1. If two clumps overlap in position, their densities are added. Each clump's radius is set to a fixed number of grid zones in a given simulation, and the logarithmic radial spacing of the grid causes the size of the clumps to grown with increasing distance from the SMBH. Overlaid on the clumps is a diffuse, smooth background gas distribution that is generated by multiplying the density distribution from section 3.2.1 by 10^{-2}. An example is pictured in Figure 3.2.

Making the gas clumpy tends to make the column density distribution bimodal, as a significant number of sightlines intersect no clumps at all, forming the lower peak of the distribution. This bi-modality persists for all clumping parameters considered in this study, although it can be avoided if a larger fraction of the mass is allocated to the diffuse phase. Such bi-modality is not seen in observations (Risaliti et al. 1999; Malizia et al. 2009; Treister et al. 2009), but the addition of clumping to our models does improve the match to observations by creating a larger number of sightlines with column densities below 10^{21} cm^{-2}.

3.2.3 Monte Carlo Radiative Transfer

The Monte Carlo technique partitions the luminosity of the accreting black hole into equal-energy photon packets that probabilistically interact with the surrounding gas. The packets were transported in three dimensions for all calculations in this study. We improve our statistics by mapping the energy and momentum deposited by the packets into a two-dimensional array of zones – a photon that scatters at spherical coordinates (r,ϕ,θ) is mapped to position (r,θ') where $\theta' = \theta$ if $0 \leq \theta \leq \pi/2$ and $\theta' = \pi - \theta$ if $\pi/2 < \theta \leq \pi$.

The radial zones span radii ranging from $r_0 = 0.1$ pc to an outer radius $r_{\rm out} = 10^{20}$ cm (≈ 32.4 pc). The 0.1 pc scale was chosen because it is a larger scale than the typical black hole accretion disk, but also small compared to the typical dust sublimation radius. We ignore all momentum deposition inside the 0.1 pc radius, and since nearly all the momentum deposition occurs at and beyond the sublimation radius, the exact choice of innermost radius has little effect on our results. We employ 64 equal spacings in the polar angle θ ranging from 0 along the z-axis to $\pi/2$ at the mid-plane. For most calculations, the photons are emitted isotropically at the edge of the 0.1 pc sphere surrounding the origin. The effect of anisotropic emission is treated in section 3.3.4.

In Monte Carlo radiative transfer, the specific intensity of the radiation $I(\boldsymbol{r}, \boldsymbol{n}, \lambda)$ is constructed by counting the number of photon packets with wavelength λ that enter into each

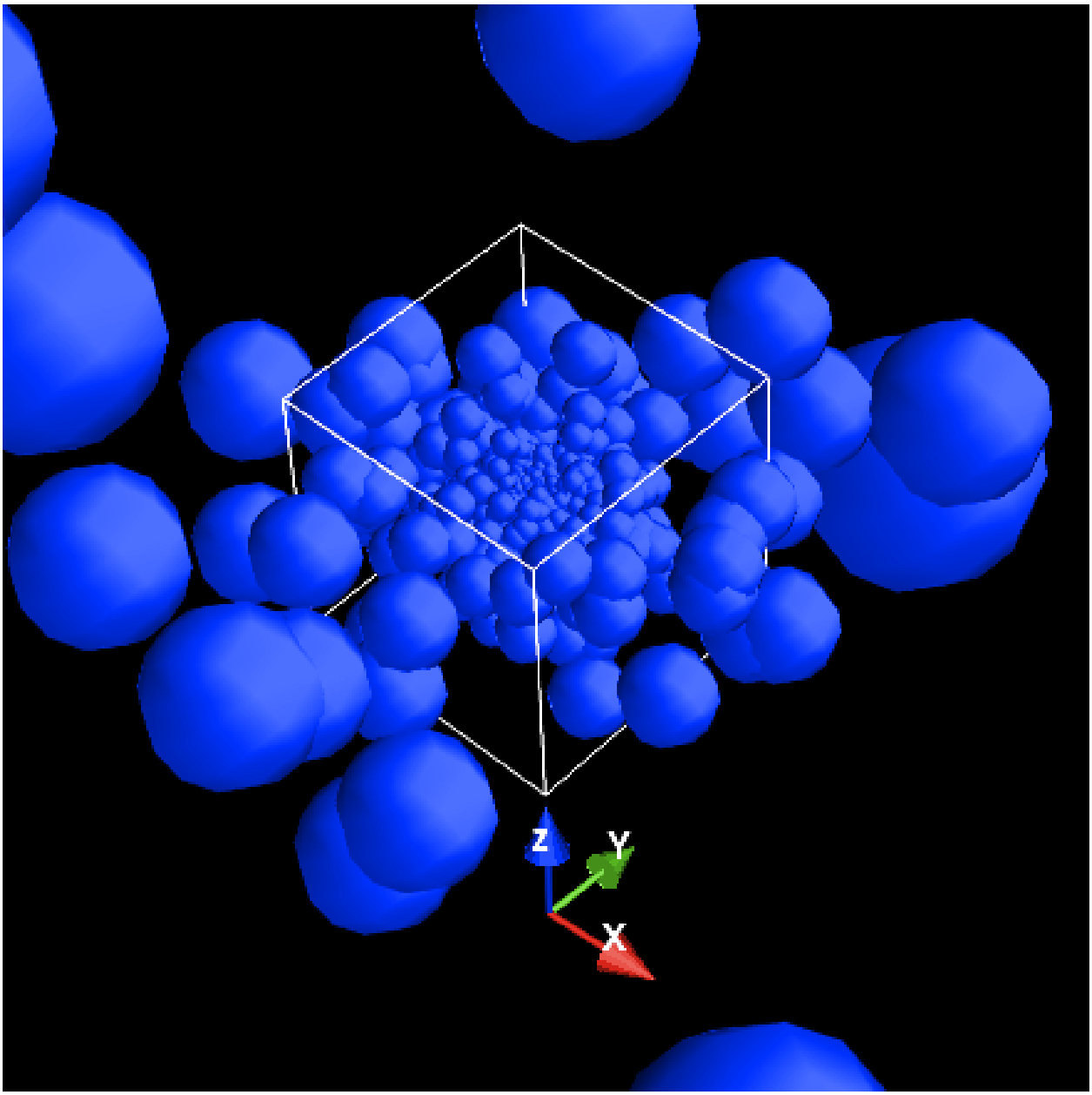

Figure 3.2: A clumpy gas distribution corresponding to the fiducial parameters in Table 3.1. The gas density in clumps of 7.8×10^8 cm^{-3} and the average clump diameter is 0.043 pc . Not pictured is the diffuse background gas. The "frame width" corresponds to the width of the white cube drawn at the center.

grid zone at position $\boldsymbol{r}$ and with direction vector $\boldsymbol{n}$ in a given interval of time. Specifically, the radiation force per volume $f_{\rm rad}$ is defined as

$$\boldsymbol{f}_{\rm rad} \equiv \frac{1}{c} \int_{\omega,\lambda} \rho\, \kappa_\lambda\, I\, \hat{n}\, d\omega\, d\lambda\ . \tag{3.10}$$

To compute $f_{\rm rad}$ in a given zone of our computational domain with volume ΔV over a time interval Δt, we perform a sum a sum over all photon packets entering the zone. Each photon packet carries with it an energy E_p, a direction of travel $\hat{n}_p$, and a wavelength λ_p. Associated with that wavelength is an opacity $\kappa(\lambda_p)$, measured per gram of gas, and which depends on whether dust is present at location $\boldsymbol{r}$. The packet traverses a path of length Δr within a zone at position $\boldsymbol{r}$. The force is then

$$\boldsymbol{f}_{\rm rad} = \left(\frac{1}{\Delta V \Delta t}\right)\, \rho(\boldsymbol{r})\, \sum_p \frac{E_p}{c}\, \kappa(\lambda_p, \boldsymbol{r})\, \Delta r\, \hat{n}_p\ . \tag{3.11}$$

The radiative acceleration $a_{\rm rad}$ is simply defined as $f_{\rm rad}/\rho$.

Our calculations apply the stationarity approximation, in which we solve the steady-state radiative transfer problem for a fixed gas density distribution. This approximation is justified if the radiative heating time scale and the radiative diffusion time scale are much shorter than the dynamical time scale.

For a sound speed of 200 km s^{-1} and a characteristic length scale of 10 pc, the dynamical time is approximately 10^{12} seconds. Meanwhile, the photon diffusion time through the disk never exceeds 10^{11} seconds, and for many disk parameters the diffusion time is substantially shorter than that. The radiative heating time, estimated by dividing the thermal energy of the gas by the rate of radiative energy deposition, is

$$\begin{aligned} t_{\rm heat} &\approx \left(\frac{\rho\, k_B\, T_{\rm gas}}{\mu m_p}\right) \left(\frac{1}{\rho\, \kappa\, c\, a\, T_{\rm rad}^4}\right) \\ &= 2.4 \times 10^5\ {\rm s} \left(\frac{T_{\rm gas}}{100\ {\rm K}}\right) \left(\frac{T_{\rm rad}}{100\ {\rm K}}\right)^{-4} \left(\frac{\kappa}{10\ {\rm cm}^2/{\rm g}}\right)^{-1}\ , \end{aligned} \tag{3.12}$$

which is also much shorter than the dynamical time.

In this case, the condition of radiative equilibrium allows us to compute the dust temperatures by balancing radiative heating and cooling,

$$\begin{aligned} &4\pi \textstyle\int_\lambda \rho\, \kappa_{\rm abs}(\lambda)\, B_\lambda(T_{\rm dust})\, d\lambda \\ &\quad = \textstyle\int_{\omega,\lambda} \rho\, \kappa_{\rm abs}(\lambda) I_\lambda\, d\omega\, d\lambda\ , \end{aligned} \tag{3.13}$$

We emit photons and follow their propagation for time intervals of 5×10^9 seconds, at which point we update the temperature of the dust in each grid zone. We treat dust as present everywhere where the dust temperature is below 1400 Kelvin. The dust temperatures are updated until convergence is obtained at the one percent level, which typically takes fewer than 40 iterations if the initial dust temperature is set to 100 Kelvin in every zone.

Finally, for estimating the dynamics of the gas based on the radiation pressure on the dust, we assume perfect hydrodynamical coupling between the dust and the gas, as justified in Murray et al. (2005).

3.2.4 Intrinsic AGN spectrum

We use the "intrinsic" (unreddened) AGN spectral energy distribution described in Marconi et al. (2004). The majority of the spectral energy is found in the optical and near-UV and originates from the accretion disk, which resembles a 10^5 Kelvin black body emitter. The spectrum also contains a sizable x-ray component. Intentionally absent from this spectrum is any infrared component, which we will calculate self-consistently based on the reprocessing of the radiation by dust.

3.2.5 Dust and electron interactions

We use tabulated dust opacities and albedos based on Draine (2003a) for wavelengths greater than 10 Angstroms, and Draine (2003b) for shorter wavelengths, all corresponding to visual extinction ratio $R_V = 3.1$ and assuming a fixed dust-to-gas mass ratio of 1/125. These values were interpolated between 48 reference wavelengths. In practice, the difference between scattering and absorption is that for an absorption interaction, the wavelength of the re-emitted photon packet will be sampled from a probability distribution that depends on the dust's temperature, whereas the wavelength will remain unchanged for a scattering interaction. For wavelengths less than 100 Angstroms, we ignore scattering by dust since it will be almost entirely in the forward direction and hence will not lead to a net transfer of momentum, although we still allow for absorption by dust.

Electron scattering is only relevant for photons with wavelengths less than ~ 10 Angstroms, when the dust absorption cross section drops below that of the Thompson cross section, and when the photons are energetic enough to scatter equally well off of both bound and free electrons. We account for anisotropic, inelastic electron scattering in accordance with the Klein-Nishina formula.

3.3 Results

3.3.1 Dust temperature and radiative acceleration dependence on smooth gas geometry

Figure 3.3 shows slices of the equilibrium dust temperature and the radiative acceleration vector field for disks of two opening angles and with a smooth gas distribution. The color scheme is set so that all temperatures above the dust sublimation temperature appear as solid gray. Arrows representing the acceleration are plotted in zones where the dust is not sublimated and where the gas density exceeds 10^{-21} g cm^{-3}.

We find that the dust sublimation region has an aspherical, hour-glass shape. Sublimation extends to larger radii in the polar regions where the dusty gas is optically thin in the infrared. There, dust emits at longer wavelengths than it absorbs, and so is forced to reach higher temperatures in order to maintain radiative equilibrium.

Interestingly, nearly all the angular redistribution of the radiation occurs near the surface of the dust sublimation region. Light from the central source initially travels isotropically to the inner edge of the dusty gas, and a large fraction of the photons are absorbed at the dust interface. When photons are re-emitted in the infrared, many are sent back into the sublimation region. It is through this re-emission that the net flux becomes anisotropic at small radii. When infrared photons succeed in penetrating deep into the dusty gas, they generate a nearly radial radiative flux, as they would in a spherically symmetric problem (see Figure 3.4).

Figure 3.5 displays how the radiative acceleration varies with radius and polar angle for the fiducial simulation. The behavior of the acceleration is quite different inside and outside the dust sublimation region – the presence of dust raises the opacity of the gas and therefore raises the radiative acceleration (as in equation 3.10). In a given solid angle the acceleration is highest just beyond the edge of the dust sublimation region, where ultraviolet and optical photons can push on optically thick, dusty gas. The acceleration rapidly drops as the radiation penetrates farther into the dusty gas and ultraviolet/optical light is converted into infrared, to which the dust is less opaque. For all solid angles, the acceleration settles to a constant ratio above gravity at sufficiently large radius, indicating that the acceleration eventually becomes proportional to $1/r^2$, further evidence that the infrared radiation diffuses primarily in the radial direction. In addition to the radial dependence of the acceleration, there is an angular dependence that arises from the diversion of flux from the mid-plane to the polar regions of the disk at the surface of the sublimation region.

Slices of the net acceleration with gravitational acceleration included are shown in Figure 3.6. In all cases the acceleration is primarily radial in direction, either outward or inward. Note that for opening angles $h_s/R < 0.3$ there is a critical polar angle below which radiation dominates over gravity and above which gravity dominates. In these cases inflow may persist in the equatorial region while gas is blown out at angles directed farther away from the mid-plane, potentially leading to a steady state outflow. However, the radiative acceleration dominates over gravity everywhere when $h_s/R \geq 0.3$ for this AGN luminosity and column density.

For another perspective, in Figure 3.7 we plot the integrated radiative acceleration for columns of gas as a function of polar angle (without gravitational acceleration included). We assume there are no forces in the tangential directions (i.e., each column is accelerated independently), and that the radiation force is shared along the whole column as the inner gas pushes on outer gas. To compute this net acceleration, we first compute the integrated net force in each solid angle (including the effects of both gravity and radiation),

$$\frac{dF_{\rm net}}{d\omega}(\theta) \equiv \int_{r_{\rm sub}}^{r_{\rm out}} \left(f_{\rm rad} - \frac{G\,M_{\rm BH}\,\rho}{r^2} \right) r^2\,dr\ , \tag{3.14}$$

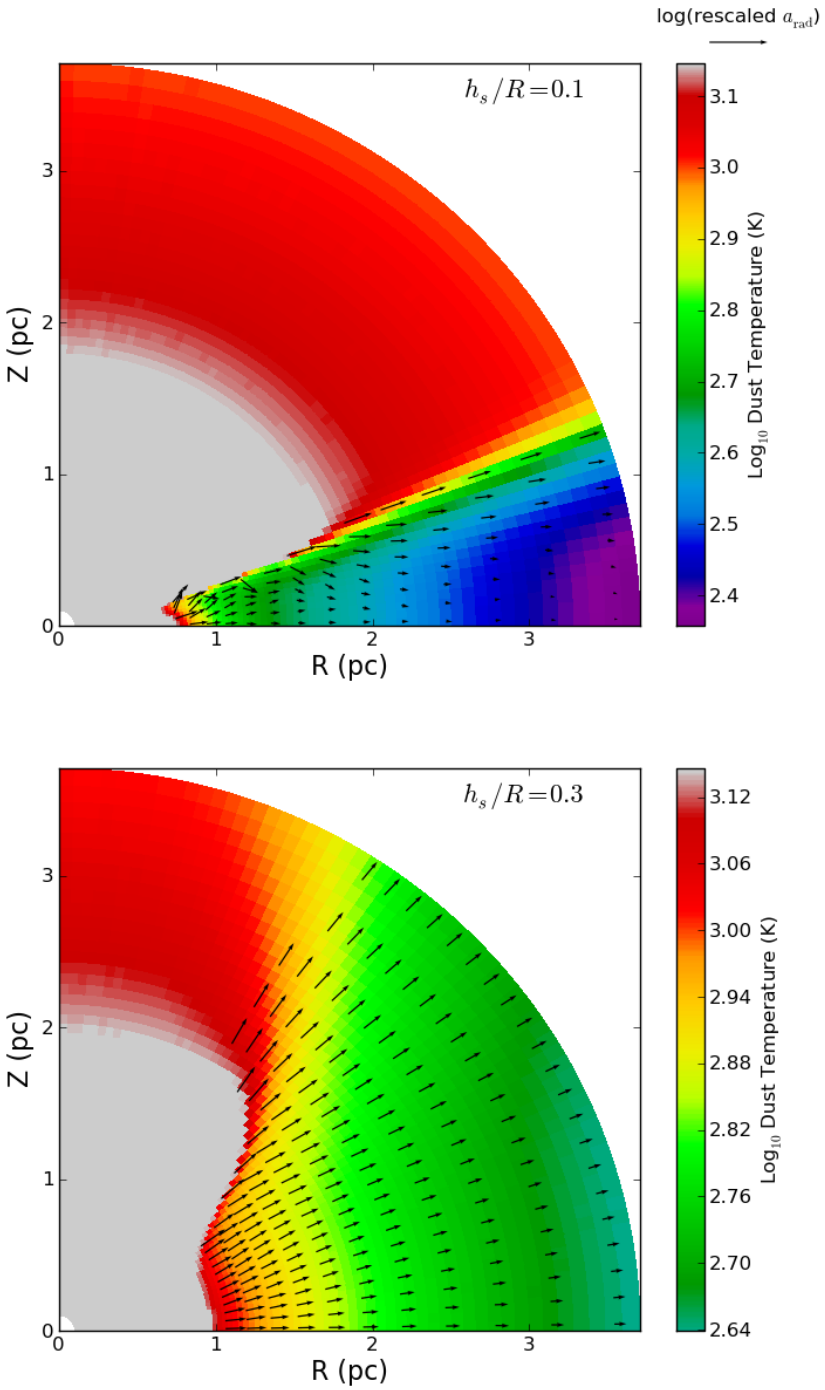

Figure 3.3: Arrows indicating the direction and strength of the radiative acceleration are plotted over slices of dust temperature. All parameters correspond to the fiducial values in Table 3.1, except for opening angles which vary as indicated (while conserving mass in the calculation domain).

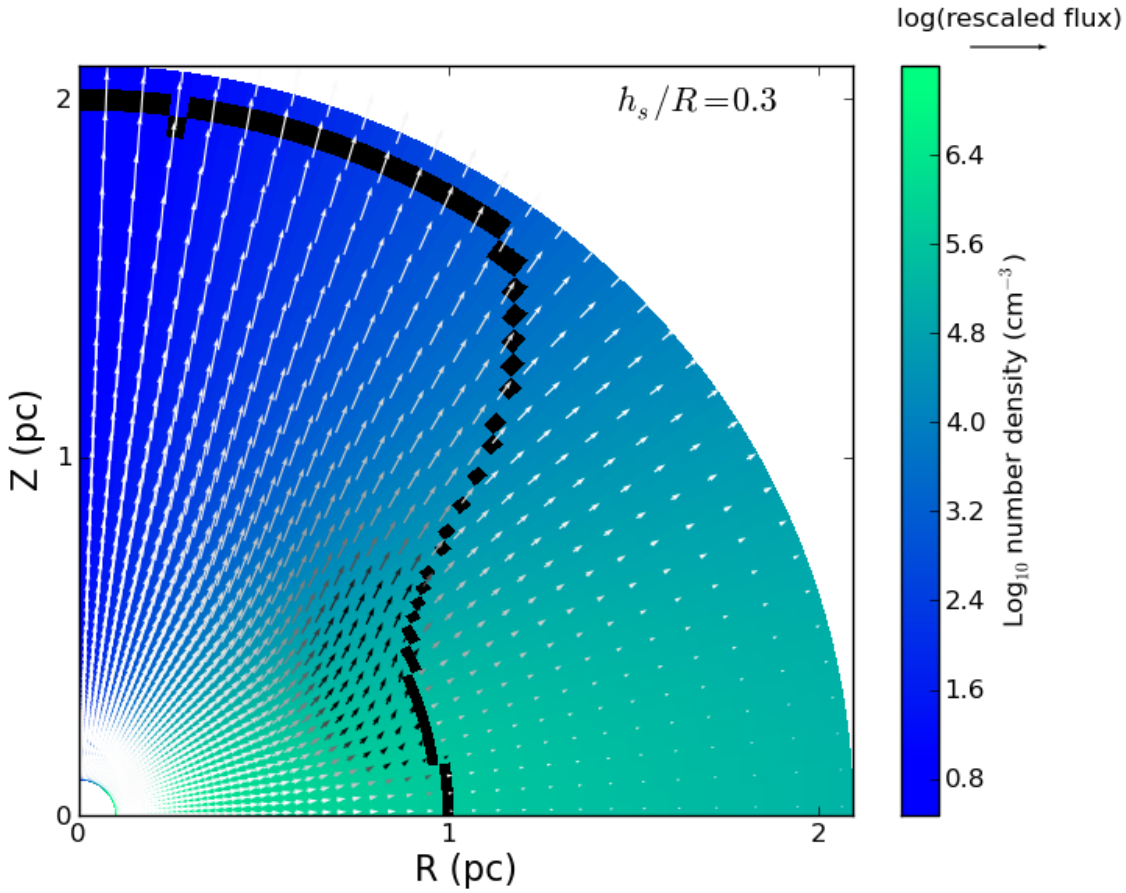

Figure 3.4: Arrows representing the net radiation flux are plotted over gas density. All parameters in this calculation correspond to the fiducial values listed in Table 3.1. Arrows with significant deviation from the radial direction are colored black, while the boundary of the dust sublimation region is marked with black cells. Arrow lengths are proportional to $\log_{10}(10^{-14}\times$ net flux (cgs)). Through a process of absorption of UV light and re-emission in the IR at the inner wall of the dusty gas, flux is channeled toward the poles in the outermost part of the dust sublimation region. The radiation travels radially in the dusty portion of the gas.

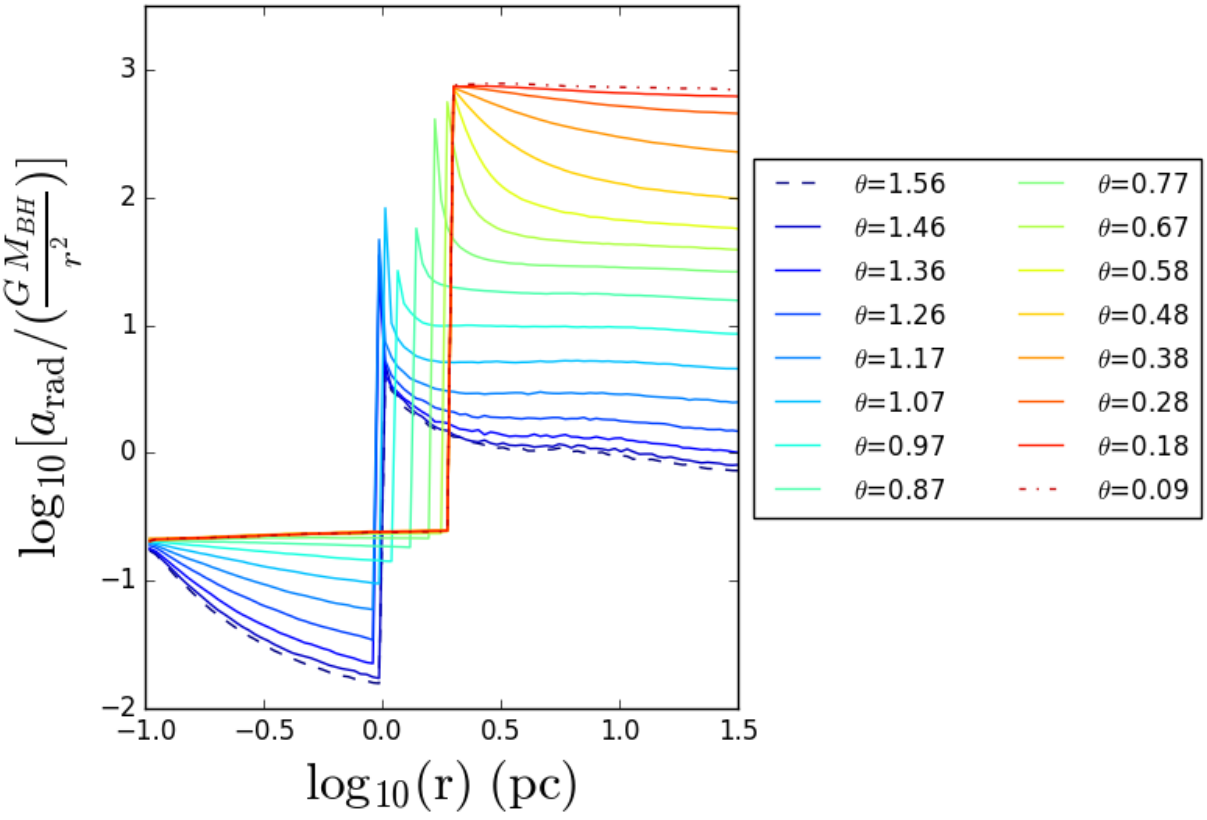

Figure 3.5: Radiative acceleration in radius and solid angle. All parameters in this calculation correspond to the fiducial values listed in Table 3.1. The acceleration is normalized at each radius by the gravitational acceleration $GM_{\rm BH}/r^2$, and the logarithm of that ratio is plotted. Thus, points with y-values above zero correspond to locations where the radiative acceleration exceeds gravity. The abrupt jump in acceleration occurs at the boundary of the dust sublimation region, where dust begins to contribute to the radiative opacity. As the radius increases beyond this boundary, the mean wavelength of the radiation transitions from the UV to the IR, rapidly lowering the radiative opacity in the process and reducing the radiative acceleration until eventually obeying an inverse square law dependence on radius.

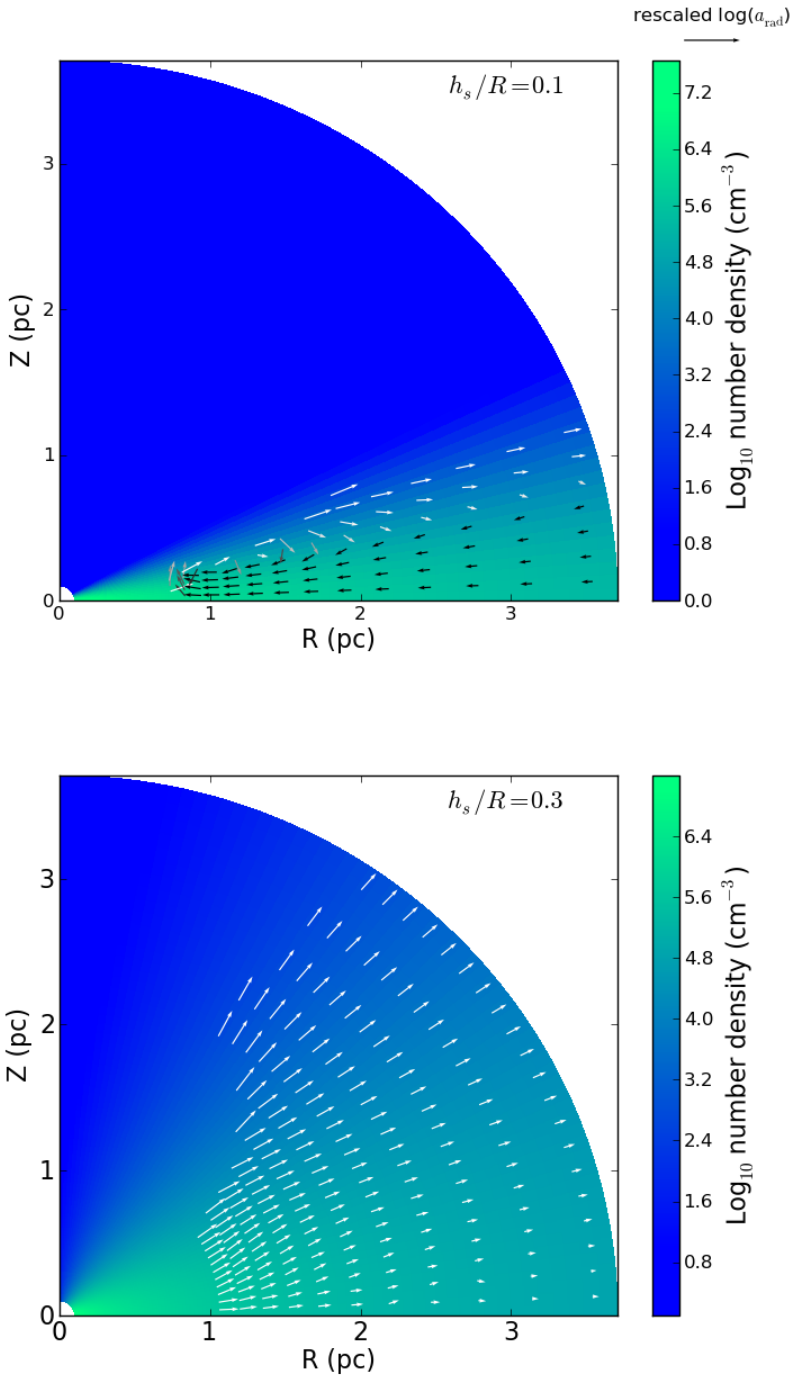

Figure 3.6: Arrows representing net acceleration (radiation + gravity) as a function of position. All parameters for this calculation correspond to the fiducial values listed in Table 3.1, except for opening angles which vary as indicated. Inward-directed arrows are colored black.

along with the mass in that solid angle,

$$\frac{dM_{\rm gas}}{d\omega}(\theta) \equiv \int_{r_{\rm sub}}^{r_{\rm out}} \rho\, r^2\, dr\ , \tag{3.15}$$

where $r_{\rm sub}$ denotes the edge of the dust sublimation region for each value of θ. Then, the net integrated acceleration is simply

$$a_{\rm net}(\theta) \equiv \left[\frac{dF_{\rm net}}{d\omega}\right] \Big/ \left[\frac{dM_{\rm gas}}{d\omega}\right]\ . \tag{3.16}$$

The value of $a_{\rm net}$ depends on the choice of $r_{\rm out}$. However, we will show in section 3.3.5 that the dependence of the rate of mass outflow on $r_{\rm out}$ is very small.

From Figure 3.7 we see that as the opening angle of the parsec-scale disk becomes smaller, the radiative acceleration becomes more sharply divided between the optically thin and optically thick portions of the disk. This primarily reflects the sharper density gradients present for smaller opening angles. As we will show in section 3.3.2, even though the radiative force is greater in the optically thick portion of the disk, the force does not rise as quickly as the mass. This causes the acceleration to decrease toward the mid-plane, even though the radiation force is stronger in the direction of the mid-plane.

3.3.2 Enhancement of radiation force above L/c and the dependence on smooth gas geometry

The ability of radiation to clear away ambient gas is enhanced by the fact that diffusing photons deposit their momentum multiple times as they random walk outwards. We can quantify this effect in each solid angle by dividing the integrated force on the gas column in that solid angle by the radiative momentum per time per solid angle leaving the black hole. We call the resulting quantity $\tau_{\rm eff}(\theta)$, which is computed as

$$\tau_{\rm eff}(\theta) = \frac{\left(\frac{dF_{\rm rad}}{d\omega}\right)}{\left(\frac{1}{4\pi}\right)\frac{L_{\rm BH}}{c}}\ , \tag{3.17}$$

and we extend the lower limit of the integral defining $dF_{\rm rad}/d\omega$ from $r_{\rm sub}$ to 0 when computing this quantity. We may also compute an average value of this quantity averaged over all lines of sight,

$$\overline{\tau}_{\rm eff} \equiv \frac{1}{4\pi}\int_{\omega} \tau_{\rm eff}\, d\omega = \int_0^{\pi/2} \tau_{\rm eff}\, \sin\theta\, d\theta\ . \tag{3.18}$$

Figure 3.8 summarizes our results for $\tau_{\rm eff}$ for various disk opening angles while holding the other parameters at their fiducial values as listed in Table 3.1. Increasing the opening angle boosts $\tau_{\rm eff}(\theta)$ for all θ, up to a maximum value of approximately 5-6 for these parameters. In the polar region, this effect can be understood simply in terms of the presence of more mass in that region when the opening angle is larger. Meanwhile, even though there is less

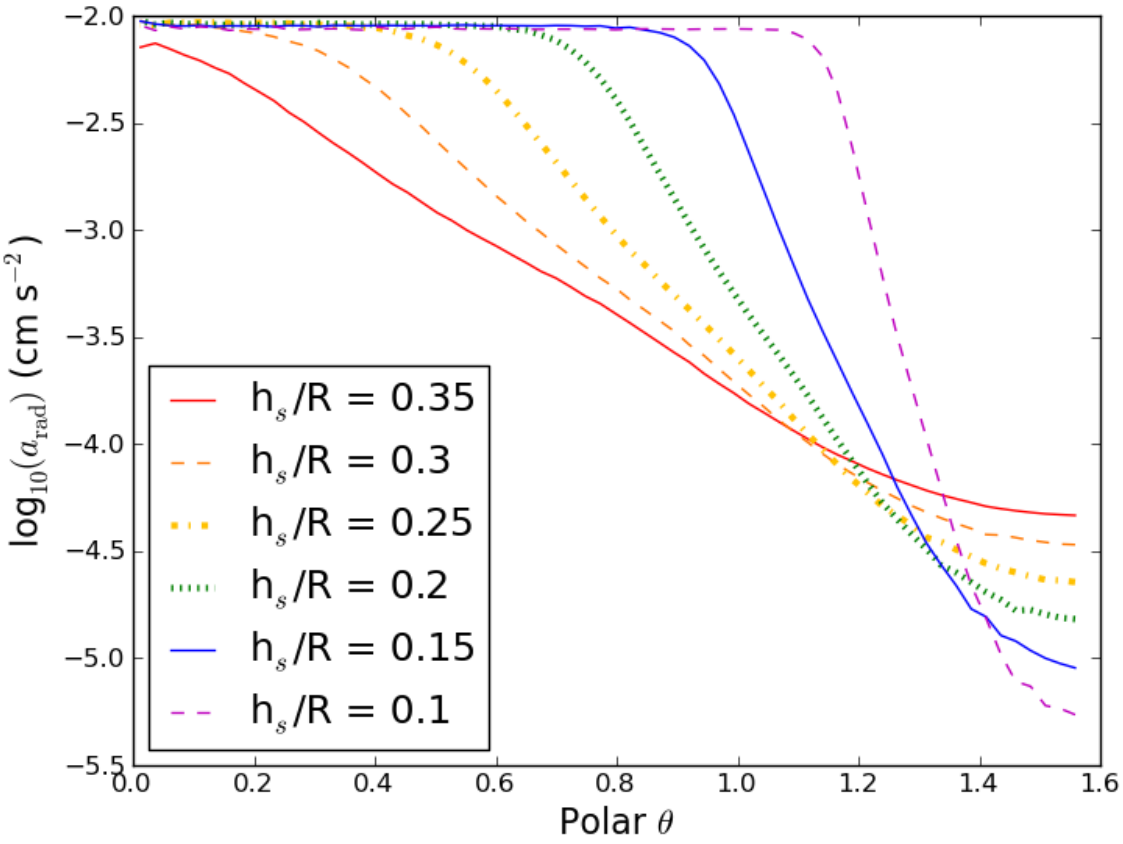

Figure 3.7: Radiative acceleration as a function of polar angle (gravity not included). All parameters for this calculation correspond to the fiducial values listed in Table 3.1, except for opening angles which vary as indicated (while conserving mass in the calculation domain). The acceleration is lowest in the equatorial region, even though the force from radiation pressure is highest there, because the force does not rise as quickly as the mass as the polar angle increases.

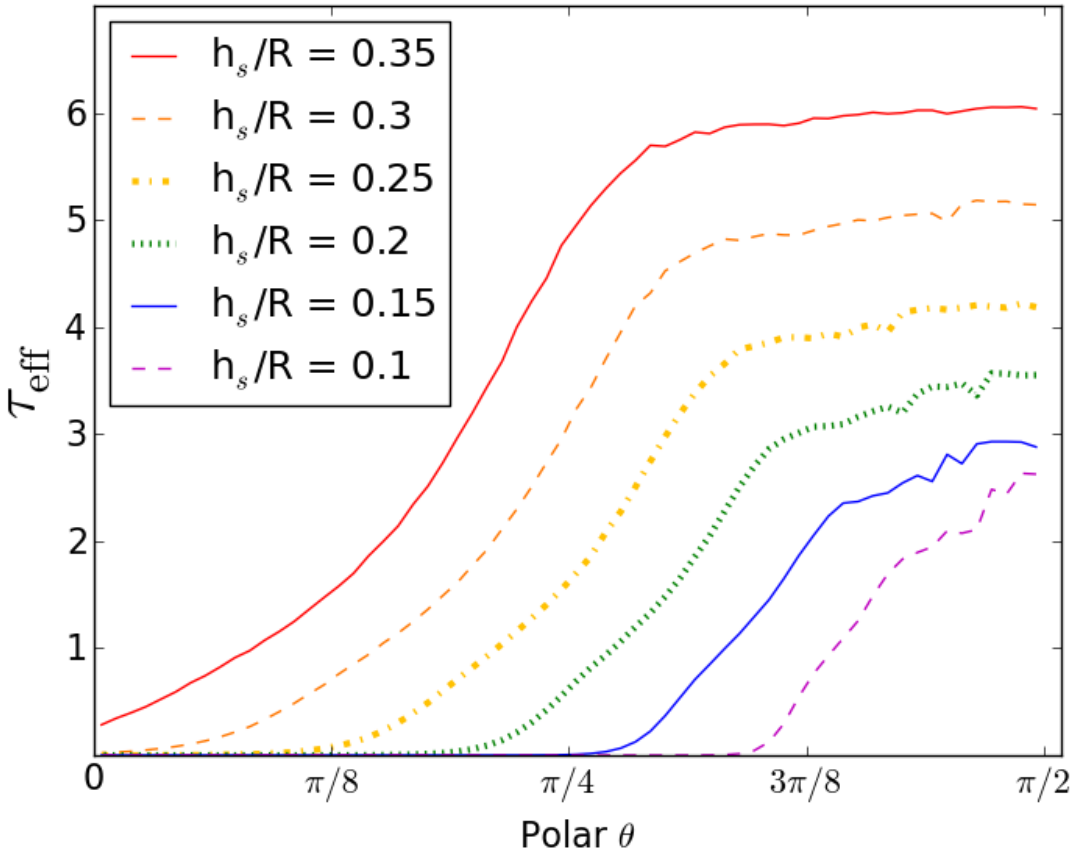

Figure 3.8: $\tau_{\rm eff}(\theta)$ for various opening angles (see equation 3.17). Parameters correspond to the fiducial values in Table 3.1, except for opening angles which vary as indicated (while conserving the total mass in the calculation domain). $\tau_{\rm eff}(\theta)$ is a measure of the radiative force on the gas column at a given polar angle, and it reaches its highest values in the equatorial region.

mass present in the equatorial region as the opening angle increases, the radiative flux in that region increases such that $\tau_{\rm eff}(\theta)$ is able to increase there as well.

If we calculate the radiation force on spherically distributed gas with the same $\overline{N}_{\rm H}$, we find that $\tau_{\rm eff} = 13$. Thus although the effective radiation force exceeds L/c in Figure 3.8, the enhancement is not as large for a realistic disk geometry as it is in the spherically symmetric case. For the largest opening angle considered in this study ($h_s/R = 0.35$), $\overline{\tau}_{\rm eff}$ is smaller than the spherically symmetric value by a factor of ~ 2.

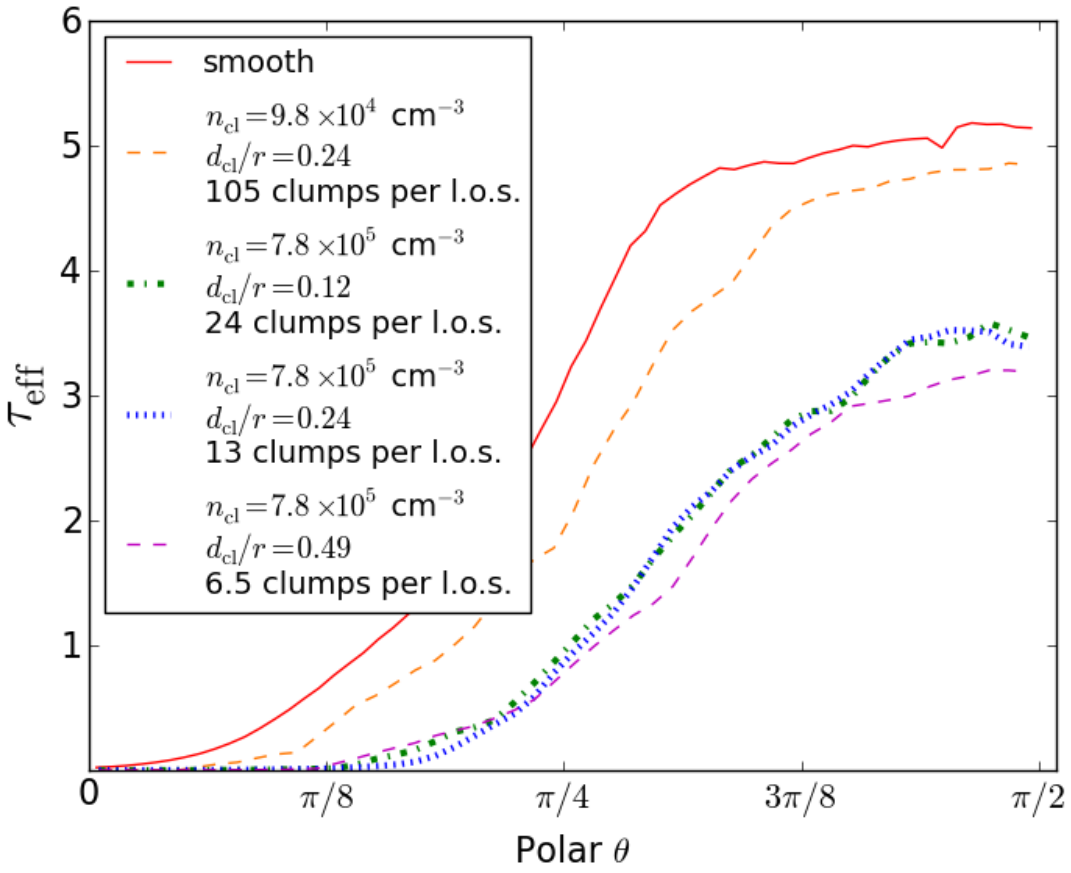

Figure 3.9: $\tau_{\rm eff}(\theta)$ for various clump densities $n_{\rm cl}$ and average clump diameters $d_{\rm cl}$. In all simulations the number of clumps is varied such that the total mass of the gas in the simulations domain is held constant. The diffuse background makes up 1% of the mass in all simulations.

3.3.3 Results for Clumpy Gas

Figure 3.9 shows how $\tau_{\rm eff}(\theta)$ varies with the clumpiness of the gas. For each clumpy gas distribution, the total mass in the computational domain was set equal to that of our fiducial smooth density model. The shape of the momentum deposition as a function of θ appears generally the same for the clumpy and smooth cases. This suggests that the smooth density distributions employed throughout most of this study provide accurate approximations to the behavior of more realistic clumpy density distributions, although they should systematically overestimate the radiation force on the dusty gas by a factor of ~ 2 in the most extreme cases of clumping.

Figure 3.10 illustrates how the radiation force acts on portions of individual clumps. Note how the force remains radially directed even in the presence of clumps, and how clumps shadow gas behind them.

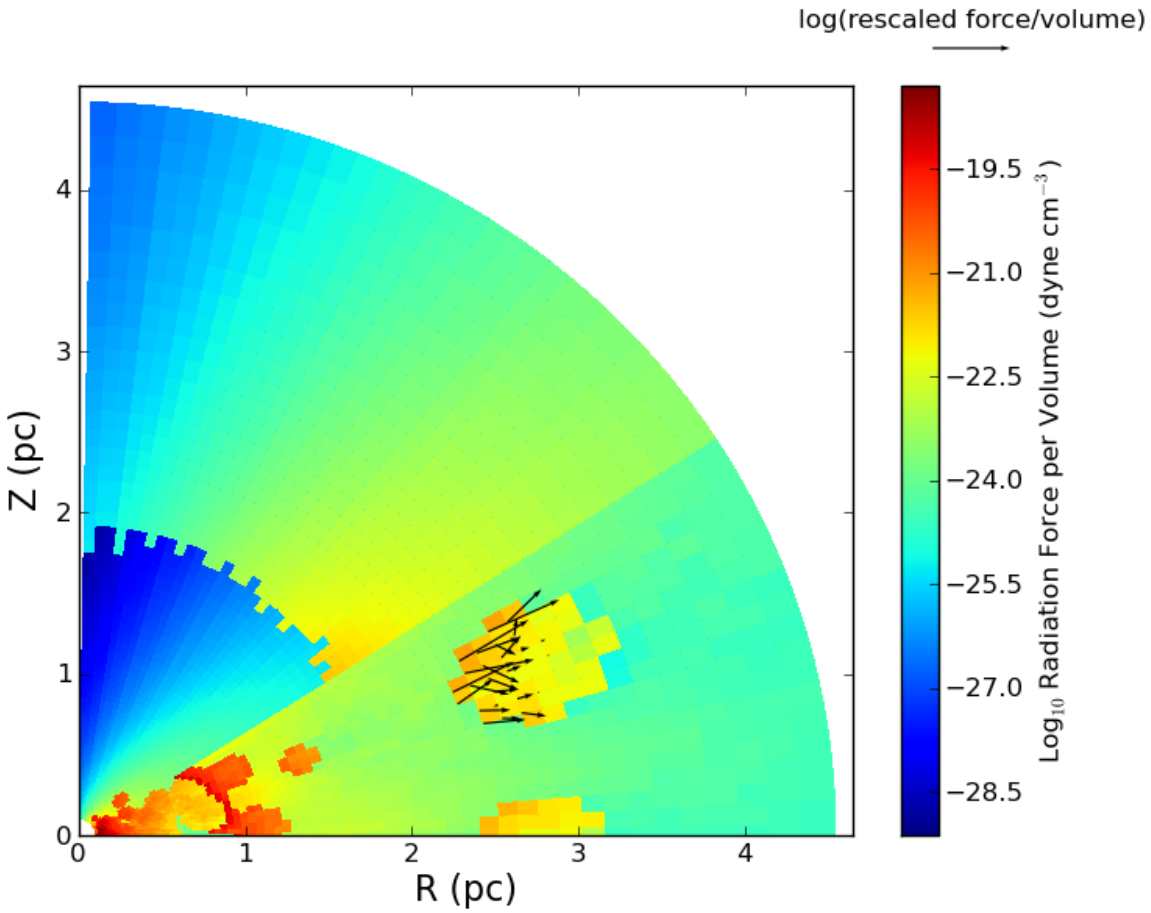

Figure 3.10: Arrows indicating the direction and magnitude of the radiation force are plotted over a slice of the magnitude of the force for a clumpy gas distribution just outside the sublimation boundary. The arrows are proportional to $\log_{10}(10^{22}) \times f_{\rm rad}$ (cgs))

3.3.4 Results for Anisotropic AGN Emission

If the black hole accretion disk is aligned with the mid-plane of the gas present at the scale of our calculation, one might expect that there would be more flux emitted in the polar directions than in the mid-plane direction. According to one prescription (Netzer 1987), the emitted flux should obey

$$F_{\rm emitted} \propto \cos\theta\,(1+2\cos\theta)\ , \tag{3.19}$$

where the first factor accounts for projected surface area and the second factor accounts of limb-darkening in an optically thick atmosphere.

Unlike the case of isotropic emission, we find that for anisotropic emission $\tau_{\rm eff}(\theta)$ peaks at an intermediate angle $< \pi/2$. The peak arises because at small polar angles there is hardly any gas present to provide optical depth, whereas hardly any light penetrates into the dusty gas at large polar angles. For a calculation with our fiducial parameters, the ratio of $\overline{\tau}_{\rm eff}$ in the case of anisotropic emission versus $\overline{\tau}_{\rm eff}$ for the case of isotropic emission is 0.72, indicating that photons tend to escape from the disk with fewer interactions when they are emitted in an anisotropic manner. This ratio will be even smaller for smaller disk opening angles.

From this point on, we will only consider models with a smooth density distribution and isotropic central emission. Nevertheless, it is important to keep in mind that the integrated force and $\dot{M}$ are likely to be reduce by factors of a few due to the effects of gas clumping and anisotropic emission of radiation.

3.3.5 Estimating the mass outflow rate

We cannot determine precisely the dynamics of the gas without coupling the radiative transfer calculation to a hydrodynamic solver in a time-dependent calculation. However, we may apply an Eddington-type argument to approximate whether gas will be blown away in a given solid angle and to estimate the mass-loss rate. This argument considers the gravitational and radiation forces but ignores centrifugal acceleration of the gas, viscous or gravitational torques, and shocks.

Let $\bar{t}(\theta)$ denote the time taken to accelerate the gas in a given column with mass $dM_{\rm tot}$ to a distance $r_{\rm out}$ at constant acceleration $a_{\rm net}(\theta)$. Then

$$\bar{t}(\theta) \approx \sqrt{\frac{2\,r_{\rm out}}{a_{\rm net}}} = \sqrt{2\,r_{\rm out}\,\frac{\frac{dM_{\rm gas}}{d\omega}}{\frac{dF_{\rm net}}{d\omega}}}\ . \tag{3.20}$$

We define a differential mass outflow rate per solid angle $d\dot{M}/d\omega$,

$$\frac{d\dot{M}}{d\omega}(\theta) \equiv \frac{\frac{dM_{\rm gas}}{d\omega}}{\bar{t}(\theta)} = \sqrt{\frac{\left(\frac{dM_{\rm gas}}{d\omega}\right)\left(\frac{dF_{\rm net}}{d\omega}\right)}{2\,r_{\rm out}}}\ . \tag{3.21}$$

We can also define a mass outflow rate integrated over the entire volume (all of θ),

$$\dot{M} \equiv \int_{\omega} \frac{d\dot{M}}{d\omega}\, d\omega = 2\,(2\pi) \int_{0}^{\pi/2} \frac{d\dot{M}}{d\omega} \sin\theta\, d\theta \ , \tag{3.22}$$

where we have taken advantage of the assumed symmetry for $\theta \rightarrow \pi - \theta$. Whenever $d\dot{M}/d\omega$ is less than zero for a particular value of θ, we do not add it to the total reported value for the total volume-integrated $\dot{M}$, since we are only interested in the gas that gets blown away.

Our gas density prescription (section 3.2.1) indicates that for any given polar angle, the density goes as $r^{-\gamma}$. This allows us to compute $dM_{\rm gas}/d\omega$ in terms of $r_{\rm out}$ and the sublimation radius $r_{\rm sub}(\theta)$,

$$\begin{aligned} \tfrac{dM_{\rm gas}}{d\omega} &= \textstyle\int_{r_{\rm sub}}^{r_{\rm out}} \rho(r_{\rm sub}) \left(\tfrac{r}{r_{\rm sub}}\right)^{-\gamma} r^2\, dr \\ &= \tfrac{1}{3-\gamma}\, \rho(r_{\rm sub})\, r_{\rm out}^3 \left(\tfrac{r_{\rm sub}}{r_{\rm out}}\right)^{\gamma} \left[1 - \left(\tfrac{r_{\rm sub}}{r_{\rm out}}\right)^{3-\gamma}\right] \ . \end{aligned} \tag{3.23}$$

In section 3.3.6 we will present values for $d\dot{M}/d\omega$ calculated using equations 3.21, 3.23, and the values of $dF_{\rm net}/d\omega$ calculated using the Monte Carlo. For the rest of this section, we present a simple scaling argument to demonstrate that our estimates of the mass outflow rate depend only weakly on our choice of the outer radius $r_{\rm out}$ (which is somewhat arbitrary).

Our results from section 3.3.1 indicate that we can think of the radiative acceleration as being divided into two parts: a spike in acceleration at the sublimation radius that arises from the absorption of ultraviolet and optical photons, and acceleration due to absorption of infrared photons that goes as r^{-2} at large radii. Only the second type of acceleration is sensitive to our choice of $r_{\rm out}$. We may approximate the infrared radiation force as

$$\begin{aligned} &\tfrac{dF_{\rm net}}{d\omega}_{\rm IR} \approx \\ &\textstyle\int_{r_{\rm sub}}^{r_{\rm out}} \rho(r_{\rm sub}) \left(\tfrac{r}{r_{\rm sub}}\right)^{-\gamma} \left[\tfrac{a_{\rm rad}(r_{\rm sub}) r_{\rm sub}^2 - G\,M_{\rm BH}}{r^2}\right] r^2 dr \\ &= \tfrac{1}{\gamma-1}\, \rho(r_{\rm sub}) \left[a_{\rm rad}(r_{\rm sub}) - \tfrac{G\,M_{\rm BH}}{r_{\rm sub}^2}\right] r_{\rm sub}^3 \\ &\qquad \times \left[1 - \left(\tfrac{r_{\rm sub}}{r_{\rm out}}\right)^{\gamma-1}\right] \ , \end{aligned} \tag{3.24}$$

where $a_{\rm rad}(r_{\rm sub})$ refers to the value of the radiative acceleration at the sublimation radius that provides the correct normalization for the inverse-square law acceleration at large radii.

Using equation 3.21, dropping factors of order unity, and assuming $r_{\rm out} \gg r_{\rm sub}$, we finally arrive at

$$\begin{aligned} &\tfrac{d\dot{M}}{d\omega}_{IR} \approx \\ &\rho(r_{\rm sub}) \left[a_{\rm rad}(r_{\rm sub}) - \tfrac{G\,M_{\rm BH}}{r_{\rm sub}^2}\right]^{1/2} r_{\rm sub}^{5/2} \left(\tfrac{r_{\rm out}}{r_{\rm sub}}\right)^{1-\frac{1}{2}\gamma} \ . \end{aligned} \tag{3.25}$$

From the simulations performed in Hopkins & Quataert (2011a), γ tends to fall between 1.5 and 2, and as already noted we have fixed γ at 1.5 for all numerical calculations in this study. We expect that the density profile will ultimately truncate at about 1 kpc. So, the ratio of the $d\dot{M}/d\omega$ due to absorption of infrared photons that we would calculate using $r_{\rm out}$ of 1 kpc versus $r_{\rm out}$ of 32.4 pc would be, for $\gamma = 1.5$, only 2.4. For $\gamma = 2$, $d\dot{M}/d\omega$ would be invariant with respect to choice of $r_{\rm out}$, and for $\gamma = 2.5$ the ratio would be 0.42. The fact that a significant portion of the radiative acceleration in the Monte Carlo calculations comes from the spike near the dust sublimation radius further reduces the sensitivity of our results to our choice of $r_{\rm out}$.

A final quantity that will be useful to us is the velocity of the gas in a solid angle $v_{\rm out}(\theta)$,

$$v_{\rm out}(\theta) \equiv \sqrt{2\, a_{\rm net}\, r_{\rm out}}\ . \tag{3.26}$$

Once again focusing on the infrared acceleration at large radii and making the same approximations as we did for estimating $d\dot{M}/d\omega$, we find

$$\begin{aligned} v_{\rm out}(\theta) &= \sqrt{2\,\frac{\frac{dF_{\rm net}}{d\omega}}{\frac{dM_{\rm gas}}{d\omega}}\, r_{\rm out}} \\ &\approx \sqrt{2\left[a_{\rm rad}(r_{\rm sub}) - \frac{G\,M_{\rm BH}}{r_{\rm sub}^2}\right] r_{\rm sub}}\left(\frac{r_{\rm out}}{r_{\rm sub}}\right)^{\frac{1}{2}\gamma - 1}\ . \end{aligned} \tag{3.27}$$

Therefore our calculations for the velocity of the gas will have a similarly weak dependence on $r_{\rm out}$ as that of the mass-loss rate.

3.3.6 Variation of mass outflow with opening angle

Figure 3.11 shows the differential mass outflow rate $d\dot{M}/d\omega$ calculated using equation 3.21 for disks with various opening angles. The densities of the innermost radial grid zones have been re-scaled to keep the total mass in the calculation domain constant in each case.

The overall mass outflow rate declines with smaller h_s/R due to the increased funneling of radiation into the low-density polar regions. For $h_s/R \geq 0.25$ the differential mass outflow rate peaks at $\theta = \pi/2$, while for $h_s/R \leq 0.25$ the peak is at an intermediate polar angle. This is due to an interplay between the amount of mass available to be cleared away, its inertia, and the gravitational force acting upon it. Near the equator, however, the large amount of gas cannot be unbound by the radiative acceleration and so there is not outflow, even though the force due to radiation is strongest there.

We emphasize that Figure 3.11 represents only a snapshot in time of the mass outflow rate for an accreting SMBH. The evolution of $d\dot{M}/d\omega$ with time is not calculated here and requires a fully coupled radiation-hydrodynamics calculation. Nevertheless, these snapshots provide insight into how a SMBH may self-regulate its accretion. One possible scenario is that an initially optically thick and puffy disk will blow away gas in the polar region. In the absence of a replenishing mechanism that operates on a timescale shorter than $\bar{t}$, this will cause the disk to become thinner, reducing the tendency for radiation to blow out more gas.

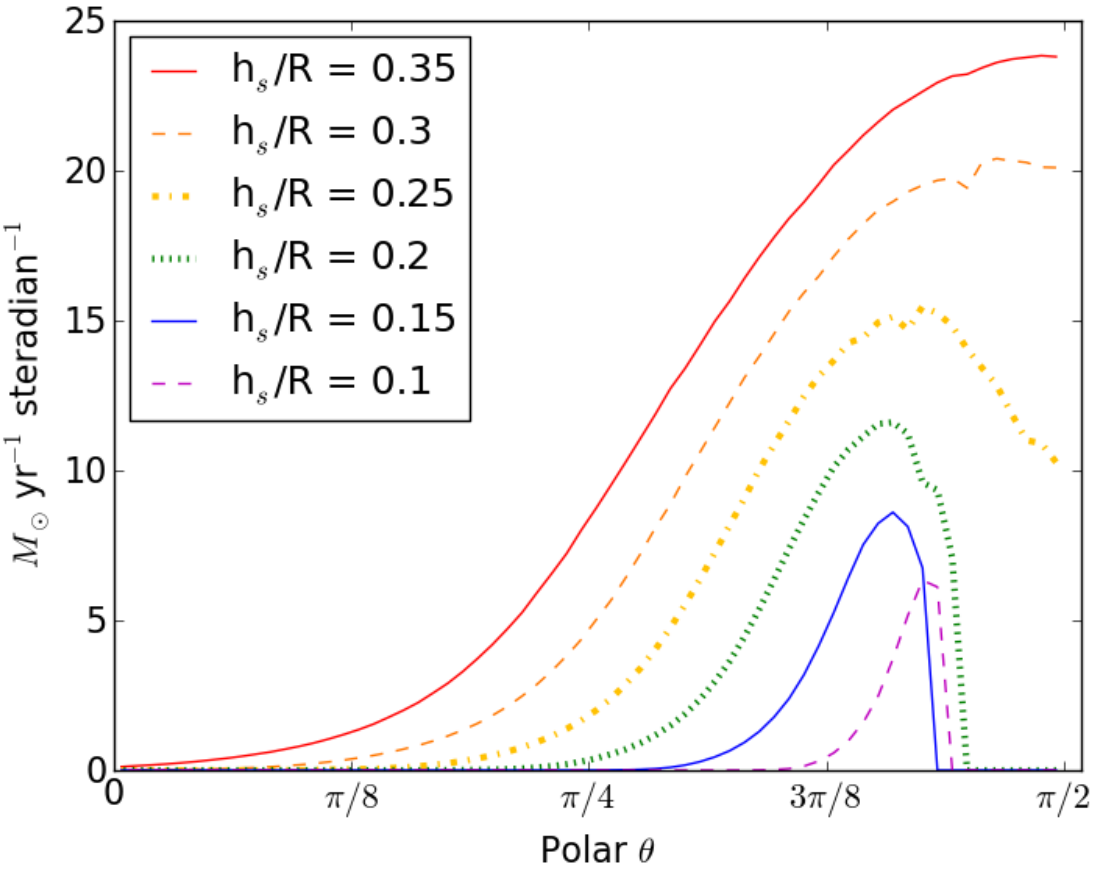

Figure 3.11: Differential mass outflow rate $d\dot{M}/d\omega$ for various opening angles. Parameters correspond to the fiducial values in Table 3.1, except for opening angles which vary as indicated (while conserving the total mass in the calculation domain).

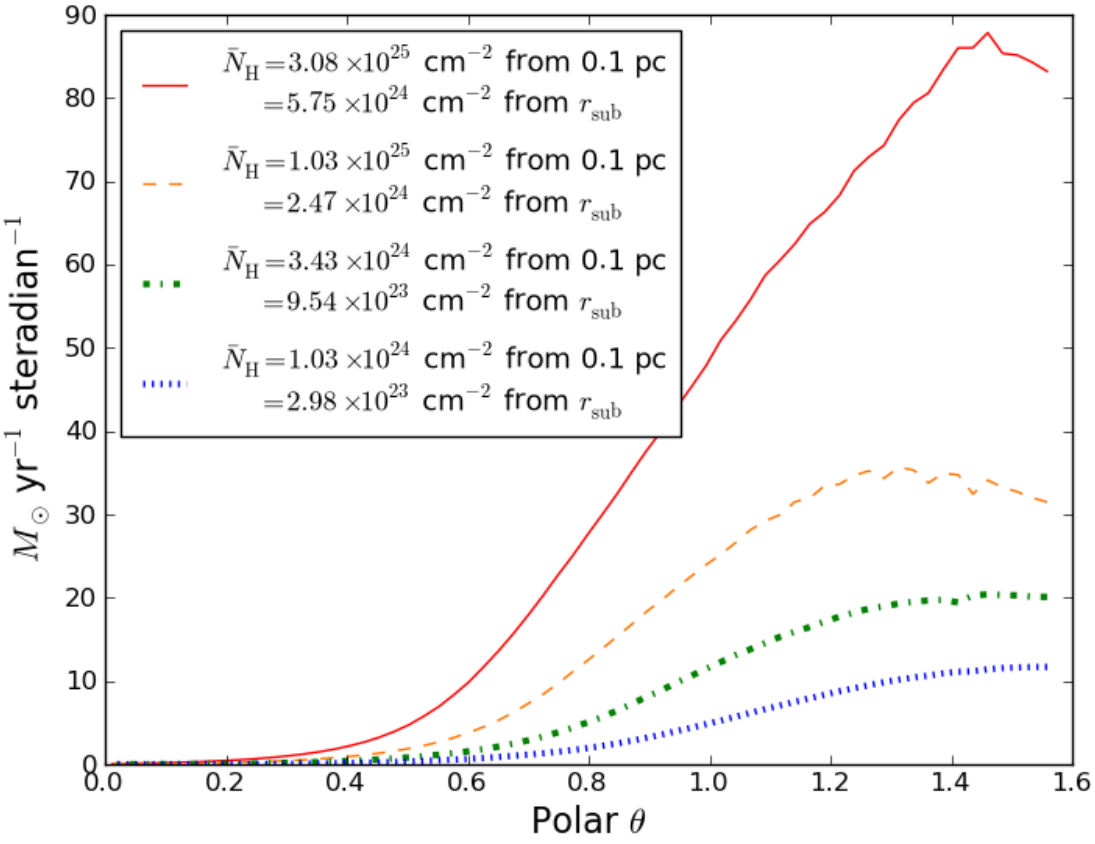

Figure 3.12: Differential mass outflow rate $d\dot{M}/d\omega$ for various sightline-averaged column densities (measured to 0.1 pc from the black hole). Parameters correspond to the fiducial values in Table 3.1, except for the average column densities which vary as indicated. The total mass in the calculation domain varies proportionally with the average column density.

3.3.7 Variation of mass outflow with other parameters

Figure 3.12 shows the differential mass outflow rate $d\dot{M}/d\omega$ for disks with varying column densities (the column density is averaged over all lines of sight, and includes both dusty and non-dusty gas). The variation in column density is directly proportional to variation in the total mass present in the calculation domain.

As expected, more mass can be ejected when there is more mass present to begin with. However, we find the scaling to be sub-linear: $\dot{M} \propto \overline{N}_{\rm H}^{0.49}$ for the range of column densities included in this study (power-law scaling relations for all the free parameters in the problem will be summarized in section 3.3.8). The slow growth of $\dot{M}$ with column density is due to the fact that at higher column densities, the radiative force on the gas in the densest

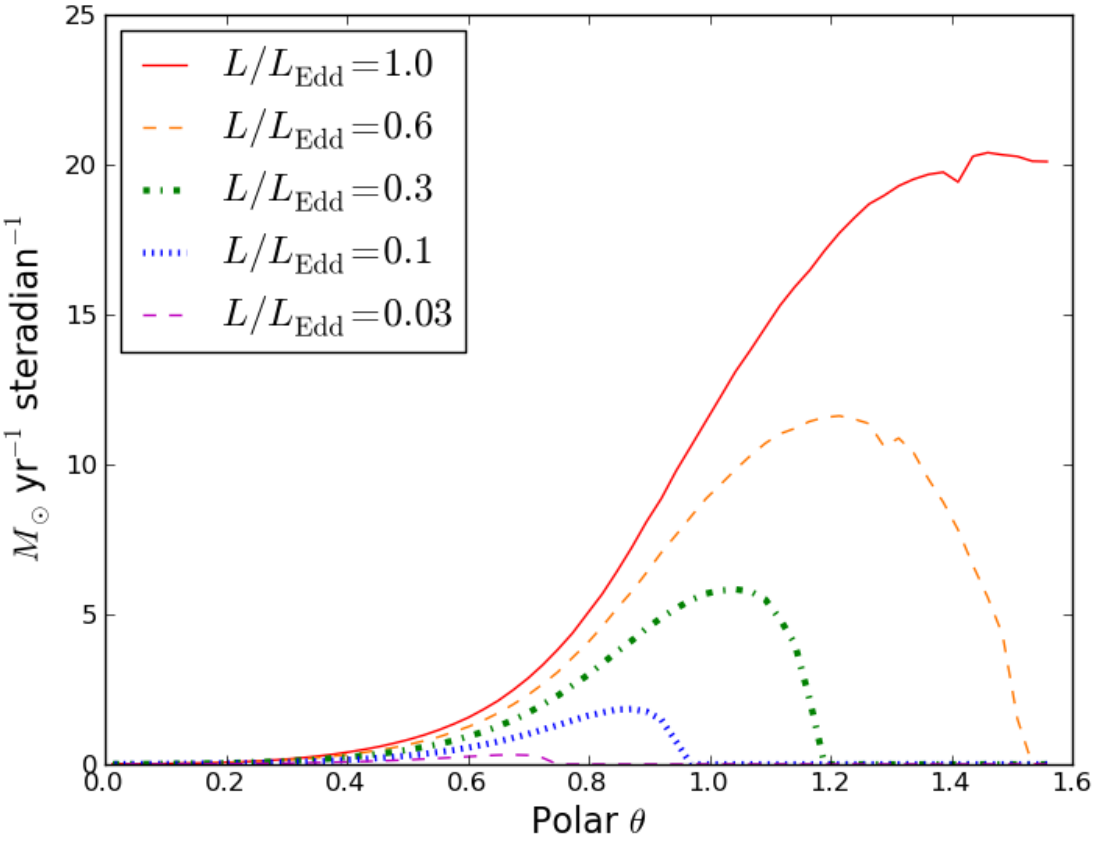

Figure 3.13: Differential mass outflow rate $d\dot{M}/d\omega$ for various luminosities. Parameters correspond to the fiducial values in Table 3.1, except for the luminosities which vary as indicated.

portions of the disk does not rise as quickly as the mass present there, and so gravity becomes increasingly effective at limiting the outflow rate.

Finally, Figure 3.13 shows the differential mass outflow rate $d\dot{M}/d\omega$ for calculations with varying black hole luminosities. For higher AGN luminosities, not only is there a higher net force on a column at a given value of θ for which the net force was already outward (positive), but also the net force becomes positive on columns at larger polar angles. For all other parameters held constant, there exists a critical luminosity at which the radiation force exceeds gravity for all polar angles, and all the gas would be blown away. For opening angle $h_s/R = 0.3$ and our fiducial mean column density 3.4×10^{24} cm^{-2}, radial density power-law $\gamma = 1.5$ and black hole mass $M_{\rm BH} = 10^8\ M_\odot$, this critical luminosity is $L/L_{\rm Edd} \approx 0.7$. The existence of such a critical luminosity might help to explain the dearth of quasars observed to be radiating at the full value of their inferred Eddington limit, although time-dependent calculations will be necessary to test this hypothesis.

3.3.8 Summary scalings of integrated quantities

The scalings of $\overline{\tau}_{\rm eff}$ with the parameters of the problem, varied one at a time from the fiducial values listed, for a black hole with mass $10^8\ M_\odot$, can be summarized as follows:

$$\begin{aligned}\overline{\tau}_{\rm eff} = 3.8 & \left(\frac{h_s/R}{0.3}\right)^{1.5} \\ & \times \left(\frac{\overline{N}_{\rm H}}{3.4\times10^{24}\ {\rm cm}^{-2}}\right)^{0.49} \\ & \times \left(\frac{L}{1.26\times10^{46}\ {\rm ergs\ s}^{-1}}\right)^{-0.13}\end{aligned} \tag{3.28}$$

We may also present a summary scaling relation for the volume-integrated mass outflow rate $\dot{M}$:

$$\begin{aligned}\dot{M} = 144\ M_\odot\ {\rm yr}^{-1} & \left(\frac{h_s/R}{0.3}\right)^{2.6} \\ & \times \left(\frac{\overline{N}_{\rm H}}{3.4\times10^{24}\ {\rm cm}^{-2}}\right)^{0.62} \left(\frac{L}{1.26\times10^{46}\ {\rm ergs\ s}^{-1}}\right)^{1.6}\end{aligned} \tag{3.29}$$

Note that $\overline{N}_{\rm H}$ in these scaling relations corresponds to column densities integrated from 0.1 pc to large radii. If instead we use the column density integrated from the edge of the dust sublimation radius outward, then the fiducial column density becomes $9.5\times10^{23}\ {\rm cm}^{-2}$, the column density power-law in equation 3.28 changes to 0.56, and the column density power-law in equation 3.29 changes to 0.71. Also note that the rates in equation 3.29 correspond to a radius of 32 parsecs from the central SMBH, and there is a weak dependence on radius (no stronger than $r^{1/4}$ when $\gamma = 1.5$; refer to section 3.3.5.)

The fiducial value for the mass outflow rate of 144 $M_\odot$ per year may seem surprisingly large. That value was computed for a black hole radiating at its full Eddington luminosity, and at that luminosity the radiative acceleration beats out gravity at all solid angles. Therefore, there is reason to suspect that such a large outflow rate is not sustainable for many gas dynamical times at the parsec scale, as the amount of mass present and the opening angle of the disk readjust during the outflow. The quoted outflow rate also does not incorporate the effects of making the gas distribution clumpy, and as was demonstrated in section 3.3.3, this reduces the integrated force by a factor of ~ 2 for significant clumping.. Since the mass loss rate should roughly scale as the integrated force to the 1/2 power (as argued in section 3.3.5), the mass outflow rate will be reduced approximately by a factor of $1\sqrt{2}$ in the case of significant clumping. On the other hand, the mass-loss rates calculated above correspond to the mass swept up within a radius of approximately 30 parsecs from the central black hole. Extrapolating our results out to 1 kpc, as discussed in section 3.29, might boost the outflow rates by roughly a factor of 2 for $\gamma = 1.5$.

With those caveats in mind, the important conclusions to be drawn from equations 3.28 and 3.29 are that the radiation force may reach several times (~ 3) L/c, and that the mass outflow rates can easily reach tens of solar masses per year for parameters close to our fiducial values. In the proper circumstances ($\overline{N}_{\rm H} \gtrsim 10^{24}$ cm^{-2}, $h_s/R \gtrsim 0.25$, and $L/L_{\rm Edd} \approx 1$), the mass outflow rates can reach up to 100 $M_\odot$ per year.

It is also interesting to note that the momentum enhancement and mass outflow rate depend relatively strongly on the AGN luminosity and disk opening angle h_s/R. The fact that the dependence of the mass outflow rate on luminosity is steeper than the dependence of the radiation force on luminosity may at first seem surprising. This scaling has its origins in an effect noted in section 3.3.7, specifically that increasing the luminosity allows the radiation force to exceed gravity for a larger fraction of the solid angle, adding more mass to the outflow than was present at lower luminosities.

Finally, to drive home the point that momentum deposition, not heating, is responsible for the large computed outflow rates, we can estimate the corresponding kinetic luminosities. We use our estimate of the gas velocity as a function of solid angle $v_{\rm out}(\theta)$ (equation 3.26) to compute the fraction of the accretion luminosity L that goes into kinetic luminosity:

$$\begin{aligned}\epsilon_{\rm k} &\equiv \left[\frac{1}{L}\right]\left[\int \frac{1}{2}\frac{d\dot{M}}{d\omega}(\theta)\, v_{\rm out}^2(\theta)\, d\omega\right] \\ &= \left[\frac{2(2\pi)}{L}\right]\left[\int_0^{\pi/2} \frac{1}{2}\frac{d\dot{M}}{d\omega}(\theta)\, v_{\rm out}^2(\theta)\, \sin\theta\, d\theta\right]\end{aligned} \tag{3.30}$$

Once again by varying each parameter one at a time with respect to the fiducial values, our results for a 10^8 solar mass black hole can be summarized as

$$\begin{aligned}\epsilon_{\rm k} = 0.009 &\left(\frac{h_s/R}{0.3}\right)^{1.9} \\ \times &\left(\frac{\overline{N}_{\rm H}}{3.4\times10^{24}\ {\rm cm}^{-2}}\right)^{0.19} \times \left(\frac{L}{1.26\times10^{46}\ {\rm ergs\ s}^{-1}}\right)^{1.8}\end{aligned} \tag{3.31}$$

If the column density is computed by integrating from the dust sublimation radius outward, the corresponding power-law in equation 3.31 barely changes at all, increasing to 0.21.

The mass-weighted average velocity of the gas in the outflow will be approximately equal to $\overline{\tau}_{\rm eff} L/(c\dot{M})$, although a more accurate value can be obtained by integrating $v_{\rm out}(\theta)$ weighted by $dM_{\rm gas}/d\theta$ and only counting contributions from solid angles and radii for which gas can be blown out. For our fiducial parameters this average velocity at 32 parsecs from of the computational domain is approximately 1000 km s^{-1}.

3.4 Conclusion

We have calculated how radiation pressure from a luminous accretion disk around a SMBH drives a powerful outflow of gas via continuum radiation pressure on dust at distances

of 0.1-30 pc from the black hole. Using ambient gas conditions motivated by observational constraints on nuclear obscuration in AGN ($h_s/R \gtrsim 0.25$, $\overline{N}_{\rm H} \gtrsim 10^{24}$ cm^{-2}) we find that a $10^8 M_\odot$ SMBH radiating at Eddington can drive a wind with velocities of $\sim$ 1000's of km s^{-1} and an instantaneous mass loss rate of $\sim$ 10-100 $M_\odot$ per year (see equation 3.29). For SMBHs with masses $\gtrsim 10^9 M_\odot$, the outflow rates could approach $\sim 1000 M_\odot$ per year.

Radiative heating sublimates the dust out to distances of roughly 0.5 to 1 pc in the mid-plane, and radiation pressure drives away the gas and dust in the polar regions, leaving behind what may constitute the observed dusty torus. The wide-angle bipolarity of these outflows corresponds well to observations of obscured quasars (Greene et al. 2012) and Seyfert 2s (Crenshaw & Kraemer 2000). Although the radiative acceleration is greatest in the polar regions, the majority of the ejected mass comes from oblique angles where there is a more significant reservoir of gas. By contrast, gas in the equatorial plane is more difficult to unbind because of its large inertia and large integrated gravitational attraction.

The net momentum flux in the resulting outflow can exceed L/c by factors of up to 5 for the parameters studied, as infrared photons interact multiple times during their outward diffusion. As recently demonstrated in the calculations of Ciotti et al. (2010); Novak et al. (2011); Debuhr et al. (2011), outflows with these properties have a significant impact on gas in the surrounding host galaxy. Our results for the outflows match reasonably well the observed outflows in local ULIRGs such as Mrk 231 (Rupke & Veilleux 2011). The mass-loss rates and kinetic luminosity fractions we calculate also provide a reasonable match to observations of obscured quasars (Moe et al. 2009; Dunn et al. 2010), although our model does not provide a mechanism for launching large amounts of gas at the high velocities ($>$ 20000 km s^{-1}) observed in these systems at small radii. One possibility is that these quasars are exhibiting both line and continuum radiation pressure driven outflows.

We find that the net effect of the AGN radiation on the surrounding gas is a strong function of the opening angle of the accreting gas at the parsec-scale (the torus). Increasing the opening angle allows more momentum to be deposited in all directions because the mass distribution and emergent radiative flux become more isotropic. We also find a steep dependence of the outflow rate on the luminosity of the accretion disk, because at higher luminosities gas becomes unbound over a greater range of solid angles. This result is also in agreement with the observed anti-correlation between obscured AGN fraction and AGN luminosity (Simpson 2005; Hasinger et al. 2007; Maiolino et al. 2007), although we are restricting our attention to a single black hole mass.

Keeping all of our parameters at the fiducial values listed in Table 3.1 but varying the luminosity, we find that outward radiative acceleration begins to exceed gravity at all angles once $L/L_{\rm Edd}$ reaches a value of ~ 0.7 (for mean column densities and/or opening angles larger than those given in Table 1, this critical value of $L/L_{\rm Edd}$ would be smaller). This finding may help to explain the relative dearth of broad-line quasars observed to be radiating at their full Eddington luminosity (Kelly et al. 2010).

The effects of dust sublimation play a crucial rule in determining the angular dependence of the radiative force on the torus. The redistribution of flux between polar angles takes place almost entirely in the region of gas in which dust has been sublimated, where infrared

radiation is re-emitted from the edge of the dusty gas at angles deviating from the radial direction. Once photons penetrate into the dusty gas, they tend to diffuse radially and deposit momentum almost entirely in the radial direction.

A fully coupled radiation-hydrodynamic calculation will be needed to fully understand the subsequent behavior of the gas in time. Future work will focus on incorporating the results of this study into hydrodynamic simulations of black hole accretion. In addition to the coupling to the hydrodynamics, more details pertinent to the radiative physics may be addressed in such calculations, including line absorption, anisotropic scattering off of dust, metallicity gradients, and variations in the average dust-to-gas ratio.

3.5 Acknowledgments

We thank Jason Dexter, Claude-André Faucher-Giguère, and Nahum Arav for helpful conversations. During this work Nathaniel Roth was supported by the Department of Energy Office of Science Graduate Fellowship Program (DOE SCGF), made possible in part by the American Recovery and Reinvestment Act of 2009, administered by ORISE-ORAU under contract no. DE-AC05-06OR23100. Daniel Kasen was supported by a Department of Energy Office of Nuclear Physics Early Career Award (DE-SC0008067). Eliot Quataert was supported in part by the David and Lucile Packard Foundation. Support for Philip F. Hopkins was provided by NASA through Einstein Postdoctoral Fellowship Award Number PF1-120083 issued by the Chandra X-ray Observatory Center, which is operated by the Smithsonian Astrophysical Observatory for and on behalf of NASA under contract NAS8-03060. This work is supported by the Director, Office of Energy Research, Office of High Energy and Nuclear Physics, and Divisions of Nuclear Physics, of the U.S. Department of Energy under contract No. DE-AC02-05CH11231. This research used resources of the National Energy Research Scientific Computing Center, which is supported by the Office of Science of the U.S. Department of Energy under contract No. DE-AC02-05CH11231.

Chapter 4

The X-ray through Optical Flux and Line Strengths of Tidal Disruption Events

The content of this chapter, excluding Section 4.1, is drawn from Roth et al. (2015), with permission of the co-authors.

We study the emission from tidal disruption events (TDEs) produced as radiation from black hole accretion propagates through an extended, optically thick envelope formed from stellar debris. We analytically describe key physics controlling spectrum formation, and present detailed radiative transfer calculations that model the spectral energy distribution (SED) and optical line strengths of TDEs near peak brightness. The steady-state transfer is coupled to a solver for the excitation and ionization states of hydrogen, helium and oxygen (as a representative metal), without assuming local thermodynamic equilibrium. Our calculations show how an extended envelope can reprocess a fraction of soft x-rays and produce the observed optical fluxes of order 10^{43} erg s^{-1}, with an optical/UV continuum that is not described by a single blackbody. Variations in the mass or size of the envelope may help explain how the optical flux changes over time with roughly constant color. For high enough accretion luminosities, x-rays can escape to be observed simultaneously with the optical flux. Due to optical depth effects, hydrogen Balmer line emission is often strongly suppressed relative to helium line emission (with HeII-to-H line ratios of at least 5:1 in some cases) even in the disruption of a solar-composition star. We discuss the implications of our results to understanding the type of stars destroyed in TDEs and the physical processes responsible for producing the observed flares.

4.1 TDE preliminaries

The discussion in this section is provided for background and is almost entirely drawn from work that is not my own. In particular, it follows Rees (1988), Ulmer (1999), and Li

et al. (2002) very closely. For simplicity, the discussion only uses Newtonian gravity. It does not, for example, account for general relavistic precession of the initial stellar orbit (see Dai et al. (2015) for a particularly nice treatment of this analytically), or relativistic corrections to the gravitational potential of the black hole (BH). Therefore, this will all be most accurate when the tidal radius (defined below) is much larger than the BH event horizon.

Additional complications, not accounted for here, arise when the BH has appreciable spin. In this case the stellar orbit is not confined to a single plane. See (Guillochon & Ramirez-Ruiz 2015) for more on that case and its observational implications (it has some implications for the observed TDE rates).

The tidal radius is defined as the distance from the BH where the acceleration from self-gravity of the star at its surface equals the acceleration due to the tidal potential of the BH. Equating these gives

$$\frac{GM_*}{R_*^2} = \frac{GM_{\rm BH}}{{r_{\rm T}}^2}\left(\frac{R_*}{r_{\rm T}}\right) \tag{4.1}$$

where the right-hand side comes from Taylor expanding the tidal force of the BH.

This can be easily rearranged to get

$$r_{\rm T} = R_*\left(\frac{M_{\rm BH}}{M_*}\right)^{1/3} = 7\times10^{12}\left(\frac{M_{\rm BH}}{10^6 M_\odot}\right)^{1/3}\left(\frac{R_*}{R_\odot}\right)\ {\rm cm} \tag{4.2}$$

Now we introduce the penetration parameter $\beta \equiv r_{\rm T}/r_p$, where r_p is the pericenter of the initial stellar orbit bringing it close to the BH. A higher value of β means a deeper encounter. The ratio of the typical kinetic energy of stars far from the black hole, in a stellar bulge with velocity dispersion σ, to the kinetic energy they obtain upon close passage of the BH is then

$$\frac{\sigma^2}{2}\frac{r_{\rm T}}{\beta G M_{\rm BH}} = 2.6\times10^{-6}\ \frac{1}{\beta}\left(\frac{\sigma}{100\ {\rm km\ s^{-1}}}\right)^2\left(\frac{M_{\rm BH}}{10^6 M_\odot}\right)^{-2/3}\left(\frac{R_*}{R_\odot}\right) \tag{4.3}$$

In other words, the stars are almost at rest far from the BH, when compared to the energies they obtain on close orbits to the BH. So a stellar orbit near the BH will typically be close to parabolic. Depending on the exact velocity of the star as it is nudged into its orbit that brings it close to the BH, it may technically be energetically bound (so orbit becomes elliptical) or unbound (hyperbolic orbit).

So we take the total energy of the star (kinetic plus gravitational potential) to be zero for the typical example. This total energy must be conserved globally over the course of the encounter, but will become non-uniformly distributed over parts of the star. In particular, at r_p there is a large spread in energy across the star, with the material closest to the BH being more energetic than the material far away form the BH. This spread in *specific* total energy (energy per unit mass) falls in the range

$$|\Delta E| \le \Delta E_{\rm max} = k\frac{GM_{\rm BH}}{r_p}\frac{R_*}{r_p} \tag{4.4}$$

(equation 7 of Li et al. (2002)). It is easy to understand the $k = 1$ case based on Taylor expansion of the gravitational potential of the BH, and then using equation (4.2) to substitute for $r_{\rm T}$. However, k might reach values as large as 3 if the star has also been spun up during the orbit. This spin-up is discussed but ultimately not quantitatively accounted for in Rees (1988). After performing some manipulations we arrive at

$$\Delta E_{\rm max} = k\beta^2 \, \frac{GM_*}{R_*} \left(\frac{M_{\rm BH}}{M_*}\right)^{1/3} \tag{4.5}$$

Regardless of the value of k, the spread in energy is much larger than any of the initial binding energy of the star to the BH (which we already said was small, as discussed above), and much larger than the gravitational self-binding energy of the star, which is on the order of GM_*/R_*. So half the mass of the star becomes unbound and is flung away from the BH, never to return. This unbound material is generally confined to a narrow stream because of self-gravity (Kochanek 1994; Guillochon et al. 2014), so it will intercept a very small fraction of any radiation produced close to the BH.

The remaining half of the star remains bound with elliptical orbits with energies distributed in the range from $-\Delta E_{\rm max}$ to 0. We can use Kepler's laws to determine the time for the material to return to pericenter given its orbital energy. For the ellpitical orbits of the bound debris, assuming that the black hole mass completely dominates the dynamics, the specific total energy E (kinetic plus potential energy divided by mass) is

$$E = -\frac{GM_{\rm BH}}{2a} \tag{4.6}$$

And Kepler's third law is

$$\frac{P^2}{a^3} = \frac{4\pi^2}{GM_{\rm BH}} \tag{4.7}$$

Using equation (4.6) to eliminate a, the periods of the orbits of the bound material are given by

$$P = 2\pi GM_{\rm BH} \left(-2\Delta E\right)^{-3/2} \tag{4.8}$$

Then, using equation (4.5)

$$P_{\rm min} = \frac{2\pi}{(2k)^{3/2}} \beta^{-3} \sqrt{\frac{R_*^3}{GM_*}} \left(\frac{M_{\rm BH}}{M_*}\right)^{1/2} \tag{4.9}$$

Putting in values,

$$P_{\rm min} = 7.88 \text{ days } \left(\frac{k}{3}\right)^{-3/2} \beta^{-3} \left(\frac{M_{\rm BH}}{10^6 M_\odot}\right)^{1/2} \left(\frac{M_*}{M_\odot}\right)^{-1} \left(\frac{R_*}{R_\odot}\right)^{3/2} \tag{4.10}$$

There are a few ways to now see the famous $t^{-5/3}$ law for the rate at which bound debris continues to return. Start with the chain rule

$$\frac{dM}{dt} = \frac{dM}{dE}\frac{dE}{dt} \, . \tag{4.11}$$

All simple derivations now need to assume that the stellar mass is uniformly distributed in specific energy post disruption, that is, dM/dE is constant. This is justified by the numerical work in Evans & Kochanek (1989) and Ayal et al. (2000), although some deviations do appear when more realistic stellar models are used (Guillochon & Ramirez-Ruiz 2013). Referring to equation (4.8), we rearrange to get E in terms of the period, which is t, and the -5/3 law falls out immediately.

4.2 TDE observations and puzzles

Observational candidates for TDEs are rapidly accumulating. A number of flares from galactic centers have been discovered in x-rays (Komossa & Bade 1999; Donley et al. 2002; Komossa et al. 2004; Halpern et al. 2004; Esquej et al. 2007; Cappelluti et al. 2009; Maksym et al. 2010; Saxton et al. 2012; Hryniewicz & Walter 2016; Lin et al. 2015; Komossa 2015). The peak luminosity is high, $\gtrsim 10^{44}$ erg s^{-1}, and the spectral energy distribution peaks at soft x-ray energies $\lesssim 0.1$ keV. After peak, the luminosity fades as a power-law in time similar to $L \propto t^{-5/3}$, a dependence predicted for the fallback of disrupted stellar debris (Rees 1988; Phinney 1989; Evans & Kochanek 1989; Lodato et al. 2009; Guillochon & Ramirez-Ruiz 2013).

There have also been TDE candidates found in the ultraviolet (UV) (Gezari et al. 2006, 2009), and in the optical in SDSS (van Velzen et al. (2011); van Velzen & Farrar (2014), Pan-STARRS1 (Gezari et al. 2012; Chornock et al. 2014), ASASSN (Holoien et al. 2014, 2016b,a), PTF (Cenko et al. 2012a; Arcavi et al. 2014), and ROTSE (Vinkó et al. 2015). These events typically rise to a peak (observer frame) R-band luminosity of $\sim 2{\times}10^{43}$ ergs s^{-1} on a timescale of $\sim$ months (Arcavi et al. 2014), with a late time fall consistent with $t^{-5/3}$. Intriguingly, PTF10iya, Swift J2058.4, ASASSN-14li, and ASASSN-15oi have been simultaneously observed in both optical and x-ray (Cenko et al. 2012a,b; Holoien et al. 2016b; Miller et al. 2015; Cenko et al. 2016; Holoien et al. 2016a).

A few long-lived ($\sim 10^7$ sec) transients have also been observed at hard x-ray and gamma-ray energies (Bloom et al. 2011; Cenko et al. 2012b; Brown et al. 2015). Occasionally, associated optical emission is also detected. These events have been interpreted as due to a relativistic jet generated via BH accretion; such "jetted" TDEs appear to be observationally rare compared to the soft x-ray and UV/optical flares (van Velzen & Farrar 2014; Arcavi et al. 2014), in line with theoretical expectations (De Colle et al. 2012).

While many aspects of the TDE candidates remain poorly understood, the nature of the optical/UV emission is perhaps the most puzzling. Two fundamental questions await full explanation: 1) Why is the observed optical flux in the UV/optical transients orders of magnitudes higher than that predicted by a standard BH accretion disk, and with a blue color that remains roughly constant over time? 2) Why do the optical spectra show strong lines of helium, but little or no hydrogen line emission (Gezari et al. 2012; Arcavi et al. 2014)?

The first puzzle stems from the fact that the tidal disruption radius, $R_{\rm td} = (M_{\rm bh}/M_\star)^{1/3} R_\star$,

is $\approx 10^{13}$ cm for the disruption of a solar-like star (mass $M_\star = M_\odot$, radius $R_\odot$) by a BH of mass $M_{\rm bh} \sim 10^6\ M_\odot$. Thermal emission from this radius should be in the soft x-ray (temperatures $\gtrsim 10^5$ K) with low optical luminosity ($\lesssim 10^{42}$ ergs s^{-1}). The problem has been addressed by postulating the presence of gas at large radii ($\sim$ 100 times $R_{\rm td}$) that absorbs (or advects) radiation and re-emits it at lower temperatures of a few times 10^4 K. This reprocessing region may be due to the formation of a hydrostatic (or quasi-static) envelope around the BH (Loeb & Ulmer 1997; Guillochon et al. 2014; Coughlin & Begelman 2014), or a super-Eddington mass outflow (Strubbe & Quataert 2009; Lodato & Rossi 2011; Metzger & Stone 2015; Vinkó et al. 2015; Miller 2015), or the circularization of material at radii much greater $R_{\rm td}$ (Shiokawa et al. 2015; Piran et al. 2015; Hayasaki et al. 2015; Bonnerot et al. 2016; Guillochon & Ramirez-Ruiz 2015; Dai et al. 2015). As of yet, however, no detailed radiative transfer calculations have determined how, or if, TDE radiation can be so reprocessed, and if so how the emergent optical through x-ray emission depends on the gas properties. These are key questions we hope to address here.

The solution to the second puzzle – the low hydrogen to helium emission line ratios – continues to be debated. Early theoretical modeling of the Hα emission by Bogdanović et al. (2004) raised the possibility that this line emission might be destroyed due to the high optical depth to Hα photons in a reprocessing region surrounding the inflowing stellar debris. Gezari et al. (2012) argued that the absence of H lines in PS1-10jh implies the disruption of a He-rich stellar core. The simulations of MacLeod et al. (2012), however, show that it is difficult to remove the H envelope of a red giant and disrupt only the He core. Noting that He star disruptions would be exceedingly rare, Guillochon et al. (2014) instead argued for the disruption of a normal main sequence star but with the hydrogen line emission suppressed by photoionization effects (e.g., Korista & Goad 2004). Gaskell & Rojas Lobos (2014) also argued in favor of a main-sequence star based on new calculations using the photoionization code CLOUDY. However, a separate CLOUDY parameter study performed by Strubbe & Murray (2015) disputed this interpretation, concluding that, for the conditions relevant to TDEs, hydrogen lines would not be suppressed enough to be consistent with the observations of PS1-10jh.

All previous studies of TDE line emission, however, have suffered from the limitation of the CLOUDY code, which assumes that the gas is optically thin in the continuum. Here we show that TDE envelopes are optically thick and highly scattering dominated, and that this profoundly changes the nature of line and continuum formation. We first use analytic arguments to delineate the physical conditions and key radiative processes in TDE envelopes, and then carry out the first non local-thermodynamic equilibrium (non-LTE) Boltzmann radiative transfer calculations for an idealized TDE model with a spherically, optically thick reprocessing region.

In contrast to optically thin CLOUDY models, spectrum formation in optically thick TDE envelopes more closely resembles the situation in stellar atmospheres, where the emission at a given wavelength depends on the source function at the associated thermalization depth. The thermalization depth is the radius at which emitted photons can scatter to the surface without being reabsorbed, and corresponds to a radial optical depth (integrated inward) of

approximately $\sqrt{\tau_{\rm abs}\tau_{\rm es}}$ where $\tau_{\rm abs}$ and $\tau_{\rm es}$ are the optical depths to absorptive and electron scattering processes, respectively. The thermalization depth varies with wavelength, such that lines and the continuum form at different layers (see Figure 4.1). The resulting spectrum will generally not be described by a single blackbody.

Our calculations define the conditions under which a TDE envelope may be "effectively" optically thick (i.e., $\sqrt{\tau_{\rm abs}\tau_{\rm es}} \gtrsim 1$) at soft x-ray wavelengths, and so absorb and reprocess a fraction of the accretion luminosity into optical continuum and line emission. We describe how the reprocessing efficiency depends on the mass, size, and ionization state of the envelope. Variations in these quantities may help explain the observed optical flux evolution and the occasional simultaneous appearance of x-rays. We show that escaping line photons are produced only in the outer layers of the envelope, such that the H to He line ratio is suppressed and will vary with the envelope extent. Indeed, some optical TDE candidates do show detectable, but varying, Hα emission (Arcavi et al. 2014; Holoien et al. 2016b).

In Section 4.3, we describe the assumptions of the model setup, and make analytic estimates of the degree of reprocessed luminosity. In Section 4.4 we present our numerical results from our radiative transport calculations. In Section 4.5 we discuss implications for observations and models of TDEs, and in Section 4.6 we conclude with a summary of the most important take away points.

4.3 Analytic Considerations

An accurate determination of the optical/UV luminosity from TDE envelopes requires a detailed non-LTE radiative transfer calculation, which we provide in Section 4.4. However, some insight into the physics of radiation reprocessing, and how it depends on envelope parameters, can be gained by approximate analytic arguments.

We consider a 1D configuration where radiation is emitted by a spherical source at radius $r_{\rm in}$ defining the layer at which most of the radiative luminosity is generated. Choosing $r_{\rm in}$ comparable to the original stellar pericenter passage distance (typically $\sim 10^{13}$ cm for a 10^6-10^7 $M_\odot$ BH) would approximate the luminosity arising from a viscous accretion disk formed near the disruption radius. Alternatively, the luminosity could be generated by the circularization of fallback material at a larger radius, $r_{\rm in} \sim 10^{14}$ cm (e.g. Piran et al. 2015; Dai et al. 2015).

We assume that the inner boundary radiates blackbody radiation at a source temperature $T_{\rm s}$. Our implicit assumption is that the conditions interior to $r_{\rm in}$ are sufficient to thermalize the radiation, e.g., via Comptonization or adiabatic expansion. For luminosities of order $10^{44} - 10^{45}$ ergs s^{-1}, $T_{\rm s} \sim 10^5 - 10^6$ K and source photons are emitted primarily at soft x-ray/ultraviolet wavelengths (energies $\sim 20 - 100$ eV).

Figure 4.2 shows the processes that contribute to the absorptive opacity for conditions found in a typical numerical calculation of a TDE envelope (to be described in Section 4.4). For soft x-rays near 100 Å, a primary absorptive opacity is photoionization of HeII (threshold energy of 54.4 eV). Photoionization and line absorption from other metals will also contribute

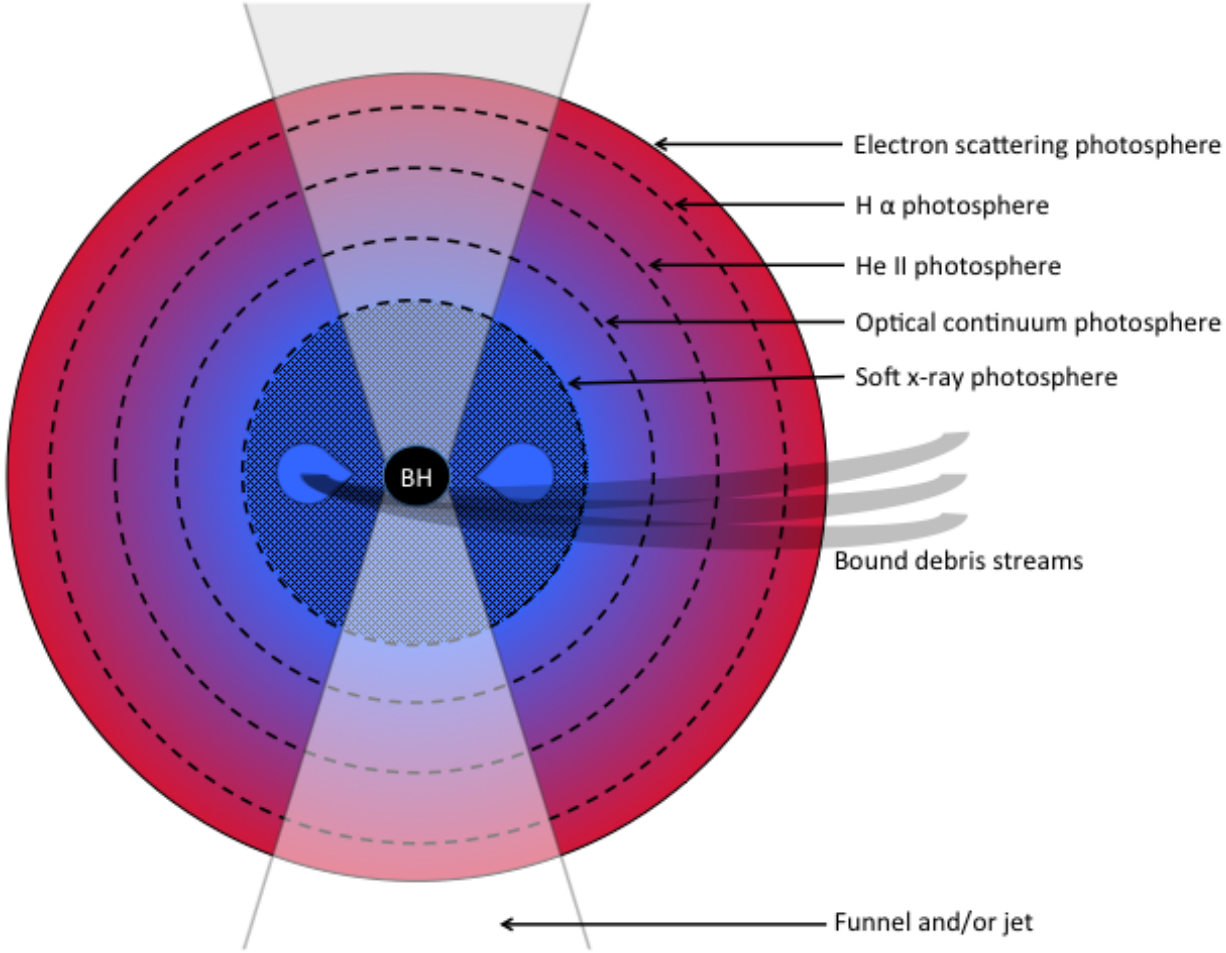

Figure 4.1: A schematic (not entirely to-scale) representation of a quasi-static TDE envelope, marking the *effective* photospheres at different wavelengths (beyond the effective photosphere, most photons will electron scatter their way out of the envelope without being re-absorbed). The soft x-ray photosphere lies deepest in, perhaps near the tidal disruption radius. The optical continuum photosphere lies farther out, followed by the He II λ4686 photosphere. The Hα photosphere lies farthest out, near to the Thomson photosphere. The larger visible volume of helium line emission results in a high He to H emission line ratio in the model TDE spectra. Although our calculations assume spherical symmetry, we have suggested the presence of possible viewing angle effects owing to the presence of a funnel or jet in the polar directions.

to the reprocessing.

In this section, we quantify the conditions in the envelope (density, temperature, and ionization state) and the effective optical depth to HeII photoionization. We then estimate the fraction of light reprocessed into the optical and its dependence on envelope parameters. The results, while approximate, will be useful in interpreting the detailed numerical spectral calculations that follow.

4.3.1 Envelope Density Structure and Optical Depth

We invoke the presence of a reprocessing envelope surrounding the source, and remain agnostic about its origin. For simplicity, we assume the envelope is spherically symmetric and quasi-static; in reality, global asymmetries and velocity gradients will complicate the picture, and are issues to be addressed in future work.

We model the envelope with a power-law density profile, $\rho(r) \propto r^{-p}$, extending from an inner radius, $r_{\rm in}$, to an outer radius, $r_{\rm out}$. An exponent $p = 3$ applies to a radiation pressure-supported envelope (Loeb & Ulmer 1997), while $p = 2$ for a steady state wind outflow (or inflow). The hydrodynamic solutions of Coughlin & Begelman (2014) find intermediate values of $p = 1.5$ to 3. In this work, we adopt $p = 2$, in which case the density profile is

$$\rho(r) = \frac{M_{\rm env}}{4\pi r_{\rm in}^2 (r_{\rm out} - r_{\rm in})} \left(\frac{r}{r_{\rm in}}\right)^{-2}. \tag{4.12}$$

The envelope mass, $M_{\rm env}$ is at most the total mass of the originally bound stellar debris (generally $\lesssim 0.5\ M_\odot$) and for a quasi-static envelope will likely change over time as material falls back, accretes or is launched in an outflow. If the density profile of Equation (4.12) is interpreted a steady wind, the corresponding mass loss rate is $\dot{M} = M_{\rm env}(v_{\rm w}/r_{\rm out})$ where $v_{\rm w}$ is the wind speed.

For quasi-static envelopes, we expect $r_{\rm out}$ to be set by the radiation pressure support, with typical values $r_{\rm out} \sim 10^{15}$ cm (Loeb & Ulmer 1997; Coughlin & Begelman 2014; Guillochon et al. 2014). For a radiatively launched outflow, $r_{\rm out}$ will be set by the extent of the expanding gas at any given time. Gas expanding at $v_{\rm w} = 10,000$ km s^{-1} for 20 days will have reached a similar radius, $r_{\rm out} \approx 10^{15}$ cm. Scaling to characteristic values, the density at the base of the envelope, $r_{\rm in}$, is

$$\rho_{\rm in} \approx \frac{8 \times 10^{-12}}{(1 - r_{\rm in}/r_{\rm out})}\ M_{\rm e,0.5} r_{\rm i,14}^{-2} r_{\rm o,15}^{-1}\ {\rm g\ cm^{-3}} \tag{4.13}$$

where $M_{\rm e,0.5} = M_{\rm env}/0.5\ M_\odot$, $r_{\rm i,14} = r_{\rm in}/10^{14}$ cm, and $r_{\rm o,15} = r_{\rm out}/10^{15}$ cm. For solar composition, the mean particle mass is $\mu \simeq 1.3 m_{\rm p}$ and the number density at the base is $n_{\rm in} = \rho_{\rm in}/\mu \approx 4 \times 10^{12}$ cm^{-3}.

For fully ionized gas of solar composition, the dominate continuum opacity is electron scattering with an opacity $\kappa = 0.32$ cm^2 g^{-1}. The optical depth through the envelope is then

$$\tau_{\rm es} = \frac{\kappa M_{\rm env}}{4\pi r_{\rm in} r_{\rm out}} \approx 270\ M_{\rm e,0.5} r_{\rm i,14}^{-1} r_{\rm o,15}^{-1}. \tag{4.14}$$

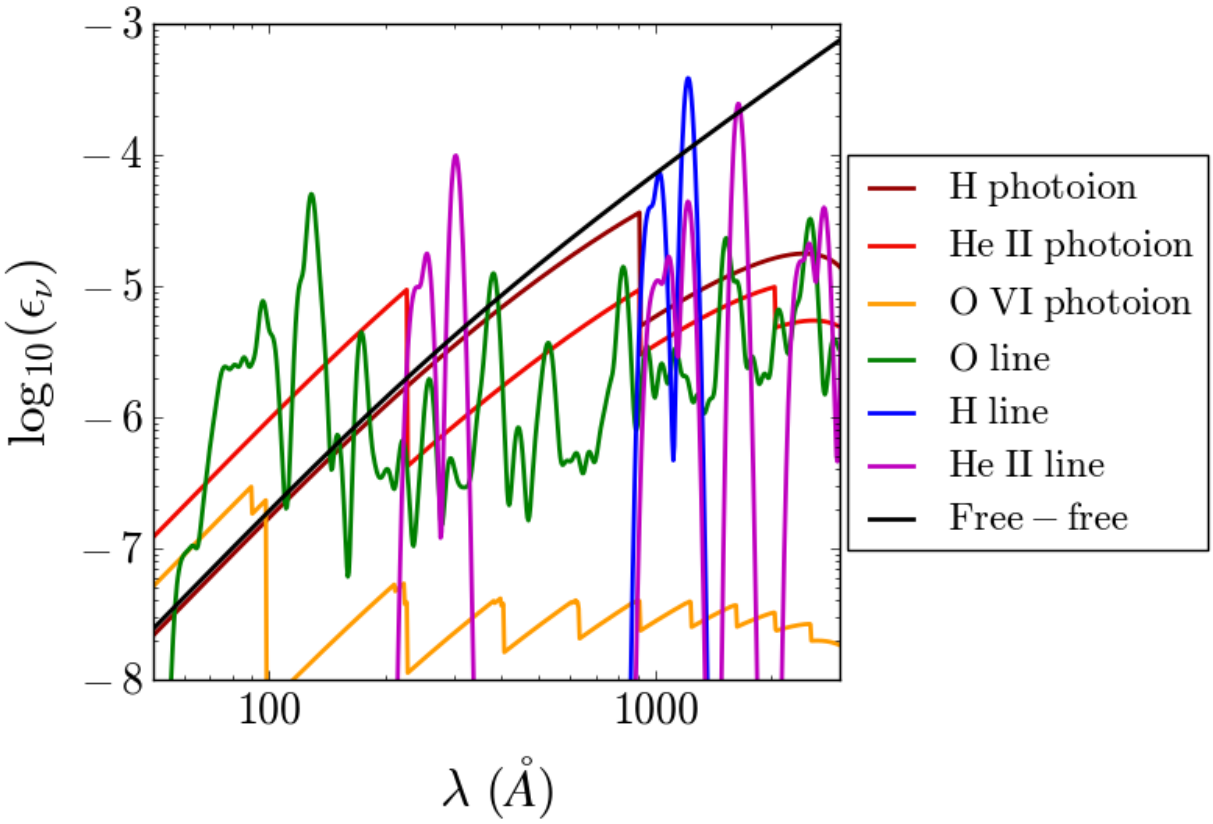

Figure 4.2: The ratio of various absorptive opacities at soft x-ray and UV wavelengths to that of electron scattering, computed near the inner boundary of a TDE envelope. The values are from the non-LTE radiation transport calculation of Section 4.4 with $M_{\rm env} = 0.5 M_\odot$, $r_{\rm in} = 10^{14}$ cm, $r_{\rm out} = 10^{15}$ cm, and $L = 10^{45}$ ergs s^{-1}. At soft x-ray wavelengths near 100 Å, photoionization of He II is a dominant absorptive process. Oxygen lines also contribute, while oxygen photoionization is negligible. The photoionization opacities begin to dip at long wavelengths due to stimulated recombination.

The envelope is highly scattering dominated, with the ratio of absorptive opacity to total opacity $\epsilon \lesssim 10^{-4}$ at x-ray/UV wavelengths (see Figure 4.2). The reprocessing of radiation to optical wavelengths is accomplished via absorptive processes (e.g., HeII photoionization), not electron scattering. However, the large scattering opacity traps photons and increases the probability that they will be absorbed. It thus has a critical effect on the formation of the optical continuum and emission lines.

The radiation diffusion time through the envelope is $t_{\rm diff} \sim \bar{r}^2 \kappa \bar{\rho}/c$ where $\bar{\rho}$ is an appropriately weighted envelope density and $\bar{r}$ a characteristic envelope length scale. Taking $\bar{\rho} = \rho(\bar{r})$ gives $t_{\rm diff} \sim 10\ M_{\rm e,0.5} r_{\rm i,14}^{-1}$ days, which is similar to the diffusion time we find in our direct numerical transport calculations of Section 4.4. For the TDE envelopes we consider here at times $t \approx$ weeks since disruption (near the peak of the light curve), $t_{\rm diff} \lesssim t$ and we can assume steady state transport above the inner boundary. However, at earlier times on the light curve rise, or for very dense envelopes, the diffusion timescale may be important in setting the emergent luminosity.

4.3.2 Envelope Temperature Structure

We assume that above our inner boundary, energy is primarily transported by radiation diffusion and there is negligible energy input from other processes such as viscosity or shocks. The temperature structure of the envelope is then set by radiative heating and cooling. Given the high electron scattering optical depth, we apply the spherical steady-state diffusion approximation to determine the frequency integrated radiation energy density, $E_{\rm rad}(r)$,

$$\frac{dE_{\rm rad}(r)}{dr} = -\frac{3\kappa\rho(r)}{4\pi c r^2} L \tag{4.15}$$

where c is the speed of light and L is the bolometric luminosity of the central source. The solution of Equation (4.15), using the density profile from Equation (4.12) and a constant electron-scattering opacity, is

$$E_{\rm rad}(r) = \frac{\tau_{\rm es} L}{4\pi c r_{\rm in}^2} \left[\frac{r_{\rm in}^3}{r^3} - \frac{r_{\rm in}^3}{r_{\rm out}^3} + \frac{4}{\tau_{\rm es}} \frac{r_{\rm in}^2}{r_{\rm out}^2} \right] \tag{4.16}$$

where we have taken as an outer boundary condition $E_{\rm rad}(r_{\rm out}) = a_{\rm rad} T_{\rm eff}^4$, where $a_{\rm rad}$ is the radiation constant, $T_{\rm eff} = [L/4\pi\sigma_{\rm sb} r_{\rm out}^2]^{1/4}$ and $\sigma_{\rm sb} \equiv c\, a_{\rm rad}/4$ is the Stefan-Boltzmann constant. Defining a radiation temperature by $T_{\rm rad} = (E_{\rm rad}/a_{\rm rad})^{1/4}$, we have in the limit $r_{\rm out} \gg r_{\rm in}$

$$T_{\rm rad}(r) = T_{\rm rad}(r_{\rm in}) \left[\frac{r_{\rm in}}{r} \right]^{3/4} \quad (r \ll r_{\rm out}), \tag{4.17}$$

where the interior temperature is

$$T_{\rm rad}(r_{\rm in}) = \left[\frac{\tau_{\rm es}}{4} \frac{L}{4\pi\sigma_{\rm sb} r_{\rm in}^2} \right]^{1/4}. \tag{4.18}$$

The temperature at the inner boundary is greater than that of a blackbody sphere emitting into vacuum by a factor of $(\tau_{\rm es}/4)^{1/4} \approx 3$. This is due to the back-heating of the source by photons trapped in the optically thick envelope. We estimate characteristic radiation temperature to be

$$T_{\rm rad}(r_{\rm in}) \approx 3.1 \times 10^5 \; L_{45}^{1/4} M_{\rm e,0.5}^{1/4} r_{\rm o,15}^{-1/4} r_{\rm i,14}^{-3/4} \; {\rm K} \; . \tag{4.19}$$

Note that the mass and size of the envelope directly affects the temperatures. For simplicity, we will usually set T_s, the blackbody temperature of our inner source, equal to $T_{\rm rad}(r_{\rm in})$. This may not hold in general; for example, the source luminosity may come from an accretion disk with radius smaller than the inner envelope edge, $r_{\rm in}$.

As defined, $T_{\rm rad}$ is simply a convenient rescaling of the local radiation energy density. However, we now show that $T_{\rm rad}$ may provide a good estimate of the gas temperature $T_{\rm gas}$. When the thermal state of the gas is determined primarily by radiative heating and cooling, the time-evolution of $T_{\rm gas}$ is

$$\frac{3}{2} n k_B \frac{dT_{\rm gas}}{dt} = -4\pi\alpha_S B(T_{\rm gas}) + 4\pi\alpha_E J, \tag{4.20}$$

where $J = cE_{\rm rad}/4\pi$ is the integrated mean specific intensity, $B(T_{\rm gas}) = \sigma_{\rm sb} T_{\rm gas}^4/\pi$ is the frequency-integrated Planck function, k_B is the Boltzmann constant, and α_E and α_S are mean absorptive extinction coefficients defined by

$$\alpha_E \equiv \frac{\int \alpha_\nu^{\rm abs}(\nu) E_\nu(\nu) d\nu}{E_{\rm rad}}, \qquad \alpha_S \equiv \frac{\int \alpha_\nu^{\rm abs}(\nu) B_\nu(\nu) d\nu}{B},$$

where $\alpha_\nu^{\rm abs}(\nu)$ is the absorptive extinction coefficient at each frequency, and $E_\nu(\nu)$ is the radiation energy density in the frequency interval between ν and $\nu + d\nu$.

Given sufficient time, the gas will reach a thermal equilibrium where radiative heating balances cooling. From Equation (4.20), the timescale, $t_{\rm heat}$, to heat gas from some lower temperature up to the equilibrium value is

$$t_{\rm heat} = \frac{3}{2} \frac{1}{c\,\alpha_E} \left[\frac{n k_B T_{\rm rad}}{a_{\rm rad} T_{\rm rad}^4} \right]. \tag{4.21}$$

The term in brackets is the ratio of gas to radiation energy density, and is $\ll 1$ for the conditions in TDE envelopes. The true absorption coefficient α_E is $\gtrsim 10^{-5}$ that of electron scattering (Figure 4.2) from which we find $t_{\rm heat}$ ranges from $\lesssim 1$ s at the base of the envelope up to $\sim$ hours at the outermost radii, which is comfortably smaller than the characteristic timescale of weeks for the evolution of observed TDE lightcurves. The gas temperature will then be able to reach a steady state, $dT_{\rm gas}/dt = 0$, and Equation (4.20) gives

$$T_{\rm gas} = (\alpha_E/\alpha_S)^{1/4} \; T_{\rm rad}. \tag{4.22}$$

Therefore, $T_{\rm gas}$ is close to $T_{\rm rad}$, with a correction factor related to the frequency dependence of $\alpha_\nu^{\rm abs}$ and the extent to which the radiation field spectrum differs from a blackbody. In our numerical calculations, we find that Equation (4.17) provides a good estimate of $T_{\rm gas}$ in the inner portions of the envelope, up to the continuum thermalization depth. Beyond that, $T_{\rm gas}$ plateaus at a higher value than $T_{\rm rad}$.

4.3.3 Envelope Ionization State

Photoionization of HeII provides one of the most important absorptive opacity at soft x-ray wavelengths (see Figure 4.2). If helium is primarily in the HeII state, the associated photoionization optical depth is $\gg 1$, and essentially all of the source x-rays will be absorbed and reprocessed to longer wavelengths. However, for high luminosity TDEs, the intense radiation field may completely ionize helium to HeIII, allowing only a small fraction of the source luminosity to be absorbed. Such an ionization effect has been explored in Metzger et al. (2014) and Metzger & Stone (2015). Determining the ionization state is therefore crucial for estimating the reprocessing efficiency of a TDE envelope.

To roughly estimate the critical luminosity, $L_{\rm ion}$, required to highly ionize the envelope, we use simple Stromgren sphere arguments. The rate at which ionized photons are produced by the central source is $\dot{Q} = L/\bar{E}_{\rm s}$ where $\bar{E}_{\rm s}$ is the average energy of source photons. The total recombination rate within a sphere of radius r is

$$\dot{R}(r) = \int_{r_{\rm in}}^{r} 4\pi r'^2 \alpha_{B,0} n_e(r') n_{\rm HeIII}(r') dr' \tag{4.23}$$

where $\alpha_{B,0} \approx 2 \times 10^{-13}$ cm^3 s^{-1} is the case B helium recombination coefficient at a temperature 10^5 K, n_e is the free electron density, and $n_{\rm HeIII}$ is the number density of HeIII. The condition $\dot{Q} = \dot{R}(r)$ allows us to solve for the Stromgren radius within which the helium is fully ionized

$$r_{\rm strom} = r_{\rm in}\left[1 - \frac{L}{4\pi A_{\rm He} n_{\rm in}^2 \alpha_{B,0} r_{\rm in}^3 \bar{E}_{\rm s}}\right]^{-1} \tag{4.24}$$

where $A_{\rm He} \approx 0.1$ is the number fraction of helium, and we have assumed n_e equals the ion number density, n, which is accurate to within 10% for the conditions that interest us. We see that the Stromgren radius of HeII diverges for luminosities above a critical luminosity $L_{\rm ion} = 4\pi\alpha_{B,0} A_{\rm He} n_{\rm in}^2 r_{\rm in}^3$ or

$$L_{\rm ion} \approx 3 \times 10^{44}\ M_{\rm e,0.5}^2 r_{\rm i,14}^{-1} r_{\rm o,15}^{-2} E_{50}\ {\rm ergs\ s^{-1}} \tag{4.25}$$

where $E_{50} = \bar{E}_{\rm s}/(50\ {\rm eV})$. A transition in the ionization state around this luminosity is confirmed by our numerical calculations in Section 4.4, and has a dramatic effect on the fraction of escaping x-ray photons.

Similar arguments could be applied to other elements that may contribute to absorption. However, the Stromgren estimates are ultimately limited by the fact that, in the true radiation transport, ionizing photons may be produced not only by the source, but also within the TDE envelope. In particular, radiation absorbed by helium will be largely re-emitted as photons capable of ionizing hydrogen. Indeed, our numerical calculations (Section 4.4) find that hydrogen remains fully ionized for luminosities less than the $L_{\rm ion}$ implied by Equation 4.25.

In the limit that helium is highly ionized ($L > L_{\rm ion}$), we can estimate the fraction of helium in the HeII state. Assuming that photoionization equilibrium holds at all radii, the number densities, $n_{\rm HeII}$ and $n_{\rm HeIII}$, of HeII and HeIII respectively are related by

$$n_{\rm HeII}\mathcal{I} = n_{\rm HeIII} n_e \alpha_{\rm B} \tag{4.26}$$

where $\mathcal{I}$ is the photoionization rate and the radiative recombination coefficient depends on temperature as $\alpha_B \propto T^{-1/2}$. Using the temperature structure Equation 4.17 gives

$$\alpha_B(r) \approx \alpha_{B,0} T_{\rm s,5}^{-1/2} \left[\frac{r}{r_{\rm in}}\right]^{3/8} \tag{4.27}$$

where $T_{\rm s,5} = T_{\rm s}/10^5$ K. For typical envelope densities, collisional ionization rates are small, while the recombination timescale, $t_{\rm rec} \sim 1/n_e\alpha_B \sim 1$ s, is short, validating the assumption of photoionization equilibrium. The photoionization rate is

$$\mathcal{I}(r) \equiv 4\pi \int_{\nu_{\rm ion}}^{\infty} \frac{\sigma_\nu^{\rm ion} J_\nu(r)}{h\nu} d\nu \tag{4.28}$$

where $\nu_{\rm ion}$ is the threshold frequency for HeII ionization, $J_\nu(r)$ is the mean specific intensity of the radiation field, and the photoionization cross-section $\sigma_\nu^{\rm ion}$ is given to good approximation (about 15% error because of neglect of Gaunt factors) for hydrogenic ions by

$$\sigma_\nu^{\rm ion}(\nu) = \sigma_0 \left(\frac{\nu}{\nu_{\rm ion}}\right)^{-3} \tag{4.29}$$

with $\sigma_0 \approx 1.5 \times 10^{-18}$ cm^2 for HeII. In the limit that only a small fraction of the source radiation is absorbed, the frequency dependence of J_ν will be a Planck distribution at the source temperature, $B_\nu(T_{\rm s})$. The radiation energy density, however, will be diluted according to the diffusion solution Equation (4.16), giving

$$J_\nu(r) = B_\nu(T_{\rm s}) \left[\frac{r_{\rm in}}{r}\right]^3 \tag{4.30}$$

which assumes $r_{\rm out} \gg r_{\rm in}$. The ionization rate is then

$$\mathcal{I}(r) = \frac{8\pi\nu_{\rm ion}^3 \sigma_0}{c^2} \left[\frac{r_{\rm in}}{r}\right]^3 \Omega(T_{\rm s}) \tag{4.31}$$

where the dimensionless factor Ω is

$$\Omega(T_{\rm s}) = \int_{\frac{h\nu_{\rm ion}}{k_B T_{\rm s}}}^{\infty} \frac{dx}{x(e^x - 1)} \approx 0.8 \left[\frac{k_B T_{\rm s}}{h\nu_{\rm ion}}\right] e^{-h\nu_{\rm ion}/k_B T_{\rm s}}. \tag{4.32}$$

The second expression approximates the integral to within a few percent over the range of temperatures of interest. The ionization equilibrium Equation (4.26) then determines the fractional ratio of HeII

$$f_{\rm HeII} = \frac{n_{\rm HeII}}{n_{\rm HeIII}} = \left[\frac{n_{\rm in}\alpha_{B,0}c^2}{8\pi\nu_{\rm ion}^3 \sigma_0 T_{\rm s,5}^{1/2} \Omega(T_{\rm s})}\right] \left[\frac{r}{r_{\rm in}}\right]^{11/8} \tag{4.33}$$

where we have again taken $n_e = n$. The fraction of HeII grows with radius, due both to the decrease of the ionizing radiation field and the increase of the recombination coefficient at larger radii. The HeII fraction at $r_{\rm in}$ is

$$f_{\rm HeII}(r_{\rm in}) = 6 \times 10^{-11} e^{\frac{6.31}{T_{\rm s,5}}} T_{\rm s,5}^{-3/2} M_{\rm e,0.5} r_{\rm i,14}^{-2} r_{\rm o,15}^{-1} \tag{4.34}$$

which shows that, for these fiducial parameters, most of the helium is in the fully ionized HeIII state. This predicted HeII fraction is very similar to what we find in our numerical transport calculations (Section 4.4) when $L \gg L_{\rm ion}$. The temperature dependence in Equation 4.34 resembles the LTE Saha equation expression, a consequence of the assumed Planckian frequency distribution of the radiation field. Near the inner boundary, where the radiation field approaches a true blackbody, the ionization state will approach its LTE value.

4.3.4 Reprocessed Luminosity

Having solved for the ionization state, we can calculate the optical depth to HeII photoionization

$$\tau_{\rm HeII}(\nu) = \int_{r_{\rm in}}^{r_{\rm out}} n_{\rm HeII}(r) \sigma_0 (\nu/\nu_{\rm ion})^{-3} dr. \tag{4.35}$$

Figure 4.2 makes it clear that other opacities (e.g., HeII and oxygen lines) also contribute to the opacity soft x-ray wavelengths; however, our analysis of the HeII photoionization provides some proxy for the more general radiative process.

When most of the helium is in the HeIII state (as indicated by Equation 4.34) we can write the number density of HeII as $n_{\rm HeII} = A_{\rm He} f_{\rm HeII} n$. For the temperature range of interest (2×10^5 K $< T_{\rm s} < 10^6$ K) we can more coarsely approximate Equation (4.32) as $\Omega \approx 6 \times 10^{-3} T_{\rm s,5}^2$. Using our ionization solution Equation (4.33) gives

$$\tau_{\rm HeII}(\nu) = \frac{A_{\rm He} n_{\rm in}^2 r_{\rm in} \alpha_{B,0} c^2}{3\pi \nu_0^3 T_{\rm s,5}^{1/2} \Omega(T_s)} \left[\frac{\nu}{\nu_{\rm ion}}\right]^{-3} \left[\left(\frac{r_{\rm out}}{r_{\rm in}}\right)^{3/8} - 1\right] \tag{4.36}$$

$$\approx 0.02 \; L_{45}^{-5/8} M_{\rm e,0.5}^{11/8} r_{\rm i,14}^{-3/2} r_{\rm o,15}^{-1} (\nu/\nu_{\rm ion})^{-3}. \tag{4.37}$$

The expected fraction of absorptive to electron scattering opacity at threshold is $A_{\rm He} f_{\rm HeII}(r_{\rm in}) \sigma_0 / \sigma_T \approx 2 \times 10^{-5}$ (where σ_T is the Thomson cross-section for electron scattering), in rough agreement with our numerical results (Figure 4.2).

In the radial direction, the envelope is optically thin to HeII photoionization. However, the electron scattering opacity increases the path length of photons as they random walk through the envelope, enhancing the probability of absorption. The typical number of scatters is $\tau_{\rm es}^2$, and so the effective optical depth for a photon to be absorbed is $\tau_{\rm r} = \sqrt{\tau_{\rm HeII} \tau_{\rm es}}$, or

$$\tau_{\rm r}(\nu) \approx 2 L_{45}^{-5/16} M_{\rm e,0.5}^{19/16} r_{\rm i,14}^{-5/4} r_{\rm o,15}^{-1} (\nu/\nu_{\rm ion})^{-3/2} \tag{4.38}$$

For frequencies near the HeII threshold, the envelope can thus absorb and re-emit a fraction of the source luminosity, L. As a simple estimate of the reprocessed luminosity, we assume that a fraction $e^{-\tau_{\rm r}}$ of the source luminosity is absorbed and re-emitted as a blackbody at an envelope temperature $T_{\rm r}$. The specific luminosity of reprocessed light is then

$$L_\nu(\nu) = e^{-\tau_{\rm r}} L \frac{B_\nu(T_{\rm r})}{\int_0^\infty B_\nu(T_{\rm r}) d\nu}. \tag{4.39}$$

If observations are taken at a frequency $\nu_{\rm opt} = 4000$ Å that is on the Rayleigh-Jeans tail of the blackbody ($h\nu_{\rm opt} \ll k_B T_{\rm r}$), and when $\tau_{\rm r} \ll 1$ the observed luminosity is

$$\nu_{\rm opt} L_\nu(\nu_{\rm opt}) = \nu_{\rm opt} \tau_{\rm r} L \left[\frac{2\pi \nu_{\rm opt}^2 k_B}{c^2 \sigma_{\rm sb} T_{\rm r}^3} \right] \tag{4.40}$$

$$\approx 1.1 \times 10^{43}\ L_{45}^{-1/16} M_{\rm e,0.5}^{7/16} r_{\rm i,14} r_{\rm o,15}^{-1/4}\ {\rm ergs\ s^{-1}}. \tag{4.41}$$

The normalization in the second expression depends on the assumed temperature $T_{\rm r}$ of the reprocessed radiation; the value in Equation 4.41 assumes is emitted a radius of $5r_{\rm in}$ where $T_{\rm r} \approx T_{\rm s}/3$.

Though approximate, our analytic treatment provides insight into how reprocessing takes place in highly ionized TDE envelopes. The reprocessed optical luminosity increases with $M_{\rm env}$, though sub-linearly. Having more mass in the envelope increases the effective absorptive optical depth, but there is also a counteracting effect; a higher $M_{\rm env}$ produces higher envelope and source temperatures, which increases the ionization state and shifts the reprocessed emission to shorter wavelengths.

In the highly ionized regime, the reprocessed optical luminosity depends very weakly on the source luminosity. This is because a higher L leads to higher ionization state, and hence a lower HeII effective optical depth; although the input radiation is brighter, a smaller fraction of it is absorbed and reprocessed. This behavior, however, only holds in the limit that a small fraction of the source x-rays are absorbed. When $L \lesssim L_{\rm ion}$, HeIII will recombine and a HeII ionization front will develop in the envelope. In this case, nearly all of the source photons with energies $\gtrsim 54.4$ eV are absorbed. The reprocessing becomes highly efficient and the optical luminosity will more closely track the input luminosity, in contrast to the weak dependence found in Equation (4.41).

The scalings in Equation (4.41) also do not reflect the likely correlation between the parameters. For example, both the envelope mass and bolometric luminosity may be decreasing at the light curve peak. In this situation, the bolometric luminosity and the reprocessed luminosity will track each other more closely than what Equation (4.41) predicts when L is varied on its own.

4.3.5 Optical Line and Continuum Formation

The soft x-rays absorbed by photoionization in the envelope can be re-emitted at longer wavelengths. In an optically thin medium (e.g., an HII region) absorbed photons are primarily re-emitted in lines. In TDE envelopes, in contrast, the medium can be effectively

optically thick in the continuum, and radiation will be reprocessed into both continuum and lines.

Figure 4.3 shows an example of the relevant opacities for TDE envelopes at optical wavelengths from a numerical calculation to be discussed in Section 4.4. The primary continuum opacity is free-free (bremsstrahlung), with some contribution from bound-free absorption from excited states of hydrogen and helium. The free-free absorption coefficient in the Rayleigh-Jeans limit ($h\nu \ll k_B T$) is

$$\alpha_{\rm ff} \approx 2 \times 10^{-2} n \; n_e T^{-3/2} g_{\rm ff} \nu^{-2} \tag{4.42}$$

where the free-free Gaunt factor, $g_{\rm ff}$, is of order unity. This can be compared to the electron scattering absorption coefficient $\alpha_{\rm es} = n_e \sigma_t$ to give the absorption ratio $\epsilon_{\rm ff} = \alpha_{\rm ff}/(\alpha_{\rm ff} + \alpha_{\rm es}) \approx \alpha_{\rm ff}/\alpha_{\rm es}$ of

$$\epsilon_{\rm ff} \approx 10^{-3} L_{45}^{-3/8} M_{\rm e,0.5}^{5/8} r_{\rm i,14}^{-7/8} r_{\rm o,15}^{-5/8} \left[\frac{\nu}{\nu_{\rm opt}}\right]^{-2} \tag{4.43}$$

which has only a weak dependence on radius. The radial optical depth to free-free is $\tau_{\rm ff} = \epsilon_{\rm ff} \tau_{\rm es} < 1$. However, the multiple electron scattering enhances the effective optical depth of free-free absorption. The continuum emission originates roughly from the thermalization depth to free-free absorption at an electron scattering optical depth of $\tau_{\rm therm} = 1/\sqrt{\epsilon} \approx 30$.

The opacity of some optical lines may also be effectively optically thick. The absorption coefficient for a bound-bound transition between and lower and upper level with number densities n_l and n_u is

$$\alpha_{\rm bb} = \left(\frac{\pi e^2}{m_e c}\right) n_l f_{\rm osc} \phi_\nu(\nu) \left[1 - \frac{g_l n_u}{g_u n_l}\right] \tag{4.44}$$

where $f_{\rm osc}$ is the oscillator strength and ϕ_ν the line profile function. The term in brackets is the correction for stimulated emission where g_l and g_u are the statistical weights. To estimate the extinction at the line center frequency, ν_0, we approximate $\phi(\nu_0) \approx 1/\Delta\nu$, where for a line Doppler broadened by a velocity v the line width $\Delta\nu = \nu_0(v/c)$. When the radiation field takes the form of a diluted blackbody (Equation 4.30), the relative level populations will approximate their LTE values, e.g., $n_u/n_l \approx (g_u/g_l) e^{-\Delta E_l/kT_{\rm s}}$. In the limit $h\nu_0 \ll kT_{\rm s}$, Equation 4.44 then becomes

$$\alpha_{\rm bb,0} \approx \left(\frac{\pi e^2}{m_e c}\right) n_l f_{\rm osc} \left[\frac{c}{v}\right] \frac{h}{k_B T_{\rm s}}. \tag{4.45}$$

The ratio $\epsilon_{\rm bb} = \alpha_{\rm bb}/\alpha_{\rm es}$ is then

$$\epsilon_{\rm bb} \approx 0.06 \frac{n_l}{10^{-10} n_{\rm in}} f_{\rm osc} v_9^{-1} T_{\rm s,5}^{-1} \tag{4.46}$$

where $v_9 = v/10^9$ cm s^{-1} and the density n_l is scaled by the expected ionization fraction of Equation 4.34. The Hα line emission thus originates from a region of electron scattering depth of $\tau_{\rm therm} = 1/\sqrt{\epsilon} \approx 6$. Due to the lower abundance of helium, $A_{\rm He} \approx 0.1$, the optical

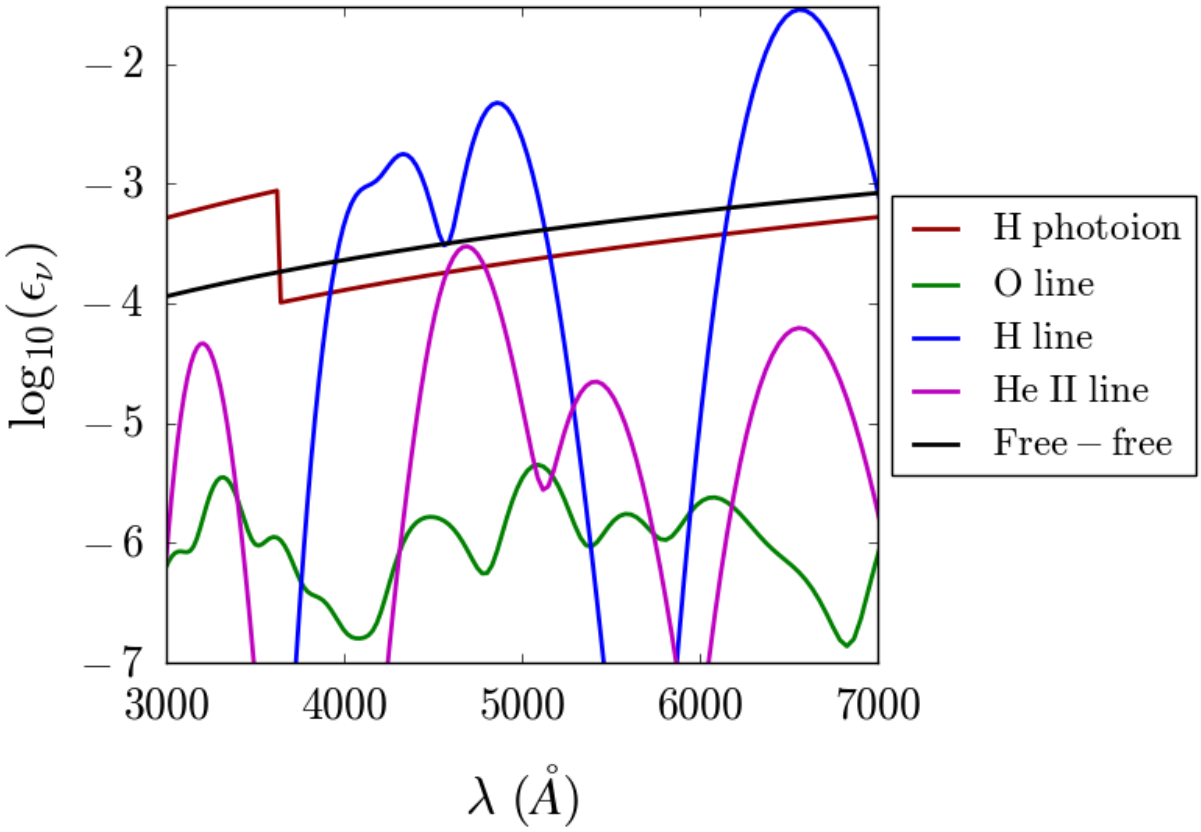

Figure 4.3: The ratio of various absorptive opacities at optical wavelengths to that of electron scattering, computed near the outer edge of a TDE envelope. The values are from the non-LTE radiation transport calculations of Section 4.4 with $M_{\rm env} = 0.5 M_\odot$, $r_{\rm in} = 10^{14}$ cm, $r_{\rm out} = 10^{15}$ cm, and $L = 10^{45}$ ergs s^{-1}. Free-free is the dominant continuum opacity at wavelengths longer than the Balmer break. Hydrogen Balmer series lines provide the highest opacities of all, with Hα being the most opaque. Oxygen lines provide negligible opacity.

depth of the HeII λ4686 line (all other things being roughly equal) should be smaller than Hα by a factor ~ 10, suggesting a larger thermalization depth $\tau_{\rm therm} \approx 20$. The values roughly agree with the numerical results of Figure 4.3.

These arguments motivate the physical picture illustrated in the schematic of Figure 4.1. In this quasi-static picture, spectrum formation resembles that of a stellar atmosphere, with the emission at different wavelengths originating from the source function at different thermalization depths. Soft x-rays are generated in the interior (at our inner boundary). The optical continuum forms further out, while the effective photospheres of strong lines of hydrogen and helium lie even nearer the surface. All of the observed emission is generated below the electron scattering photosphere.

4.4 Numerical Results

In this section, we present synthetic non-LTE spectra for TDE envelopes, discussing the physics of optical line and continuum formation and the dependence on envelope parameters. Details of the numerical method and radiative processes treated are given in the appendix. In all models, a luminosity L is emitted as a blackbody of temperature $T_{\rm s}$ at the absorbing inner boundary $r_{\rm in}$, and transported through the spherical envelope of mass $M_{\rm env}$ with a density structure $\rho(r) \propto r^{-2}$ extending from radii $r_{\rm in}$ to $r_{\rm out}$. In order to avoid an artificially abrupt truncation of the envelope, we allow the envelope extend beyond $r_{\rm out}$ following an r^{-10} density profile (we find that our results are not highly sensitive to the exact value of this power-law). We include opacities from hydrogen, helium, and oxygen, in solar abundances.

For the bound-bound transitions, we assume a Gaussian line profile with a Doppler velocity of 10^4 km s^{-1}. This velocity, which is motivated by the width of line features observed in TDE candidate spectra (e.g., Gezari et al. 2012; Arcavi et al. 2014), is much higher than the ion sound speed, but comparable to the virial velocity in TDE envelopes. Our setup thus resembles a quasi-static envelope with disordered velocities due to, e.g., turbulence or irregular motion driven by fallback streams, as seen in numerical simulations (Ramirez-Ruiz & Rosswog 2009; Guillochon et al. 2014). In envelopes with ordered bulk velocity due to, e.g., outflow or rotation, the line formation may differ from that discussed here. Future calculations will consider more general velocity structures, and include a more complete metal composition.

4.4.1 Spectral Energy Distributions

Figure 4.4 shows computed spectral energy distributions (SEDs) for two models with $M_{\rm env} = 0.25\ M_\odot$ and $L = 10^{45}$ ergs s^{-1} ($\approx L_{\rm Edd}$ of a $10^7\ M_\odot$ BH) but with two different values of the inner boundary radius. The dashed curves show the unprocessed blackbody spectrum from the inner boundary. We find that reprocessing of the source light by the TDE envelope enhances the optical luminosity by several orders of magnitude. The presence of the extended envelope is clearly required to approach the optical luminosity of $\sim 10^{43}$ ergs s^{-1}

observed in TDE candidates.

As suggested by our analytic estimates (Equation 4.38) for the chosen values of L and $M_{\rm env}$, most of the soft s-ray source emission is able to propagate through the envelope without being absorbed. Those photons that are absorbed are mostly used to photoionize HeII at wavelengths near 220 Å. For the $r_{\rm in} = 5 \times 10^{13}$ cm model, oxygen absorption at the shortest wavelengths also plays a role. The radiation absorbed by photoionization (though small) is re-emitted over a wide range of longer wavelengths and significantly enhances the optical flux. The simultaneous emission of both soft x-rays and optical light with an SED that does not follow a single blackbody bears a qualitative resemblance to PTF10iya, ASASSN-14li, and ASASSN-15oi (Cenko et al. 2012a; Holoien et al. 2016b; Miller et al. 2015; Cenko et al. 2016; Holoien et al. 2016a).

The reprocessed optical continuum in Figure 4.4 is relatively insensitive to the chosen inner radius, and follows a power law that superficially resembles the Rayleigh-Jeans tail of a blackbody. However, the emission is not that of a single blackbody; the thermalization depth varies with wavelength, and the continuum is the superposition of thermal emission from different temperature blackbodies at different radii. Due to this effect, the slope of our model continuum, $L_\lambda \propto \lambda^{-3}$, is somewhat shallower than that of a true Rayleigh Jeans tail, $L_\lambda \propto \lambda^{-4}$.

Given the non-blackbody nature of the emergent spectrum, the turn-over that one begins to see at bluer wavelengths cannot necessarily be extrapolated with a Planck function. This suggests caution when inferring a bolometric luminosity by fitting a single blackbody temperature to the optical continuum. In both models of Figure 4.4, the bolometric luminosity is 10^{45} erg s^{-1}, much larger than one might estimate based on fitting a single blackbody to the optical/UV data.

Figure 4.5 shows how the model SEDs depend on the envelope mass, $M_{\rm env}$. For this figure, $r_{\rm in} = 10^{14}$ cm and for clarity we held the temperature of the inner boundary emission fixed at 3.29×10^5 K (unlike the rest of the models we present in this work, we did not set $T_{\rm s}$ equal to $T(r_{\rm in})$ as given by Equation 4.18). As expected from our analytic arguments (Equation 4.41) the optical luminosity increases with $M_{\rm env}$ due to the greater degree reprocessing by higher mass envelopes. For the smallest envelope mass ($M_{\rm env} = 0.02\ M_\odot$) essentially none of the source luminosity is reprocessed, despite the fact that the gas is optically thick to electron scattering ($\tau_{\rm es} \approx 20$). The emphasizes that in scattering dominated TDE envelopes, an optical depth $\gg 1$ is required to thermalize and reprocess x-rays to optical wavelengths.

Figure 4.6 shows how the model SEDs depend on the source luminosity, L. Interestingly, the optical continuum luminosity remains largely unchanged even as L is varied by a factor of ~ 10 (again, holding the mass and size of the envelope fixed). This is consistent with the weak L dependence found in our analytic arguments (Equation 4.41) and reflects a self-regulating effect in the radiation transport. Higher L leads to a higher ionization state and higher envelope temperatures, which reduces the fraction of x-ray emission that is reprocessed to longer wavelengths.

A dramatic change in the spectra of Figure 4.6 is seen when the source luminosity is reduced to 2.5×10^{44} ergs s^{-1}. This is due to the formation of a HeII recombination front

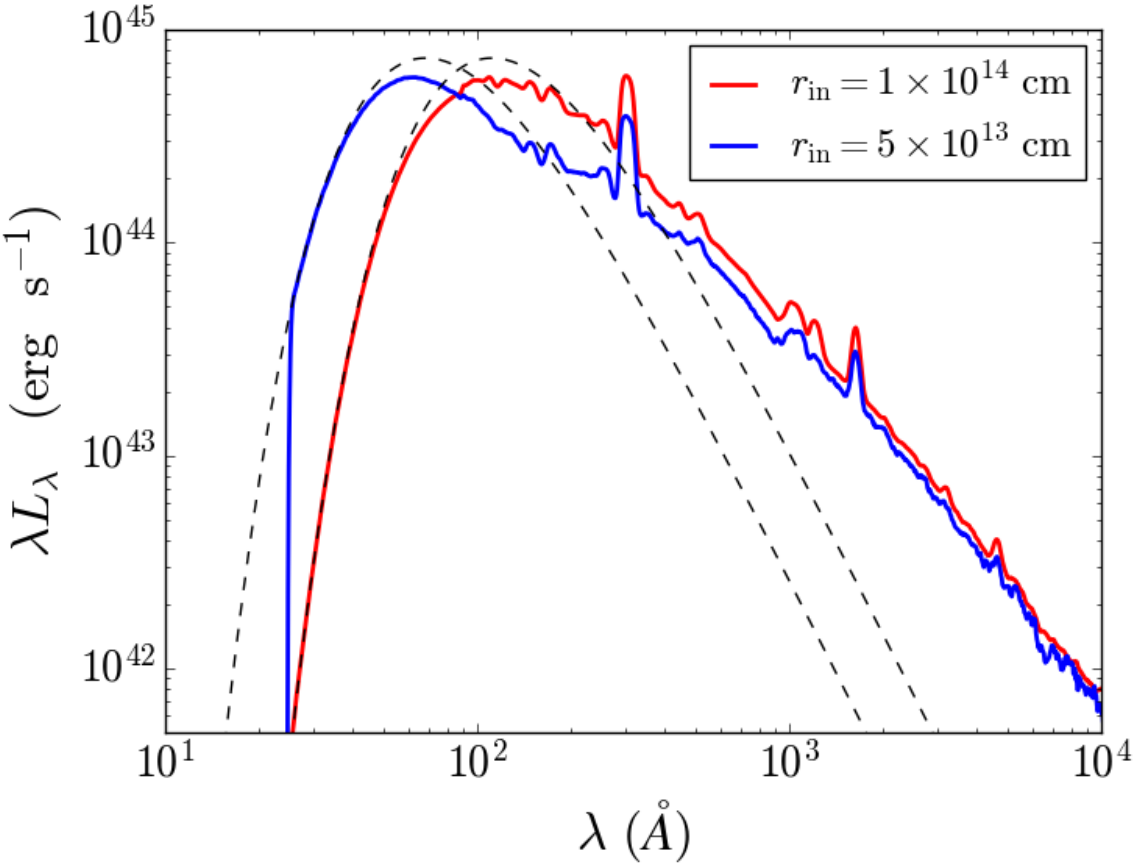

Figure 4.4: Model spectra for two calculations with different inner boundary conditions. The two dashed curves represent the input radiation fields at the inner boundaries, with temperatures set by Equation (4.18). In both cases, a fraction of the intrinsic spectrum is absorbed and re-radiated at UV and optical wavelengths; the colored curves show the SED of the radiation that escapes. In both calculations, $M_{\rm env} = 0.25\ M_\odot$, $r_{\rm out} = 5 \times 10^{14}$ cm (not including the $\rho \propto r^{-10}$ density tail), and $L = 10^{45}$ ergs s^{-1}. Changing $r_{\rm in}$ shifts the peak of the escaping x-ray emission, but leads to only small changes in the optical emission.

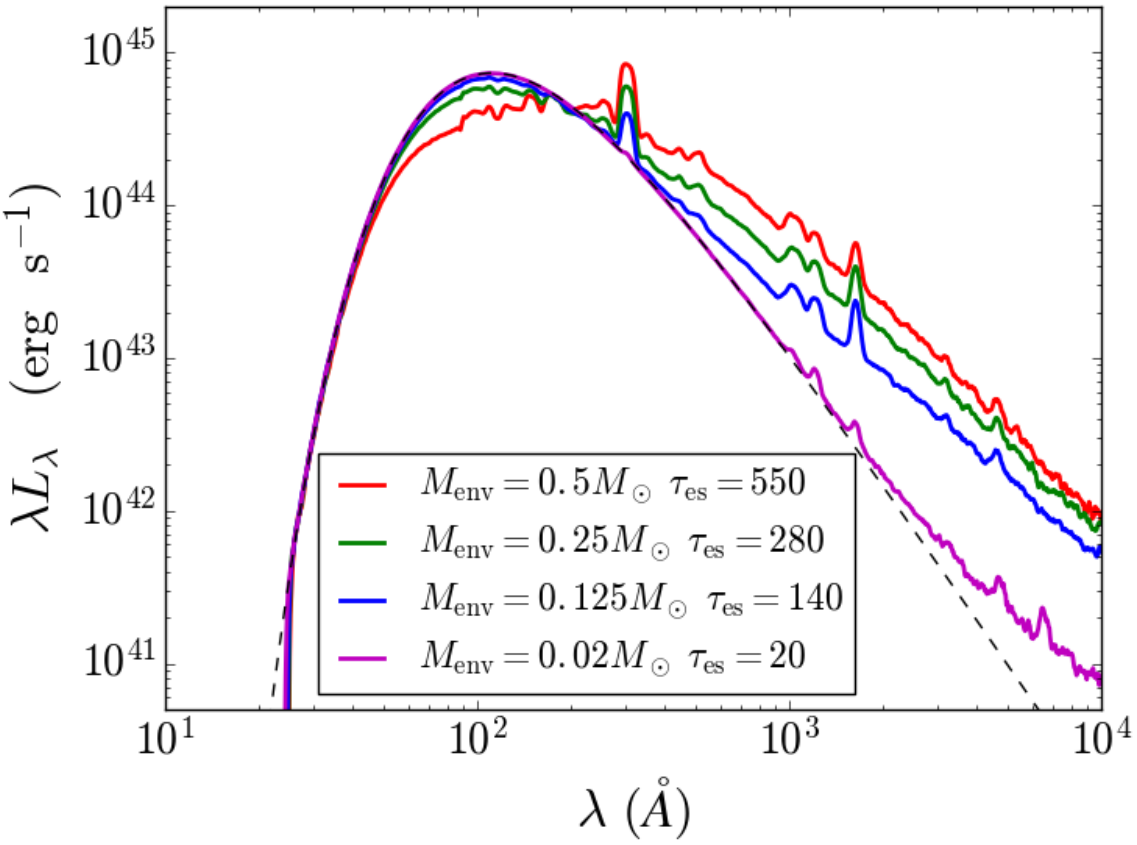

Figure 4.5: Model spectra for calculations with varying mass in the reprocessing envelope. In all models, $L = 10^{45}$ ergs s^{-1}, $r_{\rm in} = 10^{14}$ cm, $r_{\rm out} = 5 \times 10^{14}$ cm (not including the $\rho \propto r^{-10}$ density tail, which contributes negligible mass), and the inner boundary temperature is held fixed at 3.29×10^5 K. Varying $M_{\rm env}$ changes the amount of reprocessed optical emission in a manner similar to the prediction from Equation (4.41). Such behavior could represent the time-dependent depletion of the envelope depletion after peak light. This variation leaves the shape of the optical continuum mostly unchanged, at least until $M_{\rm env}$ drops so low that barely any radiation is reprocessed.

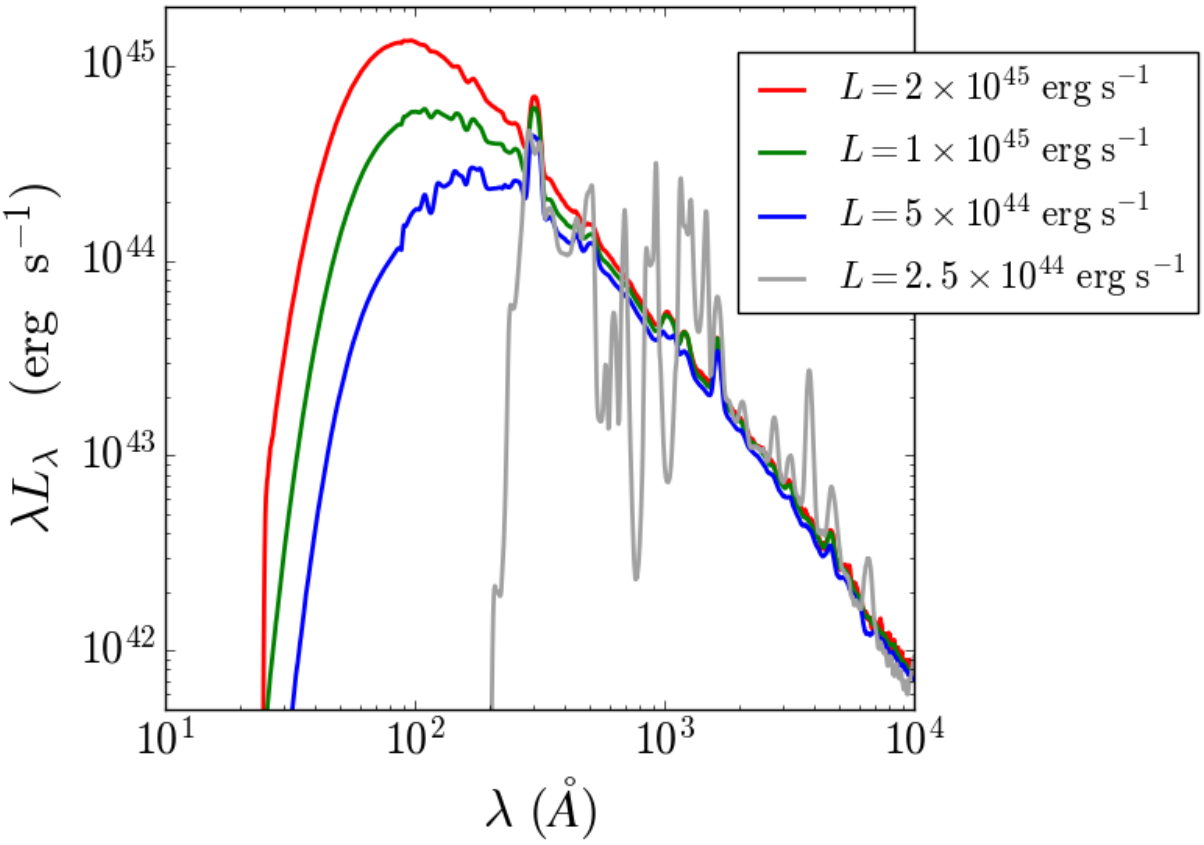

Figure 4.6: Model spectra for calculations with varying bolometric luminosity. In all models, $M_{\rm env} = 0.25 M_\odot$, $r_{\rm in} = 10^{14}$ cm and $r_{\rm out} = 5 \times 10^{14}$ cm (not including the $\rho \propto r^-10$ density tail). Varying the bolometric luminosity alone has only a minor effect on the emitted optical flux, as predicted in Equation (4.41). The pattern changes when the luminosity drops low enough that a helium recombination front begins to form at $L \lesssim 3 \times 10^{44}$ ergs s^{-1}.

that absorbs essentially all radiation at wavelengths below the photoionization threshold ($\lesssim 220$ Å). This transition occurs roughly near the critical luminosity estimated by Strom-gren arguments in Equation (4.25). For these lower luminosities, nearly all of the radiation emerges at UV/optical wavelengths, with essentially no flux escaping in x-ray bands. In this regime, the UV/optical luminosity will track the source luminosity, in contrast to the weak L dependence found in the fully-ionized regime.

4.4.2 Spectral Line Features

The spectra of Figures 4.4–4.6 show a number of line features superimposed on the continuum. In the soft x-ray/UV bands, the strongest lines are those of the He II Lyman series at wavelengths between 200 and 400 Å. Other UV lines from highly ionized species might appear if more metals had been included in our calculations. In the optical bands, lines of hydrogen (the Balmer series) and HeII (the 4686 Å and 3203 Å lines) may be visible. We find that the line corresponding to the n = 7 to n = 4 transition in He II with wavelength 5412 Å (a Pickering series line, analogous to Brackett γ in H) appears for some of our models. Finally, we note that the He II Pickering line at 6560 Å has a small contribution to emission and opacity near Hα , as pointed out in Gaskell & Rojas Lobos (2014).

The relative strength of the optical hydrogen and helium lines has generated particular interest in the literature, as this bears on the gas composition and hence the nature of the disrupted star. Figure 4.7 shows the optical spectra for three models with $L = 10^{45}$ ergs s^{-1}, $M_{\rm env} = 0.25\ M_\odot$, but different values for the outer radius of the envelope, $r_{\rm out}$. In all cases, the emission in the HeII λ4686 line exceeds that of Hα, despite the gas having solar composition. As $r_{\rm out}$ is decreased, the Hα emission decreases with respect to the continuum. The line ratios can be seen more clearly in Figure 4.8, in which we have subtracted off a power-law to approximate the underlying continuum. The hydrogen-to-helium line ratios are roughly 3:1 and 5:1 for $r_{\rm out}$ of 2×10^{15} and 1×10^{15}, respectively. For $r_{\rm out} = 5 \times 10^{14}$, the H$\alpha$ feature has transitioned into a shallow absorption.

Our calculations thus lend further support to the interpretation that the absence of a conspicuous Hα feature – as observed in PS1-10jh and PTF-09ge – is consistent with the disruption of a main-sequence star of solar composition, as suggested by Guillochon et al. (2014). In general, TDE envelopes can produce a range of Hα equivalent widths and hydrogen-to-helium line ratios, depending on the gas configuration and bolometric luminosity. Such a variation might help to explain the diversity of hydrogen-to-helium line ratios seen in observed TDE candidates (Arcavi et al. 2014).

For lower luminosities ($L < L_{\rm ion}$) recombination fronts of helium, and eventually hydrogen form in the envelope. The recombination fronts are generally accompanied by an increase in the strength of spectral features (see Figure 4.6), including lines of hydrogen, helium, and oxygen. A more featureless spectrum is more easily obtained when the ionization is high, which for lower luminosities ($L \lesssim 10^{44}$ ergs s^{-1}) may require a correspondingly smaller envelope mass or a larger outer radius.

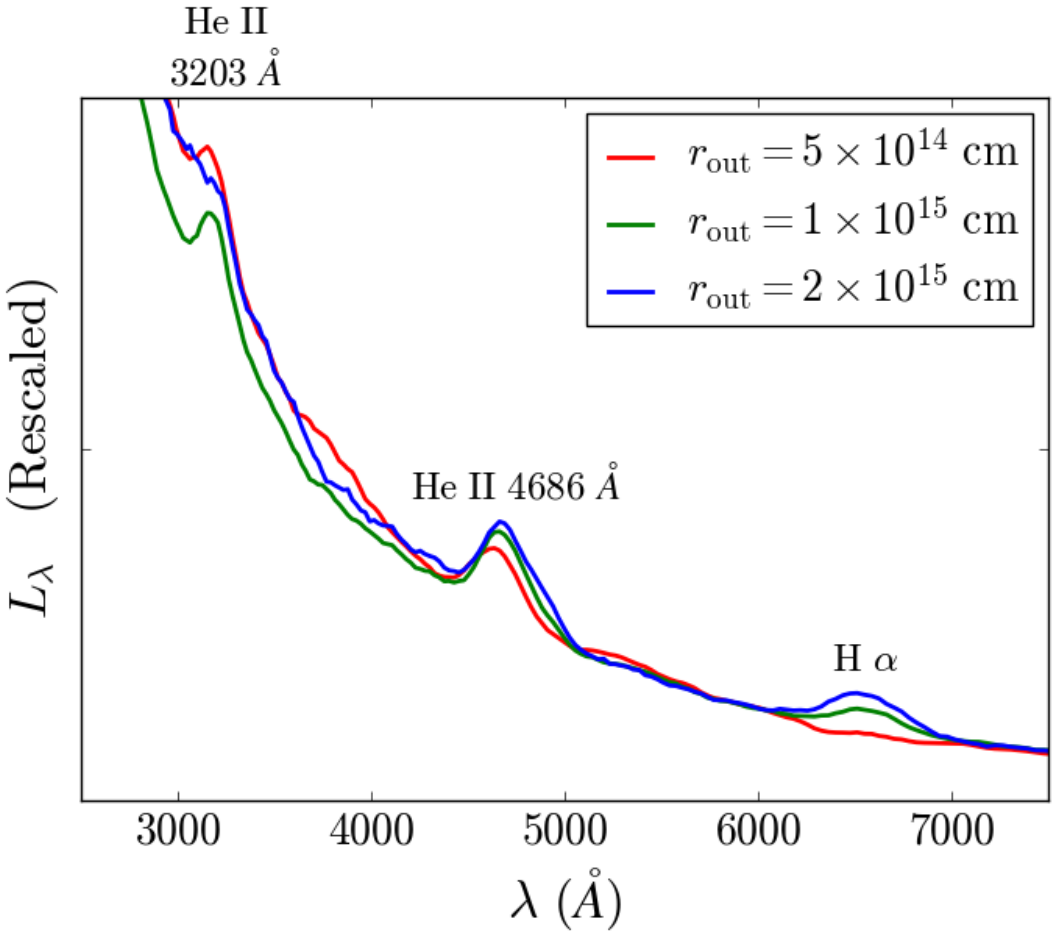

Figure 4.7: Optical spectra for three calculations with varying outer radii for the reprocessing envelope. All models have $M_{env} = 0.25\ M_\odot$, $r_{in} = 10^{14}$ cm, and $L = 10^{45}$ ergs s^{-1}. The flux units have been rescaled so that the continua of all three calculations overlap at 6000 . Two emission lines of HeII are visible at 3203 Å and 4686 Å. The Hα equivalent width decreases as the envelope is made more compact. All calculations used 1600 logarithmically spaced wavelength bins between 10 and 10^5 . In order to suppress the Monte Carlo noise, we have smoothed the data here to an effective resolution of 400 bins. N.B., the indicated outer radius does not include the $\rho \propto r^{-10}$ tail.

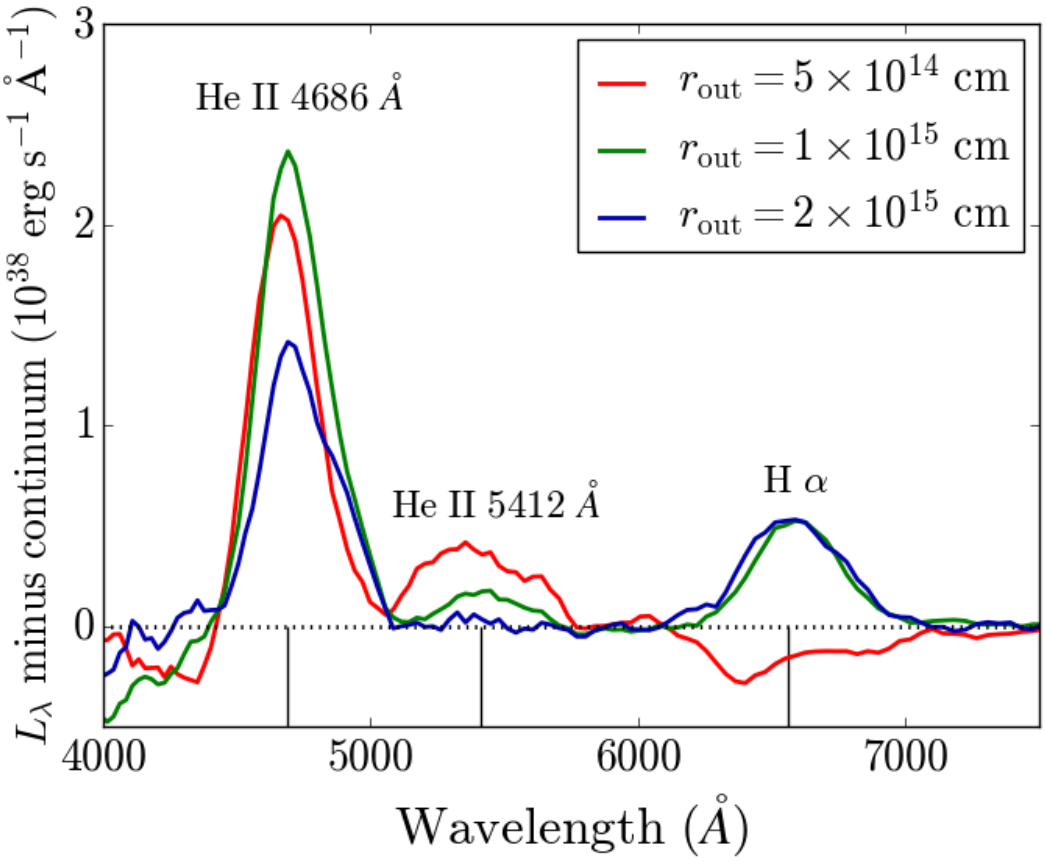

Figure 4.8: Continuum-subtracted spectra for the same three calculations shown in Figure 4.7. We have subtracted off a power-law continuum to facilitate comparison of the line strengths. The helium-to-hydrogen line ratio is approximately 3:1 for the calculation with $r_{\rm out} = 2 \times 10^{15}$ cm, and is 5:1 for the calculation with $r_{\rm out} = 1 \times 10^{15}$ cm. For the calculation with $r_{\rm out} = 5 \times 10^{14}$ cm, Hα has transitioned to a shallow absorption feature. The vertical black lines at the bottom of the plot indicate the line-center wavelengths of the three labeled spectral features.

4.4.3 Understanding the Line Ratios

The low Hα to HeII line emission found in our models differs from previous photoionization studies using the CLOUDY code (Strubbe & Murray 2015; Gaskell & Rojas Lobos 2014). This is due to our inclusion of optically thick radiation transport effects. The previous CLOUDY calculations assumed that all line photons produced within some photoionized volume escape to be observed. In a realistic TDE envelope, however, emitted line photons random walk through multiple electron scatters and are subject to re-absorption either in the line itself, or by continuum processes.

As we have noted earlier, an observer will primarily see radiation at a given wavelength emitted from the volume where the electron scattering optical depth (integrated from the outside in) is less than the thermalization depth $\tau_{\rm therm} = 1/\sqrt{\epsilon}$ for that wavelength. Since this is only an estimate, there is some flexibility in the definition of $\tau_{\rm therm}$, especially because ϵ varies with radius, along with the wavelength variation displayed in Figure 4.3. Once we have a thermalization depth, we can estimate the observed specific luminosity at any given wavelength by integrating the emissivity, j_λ, outside of the thermalization depth:

$$L_\lambda \approx \int_{r_{\rm therm}}^{\infty} 4\pi j_\lambda (4\pi r^2) dr. \tag{4.47}$$

The emissivity in Equation (4.47) is a sum over both line and continuum processes, but not electron scattering.

Note that photons absorbed in a line have some probability of either being line-scattered (re-emitted in the same bound-bound transition), or destroyed via multiple mechanisms (e.g. the atom de-exciting through a different line transition, being collisionally de-excited, being photoionized, or being radiatively excited to another bound electron level). The line contribution to the emissivity j_λ in Equation (4.47) accounts for all of these possibilities; it depends on the level populations of the bound electrons, which is in turn governed by balancing the transition rates between all bound levels and the continuum (see Appendix).

Figure 4.9 applies this estimate of L_λ to the calculation corresponding to the red curve in Figure 4.8 (with $r_{\rm out} = 5 \times 10^{14}$ cm). We plot the integrated emissivity (Equation (4.47)) at the wavelengths corresponding to Hα and He II λ4686.

For each wavelength, we have separated the contributions from continuuum processes (the solid curves) and from lines (the dashed curves). We have indicated the approximate location of the thermalization depth, including contributions from both line and continuum opacity, with vertical dash-dotted lines. Meanwhile, thermalization depths that account for only continuum opacities are indicated with solid vertical lines. To compute the thermalization depths, we have evaluated ϵ at $r_{\rm out}$, in this case 5×10^{14} cm. By summing the contributions of the integrated emissivity for both the lines and the continuum processes at the thermalization depth, we obtain an estimate for the luminosity observed at each wavelength. These estimates are represented by the points plotted on top of the dash-dotted vertical lines. For reference, we have also estimated the emission from the continuum alone at these wavelengths by evaluating the integrated continuum-only emissivity at the continuum-only

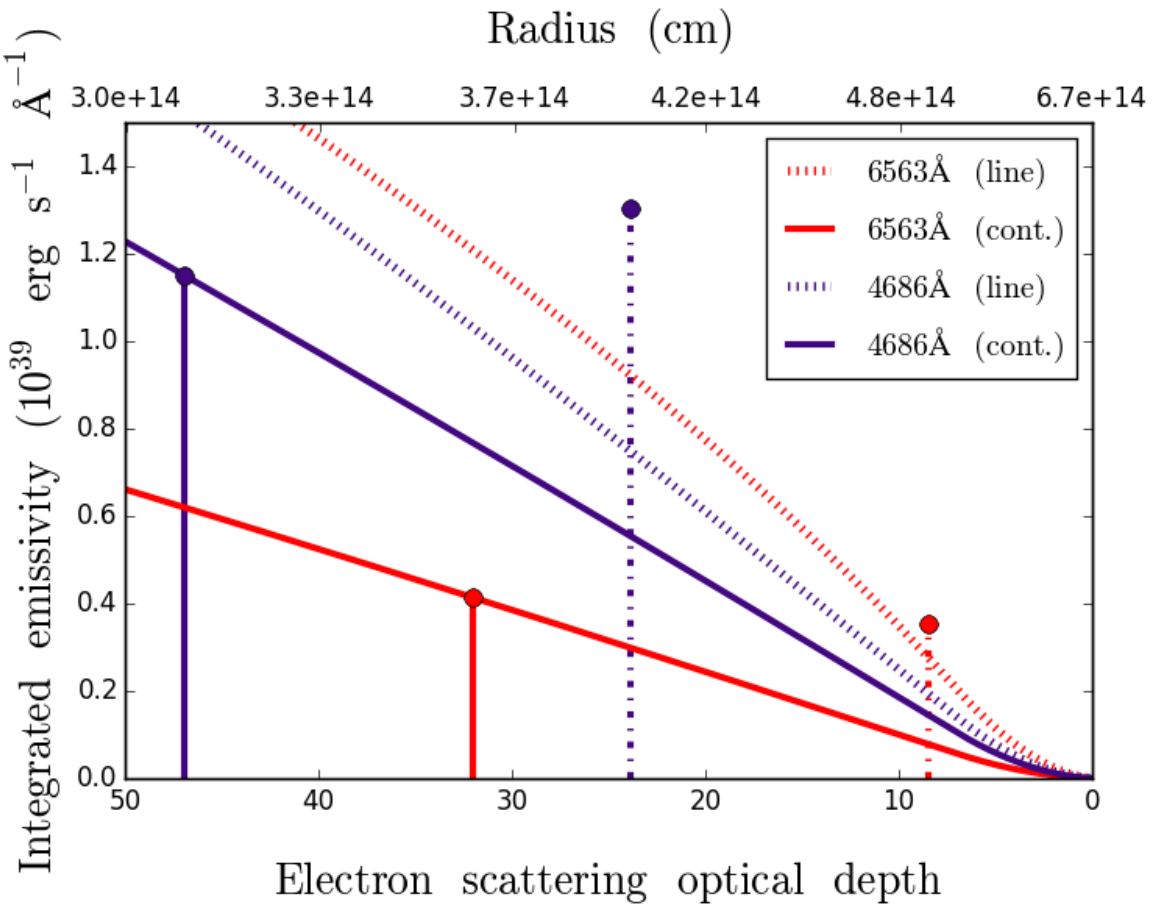

Figure 4.9: Volume-integrated emissivity as a function of optical depth. The integrated emissivity is that expressed in equation (4.47). The vertical lines represent the approximate thermalization depths at the indicated wavelength, either accounting for both line and continuum opacities (the dash-dotted vertical lines), or only the continuum opacities (the solid vertical lines). The plotted points represent the emission as estimated by the integrated emissivity down to the the thermalization depth, either accounting for emission from both line and continuum processes (the points on top of the dash-dotted vertical lines), or from the continuum alone (the points on top of the solid vertical lines). The line-plus-continuum emission at the Hα wavelength lies very close to the emission from the continuum on its own. In contrast, the line-plus-continuum emission at 4686 lies above the emission from the continuum on its own at that wavelength.

thermalization depth. These reference luminosities are plotted as points on top of the solid vertical lines.

As suggested by our analytic arguments (Section 4.3), the thermalization depth at the Hα wavelength (the red dash-dotted vertical line) lies within several electron scattering mean free paths from the Thomson photosphere, while HeII λ4686 has a thermalization depth several times deeper (the purple dash-dotted line). The thermalization depths of the continuum alone at optical wavelengths are deeper still (the solid vertical lines). Even though the Hα emissivity is greater at each radius than the emissivity in the HeII line, the self-absorption of line photons reduces the effective emitting volume. The end result is that the total emission at the Hα wavelength lies very close to the emission from the continuum alone at that wavelength. In contrast, the total emission at 4686 lies above the emission from the continuum alone at that wavelength.

The method described above provides insight into the relative strengths of the line and continuum emission at each wavelength, once the envelope ionization state and bound electron level populations are known. More accurate values for the emission are provided directly from the Monte Carlo radiative transfer, which is why the estimates for the emission in Figure 4.9 differ slightly from what is shown in Figure 4.8.

Figure 4.9 makes it clear that the emergent Hα feature is sensitive to the particular model parameters, which set the exact location of $r_{\rm therm}$ and the line emissivity above it. For different envelope configurations, the Hα line will therefore show different levels of emission, as we found in our synthetic spectra (Figure 4.7). For TDEs from massive BHs and near peak brightness, however, we typically expect a situation similar to that of Figure 4.9, where the Hα emission is suppressed relative to that of HeII.

4.5 Implications for Observations and Models of TDEs

In many ways, our synthetic spectra resemble those of observed TDE candidates, such as PS1-10jh, near maximum light. In particular, the spectrum is largely featureless and blue, with two emission lines of HeII and a weak or absent Hα feature. In detail, however, some discrepancies are apparent. Our model continua slopes are somewhat shallower, $L_\lambda \propto \lambda^{-3}$, than the Rayleigh-Jeans tail, $L_\lambda \propto \lambda^{-4}$, seen in PS1-10jh (Gezari et al. 2012). Nevertheless, our slope is consistent with HST UV data for ASASSN-14li (Cenko et al. 2016), as well as the spectral indices measured in TDE1/TDE2 (van Velzen et al. 2011), in the absence of strong dust extinction.

Our optical luminosity for a massive envelope ($M_{\rm env} = 0.5\ M_\odot$) tops out at $\approx 10^{43}$ ergs s^{-1}, which is a factor of ≈ 2 less than some observed TDEs. This may in part be due to our incomplete inclusion of metals, which may result in an underestimate of the net reprocessing efficiency. The efficiency could also be enhanced if the gas is confined to e.g., a shell or disk, which would increase the density. The radiation from an aspherical envelope will also be anisotropic, with the observed luminosity brighter from viewing angles that maximize the projected surface area.

Observations of ASASSN-14li showed simultaneous x-ray, UV, and optical emission (Holoien et al. 2016b; Miller et al. 2015; Cenko et al. 2016). The SED cannot be fit by a single blackbody, but appears consistent with the superposition of different temperature blackbodies for the x-rays and optical/UV. Such an SED resembles our highly ionized reprocessing envelopes (e.g., Figure 4.4) for which thermal x-rays characteristic of the hot inner accretion regions are only partially reprocessed to optical radiation characteristic of the lower envelope temperatures, resulting in a multi-blackbody SED.

Our calculations have focused on radiation transport in generic TDE envelopes, remaining largely agnostic about the origin of the envelope. The mechanism for forming an extended gas distribution is unclear, and several classes of explanations have been suggested. The insights from our radiative transfer studies can be applied (within limit) to illuminate the possible observable properties of various scenarios.

4.5.1 Quasi-static Envelopes

Loeb & Ulmer (1997) predicted that TDEs could form an optically thick, roughly spherical, radiation pressure supported envelope with radius $r_{\rm out} \sim 10^{15}$ cm. The stability of such an envelope depends on the luminosity being regulated to be near $L_{\rm Edd}$ (Ulmer et al. 1998). Analytic studies by Coughlin & Begelman (2014) suggest that even if the accretion rate is super-Eddington, the flow can equilibrate in a quasi-stable configuration by allowing energy to escape in a narrowly confined jet. The earliest three-dimensional hydrodynamic simulations of TDEs that followed the event past the initial disruption and into the accretion phase, such as Ayal et al. (2000) and Bogdanović et al. (2004), provided some evidence for the build-up of material at large radii that could reprocess accretion luminosity. More recent calculations such as Guillochon et al. (2014) (see also Ramirez-Ruiz & Rosswog 2009; Rosswog et al. 2009) show the development of an extended gas distribution around the eventual accretion disk, which is produced as shock-heated material is lifted above and below the original orbital plane of the disrupted star's orbit; (such calculations, however, have not followed the longer term radiative evolution of this debris).

Our model calculations provide a fair representation of the radiative transfer in such quasi-static envelopes, and suggest that such a scenario (with a solar composition envelope of mass $M_{\rm env} \approx 0.1 - 0.5\ M_\odot$) can likely reproduce the maximum light spectra of observed optical TDEs like PS1-10jh. More specific model calculations are warranted; the power law exponent of the envelope density structure may differ from our choice $\rho \propto r^{-2}$ (for a static radiation pressure-supported envelope, $\rho \propto r^{-3}$ as in Loeb & Ulmer (1997)) and the velocity dispersion may be due in part to rotational or circulatory motion, not the random motion adopted in our calculations.

The properties of a quasi-static envelope can be expected to vary over time. Initially, over the timescale for the most-bound debris to fall back to the BH ($t_{\rm fb} \approx 25[M_{\rm BH}/10^7\ M_\odot]^{1/2}$ days for the disruption of a solar mass star), the envelope mass may increase. For highly-ionized envelopes, a larger $M_{\rm env}$ leads to more efficient reprocessing (see Figure 4.5). The initial rise of the optical TDE light curves could therefore reflect the gradual accumulation of mass in an

envelope. The decline of the light curve with roughly constant color could likewise reflect the draining of the envelope. Such an evolution is hinted at by observations of PS1-10jh, which appears to have a photosphere that first grows and later recedes (Strubbe & Murray 2015). The weak dependence of the reprocessed luminosity on the source luminosity, when the mass and extent of the envelope are held fixed, suggests that the peak luminosity of TDEs with $M_{\rm bh} \gtrsim 10^6$ may be regulated to be near a few times 10^{43} ergs s^{-1}, with a stronger dependence on the envelope mass than the BH mass.

If, after being assembled, the mass of the envelope remains roughly fixed, then at some time after maximum light the source luminosity should decline to $L < L_{\rm ion}$ where recombination fronts form. The source luminosity would then be nearly completely absorbed and reprocessed, and the optical luminosity may track the accretion rate, as perhaps suggested by the observed $t^{-5/3}$ decline in the optical light curves. Little soft x-ray emission would be expected at these later times unless deviations from spherical symmetry allows for channels for x-rays to escape, or the envelope mass is at some point depleted.

4.5.2 Outflows

A different mechanism for generating an extended gas distribution is through outflows. Super-Eddington accretion onto the BH is likely to unbind some fraction of the infalling debris (Strubbe & Quataert 2009; Lodato & Rossi 2011; Vinkó et al. 2015; Metzger & Stone 2015). Miller (2015), drawing on work by Laor & Davis (2014), suggest that line-driven winds analogous to those launched from the atmospheres of massive stars might also be responsible for launching outflows. For a wind launched near the tidal disruption radius, the expected escape velocities are $\sim 10^5$ km s^{-1}, which is much greater than that observed in the line widths of observed TDE spectra. However, if debris circularizes at radii much larger than $R_{\rm td}$, or if the winds are mass loaded, the expansion velocities may be lower.

Strubbe & Quataert (2009) argued that accretion may continuously generate an optically thick outflow, which would advect the energy dissipated at the accretion disk to larger radii. That advection may circumvent some of the complexities of absorption and reprocessing that we have studied here. Photons trapped in an outflow will be adiabatically degraded, which provides a robust mechanism for shifting the spectral energy distribution to longer wavelengths. The photons finally decouple from the flow at a trapping radius set by $\tau \sim c/v$. This scenario most closely resembles the calculations presented here only if the advection velocity is relatively low ($v \approx 1000$ km s^{-1}), in which case the trapping radius coincides with the inner boundary used in our calculations ($\tau \approx 300$). Based on analysis of the data of PS1-10jh, Strubbe & Murray (2015) suggest an outflow that does move at such a low velocity. However, their suggested outflow mass of 0.02 $M_\odot$ is likely too low to efficiently reprocess the source radiation, as shown in Figure 4.5.

Metzger & Stone (2015) present a modified outflow picture in which a large fraction of the inflowing tidal debris is promptly unbound, forming a quasi-spherical outflow with expansion velocities $\approx 10^4$ km s^{-1}. Radiation from the accretion disk of the BH is then absorbed and reprocessed by the outflow. At times near the peak of the optical TDE light curve ($\sim$

weeks) that outflow will have reached radii $r_{\rm out} \approx 10^{15}$ cm and the diffusion time is of order the expansion time. Our models provide a fair representation of such density distributions, although we do not include a radial velocity gradient. Nonetheless, the indications are that such a scenario can likely reproduce the near maximum light spectra of observed TDEs.

In contrast to the quasi-static or steady wind models, the optical depth of a prompt outflow necessarily decreases with time, given that $r_{\rm out} \propto t$. At some point, the envelope should become inefficient at reprocessing, at which time soft x-rays will escape and the optical light curve may no longer track the accretion rate. Since the critical luminosity (Equation 4.25) decreases more steeply ($L_{\rm ion} \propto t^{-2}$) than the expected accretion luminosity ($L \propto t^{-5/3}$), the condition $L > L_{\rm ion}$ is expected to occur at some late time. Metzger & Stone (2015) have discussed this possible "ionization break-out" and estimated its properties.

4.5.3 Circularization at Large Radius

Recent numerical work has suggested that the optical emission might arise from dissipation in material in the process of circularizing at large radii. Shiokawa et al. (2015) performed general relativistic (GR) hydrodynamics simulations and found that shocks located at the apoapse of orbits of returning material lead to build-up of material with enough angular momentum to support wide orbits, with a semi-major axis corresponding to that of the most bound debris from the initial disruption, several times 10^{14} cm. This is at least an order of magnitude larger than the periapse of the initial stellar orbit, where most earlier work had suggested that circularization should occur. Similar but less pronounced effects were found in the smoothed particle hydrodynamics simulations including leading-order GR effects performed by Bonnerot et al. (2016) and Hayasaki et al. (2015), and the grid-based Newtonian gravity calculation of Guillochon et al. (2014). Emission from the circularizing gas at these large radii has been suggested to give rise to the observed optical emission (Piran et al. 2015).

If the gas distribution formed from such circularization processes (or perhaps their associated outflows) extends from $\sim 10^{14} - 10^{15}$ cm, the situation resembles the numerical calculations presented here. Given that the gas is highly scattering dominated, a relatively high optical depth $\tau_{\rm es} \gtrsim 40$ in that material is required to thermalize the radiation in the circularization region. Assuming the optical depth is at least that high, we find that it makes little difference to the optical spectra whether the luminosity is generated at a circularization radius of $\sim 10^{14}$ cm or nearer the BH at $\sim 10^{13}$ cm (see Figure 4.4). Indeed, much more energy is expected to be liberated as material accretes onto the BH than from the circularization process itself, although mechanisms for hiding the accretion energy have been suggested (Piran et al. 2015; Svirski et al. 2015).

Simultaneous x-ray and optical observations for events such as PTF10iya, ASASSN-14li, and ASASSN-15oi (Cenko et al. 2012a; Holoien et al. 2016b; Miller et al. 2015; Holoien et al. 2016a) provide some hope at distinguishing the source of the luminosity, since for highly ionized envelopes the x-ray spectrum will be largely preserved as it propagates through the scattering dominated envelope. The peak of the x-ray flux then reflects the temperature at

the depth at which it was produced (see Figure 4.4).

4.6 Conclusions

4.6.1 Summary of Key Results

This paper has presented analytic estimates and detailed radiative transfer calculations that clarify how the spectra of TDEs can be generated within an extended envelope. We have focused our attention on TDEs around the optical light curve peak, with bolometric luminosities in the range $10^{44} - 10^{45}$ ergs s^{-1} (corresponding to the Eddington luminosity of $10^6 - 10^7 M_\odot$ BHs). We accounted for non-LTE effects and the high electron scattering optical depth of the reprocessing material, which we show are crucial for understanding both the thermalization of the optical continuum and the emission line ratios.

We identified two regimes of reprocessing, depending on the envelope ionization state. When the envelope is highly ionized ($L > L_{\rm ion}$), we find that the intrinsic x-ray emission from the accretion disk is only partially absorbed, giving rise to an SED that peaks in the soft x-ray but is accompanied by an enhanced optical emission component ($\gtrsim 10^{43}$ ergs s^{-1} at wavelengths longer than 1000 Å). In addition to providing an optical flux at a sufficient brightness to match observations, this can explain TDEs observed simultaneously in the optical and x-ray, such as PTF10iya, ASASSN-14li, and ASASSN-15oi.

If the bolometric luminosity declines rapidly enough compared to the mass of the envelope, a critical value can be reached ($L < L_{\rm ion}$) for which a helium recombination front forms and the soft x-rays are completely absorbed. This second regime resembles TDEs that have been observed at optical wavelengths without a coincident x-ray signal, such as PS1-10jh and ASASSN-14ae. In this regime, the reprocessing is completely efficient and the optical/UV should closely track the accretion luminosity.

In general, the x-ray through optical SED is not well described by a single blackbody, but is a blend of emission from a variety of depths and temperatures. For this reason, one must be cautious if attempting to fit a single blackbody temperature to optical data. One is likely to underestimate the bolometric luminosity in this way, as the SED can peak at shorter wavelengths than would be inferred from the optical data.

The light curve evolution of TDEs will depend on how the source luminosity, envelope mass, and envelope radius change with time. When the envelope is highly ionized ($L > L_{\rm ion}$), the optical luminosity depends more on the envelope mass than the source luminosity. This is because increasing L leads to higher envelope ionization, which reduces the efficiency with which x-rays are reprocessed to the optical. It is thus possible that the rise and fall of TDE light curves reflects in large part the growth and subsequent depletion of mass in the reprocessing envelope. As the mass of the envelope decreases, so does the reprocessing efficiency and the optical flux, but the shape of the continuum remains mostly unchanged. This points to an explanation for the near-constant color of the optical continuum.

We have demonstrated that the strength of line features in TDEs depends on optically

thick radiation transport effects that are not well captured by photoionization codes like CLOUDY. Even in envelopes of solar composition, the Hα line may be highly suppressed relative to HeII lines due to optical depth effects. By varying the configuration of material in the reprocessing envelope, a variety of helium-to-hydrogen line ratios can be realized in the optical spectrum. In particular, we have explored what happens as we vary the outer radius of the envelope while keeping the total mass fixed, and have shown a transition of Hα from emission to shallow absorption. Although the radial extent of the envelope is a key parameter, other parameters also influence the line ratios, including the bolometric luminosity and the mass of the envelope.

4.6.2 Outstanding Issues

While our studies have outlined many of the key physical processes at play in TDE envelopes, several questions remain to be addressed. An obvious area for improvement is relaxing the assumption of spherical symmetry. Variation in the density and temperature structure of the envelope with polar angle could lead to important viewing-angle effects which may be important for explaining why soft x-rays are visible in only a subset of observed TDEs. The density and temperature profile of the envelope may also vary with viewing angle, which may have implications for observables such as the slope of the optical continuum.

Another critical area needing further study is the kinematic structure of the envelope. We have only crudely accounted for motions via a Doppler line-width set to a value of order the virial velocity. In many scenarios, velocity gradients are due instead to bulk motions – outflows or rotation – that may alter the formation of line features. Radiative transfer studies of the detailed line profiles may illuminate the kinematics of the envelope. Radially expanding outflows like supernovae, for example, generally produce P-Cygni type absorption features, whereas the optical lines observed in TDEs are usually purely in emission, and occasionally show substructure (Arcavi et al. 2014; Holoien et al. 2016b).

Our calculations have only directly tracked bound-bound and bound-free opacities from hydrogen, helium, and oxygen. In reality, other metals likely increase the opacity, especially in the x-ray and UV, and ionization edges and lines from these other metals are likely to appear in the spectrum. Nevertheless, for the luminosities we studied, we found that the optical continuum and optical helium-to-hydrogen line ratios do not seem to be greatly influenced by the presence of oxygen, the most abundant metal.

Our assumed inner boundary condition of blackbody radiation emitted at $r_{\rm in}$ deserves further study. In reality, the source emission spectrum may be that from an accretion disk smaller than $r_{\rm in}$. On the other hand, dense hot gas just below our inner boundary may have a Compton y-parameter $\gg 1$, in which case Comptonization may indeed thermalize the radiation to the gas temperature near the envelope base. Outside of our inner boundary, the Compton y-parameter can be of order unity, and may have some effect on the spectrum. The physics of Compton scattering will be directly included in our future Monte Carlo transport calculations.

Future work will include a more detailed exploration of the parameters governing the

spectrum, including the mass of the envelope, accretion disk luminosity, and gas density gradient, as well as how these parameters evolve over time in different scenarios. Studies of this sort, in comparison to improved observations of TDEs, will hopefully clarify the physics governing these transients.

Acknowledgments

We thank Janos Botyanszki for code for photoionization cross-sections, and Tamara Bogdanović, Eric Coughlin, Brad Cenko, Ryan Chornock, Moshe Elitzur, Aleksey Generosov, Julian Krolik, Brian Metzger, Eliot Quataert, Todd Thompson, and Sjoert van Velzen for helpful comments and conversations. This research used resources of the National Energy Research Scientific Computing Center, which is supported by the Office of Science of the U.S. Department of Energy under Contract No. DE-AC02-05CH11231. This research also used the Savio computational cluster resource provided by the Berkeley Research Computing program at the University of California, Berkeley (supported by the UC Berkeley Chancellor, Vice Chancellor of Research, and Office of the CIO). Daniel Kasen was supported in part by a Department of Energy Office of Nuclear Physics Early Career Award, and by the Director, Office of Energy Research, Office of High Energy and Nuclear Physics, Divisions of Nuclear Physics, of the U.S. Department of Energy under Contract No. DE-AC02-05CH11231. This work was supported by Einstein grant PF3- 140108 (James Guillochon), the Packard grant (Enrico Ramirez-Ruiz), and a NASA ATP grant NNX14AH37G (Enrico Ramirez-Ruiz).

4.A Numerical Method

To generate model spectra of TDE events, we carry out NLTE radiative transport calculations using the Monte Carlo radiative transfer code SEDONA (Kasen et al. 2006; Roth & Kasen 2015). The calculation is divided into two steps. First, the multi-wavelength radiation transport is calculated using Monte Carlo method which includes scattering, bound-bound, bound-free, and free-free radiative processes. Second, the gas temperature and atomic level populations are determined via a solution of the equations of statistical and thermal equilibrium. Since the photon opacities and emissivities depend on the level populations and temperature, these two steps are iterated (typically 20-60 times) until the envelope structure and output spectra have converged.

For the transport problem, we assume a stationary envelope, which should be applicable for TDE light curves near peak, when the diffusion time through the envelope is less than or comparable to the peak time. We enforce radiative equilibrium, justified by the heating-time arguments in Section 4.3, by "effectively scattering" photon packets during each interaction, thereby ensuring energy conservation. At each interaction, the outgoing packet is reassigned a wavelength, sampled from the NLTE emissivity distribution across all wavelengths, as in Carciofi & Bjorkman (2006).

To calculate the NLTE level populations, we use Monte Carlo estimators of the photoionization rates and the bound-bound radiative rates. We assume statistical equilibrium and solve the set of coupled linear equations such that the net transition rate for each electron level is zero.

4.A.1 Setup and initial conditions

We divide our spherical grid into 512 zones, equally spaced in radius from zero to $r_{\rm out}$. In order to avoid an artificially abrupt truncation of the envelope, we add roughly 100 zones that follow an r^{-10} density profile beyond $r_{\rm out}$(we find that our results are not highly sensitive to the exact value of this power-law). We initialized each zone with approximately 1000 photon packets sampled from a blackbody wavelength distribution at the temperature in the zone computed from Equation (4.17). During each iteration, we emit approximately 100 million packets at the zone corresponding to our inner radius $r_{\rm in}$.

We impose an absorbing boundary condition at the inner radius — photons that scatter back below that radius are removed from the calculation. Likewise, photons that escape at the outer radius are tallied and removed from the calculation.

4.A.2 Radiative processes included

The radiative processes included in our calculation are electron scattering, free-free (bremsstrahlung), bound-free (photoionization) and bound-bound (line) transitions. The extinction coefficient for electron scattering is $\alpha_{\rm es} = n_e \sigma_t$, while the free-free extinction coefficient is given by

$$\alpha_\nu^{ff} = \frac{4e^6}{3mhc}\left(\frac{2\pi}{3mkT}\right)^{1/2} Z^2 n_e n_{\rm ion} \nu^{-3}\left(1 - e^{-h\nu/kT}\right). \tag{4.48}$$

By Kirchhoff's law, the free-free emissivity is $j_\nu^{\rm ff} = \alpha_\nu^{\rm ff} B_\nu(T)$.

The bound-bound extinction coefficient is given by Equation (4.44). The corresponding emissivity is

$$j_\nu^{bb} = \frac{h\nu}{4\pi} n_2 A_{ul} \phi(\nu) \tag{4.49}$$

where A_{ul} is the Einstein coefficient for spontaneous emission, and $\phi(\nu)$ is the line profile. For $\phi(\nu)$, we assume a Gaussian profile with a width corresponding to Doppler velocity of 10^4 km s^{-1}.

We include bound-free transitions from all excited atomic levels. For hydrogen and HeII, we use the photoionization cross-section (Rybicki & Lightman 1986)

$$\sigma_\nu^{\rm ion} = \frac{n_{q,i}\sigma_{0,\rm H}}{Z^2}\left(\frac{h\nu}{\chi_i}\right)^{-3} \tag{4.50}$$

where $n_{q,i}$ is the principal quantum number of the bound electron level labeled by index i, $\sigma_{0,H} = 6.3 \times 10^{-18}$ cm^2 and χ_i is the ionization potential to remove an electron from level i.

For the ground state HeI, we use the photoionization cross-section fits of Verner et al. (1996). For oxygen, we use the TOPbase photoionization cross-sections smoothed over resonances. For atomic levels that do not have data, we use an approximate hydrogenic cross-section of the form Equation (4.50), with Z corresponding to the net nuclear charge seen by the valence electrons and $n_{q,i}$ the principal quantum number of the valence electron being ionized.

When computing the photoionization extinction coefficient, we include the non-LTE correction for stimulated radiative recombination, yielding (e.g. Mihalas 1978)

$$\begin{aligned} \alpha_\nu^{\rm ion} &= n_i \sigma_\nu^{\rm ion} \left[1 - \frac{n_e n^+}{n_i} f(T) \exp\left(-\frac{h\nu}{k_B T}\right)\right] , \\ f(T) &= \left(\frac{h^2}{2\pi m_e k_B T}\right)^{3/2} \frac{g^-}{2g^+} \exp\left(\frac{\chi_i}{k_B T}\right) \end{aligned} \tag{4.51}$$

where n_i is the number density of particles with bound electron in level i, n^+ is the number density for the ions in the ground state of the next highest ionization state, g^- and g^+ are the statistical weights of the species being ionized and the ionized state, respectively, and T is the temperature of the free electrons.

This opacity must be summed over all elements and all bound electron levels labeled by the index i within each ionization state.

To derive radiative recombination cross-sections, $\sigma^{\rm rec}(u_e)$, as a function of electron speed u_e, we use the Milne relations which relate $\sigma^{\rm rec}(u_e)$ to the photoionization cross-sections. The associated emissivity for bound-free recombination is (see Osterbrock & Ferland 2006).

$$\begin{aligned} j_\nu^{\rm recomb} &= \frac{n^+ n_e}{4\pi} u_e f_u \sigma^{\rm rec}(u_e) h\nu \frac{du}{d\nu} , \\ u_e &= \sqrt{\frac{2}{m_e}(h\nu - \chi_i)} , \\ f_u &= \frac{4}{\sqrt{\pi}} \left(\frac{m_e}{2kT}\right)^{3/2} u_e^2 \exp\left(-\frac{m_e u_e^2}{2kT}\right) . \end{aligned} \tag{4.52}$$

This emissivity must be summed over all elements and all bound electron levels to which the free electron may recombine. We derive the temperature-dependent radiative recombination coefficient for each atomic level by integrating $\sigma^{\rm rec}(u_e)$ over the electron Maxwell-Boltzmann distribution.

Chapter 5

Prospects for Future work

This dissertation has presented the development of tools to study the feeding of SMBHs, and some exciting results demonstrating the capabilities of these tools. This marks more of a beginning than an end. The following sections describe plans for follow-up research.

5.1 Time-dependent calculations of TDE light-curves and spectra

While the previous calculations presented in this dissertation considered the emission from quasi-static TDE envelopes, many theories of TDEs predict significant time evolution of the debris, as discussed in Chapter 4. By calculating synthetic light curves with time-dependent transport, we can distinguish between these models. We may allow key parameters to vary such as the accretion luminosity and the mass/size of the reprocessing envelope to evolve together in accordance with analytic theories of outflows. We may then track the outgoing spectra as a function of time to see how the x-ray, UV, and optical light-curves evolve.

An outflowing or rotating envelope will have a bulk velocity gradient that will affect spectral line features. In Roth et al. (2015), we assumed random motion. For the future calculations, we will self-consistently compute the effect of velocity gradients on the line transport (a capability which we have demonstrated in Roth & Kasen (2015). Therefore, in addition to the SEDs, we will be able to generate spectra with realistic line profiles that can be compared to observations to interpret the kinematics of the gas.

As an additional extension of previous work, we will include the effects of Compton scattering into our calculations, which we expect to be important for shaping the x-ray spectrum formed near the base of the envelope. We can then compare the improved models for the x-ray spectrum with events such as ASASSN-14li (Miller et al. 2015).

5.2 Multi-dimensional models of TDEs

The flexibility of the Monte Carlo transport allows us to consider models with arbitrary geometries. Given the initial angular momentum of the disrupted star, we expect the distribution of material in the envelope to have a higher density closer to the plane of disruption than along the poles. Additionally, radiation pressure or jets might open a funnel in the polar directions. Therefore, a natural step is to consider 2D (axisymmetric) gas distributions where the density increases with polar angle. Such calculations would track the light-curves in the x-ray, UV, and optical wavebands, but this time accounting for the viewing angle. We expect that there will be strong orientation effects (e.g., x-rays may escape more readily in the polar direction than along the dense equator). By calculating such dependences, we will be able to better interpret observations, and statistically predict the fraction of TDEs visible at each of the wavelengths of interest.

5.3 The Continuum Emission from Active Galactic Nuclei

One of the long standing puzzles regarding AGN has been the origin of the spectral peak in the UV (the "big blue bump"), a feature that remains unexpectedly similar across such a wide range of luminosities. Recently, observations from both micro-lensing and reverberation mapping suggest a large size for the optically emitting material, hinting at the presence of a reprocessing region similar to what we have studied for TDEs. Our calculations therefore provide an opportunity to address one of the most persistent puzzles in AGN physics. To do so, we will set up two-dimensional, idealized axisymmetric wind calculations, very much like the axisymmetric TDE calculations described above. We may then study the interaction between radiation from the center, the wind, and the disk, which will not only be emitting, but also absorbing some of the reprocessed radiation.

The key parameters we will vary will be the mass loss rate of wind, the luminosity of the central central source, and the opening angle of wind. The outputs will include temperature profiles of the disk, which can be compared to the micro-lensing data. Additionally, we will generate reprocessed SEDs, and determine whether this geometry provides a natural explanation for the universality of the UV spectral energy peak in AGN.

Bibliography

Abdikamalov, E., Burrows, A., Ott, C. D., et al. 2012, ApJ, 755, 111
Abel, T., & Wandelt, B. D. 2002, MNRAS, 330, L53
Abramowicz, M. A., Czerny, B., Lasota, J. P., & Szuszkiewicz, E. 1988, ApJ, 332, 646
Alvarez, M. A., Bromm, V., & Shapiro, P. R. 2006, ApJ, 639, 621
Antonucci, R. 1993, ARA&A, 31, 473
—. 2015, ArXiv e-prints, arXiv:1501.02001
Arcavi, I., Gal-Yam, A., Sullivan, M., et al. 2014, ApJ, 793, 38
Aubert, D., & Teyssier, R. 2008, MNRAS, 387, 295
Ayal, S., Livio, M., & Piran, T. 2000, ApJ, 545, 772
Blandford, R. D., & Payne, D. G. 1982, MNRAS, 199, 883
Blandford, R. D., & Znajek, R. L. 1977, MNRAS, 179, 433
Bloom, J. S., Giannios, D., Metzger, B. D., et al. 2011, Science, 333, 203
Bogdanović, T., Eracleous, M., Mahadevan, S., Sigurdsson, S., & Laguna, P. 2004, ApJ, 610, 707
Bondi, H. 1952, MNRAS, 112, 195
Bonnerot, C., Rossi, E. M., Lodato, G., & Price, D. J. 2016, MNRAS, 455, 2253
Bouquet, S., Romain, T., & Chieze, J. P. 2000, ApJS, 127, 245
Brown, G. C., Levan, A. J., Stanway, E. R., et al. 2015, MNRAS, 452, 4297
Bryan, G. L., Norman, M. L., O'Shea, B. W., et al. 2014, ApJS, 211, 19
Buras, R., Rampp, M., Janka, H.-T., & Kifonidis, K. 2006, A&A, 447, 1049
Cappelluti, N., Ajello, M., Rebusco, P., et al. 2009, A&A, 495, L9
Carciofi, A. C., & Bjorkman, J. E. 2006, ApJ, 639, 1081
Carter, B., & Luminet, J. P. 1982, Nature, 296, 211
Castor, J. I. 2004, Radiation Hydrodynamics (Cambridge University Press)
Cenko, S. B., Bloom, J. S., Kulkarni, S. R., et al. 2012a, MNRAS, 420, 2684
Cenko, S. B., Krimm, H. A., Horesh, A., et al. 2012b, ApJ, 753, 77
Cenko, S. B., Cucchiara, A., Roth, N., et al. 2016, ApJ, 818, L32
Chandrasekhar, S. 1950, Radiative transfer. (Clarendon Press)
Chornock, R., Berger, E., Gezari, S., et al. 2014, ApJ, 780, 44
Ciotti, L., Ostriker, J. P., & Proga, D. 2010, ApJ, 717, 708
Colella, P. 1990, Journal of Computational Physics, 87, 171
Colella, P., & Woodward, P. R. 1984, Journal of Computational Physics, 54, 174

Commerçon, B., Teyssier, R., Audit, E., Hennebelle, P., & Chabrier, G. 2011, A&A, 529, A35
Coughlin, E. R., & Begelman, M. C. 2014, ApJ, 781, 82
Crenshaw, D. M., & Kraemer, S. B. 2000, ApJ, 532, L101
Croton, D. J., Springel, V., White, S. D. M., et al. 2006, MNRAS, 365, 11
Dai, L., McKinney, J. C., & Miller, M. C. 2015, ApJ, 812, L39
D'Angelo, G., & Bodenheimer, P. 2013, ApJ, 778, 77
Davis, S. W., Stone, J. M., & Jiang, Y.-F. 2012, ApJS, 199, 9
De Colle, F., Guillochon, J., Naiman, J., & Ramirez-Ruiz, E. 2012, ApJ, 760, 103
Debuhr, J., Quataert, E., & Ma, C.-P. 2011, MNRAS, 2150
DeBuhr, J., Quataert, E., & Ma, C.-P. 2011, MNRAS, 412, 1341
Densmore, J. D., Urbatsch, T. J., Evans, T. M., & Buksas, M. W. 2007, Journal of Computational Physics, 222, 485
Deo, R. P., Richards, G. T., Nikutta, R., et al. 2011, ApJ, 729, 108
Di Matteo, T., Springel, V., & Hernquist, L. 2005, Nature, 433, 604
Dijkstra, M., Haiman, Z., & Spaans, M. 2006, ApJ, 649, 14
Donley, J. L., Brandt, W. N., Eracleous, M., & Boller, T. 2002, AJ, 124, 1308
Dorodnitsyn, A., Bisnovatyi-Kogan, G. S., & Kallman, T. 2011, ApJ, 741, 29
Dorodnitsyn, A., & Kallman, T. 2012, ApJ, 761, 70
Draine, B. T. 2003a, ARA&A, 41, 241
—. 2003b, ApJ, 598, 1026
Dubroca, B., & Feugeas, J. 1999, Academie des Sciences Paris Comptes Rendus Serie Sciences Mathematiques, 329, 915
Dunn, J. P., Bautista, M., Arav, N., et al. 2010, ApJ, 709, 611
Ensman, L. 1994, ApJ, 424, 275
Ercolano, B., & Gritschneder, M. 2011, MNRAS, 413, 401
Esquej, P., Saxton, R. D., Freyberg, M. J., et al. 2007, A&A, 462, L49
Evans, C. R., & Kochanek, C. S. 1989, ApJ, 346, L13
Faber, S. M., & Jackson, R. E. 1976, ApJ, 204, 668
Fan, X. 2006, New A Rev., 50, 665
Feautrier, P. 1964, SAO Special Report, 167, 80
Ferrarese, L., & Merritt, D. 2000, ApJ, 539, L9
Fleck, Jr., J. A., & Cummings, Jr., J. D. 1971, J. Comput. Phys., 8, 313
Frank, J., King, A., & Raine, D. J. 2002, Accretion Power in Astrophysics: Third Edition (Cambridge University Press), 398
Garain, S. K., Ghosh, H., & Chakrabarti, S. K. 2012, ApJ, 758, 114
Gaskell, C. M., & Rojas Lobos, P. A. 2014, MNRAS, 438, L36
Gebhardt, K., Bender, R., Bower, G., et al. 2000, ApJ, 539, L13
Gentile, N. A. 2001, Journal of Computational Physics, 172, 543
Genzel, R., Pichon, C., Eckart, A., Gerhard, O. E., & Ott, T. 2000, MNRAS, 317, 348
Gezari, S., Martin, D. C., Milliard, B., et al. 2006, ApJ, 653, L25
Gezari, S., Heckman, T., Cenko, S. B., et al. 2009, ApJ, 698, 1367

Gezari, S., Chornock, R., Rest, A., et al. 2012, Nature, 485, 217
Ghosh, H., Garain, S. K., Giri, K., & Chakrabarti, S. K. 2011, MNRAS, 416, 959
Gittings, M., Weaver, R., Clover, M., et al. 2008, Computational Science and Discovery, 1, 015005
González, M., Audit, E., & Huynh, P. 2007, A&A, 464, 429
Greene, J. E., Zakamska, N. L., & Smith, P. S. 2012, ApJ, 746, 86
Greene, J. E., Peng, C. Y., Kim, M., et al. 2010, ApJ, 721, 26
Greif, T. H., Johnson, J. L., Klessen, R. S., & Bromm, V. 2009, MNRAS, 399, 639
Gritschneder, M., Naab, T., Burkert, A., et al. 2009, MNRAS, 393, 21
Gubbay, J., Legg, A. J., Robertson, D. S., et al. 1969, Nature, 224, 1094
Guillochon, J., Manukian, H., & Ramirez-Ruiz, E. 2014, ApJ, 783, 23
Guillochon, J., & Ramirez-Ruiz, E. 2013, ApJ, 767, 25
—. 2015, ApJ, 809, 166
Halpern, J. P., Gezari, S., & Komossa, S. 2004, ApJ, 604, 572
Harries, T. J. 2011, MNRAS, 416, 1500
Hasinger, G., Cappelluti, N., Brunner, H., et al. 2007, ApJS, 172, 29
Haworth, T. J., & Harries, T. J. 2012, MNRAS, 420, 562
Hayasaki, K., Stone, N. C., & Loeb, A. 2015, ArXiv e-prints, arXiv:1501.05207 [astro-ph.HE]
Hayek, W., Asplund, M., Carlsson, M., et al. 2010, A&A, 517, A49
Hayes, J. C., Norman, M. L., Fiedler, R. A., et al. 2006, ApJS, 165, 188
Heinemann, T., Nordlund, Å., Scharmer, G. B., & Spruit, H. C. 2007, ApJ, 669, 1390
Henney, W. J., Arthur, S. J., de Colle, F., & Mellema, G. 2009, MNRAS, 398, 157
Hills, J. G. 1975, Nature, 254, 295
Holoien, T. W.-S., Prieto, J. L., Bersier, D., et al. 2014, MNRAS, 445, 3263
Holoien, T. W.-S., Kochanek, C. S., Prieto, J. L., et al. 2016a, ArXiv e-prints, arXiv:1602.01088 [astro-ph.HE]
—. 2016b, MNRAS, 455, 2918
Hönig, S. F., Beckert, T., Ohnaka, K., & Weigelt, G. 2006, A&A, 452, 459
Hönig, S. F., Kishimoto, M., Gandhi, P., et al. 2010, A&A, 515, A23
Hopkins, P. F., Hernquist, L., Cox, T. J., et al. 2005, ApJ, 630, 705
Hopkins, P. F., & Quataert, E. 2010, MNRAS, 407, 1529
—. 2011a, MNRAS, 415, 1027
—. 2011b, MNRAS, 411, L61
Hryniewicz, K., & Walter, R. 2016, A&A, 586, arXiv:1505.06612v1 [astro-ph.HE]
Illarionov, A. F., & Sunyaev, R. A. 1972, Ap&SS, 19, 61
Jaffe, W., Meisenheimer, K., Röttgering, H. J. A., et al. 2004, Nature, 429, 47
Jeffery, D. J., & Branch, D. 1990, in Supernovae, Jerusalem Winter School for Theoretical Physics, ed. J. C. Wheeler, T. Piran, & S. Weinberg, 149
Jiang, Y.-F., Stone, J. M., & Davis, S. W. 2012, ApJS, 199, 14
—. 2014, ApJ, 796, 106
Johnson, H. R., & Klinglesmith, D. A. 1965, SAO Special Report, 174, 221
Kasen, D., Thomas, R. C., & Nugent, P. 2006, ApJ, 651, 366

Kasen, D., Thomas, R. C., Röpke, F., & Woosley, S. E. 2008, Journal of Physics Conference Series, 125, 012007
Keating, S. K., Everett, J. E., Gallagher, S. C., & Deo, R. P. 2012, ApJ, 749, 32
Kelly, B. C., Vestergaard, M., Fan, X., et al. 2010, ApJ, 719, 1315
Kerzendorf, W. E., & Sim, S. A. 2014, MNRAS, 440, 387
King, A. 2003, ApJ, 596, L27
Kishimoto, M., Hönig, S. F., Antonucci, R., et al. 2011, A&A, 536, A78
Kochanek, C. S. 1994, ApJ, 422, 508
Kolb, S. M., Stute, M., Kley, W., & Mignone, A. 2013, A&A, 559, A80
Komossa, S. 2015, Journal of High Energy Astrophysics, 7, 148
Komossa, S., & Bade, N. 1999, A&A, 343, 775
Komossa, S., Halpern, J., Schartel, N., et al. 2004, ApJ, 603, L17
Konigl, A., & Kartje, J. F. 1994, ApJ, 434, 446
Korista, K. T., & Goad, M. R. 2004, ApJ, 606, 749
Kormendy, J., & Richstone, D. 1995, ARA&A, 33, 581
Kourganoff, V. 1952, Basic methods in transfer problems; radiative equilibrium and neutron diffusion (Clarendon Press)
Krolik, J. H. 2007, ApJ, 661, 52
Krolik, J. H., & Begelman, M. C. 1988, ApJ, 329, 702
Krumholz, M. R., Klein, R. I., McKee, C. F., & Bolstad, J. 2007a, ApJ, 667, 626
Krumholz, M. R., Stone, J. M., & Gardiner, T. A. 2007b, ApJ, 671, 518
Kuiper, R., Klahr, H., Dullemond, C., Kley, W., & Henning, T. 2010, A&A, 511, A81
Kunasz, P., & Auer, L. H. 1988, J. Quant. Spec. Radiat. Transf., 39, 67
Lacy, J. H., Townes, C. H., & Hollenbach, D. J. 1982, ApJ, 262, 120
Laor, A., & Davis, S. W. 2014, MNRAS, 438
Lapidus, A. 1967, Journal of Computational Physics, 2, 154
Lawrence, A. 1991, MNRAS, 252, 586
Levermore, C. D., & Pomraning, G. C. 1981, ApJ, 248, 321
Li, L.-X., Narayan, R., & Menou, K. 2002, ApJ, 576, 753
Liebendörfer, M., Messer, O. E. B., Mezzacappa, A., et al. 2004, ApJS, 150, 263
Lin, D., Maksym, P. W., Irwin, J. A., et al. 2015, ApJ, 811, 43
Livne, E., Burrows, A., Walder, R., Lichtenstadt, I., & Thompson, T. A. 2004, ApJ, 609, 277
Lodato, G., King, A. R., & Pringle, J. E. 2009, MNRAS, 392, 332
Lodato, G., & Rossi, E. M. 2011, MNRAS, 410, 359
Loeb, A., & Ulmer, A. 1997, ApJ, 489, 573
Lowrie, R. B., & Edwards, J. D. 2008, Shock Waves, 18, 129
Lowrie, R. B., Morel, J. E., & Hittinger, J. A. 1999, ApJ, 521, 432
Lucy, L. B. 1999, A&A, 344, 282
—. 2002, A&A, 384, 725
—. 2005, A&A, 429, 19
Lynden-Bell, D. 1969, Nature, 223, 690

—. 1978, Phys. Scr, 17, 185
MacLeod, M., Guillochon, J., & Ramirez-Ruiz, E. 2012, ApJ, 757, 134
Madau, P., Haardt, F., & Dotti, M. 2014, ApJ, 784, L38
Magorrian, J., Tremaine, S., Richstone, D., et al. 1998, AJ, 115, 2285
Maiolino, R., Shemmer, O., Imanishi, M., et al. 2007, A&A, 468, 979
Maksym, W. P., Ulmer, M. P., & Eracleous, M. 2010, ApJ, 722, 1035
Malizia, A., Stephen, J. B., Bassani, L., et al. 2009, MNRAS, 399, 944
Marconi, A., Risaliti, G., Gilli, R., et al. 2004, MNRAS, 351, 169
Mason, R. E., Geballe, T. R., Packham, C., et al. 2006, ApJ, 640, 612
Mazzali, P. A., & Lucy, L. B. 1993, A&A, 279, 447
McKinney, J. C., Tchekhovskoy, A., Sadowski, A., & Narayan, R. 2014, MNRAS, 441, 3177
McNamara, B. R., & Nulsen, P. E. J. 2007, ARA&A, 45, 117
Metzger, B. D., Hascoët, R., Vurm, I., et al. 2014, MNRAS, 442, 713
Metzger, B. D., & Stone, N. C. 2015, ArXiv e-prints, arXiv:1506.03453v1 [astro-ph.HE]
Mihalas, D. 1978, Stellar atmospheres /2nd edition/ (W. H. Freeman and Co.)
Mihalas, D., & Auer, L. H. 2001, J. Quant. Spec. Radiat. Transf., 71, 61
Mihalas, D., Auer, L. H., & Mihalas, B. R. 1978, ApJ, 220, 1001
Mihalas, D., & Mihalas, B. W. 1984, Foundations of radiation hydrodynamics (Oxford University Press)
Miller, J. M., Kaastra, J. S., Miller, M. C., et al. 2015, Nature, 526, 542
Miller, M. C. 2015, ApJ, 805, 83
Miniati, F., & Colella, P. 2007, Journal of Computational Physics, 224, 519
Miyoshi, M., Moran, J., Herrnstein, J., et al. 1995, Nature, 373, 127
Moe, M., Arav, N., Bautista, M. A., & Korista, K. T. 2009, ApJ, 706, 525
Mortlock, D. J., Warren, S. J., Venemans, B. P., et al. 2011, Nature, 474, 616
Murray, N., Chiang, J., Grossman, S. A., & Voit, G. M. 1995, ApJ, 451, 498
Murray, N., Quataert, E., & Thompson, T. A. 2005, ApJ, 618, 569
Mushotzky, R. F., Done, C., & Pounds, K. A. 1993, ARA&A, 31, 717
Narayan, R., & Yi, I. 1994, ApJ, 428, L13
Nenkova, M., Ivezić, Ž., & Elitzur, M. 2002, ApJ, 570, L9
Netzer, H. 1987, MNRAS, 225, 55
Neufeld, D. A. 1990, ApJ, 350, 216
Noebauer, U. M., Sim, S. A., Kromer, M., Röpke, F. K., & Hillebrandt, W. 2012, MNRAS, 425, 1430
Nordlund, A. 1982, A&A, 107, 1
Nordlund, Å., & Stein, R. F. 1990, Computer Physics Communications, 59, 119
Novak, G. S., Ostriker, J. P., & Ciotti, L. 2011, ApJ, 737, 26
—. 2012, MNRAS, 427, 2734
Orban, C., Fatenejad, M., Chawla, S., Wilks, S. C., & Lamb, D. Q. 2013, ArXiv e-prints, arXiv:1306.1584 [physics.plasm-ph]
Osterbrock, D. E., & Ferland, G. J. 2006, Astrophysics of gaseous nebulae and active galactic nuclei (University Science Books)

Ott, C. D., Burrows, A., Dessart, L., & Livne, E. 2008, ApJ, 685, 1069
Paczyński, B., & Wiita, P. J. 1980, A&A, 88, 23
Petkova, M., & Springel, V. 2011, MNRAS, 415, 3731
Phinney, E. S. 1989, in IAU Symposium, Vol. 136, The Center of the Galaxy, ed. M. Morris, 543
Pier, E. A., & Krolik, J. H. 1992, ApJ, 399, L23
Piran, T., Svirski, G., Krolik, J., Cheng, R. M., & Shiokawa, H. 2015, ApJ, 806, 164
Proga, D., Stone, J. M., & Kallman, T. R. 2000, ApJ, 543, 686
Raban, D., Jaffe, W., Röttgering, H., Meisenheimer, K., & Tristram, K. R. W. 2009, MNRAS, 394, 1325
Ramirez-Ruiz, E., & Rosswog, S. 2009, ApJ, 697, L77
Rees, M. J. 1966, Nature, 211, 468
—. 1978, Nature, 275, 516
—. 1988, Nature, 333, 523
Richstone, D., Ajhar, E. A., Bender, R., et al. 1998, Nature, 395, A14
Rijkhorst, E.-J., Plewa, T., Dubey, A., & Mellema, G. 2006, A&A, 452, 907
Risaliti, G., Elvis, M., & Nicastro, F. 2002, ApJ, 571, 234
Risaliti, G., Maiolino, R., & Salvati, M. 1999, ApJ, 522, 157
Rosdahl, J., Blaizot, J., Aubert, D., Stranex, T., & Teyssier, R. 2013, MNRAS, 436, 2188
Rosswog, S., Ramirez-Ruiz, E., & Hix, W. R. 2009, ApJ, 695, 404
Roth, N., & Kasen, D. 2015, ApJS, 217, 9
Roth, N., Kasen, D., Guillochon, J., & Ramirez-Ruiz, E. 2015, ArXiv e-prints, arXiv:1510.08454 [astro-ph.HE]
Roth, N., Kasen, D., Hopkins, P. F., & Quataert, E. 2012, ApJ, 759, 36
Rupke, D. S. N., & Veilleux, S. 2011, ApJ, 729, L27
Rutten, R. J. 2003, Radiative Transfer in Stellar Atmospheres (Lecture Notes Utrecht University)
Rybicki, G. B., & Lightman, A. P. 1986, Radiative Processes in Astrophysics (Wiley-VCH)
Salpeter, E. E. 1964, ApJ, 140, 796
Saxton, R. D., Read, A. M., Esquej, P., et al. 2012, A&A, 541, A106
Sądowski, A., & Narayan, R. 2016, MNRAS, 456, 3929
Sądowski, A., Narayan, R., McKinney, J. C., & Tchekhovskoy, A. 2014, MNRAS, 439, 503
Schartmann, M., Meisenheimer, K., Camenzind, M., et al. 2008, A&A, 482, 67
Schmidt, M. 1963, Nature, 197, 1040
Sekora, M. D., & Stone, J. M. 2010, Journal of Computational Physics, 229, 6819
Shakura, N. I., & Sunyaev, R. A. 1973, A&A, 24, 337
Shiokawa, H., Krolik, J. H., Cheng, R. M., Piran, T., & Noble, S. C. 2015, ApJ, 804, 85
Siebenmorgen, R., & Heymann, F. 2012, in IAU Symposium, Vol. 284, IAU Symposium, 82
Silk, J. 2005, MNRAS, 364, 1337
Silk, J., & Rees, M. J. 1998, A&A, 331, L1
Simpson, C. 2005, MNRAS, 360, 565
Sincell, M. W., Gehmeyr, M., & Mihalas, D. 1999, Shock Waves, 9, 391

Skinner, M. A., & Ostriker, E. C. 2013, ApJS, 206, 21
Sokasian, A., Abel, T., Hernquist, L., & Springel, V. 2003, MNRAS, 344, 607
Soltan, A. 1982, MNRAS, 200, 115
Springel, V., Di Matteo, T., & Hernquist, L. 2005, ApJ, 620, L79
Stalevski, M., Fritz, J., Baes, M., Nakos, T., & Popović, L. Č. 2012, MNRAS, 420, 2756
Stein, R. F., & Nordlund, A. 1998, ApJ, 499, 914
Stone, J. M., Mihalas, D., & Norman, M. L. 1992, ApJS, 80, 819
Strubbe, L. E., & Murray, N. 2015, MNRAS, 454, 2321
Strubbe, L. E., & Quataert, E. 2009, MNRAS, 400, 2070
Sturm, E., González-Alfonso, E., Veilleux, S., et al. 2011, ApJ, 733, L16
Svirski, G., Piran, T., & Krolik, J. 2015, ArXiv e-prints, arXiv:1508.02389 [astro-ph.HE]
Swesty, F. D., & Myra, E. S. 2009, ApJS, 181, 1
Tasitsiomi, A. 2006, ApJ, 645, 792
Tchekhovskoy, A., Narayan, R., & McKinney, J. C. 2011, MNRAS, 418, L79
Terrell, J. 1967, ApJ, 147, 827
Thomas, L. H. 1930, The Quarterly Journal of Mathematics, 1, 239
Tomida, K., Tomisaka, K., Matsumoto, T., et al. 2013, ApJ, 763, 6
Treister, E., Urry, C. M., & Virani, S. 2009, ApJ, 696, 110
Tremaine, S., Gebhardt, K., Bender, R., et al. 2002, ApJ, 574, 740
Tremonti, C. A., Moustakas, J., & Diamond-Stanic, A. M. 2007, ApJ, 663, L77
Turner, N. J., & Stone, J. M. 2001, ApJS, 135, 95
Ulmer, A. 1999, ApJ, 514, 180
Ulmer, A., Paczynski, B., & Goodman, J. 1998, A&A, 333, 379
van der Holst, B., Tóth, G., Sokolov, I. V., et al. 2011, ApJS, 194, 23
van Velzen, S., & Farrar, G. R. 2014, ApJ, 792, 53
van Velzen, S., Farrar, G. R., Gezari, S., et al. 2011, ApJ, 741, 73
Vaytet, N. M. H., Audit, E., Dubroca, B., & Delahaye, F. 2011, J. Quant. Spec. Radiat. Transf., 112, 1323
Verner, D. A., Ferland, G. J., Korista, K. T., & Yakovlev, D. G. 1996, ApJ, 465, 487
Vinkó, J., Yuan, F., Quimby, R. M., et al. 2015, ApJ, 798, 12
Vögler, A., Shelyag, S., Schüssler, M., et al. 2005, A&A, 429, 335
Whalen, D., & Norman, M. L. 2006, ApJS, 162, 281
White, O. R. 1961, ApJ, 134, 85
Whitehouse, S. C., & Bate, M. R. 2004, MNRAS, 353, 1078
Wise, J., & Abel, T. 2011, MNRAS, 414, 3458
Wollaeger, R. T., van Rossum, D. R., Graziani, C., et al. 2013, ApJS, 209, 36
Zel'dovich, Y. B., & Raizer, Y. P. 1969, Elements of gas dynamics and the classical theory of shock waves. (Academic Press)
Zel'dovich, Y. B. and Novikov, I. D. 1964, Dokl. Akad. Nauk. SSSR, 158, 311
Zhang, W., Howell, L., Almgren, A., et al. 2013, ApJS, 204, 7
Zheng, Z., & Miralda-Escudé, J. 2002, ApJ, 578, 33